Ocean changes in the North Atlantic over the Late Holocene: A multi-proxy approach

Paola Lucía Moffa Sánchez

Thesis submitted for the Degree of Doctor of Philosophy
Cardiff University

July 2012

Ocean changes in the North Atlantic during the Late Holocene:
A multi-proxy approach

In today's North Atlantic, warm and salty surface waters are transported northwards from the subtropics, releasing their heat and eventually sinking to form a deep southward-flowing water mass. This process in the meridional-vertical plane is termed the Atlantic Meridional Overturning Circulation (AMOC). Changes in the strength and structure of the AMOC play a critical role in the Earth's climate system and have been thought to be implicated in the climate variability of the Late Holocene.

In this thesis, two sediment cores RAPiD-35-25B and RAPiD-17-5P recovered from the Eirik Drift (South of Greenland) and the Iceland Basin are used to produce Late Holocene palaeoceanographic reconstructions of some of the main constituents of the AMOC at sub-decadal to multidecadal resolution.

Upper water column reconstructions from the Eastern Labrador Sea based on multi-species planktonic foraminiferal $\delta^{18}O$, Mg/Ca and faunal assemblages indicate millennial to centennial variability in the influence of polar waters reaching the Labrador Sea which likely led to reductions in deep water convection in the Labrador Sea. Inferred shifts of Labrador Sea Water formation appear concomitant with climatic anomalies recorded in the North Atlantic region. It is suggested that these climatic oscillations may have resulted from a coupled ocean-atmosphere response to reductions in solar irradiance.

The paired $\delta^{18}O$ and Mg/Ca composition of the thermocline-dweller *G. inflata*, shows multi-centennial shifts in the temperature and salinity of the North Atlantic Current during the last millennium with a potential link to solar forcing. The recorded hydrographic variability is explained in terms of the effects of atmospheric blocking events on subpolar gyre dynamics.

Sortable silt mean grain size measurements show millennial-scale trends towards slower and faster vigour of the overflows east and west of Iceland during the Late Holocene. Potential upstream and downstream mechanisms are investigated and it is concluded that the millennial-scale variability in the strength of the overflow likely resulted from insolation driven Neoglacial changes in the freshwater budget and atmospheric circulation in the Nordic Seas. Furthermore, an antiphasing relationship between the strength of the two overflows is found, supporting previous predictions from modelling studies.

Acknowledgments

I would first like to thank my main supervisor, Ian Hall for giving me the opportunity to explore the Late Holocene North Atlantic palaeoceanography. I am very thankful to Steve Barker for meticulously teaching me the Mg/Ca methodology and most importantly for always making me think. Someone I cannot thank enough is David Thornalley for all of his guidance and support and for fuelling my scientific motivation, curiosity and enthusiasm through ongoing exciting scientific discussions.

I am very grateful to Julia Becker for all of the isotope measurements and to NERC for funding the radiocarbon dates for this project. My thanks also go to Carl Schleussner and Andreas Born for useful discussions arising from the comparison between their model experiments and my data. Thanks to Igor Yashayaev for providing hydrographic data and for extensive discussions that contributed to understanding ocean changes from a physical oceanography perspective. Special thanks go to Sindia Sosdian, Laura Rodriguez Sanz and Anabel Morte Rodenas for not only all of their scientific and technical help but also for always being so caring and supportive.

I thank everyone from the palaeoclimate group in Cardiff for providing such a great and friendly working environment. Thanks also go to my office mates especially Tom, Margit, Laura and James for sharing some fun lab and office times. Thank you to all of my good friends and everyone who has been part of the Shirley family specially Adam, Poppy, Lucy, Denis, Duarte and Aldina for making the 4 years of my PhD so memorable and fun. Very special thanks to Ana, Carol, Julia and Maria for always being there and making my holidays worth working hard for!

Above all, I thank my parents and sister for their unconditional love and support. A special mention goes to my four grandparents for not only supporting but for also instilling the importance of education in us.

COMMONLY USED SYMBOLS AND ABBREVIATIONS

AD	Anno Domini
AMO	Atlantic Multidecadal Oscillation
AMOC	Atlantic Meridional Overturning Circulation
AWP	Atlantic Warm Pool
BP	Before Present
$\delta^{18}O_{sw}$	$\delta^{18}O$ of seawater
DSOW	Denmark Strait Overflow Water
DWBC	Deep Western Boundary Current
EIC	East Icelandic Current
EGC	East Greenland Current
ENSO	El Niño-Southern Oscillation
GSA	Great Salinity Anomaly
IC	Irminger Current
ITCZ	Intertropical Convergence Zone
ISOW	Iceland Scotland Overflow Water
LIA	Little Ice Age
LSW	Labrador Sea Water
MCA	Medieval Climatic Anomaly
NAC	North Atlantic Current
NADW	North Atlantic Deep Water
NAO	North Atlantic Oscillation
NIC	North Icelandic Current
NIIC	North Icelandic Irminger Current
NIJ	North Icelandic Jet
NSDW	Norwegian Sea Deep Water
NwAC	Norwegian Atlantic Current
SPG	Subpolar Gyre
SPMW	Subpolar Mode Water
STG	Subtropical Gyre
Sv	Sverdrup ($10^6 m^3/s$)
TSI	Total Solar Irradiance
WGC	West Greenland Current

CONTENTS

4. Changes in the Atlantic Inflow Properties During the Last 1200 years

5. Late Holocene Changes in the Vigour of the Nordic Overflows

1. Introduction

1.1. Holocene Climate

The climate during the present interglacial, the Holocene, has traditionally been regarded as being relatively stable in comparison to the large climatic shifts of the Late Pleistocene (Grootes and Stuiver, 1997). Yet, significant climate variability relevant to humans and ecosystems has recently been found in emerging palaeoclimatic records over a range of timescales (e.g. Mayewski et al., 2004, Wanner et al., 2011).

It is widely accepted that at millennial time-scales, the climate of the Holocone has been mainly shaped by a combination of the precession driven summer insolation changes reaching the northern high latitudes and ice-sheet feedbacks deriving from the melting of the last glacial remnants of the Fennoscandian and Laurentide ice-sheets (Renssen et al., 2009). Following the warmest time during the current interglacial, the Holocene Thermal Maximum (~5000 years Before Present (BP)), the Northern Hemisphere experienced a gradual climatic deterioration in response to the decline in northern high latitude summer insolation, which terminated at the end of the Little Ice Age (~1850) most likely as a result of the 20th century anthropogenic release in CO_2 (IPCC, 2007). This period is referred to as the Neoglacial, which was named after the increase in glacial advances recorded around the North Atlantic (Porter and Denton, 1967, Denton and Karlén, 1973).

The long-term climate variability during the Holocene was punctuated by a series of centennial-scale climatic shifts which have been identified in a variety of proxy archives centred at around 8200, 6300, 4700, 2700, 1550 and 550 years BP (Mayewski et al., 2004, Denton and Karlén, 1973, Wanner et al., 2011). A number of these oscillations have been found to be synchronous with and often responsible for societal collapses such as the collapse of the Akkadian Empire (4200 years BP) (Cullen et al., 2000), the Classic Maya collapse (750-900 years AD) (Hodell et al., 1995) and the demise of the Norse settlement in Greenland (~1400 years AD) (Barlow et al., 1997). These correlations highlight the potential importance that climatic changes at these time-scales may have on human civilisation.

The frequencies involved in these climatic perturbations are not yet fully understood. Some authors isolate in the North Atlantic palaeorecords a pervasive 1,500 year cyclicity (Bianchi and McCave, 1999, Bond et al., 1997, Thornalley et al., 2009, Debret et al., 2007); whereas others have argued for a 900 year, 550 year, 400 year cyclicities (Chapman and Shackleton, 2000, Schulz and Paul, 2002, Hall et al., 2004, respectively). However, recent exhaustive analysis of published Holocene palaeoclimatic reconstructions has challenged the presence of any persistent centennial to millennial pacing of the Holocene abrupt climate changes (Wanner et al., 2011).

The nature and causes of these oscillations are more uncertain than the millennial-scale variability. Climate model studies have proposed internal variability within the climate system as a driver of these climatic anomalies (e.g. Hall and Stouffer, 2001, Schulz and Paul, 2002, Schulz et al., 2007). However, correlation of solar irradiance proxy records derived from cosmogenic nuclides with climate data and corroboration from model experiments lend support to solar irradiance as the trigger (Mayewski et al., 2004, Bond et al., 2001, Hu et al., 2003, Wang et al., 2005, Renssen et al., 2006), which may have been amplified by ocean and atmospheric feedbacks (Wanner et al., 2011 and references herein).

1.1.1. Climate of the last millennium

The advent of new high resolution proxy archives with well-constrained dating such as tree-rings, corals, molluscs, speleotherms, ice-cores, varved sediments, documentary and historical records, has enabled detailed study of climate variability during last millennium (Jones et al., 2009). The last millennium contains the last two of the Holocene centennial climate oscillations, the Medieval Climatic Anomaly (MCA) and the Little Ice Age (LIA) (Figure 1.1). It is for this reason that the study of the climate of the last millennium provides a good opportunity to further our understanding of the nature and forcings that have governed multidecadal to centennial climate variability during the Holocene.

Although these climatic anomalies were spatially and temporally heterogeneous (Hughes and Diaz, 1994, Broecker, 2001, Bradley et al., 2003, Mann et al., 2009), they have been mostly recorded to be centred in the Northern Hemisphere particularly in the North Atlantic and neighbouring regions (Grove, 1988, Mann, 2002a, Mann, 2002b and

references therein). The MCA refers to a relatively warm period recorded in Europe approximately between 900-1200 years AD (Figure 1.1). During the MCA, the reduction of Arctic pack ice and drift ice reaching Iceland and Greenland enabled colonisation and settlement at these locations. The MCA was followed by the cold LIA (1450-1850 years AD) (Figure 1.1), a period of pronounced glacial advances in the circum-North Atlantic (Denton and Karlén, 1973). The cold and prolonged winters led to crop failure and decline in the fish stocks such as cod, conditions that led to famine and widespread population reductions across Europe.

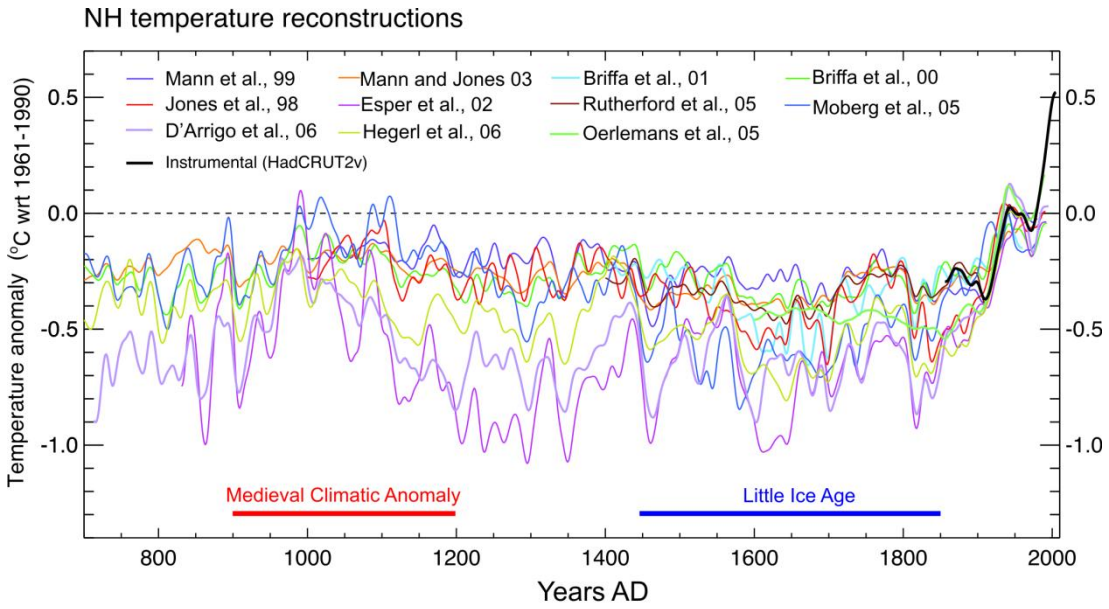

Figure 1.1. Northern Hemisphere temperature anomaly reconstruction from published proxy records (in colour) and instrumental record (in black). Adapted from IPCC(2007).

Change in solar irradiance has been one of the most commonly attributed external forcings for the MCA and the LIA (e.g. Stuiver et al., 1997, Shindell et al., 2003, Ammann et al., 2007). During the LIA solar irradiance records show a cluster of four distinct solar minima (Wolf, Sporer, Maunder, Dalton), unlike the MCA which was mostly dominated by solar maxima (Figure 1.2a). Changes in the solar activity were initially documented by sunspot observations (Eddy, 1976) (Figure 1.2a), but as these only extended back to 1600 years AD cosmogenic nuclides such as ^{14}C in tree-rings and/or ^{10}Be in ice-cores, have been used to estimate past changes in solar irradiance.

Radiocarbon and beryllium-10 are formed in the atmosphere as a result of the interaction between cosmic ray particles and atmospheric nitrogen and oxygen atoms, respectively. Changes in the intensity of the galactic cosmic rays reaching the Earth's atmosphere are

modulated by the solar magnetic field which is directly related to the activity of the Sun (Gray et al., 2010). Periods of strong solar activity correspond to stronger solar magnetic fields which shield the Earth and deflect galactic cosmic rays into space thereby increasing the formation of cosmogenic nuclides. Additionally, the intensity of incoming cosmic rays can also be modified by the Earth's magnetic field which has been reconstructed for the Holocene using palaeointensity data (Knudsen et al., 2008) and it is accounted for when calculating the solar irradiance signal within the cosmogenic nuclei (Masarik and Beer, 2009). Once these cosmogenic isotopes have formed, ^{14}C combines with CO_2 and enters the carbon cycle leaving an annual signal in tree-rings and in the case of ^{10}Be it precipitates and is deposited in polar ice. Aside from the geomagnetic and solar effects on cosmogenic nuclei production, changes in their abundance may have resulted from system effects due to either changes in the partitioning of ^{14}C between the atmosphere and the ocean reservoirs, or for ^{10}Be changes in atmospheric circulation. However, system effects on ^{10}Be are in the order of less than 40 years and therefore can be overcome by smoothing the records. Furthermore, reconstructions of total solar irradiance forcing from the two different cosmogenic nuclei show a high coherence for the entire Holocene (e.g. Bard et al., 2000, Steinhilber et al., 2009, Vieira et al., 2011, Steinhilber et al., 2012) (Figure 1.2a) which implies that changes in carbon cycling had no effects on the abundance of cosmogenic isotopes.

Additionally, the injection of aerosols, particularly sulphate aerosols, into the stratosphere from large explosive volcanic eruptions can scatter incoming solar radiation reaching the Earth's surface. Volcanic eruptions produce sulphur oxides which rise into the stratosphere and combine with water forming sulphuric acid droplets, these particles are lightly coloured and about the same the same size as visible light, and therefore scatter solar radiation back into space increasing the planetary albedo and thus reducing the amount of solar energy that reaches the Earth's surface (Robock, 2000). Sulphate aerosols will also absorb solar and terrestrial radiation within the stratosphere. The net effect of these processes results in cooling of the troposphere and heating of the stratosphere and this will last until these droplets grow bigger due to collision and eventually get washed down, a process that lasts in the order of 1-3 years (Robock, 2000, Bradley, 1988). The radiative effect of volcanic eruptions is therefore dependent on the sulphur loading, the penetration of the volcanic plume into the stratosphere and also the latitude of the volcanic eruption. For instance tropical volcanic eruptions will

increase the latitudinal temperature gradient which will modify the positioning of the polar vortex therefore affecting the atmospheric circulation. Since the radiative forcing of volcanic eruptions is related to the sulphur loading reaching the stratosphere, the combined study of sulphate concentrations in ice-cores complemented by dispersion models has enabled the reconstruction of the frequency and magnitude of past volcanic eruptions (Cole-Dai et al., 2000, Crowley, 2000, Gao et al., 2007). The latest and most complete reconstruction reveals that during the last millennium, three of the major eruptions (1258, 1450, 1805 years AD) coincide with solar minima (Figure 1.2) (Gao et al., 2007). Furthermore, the frequency and magnitude of volcanic eruptions increased at ~1175 years AD (the end of the MCA). The similar timing of the solar minima and volcanic activity has made the separation of their relative influence to the climate variability of the last millennium difficult and controversial.

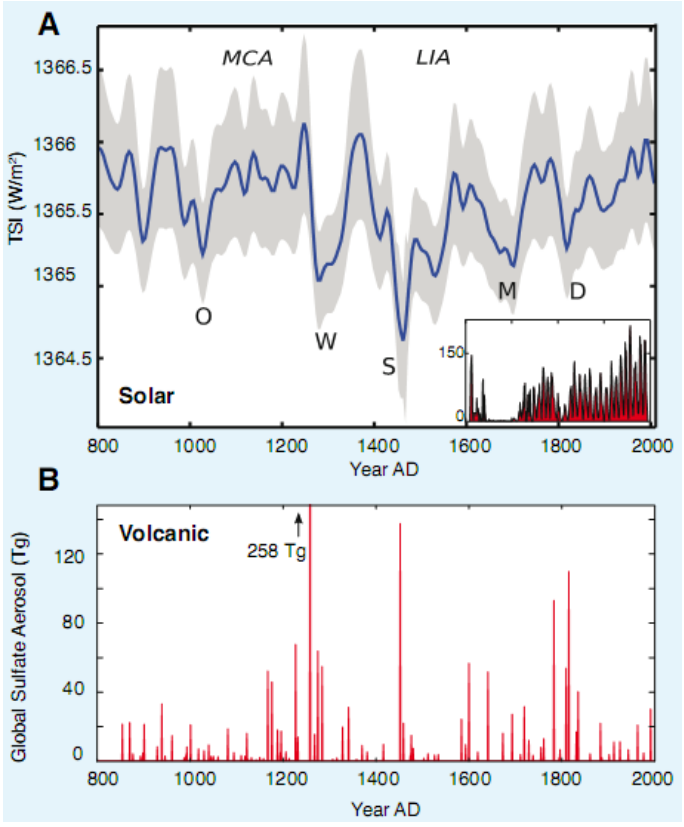

Figure 1.2. (A) Beryllium-based Total Solar Irradiance forcing for the last 1200 years (Steinhilber et al., 2009), inset shows the sunspot record obtained from telescope observations (Eddy, 1976) (solar minima indicated by initials O: Oort; W: Wolf; S:Sporer; M:Maunder; D:Dalton) (B) Total global stratospheric volcanic sulphate aerosol injection in Teragrams (Tg) (Gao et al., 2007).

The external forcings described above are not solely sufficient to explain the magnitude of the climatological changes experienced in the North Atlantic region. Thus, internal feedback mechanisms within the climate system must have amplified these triggers (e.g. Goosse et al., 2005).

1.2. Climate Amplifiers

Modern climate variability over the North Atlantic Ocean comprises three interrelated and complex phenomena: Tropical Atlantic Variability, North Atlantic Oscillation (NAO) and Atlantic Meridional Overturning Circulation (AMOC) with minor contributions from teleconnections such as El Niño-Southern Oscillation (ENSO) and the Asian Monsoon (Grossmann and Klotzbach, 2009, Marshall et al., 2001, Hurrell et al., 2006). The degree of coupling and the relative contribution of these systems to shaping the contemporary North Atlantic climate have yet to be fully resolved. The two most relevant climatic phenomena which have been frequently proposed as amplifiers of the external forcings during the Holocene are the AMOC and the NAO.

1.2.1. The Atlantic Meridional Overturning Circulation

Ocean circulation is driven by a combination of processes comprising wind forcing, density gradients and internal mixing of the oceans by tides (Rahmstorf, 2002). The Thermohaline Circulation (THC) refers to the changes in heat and freshwater fluxes at the sea surface which cause subsequent vertical mixing and density-driven ocean circulation. The large-scale pattern of the THC has also been referred to as the ‘global ocean conveyor belt’ (Broecker, 1991) (Figure 1.3). The subpolar North Atlantic is a key region for understanding climate variability, as it is one of the main localities of deepwater formation, a process that sets forth the ocean conveyor belt (Figure 1.3).

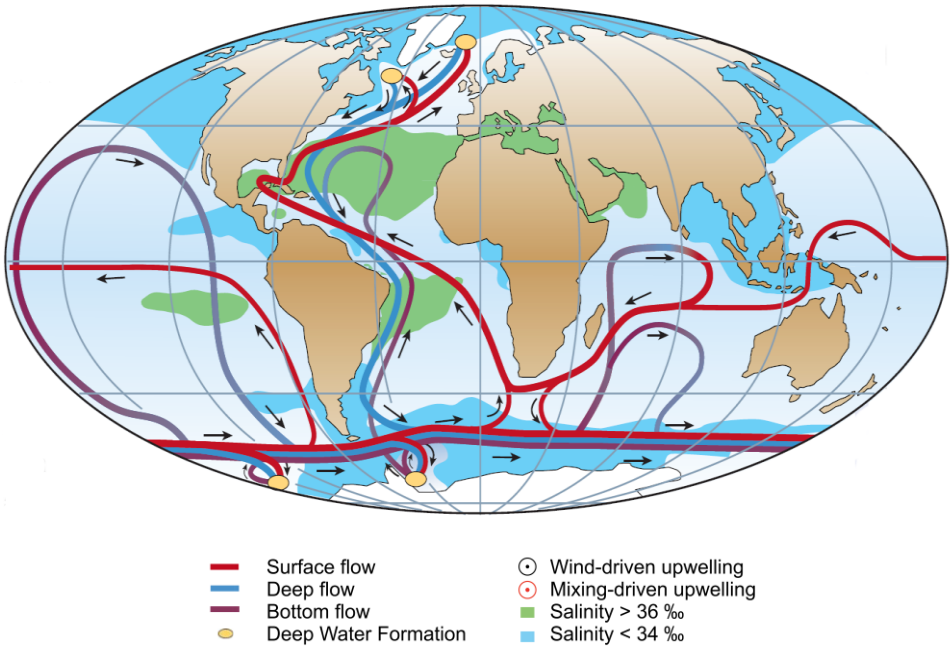

Figure 1.3. The global THC or the ocean conveyor belt (Rahmstorf, 2002).

In today's Atlantic Ocean, warm salty surface subtropical waters travel northwards within the North Atlantic Current, release their latent heat and eventually sink to form intermediate and deep water masses in the Nordic Seas. The newly formed dense waters flow over the submarine ridge which lies between Greenland and Scotland, into the North Atlantic as the Nordic Overflows. Downstream entrainment and mixing with intermediate water masses formed by open ocean convection such as Subpolar Mode Waters and Labrador Sea Water will further modify the overflows transport and properties (Figure 1.4). The combination of all of these intermediate and deep waters forms the precursor of the deep southward flowing water mass known as the North Atlantic Deep Water, a key constituent of the deep limb of the global THC. This ocean circulation process in the meridional-vertical plane is termed the Atlantic Meridional Overturning Circulation (AMOC). Changes in the strength and structure of the AMOC play a critical role in the Earth's climate variability through the distribution of heat, nutrients and gasses (Rahmstorf, 2002). Additionally, the AMOC's attendant northward heat transport contributes to maintaining the mild climate of Northwest Europe (Seager et al., 2002)

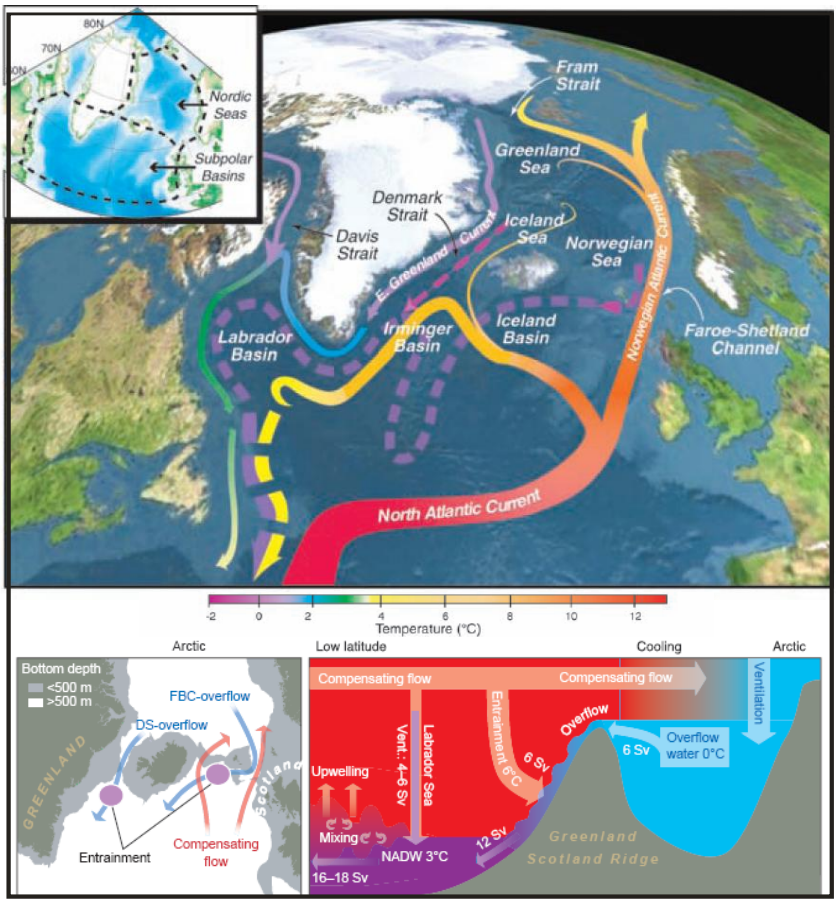

Figure 1.4. (Upper panel) Schematic circulation of surface currents (solid curves) and deep currents (dashed curves) of the AMOC. Colours indicate approximate temperatures (Curry and Mauritzen, 2005). (Lower panel) Vertical profile of the AMOC across the GSR and plan view of the pathways taken by the surface and deep limbs of AMOC (Hansen et al., 2004).

For the last 30 years a large scientific effort has focused on the direct monitoring and estimation of the variability of the AMOC strength (e.g. Hall and Bryden, 1982). The transport is estimated from geostrophic calculations based on the isopycnal gradients recorded from a mooring along a longitudinal transect across the Atlantic Basin (at 26.5^{o}N), which are complemented by a set of current metres located in the shallow and deep boundary currents. Direct transport estimates are sparse and temporarily discontinuous and the temporal coverage is thus not enough to study multidecadal variability of the strength of the AMOC. Nevertheless, so far they have revealed a large intrannual to interannual variability of the AMOC strength with a mean and standard deviation of ~18.4 ±5 Sv (1 Sverdrup=10^6 m^3 s^{-1}) (Bryden et al., 2005, Cunningham et al., 2007).

Numerical models and palaeoclimate data show that alterations in the AMOC's strength and structure have led to abrupt climate changes in past ocean circulation and climate during the past 120,000 years (Stommel, 1961, Clark et al., 2002, see Rahmstorf, 2002 for a review). In the future, modelling studies predict a 25-30% weakening of the AMOC from present values by 2100, under current anthropogenic CO_2 forcing, mainly as a result of an increase in high-latitude temperature as well as an increase in high-latitude freshwater input (Schneider et al., 2007, Gregory et al., 2005, Manabe and Stouffer, 1993, Vellinga and Wood, 2008, IPCC, 2007). However, considerable scatter and uncertainty remains amongst future AMOC predictions.

1.2.2. The North Atlantic Oscillation

The North Atlantic Oscillation (NAO) is the dominant pattern of atmospheric variability in the North Atlantic (Hurrell, 1995), accounting for 32% of monthly sea-level pressure variability and a greater variance during the boreal winter (December to March) (Hurrell, 1995). The NAO is often defined by an index of normalized, time-averaged pressure differences between stations in its two centres of action, the Icelandic Low and the Azores High (Figure 1.5).

There is ample evidence showing that much of the atmospheric circulation variability associated with the NAO arises from the internal, nonlinear dynamics of the extratropical atmosphere (Thompson et al., 2003). Since such intrinsic atmospheric variability exhibits little temporal coherence, the phase and amplitude of the NAO remains largely unpredictable (Hurrell and Deser, 2009). However, a number of different feedback mechanisms can influence the state of the NAO such as downward influences from the lower stratosphere (Gillet et al., 2003), interaction of the atmosphere with the underlying ocean (Visbeck et al., 2003, Sutton and Hodson, 2005) and sea ice and land snow cover (Deser et al., 2000).

Swings in the NAO state produce changes in the positioning and strength of the westerly winds across the mid-latitudes. These changes will affect key ocean process which are mainly wind driven such as the transport within the North Atlantic Current, open ocean convection in the Labrador and Greenland Sea, sea ice transport into the North Atlantic, and circulation of the surface gyres which significantly alter the transport of heat and moisture and have an impact on temperatures and regional

precipitation patterns in the North Atlantic region. For instance, the NAO state induces changes in the properties and surface ocean circulation through the air-sea heat and freshwater interaction with important implications for the AMOC. Some of the main effects of the NAO on the AMOC comprise changes in sea surface temperatures in the Atlantic, open ocean convective activity in the Labrador Sea and Greenland Sea (Dickson et al., 1996), Subpolar and Subtropical gyre dynamics (Bersch et al., 2007, Curry and McCartney, 2001) and Arctic sea-ice extent and transport (Deser et al., 2000).

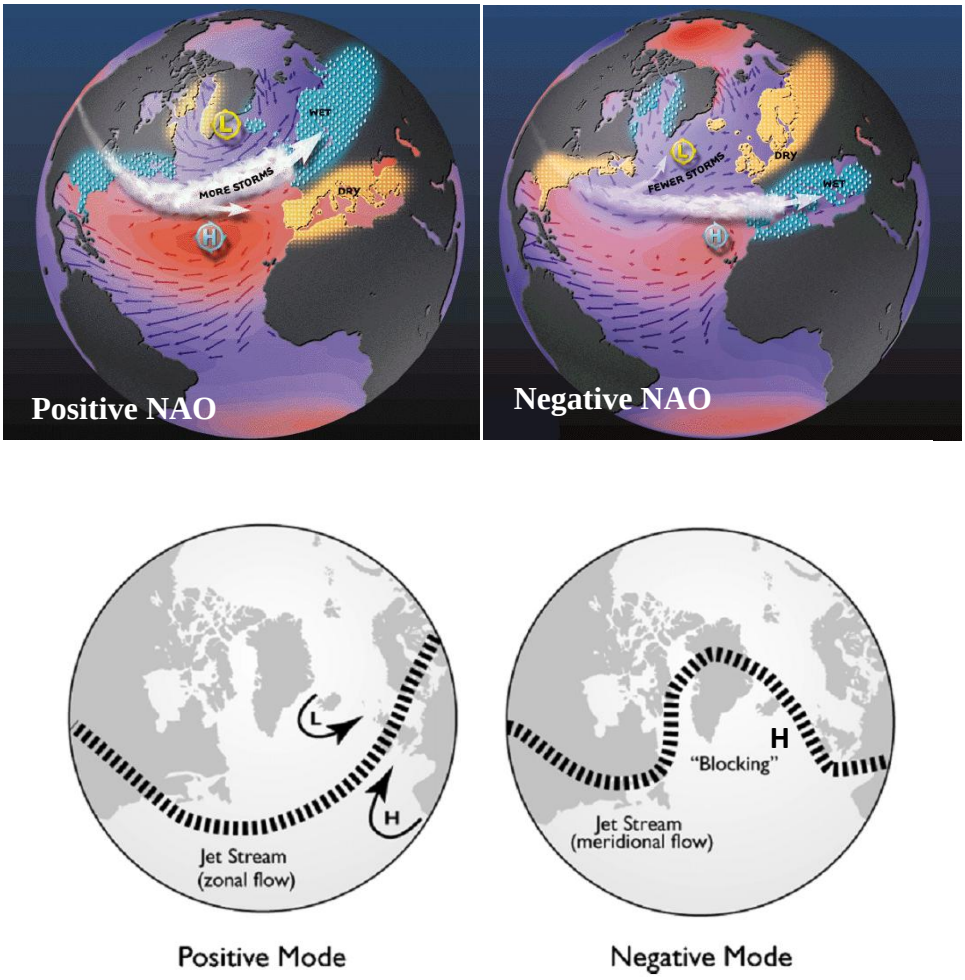

Figure 1.5. A positive state of the NAO corresponds to large pressure differences between Icelandic Low and Azores High, which results in stronger westerlies. This leads to a intensified westerlies and zonal flow and more heat and moisture being transferred to northwest Europe. The result is an increase in precipitation and milder climate in this region, and cooler dryer conditions in the Mediterranean (left). A negative NAO gives rise to weaker westerlies and stronger northerlies (a more meridional wind pattern) which corresponds to a drier and cooler northwest Europe and a wetter Mediterranean region (right) http://www.ldeo.columbia.edu/NAO by Martin Visbeck (top diagrams) and Jessen et al. (2011) (bottom diagrams). The lower schematic diagrams illustrate the positioning of the Jet Stream during a positive and negative NAO and the presence of blocking events during a negative NAO state.

An emerging view derived from models and observational data is that frequency and persistency of atmospheric blocking events in the eastern Atlantic may play a more important role in the North Atlantic climate dynamics and subpolar North Atlantic ocean circulation than the NAO state (e.g. Häkkinen et al., 2011, Langehaug et al., 2012). Atmospheric blocking events are mid-latitude weather patterns where a quasi stationary high pressure system located west of the British Isles modifies and diverts the eastward flow of the jet stream by blocking its pathway (Figure 1.5). These weather systems predominantly develop in the winter and tend to be associated with a negative NAO state (Luo, 2005, Shabbar et al., 2001) and are also responsible for European cold and dry spells (Buehler et al., 2011) such as that of 2009 and 2010 winters (Cattiaux et al., 2010).

1.2.3. Climate amplifiers and North Atlantic climate variability during the last millennium

Changes in the AMOC and the NAO have often been attributed to have played a role particularly for the onset of the LIA. Several lines of evidence have highlighted the implication of the AMOC in these climatic changes (e.g. Bianchi and McCave, 1999, Bond et al., 2001, Keigwin and Boyle, 2000, Denton and Broecker, 2008, Lund et al., 2006) and have suggested a reduction in the AMOC's strength during the cold interval of the LIA. A concomitant change in the atmospheric pattern over the North Atlantic during these climatic oscillations was initially suggested by Lamb (1965, 1979). Numerous modelling and proxy studies have shown a shift from a predominantly positive to negative NAO during the MCA-LIA transition (Shindell et al., 2001, Spangehl et al., 2010, Swingedouw et al., 2011, Trouet et al., 2009, Trouet et al., 2012, D'Arrigo et al., 2012). However, the forcing of the last millennium NAO shifts is still debated.

Some models have proposed amplification of solar irradiance variability via internal atmospheric feedbacks involving stratospheric ozone (Haigh, 1994, Shindell, 1999, Shindell et al., 2001). Ultraviolet (UV) radiation plays a key role in the formation of stratospheric ozone by dissociating oxygen molecules. In turn ozone destruction occurs from the interaction of longer wavelength solar heating with ozone molecules. Changes in solar irradiance are not uniform across the spectrum and the amplitude of change is 4-6 times higher in the UV range (Haigh et al., 2010). During periods of solar maxima a

larger increase in UV radiation will favour stratospheric ozone formation over destruction. The production of ozone is an exothermic reaction and therefore changes in ozone production will affect stratospheric temperatures which have been modelled to propagate downwards into the troposphere affecting atmospheric circulation patterns including the NAO state (Haigh, 1996, Shindell, 1999, Shindell et al., 2001). However, recent modelling studies have compared two externally forced model simulations (including changes in solar activity, volcanic eruptions and greenhouse gas concentrations) between 1630-2000 years AD with and without photochemical changes in ozone (Spangehl et al., 2010). Both simulations showed a transition towards a positive NAO state from the Maunder Minimum to the present, thereby implying the minor role that ozone feedbacks may have in the amplification of solar irradiance forcing (Spangehl et al., 2010).

Additionally, modern observations have shown strong solar modulation of the blocking frequency during the 11-year solar cycles for the last 50 years (Barriopedro et al., 2008, Woollings et al., 2010b) with important impact on UK winter temperatures. This solar modulation of the atmospheric systems is consistent with the palaeorecord, periods of solar minima such as the Maunder Minimum have been shown to correspond to low temperatures from Central England Temperature which were likely linked to periods of increase blocking and/or negative NAO state (Lockwood et al., 2011, Lockwood et al., 2010). This strong regional atmospheric response to solar forcing is still highly debated but it has been explained in terms of wind response to the changes in stratospheric temperatures forced by changes in UV radiation which can affect tropospheric dynamics and hence variability of the jet stream (Woollings et al., 2010b, Ineson et al., 2011).

Modern observations have shown that changes in ENSO have an important influence on atmospheric dynamics in the North Atlantic region, in particular the NAO state (Hoerling et al., 2001). Model and proxy data have also suggested that teleconnections from the tropical Pacific mainly changes in ENSO were likely involved in the amplification of the external forcings that lead to a shift towards a negative NAO state at the onset of the LIA (Mann et al., 2005, Graham et al., 2007, Swingedouw et al., 2011). The sensitivity of ENSO to radiative forcing arises from the differential response of the east and west tropical Pacific sea surface temperatures through a mechanism known as the ocean thermostat. Due to the slope in the depth of the thermocline across

the tropical Pacific, uniform changes in radiative forcing will cause an increase in the longitudinal temperature contrast, affecting the atmospheric circulation over the tropical Pacific. This anomalous ocean-atmosphere pattern may then propagate to the North Atlantic via modification of the Hadley cells and tropical sea surface temperatures (Hoerling et al., 2001, Rodwell et al., 1999, Pozo-Vázquez et al., 2001).

While an increasing number of high-resolution terrestrial proxy records spanning the Late Holocene have become available in recent years providing an increasingly powerful reference frame for assessing past, present and future climate conditions, a critical lack of similar quality quantitative proxy records of ocean change still remains. This is primarily due to the scarcity of highly temporally resolved marine sediment archives from which high resolution palaeoceanographic reconstructions of the ocean changes in the subpolar North Atlantic, specifically the AMOC can be reconstructed. It is for this, that the ocean-atmospheric climate feedbacks and their response to external forcings involved in the decadal to multi-centennial variability during the Late Holocene still remains unclear. Establishing and understanding natural instabilities of the AMOC beyond the instrumental record is essential in order to accurately predict future climate change under increasing anthropogenic forcing.

1.3. Aims of the Thesis

The overall aim of this study is to develop our understanding of the forcing and response sequences involved in natural variability of the North Atlantic ocean-climate system at multidecadal to millennial time-scales during the Late Holocene. Particular emphasis is placed in the investigation of the potential role of the AMOC on multidecadal to millennial climate variability during the Late Holocene.

The specific scientific objectives of this work are:

- To study the variability of the key AMOC water masses and processes in the subpolar North Atlantic over the last three millennia. The palaeoceanographic reconstructions will comprise:
    - the inference of multidecadal to millennial variability in Labrador Sea Water convection from the reconstruction of the upper water column structure of Eastern Labrador Sea.

  - the reconstruction of hydrographic variability of the North Altantic Current and the study of its linkages to subpolar gyre strength.
  - the reconstruction of near-bottom flow speed changes of the two deep Nordic Overflows (the Iceland Scotland Overflow Water and Denmark Strait Overflow Water) with the objective to investigate the potential mechanisms for this variability and study the relationship between the vigour of the two overflows.
- To investigate the Late Holocene coupling between the ocean and atmospheric dynamics in the North Atlantic and their response to external forcings.
- To study the relationship between ocean and climate variability in the North Atlantic region. This will provide an insight of the potential role of the AMOC and will improve our understanding of the causes and mechanisms that might have governed the Late Holocene climate at a range of time-scales.
- To analyse the possible periodicities present in the palaeoceanographic reconstructions to gain information about the nature of these oscillations.

1.4. Outline of the Thesis

In Chapter 2, the sedimentary setting and the description of the two marine sediment cores used in this study will be presented. Additionally, the palaeoceanographic proxies and statistical analysis are introduced and reviewed. Procedural and analytical details of the preparation and processing of the sediment samples is also given.
The three following chapters present and discuss the results obtained during this study. Each of these will focus on the study of the variability of specific key AMOC water masses during the Late Holocene. The AMOC water masses and processes will comprise: the formation of Labrador Sea Water, hydrographic variability of the North Atlantic Current and changes in the vigour of the Nordic Overflows.

The Labrador Sea is one of the most important locations of open deep water convection in the world's ocean. The intermediate water masses formed as a result of this process play a key role in the downstream entrainment of the overflows and govern the strength of the subpolar gyre. In Chapter 3, changes in summer surface water column structure in the Eastern Labrador Sea Water over the last 3000 years are reconstructed using a suite of palaeoproxies comprising paired Mg/Ca and $\delta^{18}O$ measurements on different depth-habitat planktonic foraminifera species, and faunal assemblage counts. The first part of

the results and discussion section explores the multidecadal ocean variability for the last 1200 years focusing on the onset of the LIA and the second part will focus on the centennial and millennial scale surface ocean variability during the Late Holocene (last 3000 years).

The North Atlantic Current is the main conduit of salty warm waters to the high latitudes. Its hydrographic variability is crucial for deepwater formation and the northward transport of heat. The study of sub-decadal to centennial variability for the last millennium in the hydrographic properties of the North Atlantic Current in the Iceland Basin is presented in Chapter 4. Temperature and salinity reconstructions are produced using paired Mg/Ca and $\delta^{18}O$ measurements from the thermocline-dweller *G. inflata* on a sediment core from the Iceland Basin. The results will be discussed in terms of the linkage between atmospheric forcing on subpolar gyre dynamics and hydrographic properties of the North Atlantic Current.

The Nordic Overflows are the densest waters contributing towards the deep limb of the AMOC. In Chapter 5 the vigour of the two Nordic Overflows, the Denmark Strait Overflow Water and the Iceland Scotland Overflow Water are studied using the near-bottom flow speed proxy: sortable silt mean grain size. Potential upstream and downstream mechanisms leading to Late Holocene millennial-scale variability in the vigour of the overflows are thoroughly explored. As a consequence of this exercise, a comparison between the records presented in this study arises.

The conclusions from the key findings presented in this thesis are summarised in Chapter 6. Additionally, potential future further work will be outlined.

2. Materials and Methodology

The marine sediment cores used in this study were recovered during the *RRS Charles Darwin* cruise number 159 in July 2004 (McCave, 2004) as part of the palaeoceanographic component of the RAPiD Climate Change Programme funded by the Natural Environmental Research Council, UK. The overriding scientific goal of the cruise was to recover highest resolution marine sediment cores in order to produce palaeoceanographic records of hydrographic changes associated with abrupt climate variability during the last 16,000 years.

The aim of this chapter is to describe the regional and sedimentary setting of the marine sediment cores and to give a brief overview of the methodologies that have been used in this study to reconstruct past ocean changes, also known as proxies.

2.1. Regional Sedimentary Setting

Sedimentary contourite-drifts are prominent depositional seafloor features of the North Atlantic Ocean and constitute 20% of the sediment mass between the Charles Gibbs Fracture Zone and the Greenland Scotland Ridge (GSR) (Wold, 1994) (Figure 2.1). Deposition and evolution of these sedimentary drifts is driven by the geostrophic boundary currents (such as the Nordic Overflows and the Deep Western Boundary Current (DWBC)) and controlled by pre-existing topography and sediment supply (McCave and Tucholke, 1986). The lateral sediment transport and deposition by deep ocean currents results in high sedimentation rates (typically 10-20 cm/kyrs compared to pelagic deposition 1-2 cm/kyrs), which make sediment drifts invaluable primary archives in the study of high-resolution palaeoceanography.

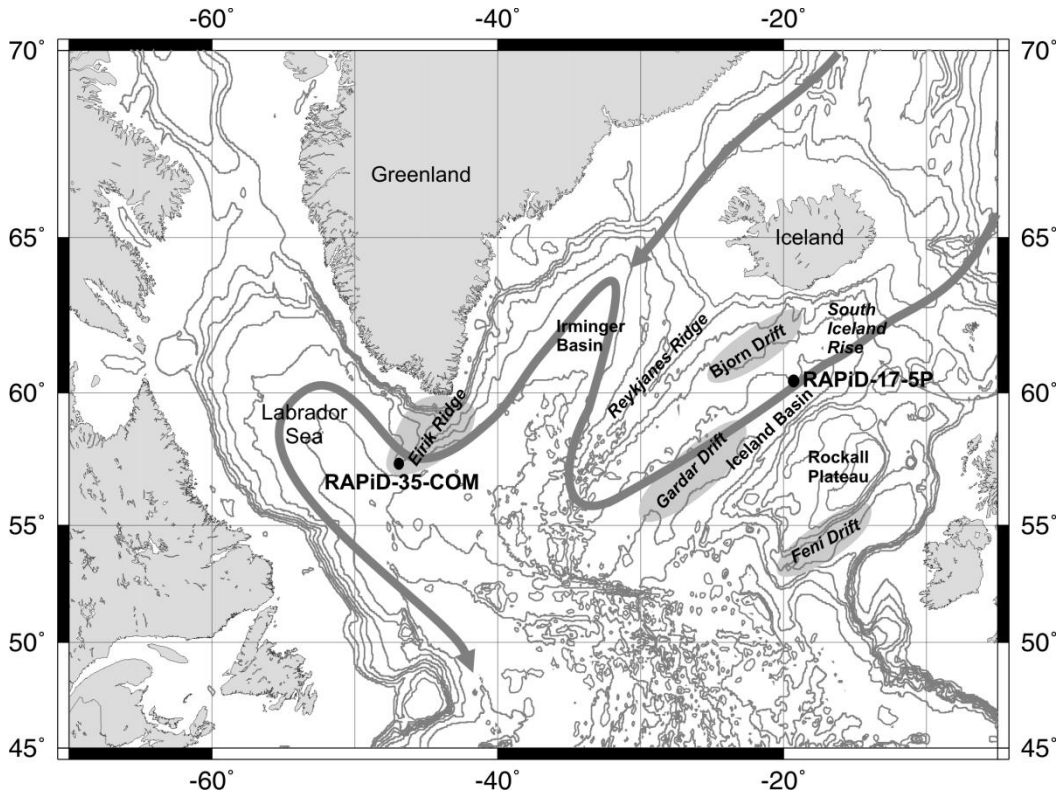

Figure 2.1. Bathymetric map of the North Atlantic showing the main contourite drifts (shaded in grey). Locations of RAPiD-17-5P and RAPiD-35-COM are indicated. A deep circulation scheme of the Nordic Overflows and the DWBC is outlined by light grey arrows.

2.1.1. Eirik Ridge

The Eirik Ridge is an elongate, mounded sediment drift with a length to width ratio of 2:1 which lies off Cape Farewell, the southern tip of Greenland (Hunter et al., 2007a). The main ridge crest extends 360 km in a southwest direction from the Greenland continental slope (~1500 m) to 3500 m deep. The southern flank of the ridge is relatively steep and has a slope of ~1.3^{o}, whereas the ridge and the northern flank present slope changes between 0.3-1.3^{o}, mainly because it contains three secondary ridges running Northwest which reflect Pliocene drift topography (Figure 2.2) (Hunter et al., 2007a).

The tectonic setting for the evolution of the Eirik Ridge comprises the basin formation and rifting of the Labrador and North Atlantic Basins and the GSR subsidence, which allowed flow of deep water into the North Atlantic during the Mid-Miocene (Hunter et al., 2007b). Since then the Eirik Drift has formed as a result of the deposition of sediment eroded from the Denmark Strait and along the Greenland continental slope and transported by the deepwater flow of the DWBC (Hunter et al., 2007a). When the

DWBC reaches Cape Farewell, the Coriolis force causes the current to reverse its direction to predominantly flow north into the Labrador Sea along the West Greenland Margin. The loss of velocity associated with the reversal of the bottom current direction results in deposition of the suspended sediment and hence the formation of the Eirik Drift (McCave and Tucholke, 1986). The drift contains a sedimentary record ranging from Early Pliocene to Holocene with extraordinarily high sedimentation rates especially in the deeper sections which are dominated by the Denmark Strait Overflow Water (DSOW) (Hunter et al., 2007b, Stanford et al., 2011). The large deposition of laterally transported sediment enables decadal to centennial resolution palaeoceanographic reconstructions spanning the Holocene.

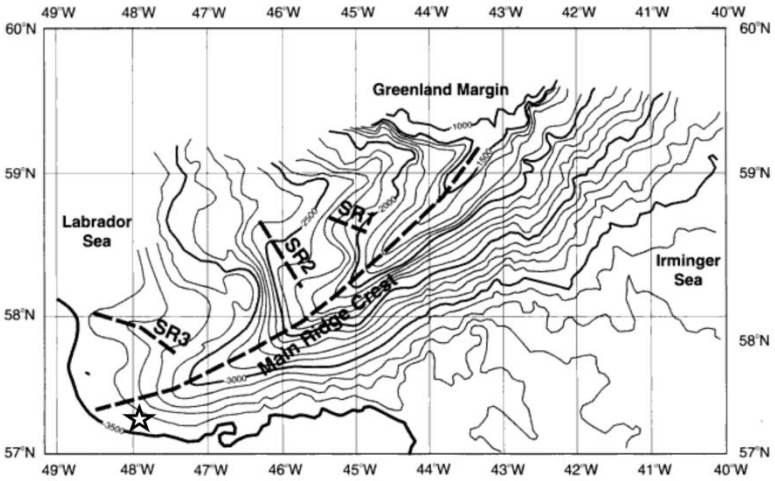

Figure 2.2. Bathymetric Map of the Eirik Ridge. Positions of the main and secondary ridges are highlighted by the dashed lines and the star indicates the location of RAPiD-35-COM (Hunter et al., 2007b).

Sediment core RAPiD-35-14P and its companion box-core RAPiD-35-25B (57° 30.25'N, 48° 43.34'W, 3484 m water depth and 57° 30.47'N, 48° 43.40'W, 3486 m water depth, respectively), were recovered from the eastern Eirik Ridge (Figure 2.1). The length the box-core and the piston-core was 44 cm and 21 m, respectively. The two cores were spliced using radiocarbon dating and weight % of the coarse fraction (further details in Section 3.2.2). The spliced core will be referred as RAPiD-35-COM hereinafter. The cores were light grey silty clay with sub-centimetre scale greenish laminae and light bioturbation throughout.

The core site is at a key location for monitoring past changes in some of the crucial AMOC water masses. At depth, the site lies in the pathway of the DWBC with a dominating signal of DSOW, the Nordic Overflow that flows west of Iceland (Holliday et al., 2009). At the site the surface and intermediate depths are bathed by the Subpolar Mode Waters and Labrador Sea Water with incursions of the Irminger Current and East Greenland Current. A detailed surface and deep oceanographic setting for this core will be given in Section 3.2.1 and 5.2.1, respectively.

2.1.2. South Iceland Basin

The South Iceland Basin is bound by the Iceland-Faroe Ridge to the north and the Reykjanes Ridge and Rockall Plateau to the northwest and southwest, respectively. The basin extends and deepens to the south. The presence of numerous sediment drifts in the Iceland Basin such as the Bjorn, Gardar and Hatton Drifts are a result of the supply of sediment from Iceland and the transport and deposition of this by the deep density driven current; the Iceland Scotland Overflow Water (ISOW) (Bianchi and McCave, 2000) (Figure 2.3).

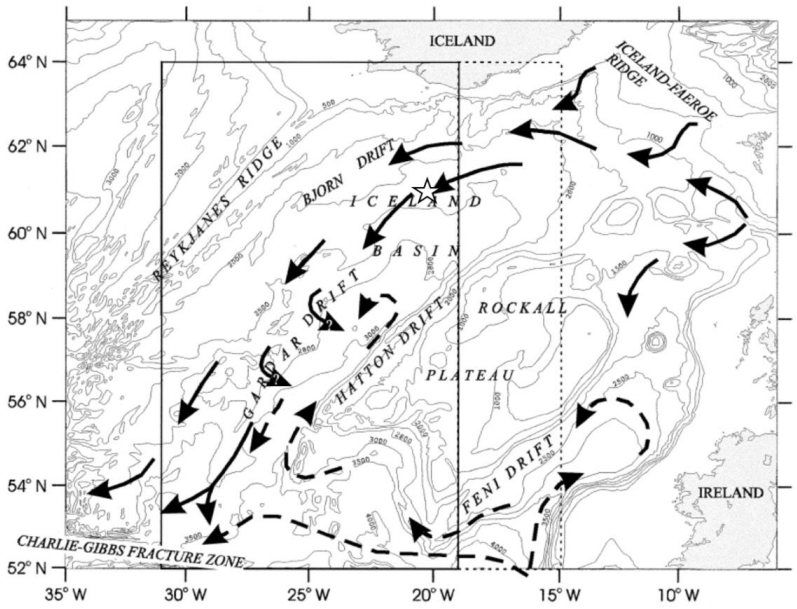

Figure 2.3. Bathymetric map of the Iceland Basin. Black arrows indicate the pathway of the ISOW, the core site of RAPiD-17-5P is indicated by a star.

Core RAPiD-17-5P (61° 28.90'N, 19° 32.16'W, 2303 m water depth) is situated on the northern edge of the South Iceland Basin as the deeper part of the south insular rise of Iceland (Figure 2.3). The RAPiD-17-5P site lies to the west of the Myrladsjokull

Suprafan (Shor, 1974) and as a result of the sediment supply from this sedimentary feature transported east via the deep current ISOW, contains an extended Holocene section (~9 m) (Section 4.2.1).

Numerous hydrographic studies and cruise CTD data show that the core location lies in the pathway of the ISOW and the surface waters are bathed by the Atlantic Inflow more specifically of the North Atlantic Current entering the Nordic Seas (Østerhus et al., 2005, Rossby and Flagg, 2012, Orvik and Niiler, 2002). The detailed description of the surface and deep oceanographic setting of this core will be described in detail in Section 4.2.1 and 5.2.1, respectively.

2.2. Physical Properties

The measurement of physical properties in sediment cores generally provides a rapid and non-destructive method for an initial characterisation of the nature and composition of the sedimentary sequences, and provide us with primary means for stratigraphic and core correlation. Colour reflectance and magnetic susceptibility properties are used as an indicator for changes in the sediment composition that could potentially be linked to climate controlled depositional processes (for example varying proportions of biogenic versus terrigenous components).

Magnetic susceptibility measurements were carried out on board using a Bartington MS2 magnetic susceptibility meter with either a MS2F probe or a 125 mm MS2C loop sensor, and measurements were made at constant temperature (6^{o}C) and at 2 cm intervals. A handheld Minolta Series CM-503c Spectrophotometer with a measurement area of 3mm in diameter and 45^{o} illumination/0^{o} viewing angle was used to measure light reflectance every 2 cm. Measurements were carried out as soon as possible after core recovery to avoid colour change. The instrument was calibrated prior to each new measurement series using the Minolta white calibration standard. The spectrophotometer measures the spectral reflectance of sediment colour that once calibrated to sediment geochemistry provides an indirect indication of sediment geochemical variation (e.g. the down-core carbonate concentration variation). The output of the colour measurements are numerical absolute colour values for L*, a*, b* (which refer to Lightness (L*), and chromacity (a* and b*) and reflectance wavelengths from 400-700 nm at 10 nm increments.

The physical properties of the Late Holocene sections of the cores RAPiD-35-14P and RAPiD-17-5P exhibit mostly uniform Lightness (*L), magnetic susceptibility and weight % of the Coarse Fraction (% CF; wt % >63 μm, see 2.3) (Figure 2.4c,d) suggesting no obvious changes in the proportions of the sediment composition in the core intervals used in this study (Figure 2.4c,d) and indicates that the sedimentary archive is likely intact without any significant influence from reworking.

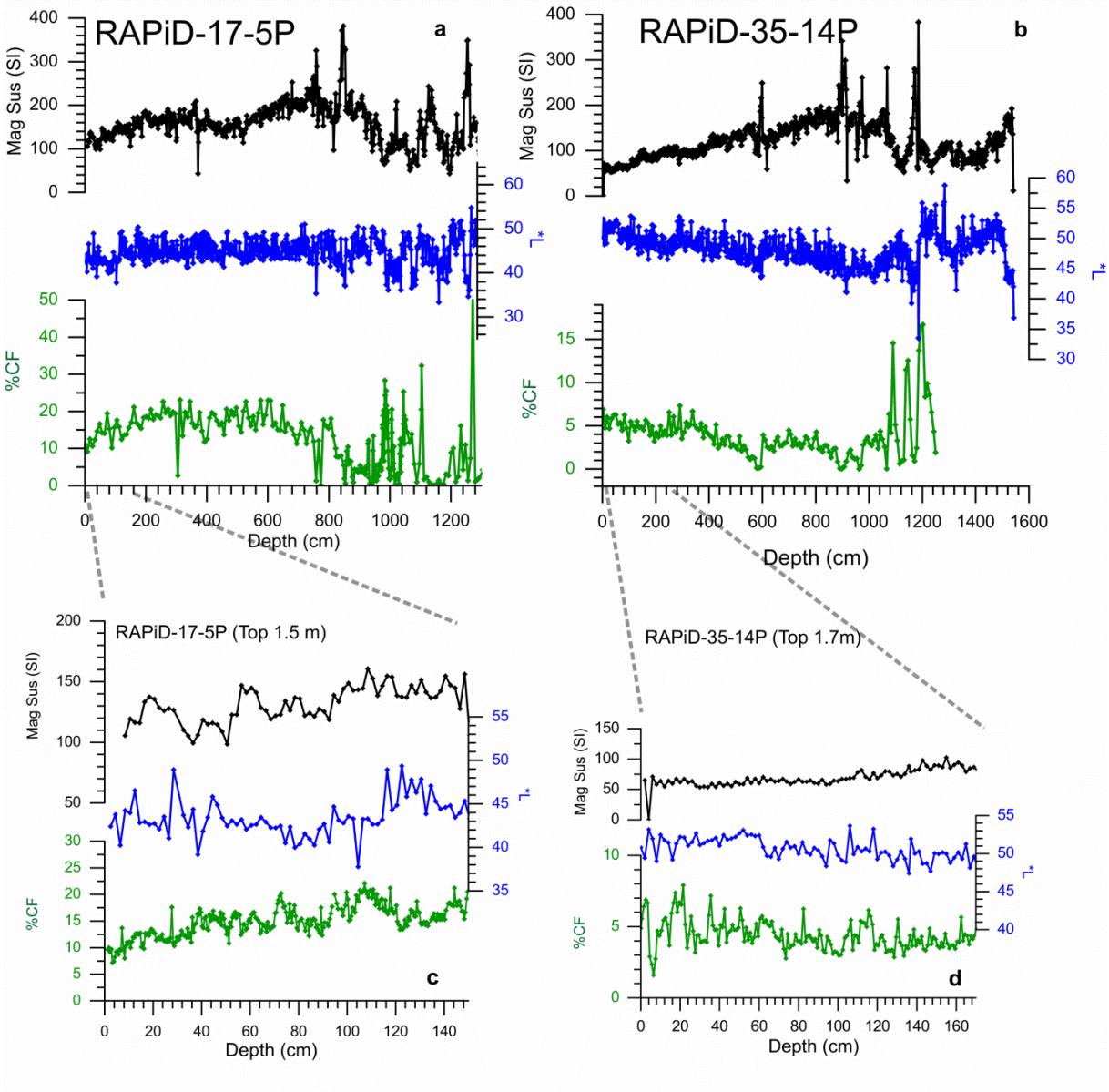

Figure 2.4. Bulk magnetic susceptibility, light colour reflectance (*L), and % weight of the coarse fraction (>63μm) (%CF) of RAPiD-17-5P (a) and (c) and RAPiD-35-14P and (c) and (d) show Late Holocene sections of RAPiD-17-5P and RAPiD-35-14P, respectively, used in this study.

2.3. Sediment Processing

The sediment cores were sliced at either 1 cm or 0.5 cm intervals, the wet sediment was weighed, disaggregated on a rotating wheel for approximately 24 hours, washed over a 63 µm sieve using fine water spray and dried in the oven at 40^{o}C. The fine (<63 µm) and coarse (>63 µm) fractions were then weighed for the calculation of the weight % of the coarse and fine fractions.

Between 4-5 g of the dried fine fraction were weighed into jars and processed for sortable silt grain size measurements. The coarse fraction was dry sieved into narrow size ranges and different planktonic foraminifera species were then picked and processed for stable isotope and Mg/Ca analysis.

2.4. Methodology

2.4.1. Sortable Silt Mean Grain Size

Sortable silt mean grain size ($\overline{SS}$) is defined as the mean grain size of the 10-63 µm terrigenous material (McCave et al., 1995). This particle size range behaves non-cohesively and its size sorting responds to hydrodynamic processes. Consequently, $\overline{SS}$ can be used to infer relative changes in the near-bottom speeds of its depositing current (McCave et al., 1995, McCave and Hall, 2006). Particle sizes <10 µm are excluded as this size range mostly dominated by clay minerals which present cohesive sediment behaviour arising from charge imbalances (Weaver, 1989) and van der Waals forces (Russel, 1980), and were therefore likely deposited as aggregates (or flocs) (McCave et al., 1995, McCave and Hall, 2006).

Sediment sorting occurs primarily during resuspension and deposition by processes of aggregate breakup and particle selection according to settling velocity and fluid shear stress (τ). The controlling variables are the critical erosion stress (τ_e), the critical suspension stress (τ_s) and the critical deposition stress (τ_d) which is the stress below which particles with a certain settling velocity will be deposited whereas those with lower settling velocity will remain suspended or will be ejected from the boundary layer. For non-cohesive materials (10-63 µm), typically $\tau_d < \tau_e < \tau_s$ applies. Thus, sorting of muds principally arises from selective deposition. And therefore larger particle mean grain sizes recorded from $\overline{SS}$ measurements in marine sediment cores are related to a stronger bottom flow currents and conversely for smaller $\overline{SS}$.

In order to prepare the sediment for $\overline{SS}$ analysis the method outlined by McCave et al. (1995) was followed. This involves the removal of carbonate and biogenic opal using 2M acetic acid and 0.2% sodium carbonate (Na_2CO_3) at 85 ^oC for 5 hours. The acid step was repeated twice (each of them was left in the sample for at least 24 hours) it was followed by a water rinse before the addition of Na_2CO_3 to the sample. The samples in Na_2CO_3 were then placed in the water bath for 5 hours at 85 ^oC and vigorous stirring was carried out 3 times during this time interval to promote dissolution of the biogenic silica. Once the carbonate and biogenic opal removal steps were completed the samples were suspended in 0.2% sodium hexametaphosphate (Calgon) dispersant in 60 ml Nalgene bottles. To ensure full disaggregation, all samples were placed on a rotating wheel for a minimum of 24 hours and were finally ultrasonicated for 3 minutes immediately prior to the sample analysis using a *Beckman Multisizer 3 Coulter Counter*.

The Coulter Counter is an electrical-zone pulse counter. It operates on the principle that a particle passing through an electric field in an electrolyte (Isoton^{TM}) will cause a voltage change which is directly proportional to its volume (Bianchi et al., 1999). Voltage pulses are then converted to the individual particles equivalent spherical volume by calibration experiments (Milligan and Kranck, 1997). As detailed in Bianchi et al. (1999), the Coulter Counter aperture size was set for 140 µm. A particle sizing and counting threshold was set to 8 µm and 10 µm respectively, with a sizing bin of 256 and the total count of 70,000 particles in the 10-65 µm size range was performed for each run. The measuring precision for the $\overline{SS}$ values in the 10-40 µm range have been estimated to be in the range of ±0.2% (Bianchi et al., 1999).

Alternative instruments to the Coulter Counter based on different theoretical principles can be used for the measurement of grain size distributions such as the Sedigraph and the laser diffraction particle sizer. The Sedigraph consists of x-ray scanning of the settling particles in a tube and is based on the settling velocity principle which is representative of the transport and depositional processes the particles were deposited in (Bianchi et al., 1999). For some time, the Sedigraph was the preferred instrument for particle size distributions and it is a good alternative to the Coulter Counter, although it measures the size distribution of the whole size spectrum down to 1 µm (also referred %SS) as opposed to the window size analysis of the coulter counter (10-63 µm) ($\overline{SS}$) (Bianchi et al., 1999, McCave and Hall, 2006). Following a study by McCave et al.,

(2006) on laser diffraction particle sizers, it was concluded that this instrumental technique should be avoided as the sizing of platy minerals could be dominated by the large projected area and when calculated as equant particles would result in erronous calculated settling velocities (McCave et al., 2006).

The $\overline{SS}$ paleocurrent proxy has been successfully applied in a number of sediment cores recovered from North Atlantic contourite drifts (e.g. Hall et al., 2004, Ellison et al., 2006, Boessenkool et al., 2007). However, problems and caveats on the application of $\overline{SS}$ measurements for past near-bottom flow speed reconstructions still remain and have been reviewed in detail by McCave and Hall (2006).

Before the application of the $\overline{SS}$ proxy the local sedimentary setting and oceanographic setting should be investigated, as sedimentary features (such as turbidity tails and small-scale changes in the topography) can lead to local variability in particle sizes. Additionally, areas dominated by eddy kinetic energy and bottom flow speeds exceeding 15 cm/s should be avoided. Furthermore, special care should be taken when interpreting single site $\overline{SS}$ reconstructions as past spatial migration of the main flow axis of the deep current could alias the $\overline{SS}$ record as a bottom flow speed proxy. However, although it was initially assumed that the source of the particles exerts a dominant influence on $\overline{SS}$, it has been shown that $\overline{SS}$ varies independently from sediment supply in current-sorted deposited muds, mainly as the large mixing in the delivery systems of sporadic deep sea gravity flows would eliminate systematic effects on <100 kyrs time-scales (McCave et al., 1995).

2.4.2. Stable isotopes in planktonic foraminifera

Planktonic foraminifera are free-floating upper ocean surface dwelling single-celled protozoa, which form calcite shells (tests) that can be structurally elaborate. The production, excellent preservation and ubiquity of these calcite tests in ocean sediments have provided an invaluable tool in the reconstruction of past ocean changes ranging from the study of their fossil assemblage for qualitative and quantitative ecological parameters to the extraction of environmental information via proxies that are recorded in the geochemical composition of their calcite test.

It has long been established that fractionation of oxygen isotopes ($\delta^{18}O$) between water and calcium carbonate is temperature sensitive (Urey, 1947, Epstein et al., 1953). This discovery was first applied as a paleothermometer tool on planktonic foraminifera shells by Emiliani (1955). However, changes in $\delta^{18}O$ of seawater such as local salinity variations and continental ice volume have since then been found to have an effect in the oxygen isotopic distribution in calcium carbonates (Shackleton, 1967), which complicates the paleothermometry application of $\delta^{18}O$ on its own (see Section 2.4.3).

The stable carbon isotopic composition ($\delta^{13}C$) of foraminiferal shells mainly reflects the carbon isotopic composition of the Dissolved Inorganic Carbon (DIC) of the ambient seawater in which they calcified. $\delta^{13}C_{DIC}$ is affected by changes in the global carbon cycle and more local changes such as the relative mixture of water masses and the balance between photosynthesis and respiration. However, foraminifera calcification is a biologically mediated process and it is therefore not in thermodynamic isotopic equilibrium with the ambient seawater. This results in additional kinetic isotopic fractionation and vital effects of the foraminiferal $\delta^{13}C$ (Ravelo and Hillaire-Marcel, 2007). The interplay of all these factors complicates the interpretation of $\delta^{13}C$ particularly in planktonic foraminiferal calcite.

In order to measure the stable isotopic composition of the planktonic foraminiferal calcite during this study, the coarse fraction was dry sieved into narrow size fractions, between 6- 200 foraminifera individuals depending on the species and its presence in the sample were picked with care by visually screening and selecting the best preserved and apparently cleanest tests. Each of the picked samples was weighed to calculate the average test weight.

To produce paired $\delta^{18}O$ and Mg/Ca measurements, the foraminifera individuals were lined up and gently crushed against two clean glass plates, homogenised and split into two aliquots for the respective analysis. Stable isotope measurements on the foraminiferal shells were measured on the Thermo Finnigan MAT 252 mass spectrometer coupled to a Kiel II carbonate preparation device at Cardiff University. The spectrometer was calibrated through the international standard NBS-19 and all isotopic results are reported as a per mil deviation from the Vienna Pee Dee Belemnite

scale (‰ VPDB). External reproducibility of carbonate standards was better than 0.08 ‰ and 0.06 ‰ for $\delta^{18}O$ and $\delta^{13}C$, respectively.

2.4.3. Mg/Ca in planktonic foraminifera

At equilibrium, the substitution of Mg^{2+} into $CaCO_3$ is associated with a change in the heat energy (or enthalpy) of the reaction, which is sensitive to temperature. As this reaction is endothermic, Mg/Ca of inorganic calcite is expected to correlate positively with temperature (Koziol and Newton, 1995). This has been corroborated by thermodynamic calculations for pure mineral phases which predict an exponential temperature dependence on Mg/Ca uptake into calcite of approximately 3% increase in Mg/Ca per ^{o}C (Lea et al., 1999), which is consistent with inorganic calcite precipitation experiments (Katz, 1973, Mucci, 1987, Oomori et al., 1987). Biologically mediated calcite precipitation in foraminifera also supports the exponential temperature dependency of Mg/Ca uptake. Although the Mg/Ca is normally between 1-2 orders of magnitude less than predicted for inorganic precipitation, which emphasises the influences that biological processes exert on the co-precipitation of metals in biogenic carbonates and highlights the need for species-specific calibrations.

Three different types of calibration approaches have been used in the study of the temperature dependence of Mg uptake into planktonic foraminiferal tests: (i) Culture-based (e.g. Lea et al., 1999, Nürnberg et al., 1996) (ii) Sediment traps (e.g. Anand et al., 2003) (iii) Core tops (e.g. Elderfield and Ganssen, 2000). Results obtained using different approaches are remarkably consistent and present an exponential dependence of temperature on the Mg/Ca in foraminiferal calcite in the form of:

$$Mg/Ca = B \exp(AT) \qquad \text{Equation (1)}$$

Where T is the calcification temperature and A and B are first order coefficients, in planktonic foraminifera a value of ~0.1 is used for the B coefficient and A varies with the species (Elderfield and Ganssen, 2000).

Paired $\delta^{18}O_c$ and Mg/Ca ratios in foraminiferal calcite provide a way to adjust for the temperature-dependency of $\delta^{18}O_c$ and isolate the $\delta^{18}O$ of ambient seawater ($\delta^{18}O_{sw}$), which can then be used to reconstruct salinity and therefore hydrographic changes.

To calculate $\delta^{18}O_{sw}$, the temperature equation based on O'Neil 1969 from Kim and O'Neil (1997) was used:

$$T=16.1-4.64\ (\delta^{18}O_c - \delta^{18}O_{sw}) + (0.09\ (\delta^{18}O_c - \delta^{18}O_{sw}))^2 \quad \text{Equation (2)}$$

For Standard Mean Ocean Water (SMOW) conversion (Hut, 1987):

$$\delta^{18}O_{sw}=\delta^{18}O_c-0.27‰ \quad \text{Equation (3)}$$

$\delta^{18}O_c$ has to be corrected for vital effect on $\delta^{18}O$ fractionation, which is species-specific (e.g. Bemis et al., 1998) and salinity can then be calculated using the regional modern $\delta^{18}O_{sw}$-salinity relationship from LeGrande and Schmidt (2006).

Several post-depositional processes such as selective dissolution of carbonate tests (Brown and Elderfield, 1996, Rosenthal et al., 2000), addition of diagenetic phases (e.g. Boyle and Keigwin, 1985, Pena et al., 2005) and presence of silicates within the foraminifera tests (e.g. Barker et al., 2003) could potentially alter the original Mg/Ca ratio of foraminiferal calcite and therefore introduce a bias in the Mg/Ca temperature reconstruction. To address and minimise some of these potential artefacts, the cleaning technique of the foraminiferal calcite for Mg/Ca analysis aims to remove silicate phases, organic matter, and iron manganese coatings (also commonly referred to Mn-coatings). In this study, samples were cleaned following the cleaning protocol outlined by Barker et al., (2003) as opposed to the Cd-cleaning protocol (Boyle and Keigwin, 1985) as Mn and Fe were not found in sufficient concentrations to affect the primary Mg/Ca signal (see Section 3.3.2.1 and Section 4.2.3.2).

The cleaning comprised several steps which aimed removing potential contaminants: (i) the clay removal step involved repeated UHQ water and methanol rinses aided by intervals of ultrasonication (ii) the oxidation step aimed to remove the organic matter by oxidation, this was achieved using alkali (NaOH 0.01M) buffered 1% H_2O_2 (iii) the dilute acid leach step (0.002M HNO_3) is done with the purpose of removing authigenic Mn-Fe coatings on the foraminifera shells and was only done once. Between step (ii) and (iii) the samples were taken out of the centrifuge tubes into a slide with a cavity and were screened under a light microscope for any remaining coarse-grained silicate particles and discoloured foraminiferal calcite that had not been removed by the

cleaning steps. These were taken out using a single-lash brush and were introduced back into centrifuge tubes. When the three cleaning steps were completed the samples were dissolved in 120 µl of 0.065M HNO_3 and centrifuged to remove any remaining small silicate particles. Samples were transferred to clean vials before stages involving acid and two water rinses were carried out in between each step.

The error on the reproducibility of the cleaning protocol was calculated by picking two large samples of approximately 1000 individuals, each of these were crushed and homogenised and in turn split into 5 aliquots. The 10 samples were cleaned and run separately. All the Mg/Ca values except for one, yielded values within 2% (1σ) indicating a reproducibility of the method better of 2% (1σ) (Table 2.1), similar to the value quoted in Barker et al. (2003).

	Sample 1	**Sample 2**
Mg/Ca (mmol/mol)	0.89	0.91
	0.89	0.84
	0.87	0.87
	0.87	0.86
	0.90	0.68
1σ	1.23	*1.97

Table 2.1. *N. pachyderma* Mg/Ca values obtained from two different sediment samples from RAPiD-35-25B (* denotes exclusion of the 5th value from Sample 2).

Between 1-2 procedural blanks were inserted in each cleaning batch (24 samples) and were carried through all of the cleaning steps and analysed to test any potential contamination during the cleaning process. None of the procedural blanks presented elemental concentrations above that of the blank during the run.

Trace metal measurements were performed using a Thermo Element XR High Resolution Inductive Coupled Plasma Mass Spectrometer (HR-ICPMS) at Cardiff University. The samples were first run for Ca concentration to enable matrix matching of the standards with the foraminiferal samples in order to calculate the elemental ratios. Three consistency standards were run at the beginning and end of every run for long-term precision calculations. During the time that the samples presented in this thesis were run in the HR-ICPMS the long-term precision for Mg/Ca measurements was better than ±2.5% (1σ).

2.4.4. Planktonic foraminiferal assemblage counts

Sediment assemblages of planktonic foraminifera reveal distinct biogeographic pattern (Bé and Tolderlund, 1971) (Figure 2.5). The study of planktonic foraminiferal ecology highlights the preference that many species display for certain environmental conditions and maximum relative abundances correlate with ecologic optima (Kucera, 2007). For this reason, planktonic foraminifera assemblage studies have long been recognised as surface-water property tracers (Murray, 1897). Based on modern studies of the foraminifera assemblage and distribution in the Northern North Atlantic (Bé and Tolderlund, 1971), we can use the proportion of polar and subpolar foraminifera planktonic species as useful indicators of past temperatures and particularly water mass distributions (Figure 2.5).

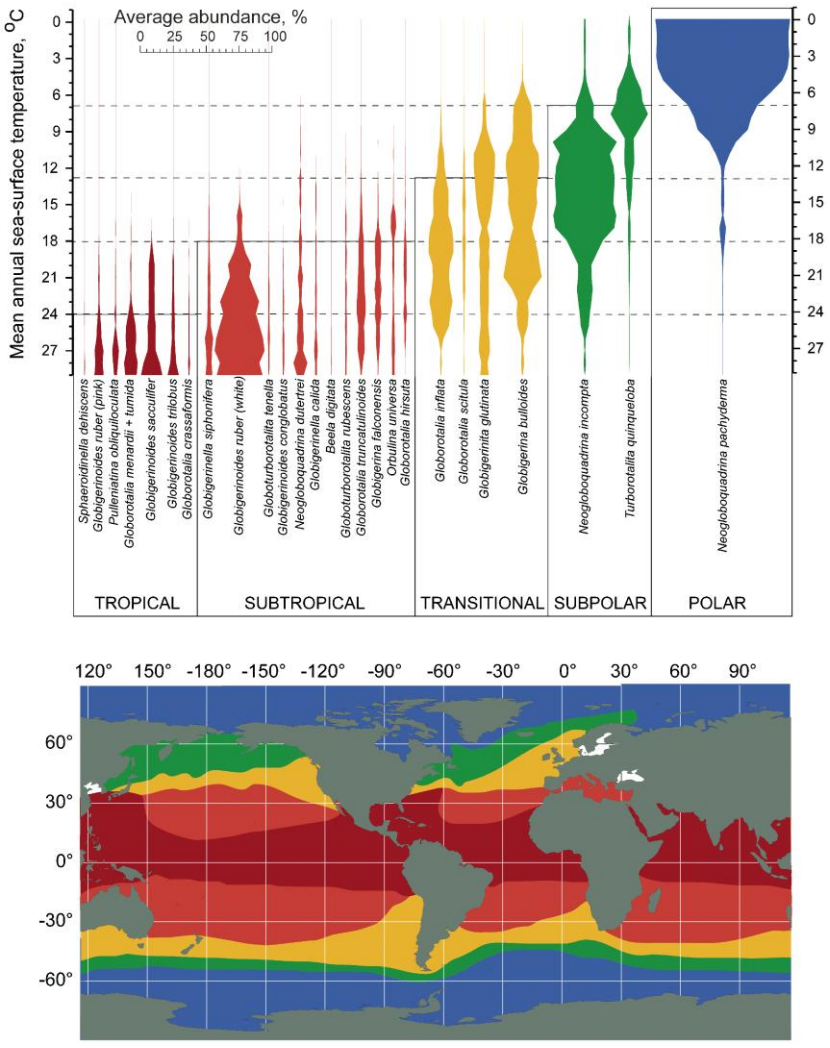

Figure 2.5. Planktonic foraminiferal provinces in the modern ocean. The distribution of the provinces (Bé 1977; Vincent and Berger 1981) follows sea surface temperature gradients reflecting the strong relationship between SST and species abundances (Kucera, 2007).

2.5. Core Chronology

The core chronologies produced for the sediment cores presented here are based on radiocarbon dating. Radiocarbon (^{14}C) is a cosmogenic isotope that is formed in the atmosphere by cosmic radiation interacting in a neutron reaction with atmospheric nitrogen (^{15}N). As soon as the ^{14}C atoms are formed they are incorporated into CO_2 molecules that then enter the global carbon cycle, including the ocean in the form of DIC. Radiocarbon has a half-life of 5730 years making it a valuable tool in the construction of chronologies in deep sea sediments for the last 40,000 years.

However, the application of radiocarbon dating in marine sediments is not straightforward. The dates have to be calibrated for the potential variability of ^{14}C production in the atmosphere as a result of magnetic field intensity and solar variability (Stuiver and Braziunas, 1993b) and/or changes in the partition of ^{14}C between the different reservoirs, particularly the ocean (e.g. Siegenthaler and Sarmiento, 1993). Additionally, marine carbonates have to be corrected for a reservoir effect because the exchange of CO_2 between the atmosphere and the ocean is finite and therefore $^{14}C/C$ ratio in HCO_3^- is always somewhat less than that in the atmospheric CO_2 and also to account for the ^{14}C activity in the ocean that can vary independently from the atmosphere, this is caused by the mixing of surface waters with upwelled deep waters which have been separated from the atmosphere for longer and are thus of an older radiocarbon age (Stuiver and Braziunas, 1993a). Other possible biases on radiocarbon dating can result from the size and abundances of the signal carriers (Manighetti et al., 1995), bioturbation (Keigwin and Guilderson, 2009), fragmentation and differential dissolution effects (also known as the 'the Barker effect') (Barker et al., 2007, Broecker and Clark, 2011).

The ^{14}C AMS dates obtained in this study were carried out on monospecific planktonic foraminiferal samples of either *Globigerina bulloides* or *Neogloquadrina pachyderma (sinistral),* and were analysed in National Ocean Sciences Accelerator Mass Spectrometry (NOSAMS) and in the NERC Radiocarbon Facility. The sample mass ranged from 4-12 g depending on the requirements of the analytical facility. Modelled marine radiocarbon reservoir corrections in the core locations show that at the core sites the reservoir ages are ~400 year which is the global mean reservoir correction

(Stuiver and Braziunas, 1993a) (Figure 2.6). Therefore radiocarbon ages were first corrected for a reservoir effect using a correction of 400 years and then converted to calendar ages using Calib.601 (Stuiver et al., 2011) and MarineCal09 (Reimer et al., 2009). The core chronology is further expanded on Sections 3.2.2 and 4.2.2.

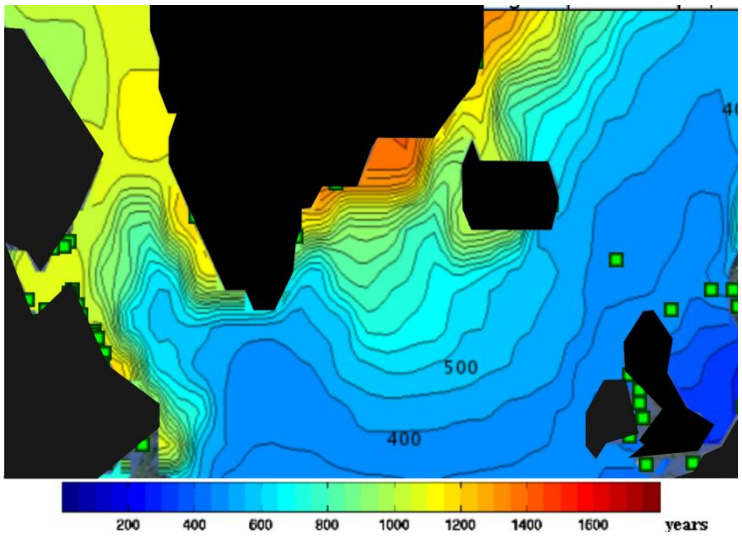

Figure 2.6. Radiocarbon reservoir correction ages from model estimates and measurements adapted from Butzin et al. (2005).

Additional ^{210}Pb-dating was undertaken in the clay size fraction of RAPiD-35-25B. ^{210}Pb is a naturally occurring radioactive form of lead and it is one of the last elements formed in the ^{238}U radioactive decay series. It is formed in the atmosphere as a by-product of radon gas. Within 10-40 days of its creation, ^{210}Pb falls out of the atmosphere (Appleby and Oldfield, 1978) and accumulates in the ocean where it is sorbed to charged sites on sediment particles, mostly clays. Therefore, freshly deposited marine sediments contain excess (unsupported) ^{210}Pb that decays by β-emission with a half-life of 22.6 years.

The dating is based on the determination of the vertical distribution of ^{210}Pb derived from atmospheric fall-out (unsupported of Pb in excess). If the sediment layers are undisturbed, then as the sediment ages, it loses is radioactivity as indicated in equation (4), and the sedimentation rate will be given by the slope of the least squares fit for the natural log of ^{210}Pb excess activity versus depth (Faure and Mensing 2005).

$$^{210}Pb_{Ax} = {}^{210}Pb^{0}_{Ax} e^{-\lambda 210 t} \qquad \text{Equation (4)}$$

$^{210}Pb_{Ax}$ is the radioactivity of ^{210}Pb at time (t); $^{210}Pb^{0}$ initial radioactivity of ^{210}Pb; λ refers to the half-life.

Analysis for ^{210}Pb were carried out in Sussex University by Prof. A. Cundy. Samples were counted on a Canberra well-type ultra-low background High Purity Germanium gamma ray spectrometer to determine the activities of ^{210}Pb. The $^{210}Pb_{excess}$ activity (unsupported) was estimated by subtraction of the average value of ^{210}Pb activity in deeper core samples (22 Bq/kg) (supported), where total ^{210}Pb activities had fallen to virtually constant values (e.g. Cundy and Croudace, 1996). Sediment accretion rates were determined by the slope of the least squares fit for the natural log of the $^{210}Pb_{excess}$ activity versus depth.

2.6. Statistical Analysis

2.6.1. Pearson correlation

The Pearson coefficient is a widely applied statistical tool that quantifies the linear correlation between two variables. However, the inherent element of persistence in climate time-series makes the confidence intervals difficult to calculate. In this study, time-series correlation was performed using the PearsonT programme (Mudelsee, 2003). In PearsonT, the Pearson's correlation coefficient is estimated employing a nonparametric stationary bootstrap confidence interval with an average block length proportional to the maximum estimated persistence time of the data (Mudelsee, 2003).

2.6.2. Single spectral analysis

Single spectral analysis is a statistical tool that is used for the detection of periodic or quasi-periodic components present in the time-series produced in this study. Spectral analysis was performed using a multi-taper method (Pardoiguzquiza et al., 1994), spectral confidence levels located using the robust AR(1) modelling of median-smoothed spectra (Mann and Lees, 1996) .

The multi-taper method reduces periodogram leakage (leakage produced by the abrupt end of the time-series) and consists in multiplying the time series by a series of values or data windows. The final spectrum is obtained by averaging over all the tapered spectra. The multi taper method is able to produce a spectrum with suppressed side-lobes, good smoothing and allows the detection of small amplitude high-frequency peaks (Weedon, 2003). According to Mann and Lees (1996) a large proportion of the spectra of climatic-proxy data have backgrounds which correspond to a first order autoregressive process AR(1). Therefore, this noise model was used in the calculation of the confidence levels.

2.6.3. Wavelet analysis

Wavelet is a type of evolutionary spectra and it is often used in the study of non-stationary processes in which the frequencies and power change with time. It is common to produce a time/frequency with power distribution contour map which aids visualisation of the time evolution of the statistically significant frequencies. In this study, wavelet analysis was performed using *Wavelet* from Torrence and Compo (1998) and was used in order to study the presence and timing of the periodicities obtained in the single spectral analysis.

3. Surface Changes in the Eastern Labrador Sea During the Late Holocene

3.1. Introduction

The Labrador Sea is an active area of deep water formation. It is one of the few places in the world's oceans where the upper water column experiences complete mixing down to 1.5-2 km (Lazier et al., 2002). During the winter, strong cold westerly winds sweep across the Labrador Sea causing heat loss to the atmosphere, which weakens the vertical density gradient and promotes open deep convection (Dickson et al., 1996, Marshall and Schott, 1999, Yashayaev, 2007a). The end-product of this process is the formation of cold, dense and homogeneous Labrador Sea Water (LSW). Additionally, deep convection in the Labrador Sea is controlled by local density gradients, which can be affected by freshwater input normally derived from the Arctic Ocean (Dickson et al., 2007, Aagaard and Carmack, 1989) and by active eddy driven restratification from Atlantic waters (e.g. Straneo, 2006). Recent studies have also highlighted several other factors that may influence the strength of deep convection in the Labrador Sea such as moderate changes in the positioning of storm tracks, Greenland tip jets (Bacon et al., 2003, Pickart et al., 2003), pack ice and sea ice cover in the Northwest Labrador Sea (Våge et al., 2009).

The formation of deep waters in the Labrador Sea contributes ~30% of the total volume flux of the lower limb of the AMOC (~15 Sv) (e.g. Rhein et al., 2002, Talley, 2003). The formation of LSW plays an important role in the AMOC as it (i) influences the properties and volume transport of the Nordic Overflows through the vigorous entrainment and mixing downstream of the Greenland Scotland Ridge (e.g. Bersch et al., 2007, Price and Baringer, 1994); (ii) drives the surface circulation around the Subpolar Gyre (SPG) (e.g. Curry and McCartney, 2001, Lu et al., 2007) and (iii) exports subpolar intermediate waters to the subtropical North Atlantic (e.g. Bower et al., 2009) and contributes to the upper DWBC and therefore North Atlantic Deep Water (NADW) (Talley and McCartney, 1982) .

Open ocean convection in the Labrador Sea comprises several stages:

1) Preconditioning of the water column that is driven by: (i) The cyclonic SPG circulation which produces doming of isopycnals bringing the interior waters towards the surface and (ii) strong surface buoyancy loss through air-sea interaction during autumn and winter. These processes, erode the seasonal stratification formed during the summer heating and modify the Subpolar Mode Waters (SPMW) (McCartney and Talley, 1982).
2) The LSW is formed in the convective stage. This newly produced water mass spreads laterally in different directions: east and northwards (Lavender et al., 2005), towards the centre of the SPG and to the subtropics through intermediate depth pathways (Lavender et al., 2000, Bower et al., 2009, Bower et al., 2011) and also joins the south flowing DWBC (Talley and McCartney, 1982).
3) The last stage of this process is the spring/summer restratification of the entire water column as a result of seasonal heating and lateral advective processes from the boundary currents into the central Labrador Sea. This process is aided by mesoscale eddies that are shed due to instabilities within the boundary current system that flows to the east of the Labrador Sea (Figure 3.1) (e.g. Gelderloos et al., 2011, Katsman et al., 2004, Lilly and Rhines, 2002, Straneo, 2006), and is important as it directly impacts convection during the subsequent winters (Lazier et al., 2002).

Over the past five decades, instrumental data has been used for the study of the effects of wind and freshwater forcing on LSW convection at interannual to decadal time-scales. In 1970, the Labrador Sea received an unusual Arctic freshwater discharge, the so-called Great Salinity Anomaly (GSA), causing a widespread freshening of the upper water column in the North Atlantic (Dickson et al., 1988). This event was accompanied by a reduction in LSW thickness and production in the 1970's (Curry et al., 1998, Lazier, 1980). The GSA is widely believed to have been induced by an anomalous, intense and persistent high pressure anomaly over Greenland and a low pressure anomaly over the northern Arctic Eurasian coast (Dickson et al., 1988 and references therein). This atmospheric regime, characteristic of a negative NAO, strengthened the northerly winds along the East Greenland coast and enhanced the southern transport of polar waters and drift-ice in the East Greenland Current (EGC), some of which was diverted to the North Iceland Sea (Aagaard and Carmack, 1989, Dickson et al., 1988, Hakkinen, 1993). The change in atmospheric circulation also caused a shift of the storm

tracks away from the Labrador Sea, decreasing the wind-stress curl over it and changing the northwest component of the wind direction (Walsh et al., 1990). Despite this explanation of atmospheric forcing on ocean dynamics, there is still doubt regarding the converse oceanic forcing on atmospheric dynamics (e.g. Rodwell et al., 1999).

The 1970's GSA is an extraordinary but non-unique event. The last century has been punctuated by several severe salinity anomalies that have impacted North Atlantic hydrography: 1910 (Dickson et al., 1988), 1980s (Belkin et al., 1998), 1990s (Belkin, 2004, Häkkinen, 2002). While each may differ in origin and nature, they are a good representation of the effects of freshwater and atmospheric forcing on the LSW formation and alterations of the AMOC. Due to the relatively short time-span of instrumental time-series, it is difficult to clarify if these anomalies have been a pervasive feature of the North Atlantic climate and if their magnitude and frequency have remained similar during the late Holocene.

On multi-centennial time-scales, the North Atlantic realm has witnessed several climatic oscillations, the most recent of which are the MCA and the LIA. Despite the apparent small-scale climatological changes associated with these periods, they still had important socio-economic and cultural repercussions in the circum-North Atlantic (Lamb, 1979). The most accepted view on the cause of these anomalies is that they were triggered by some external forcing either solar or volcanic and probably amplified by climatic feedbacks involving the ocean and the atmosphere (e.g. Goosse et al., 2006, Shindell et al., 2001, Mignot et al., 2011). Changes in the AMOC have repeatedly been invoked to have played a crucial role in these climatic oscillations (Bianchi and McCave, 1999, Bond et al., 2001, Hofer et al., 2010).

On longer time-scales, approximately 3-4 kyrs ago, the North Atlantic climate underwent a gradual millennial-scale cooling, the so-called Neoglacial, which culminated in the LIA. This cooling has been recorded in a wealth of palaeoproxies such as $\delta^{18}O$ from the Greenland Ice Sheet (Johnsen et al., 2001), glacier advances (Bakke et al., 2010, Denton and Karlén, 1973) and changes in ocean and atmospheric dynamics (Andrews et al., 1997, Jennings et al., 2002, Solignac et al., 2011). The gradual trend is consistent with the steady reduction in summer insolation at $65^{o}N$,

which supports the inference that the Neoglacial was most likely driven by orbital forcing and sustained or amplified by ocean-atmospheric feedbacks.

The aim of this chapter is to further our understanding of the forcings, mechanisms and variability of the preconditioning of LSW for convection and its potential role in the different Late Holocene climatic oscillations. High-resolution multi-proxy reconstructions based on multi-species planktonic foraminiferal $\delta^{18}O$, Mg/Ca and assemblage counts will be presented in order to investigate the surface water column structure variability in the Eastern Labrador Sea during the Late Holocene (last 3000 years) from multidecadal to multi-centennial time scales.

3.2. Materials

The uppermost 100 cm of the piston core RAPiD-35-14P and the entire box-core RAPiD-35-25B (44 cm) were sampled and processed continuously at 1 cm and 0.5 cm resolution, respectively and processed as described in Section 2.3. The box-core and the piston core were spliced based on radiocarbon dating and correlation of the % CF. The spliced record will be referred as RAPiD-35-COM. For more details on the core sedimentary setting see Section 2.2.

3.2.1. Hydrographic setting

RAPiD-35-COM was recovered from the Eirik Drift (South Greenland) and it lies in the eastern part of the Labrador Sea (Figure 3.1). The Eastern Labrador Sea is a region that is bathed by mode waters derived from a variety of sources including the Arctic and the Atlantic. The EGC is a cold low-salinity surface ocean current that originates in the Arctic Ocean and acts as the main conduit for the export of freshwater from the Arctic Ocean into the North Atlantic (Aagaard and Coachman, 1968). It flows south along the East Greenland Continental margin, and once it crosses the Denmark Strait, it encounters Atlantic waters from the Irminger Current (IC) (a branch of the North Atlantic Current- NAC). These two currents form a strong front and flow southward to Cape Farewell (Figure 3.1). Here, the boundary currents decelerate and cause a portion of the EGC and IC to flow into the Labrador and Irminger Basins which is more pronounced during summer restratification (Lavender et al., 2005, Holliday et al., 2006). The rest continues northwards along West Greenland margin as the West Greenland Current. In spite of the cold temperatures of the EGC its low-salinity keeps this current at the surface whereas the warmer but saltier IC is found deeper at depths of

~100-200 m (Figure 3.2) (Holliday et al., 2009). The temperature and salinity conditions of these water masses and their relative interaction and contribution to the centre of the Labrador Sea play a critical role in the re-stratification and hence preconditioning of the water column for winter Labrador Sea Water convection (Lazier et al., 2002).

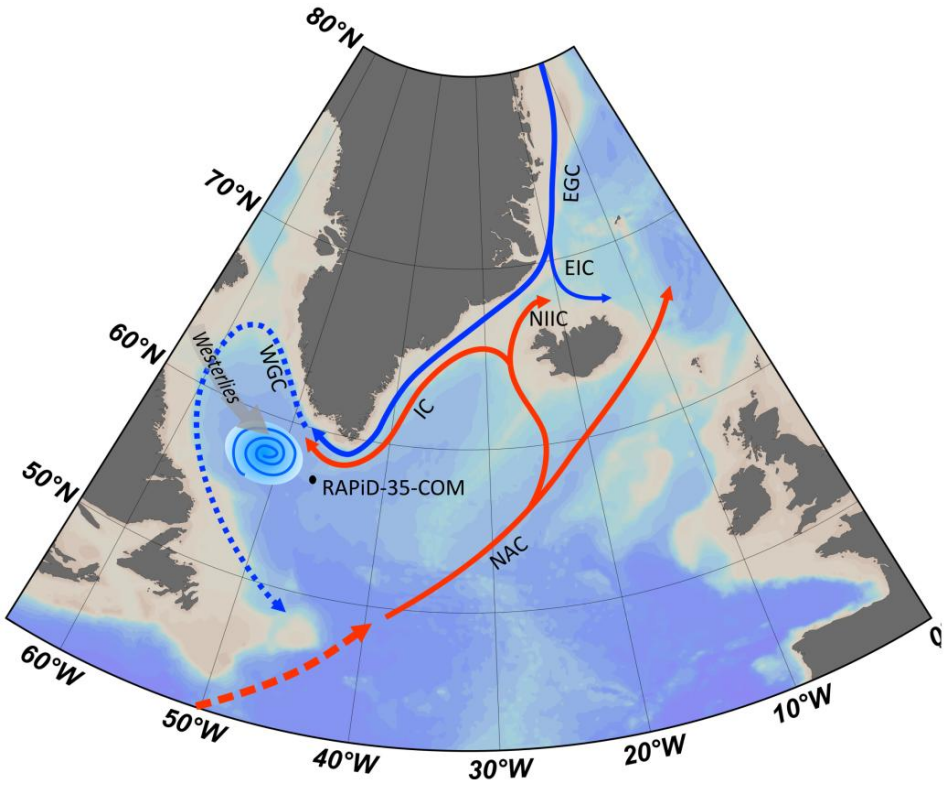

Figure 3.1. Location map of RAPiD-35-COM. Schematic surface circulation is indicated by the arrows. Blue arrows represent cold polar derived currents East Greenland Current (EGC), East Icelandic Current (EIC) and red arrows show Atlantic Inflow waters such as North Atlantic Current (NAC), North Icelandic Irminger Current (NIIC) and Irminger Current (IC), West Greenland Current (WGC).

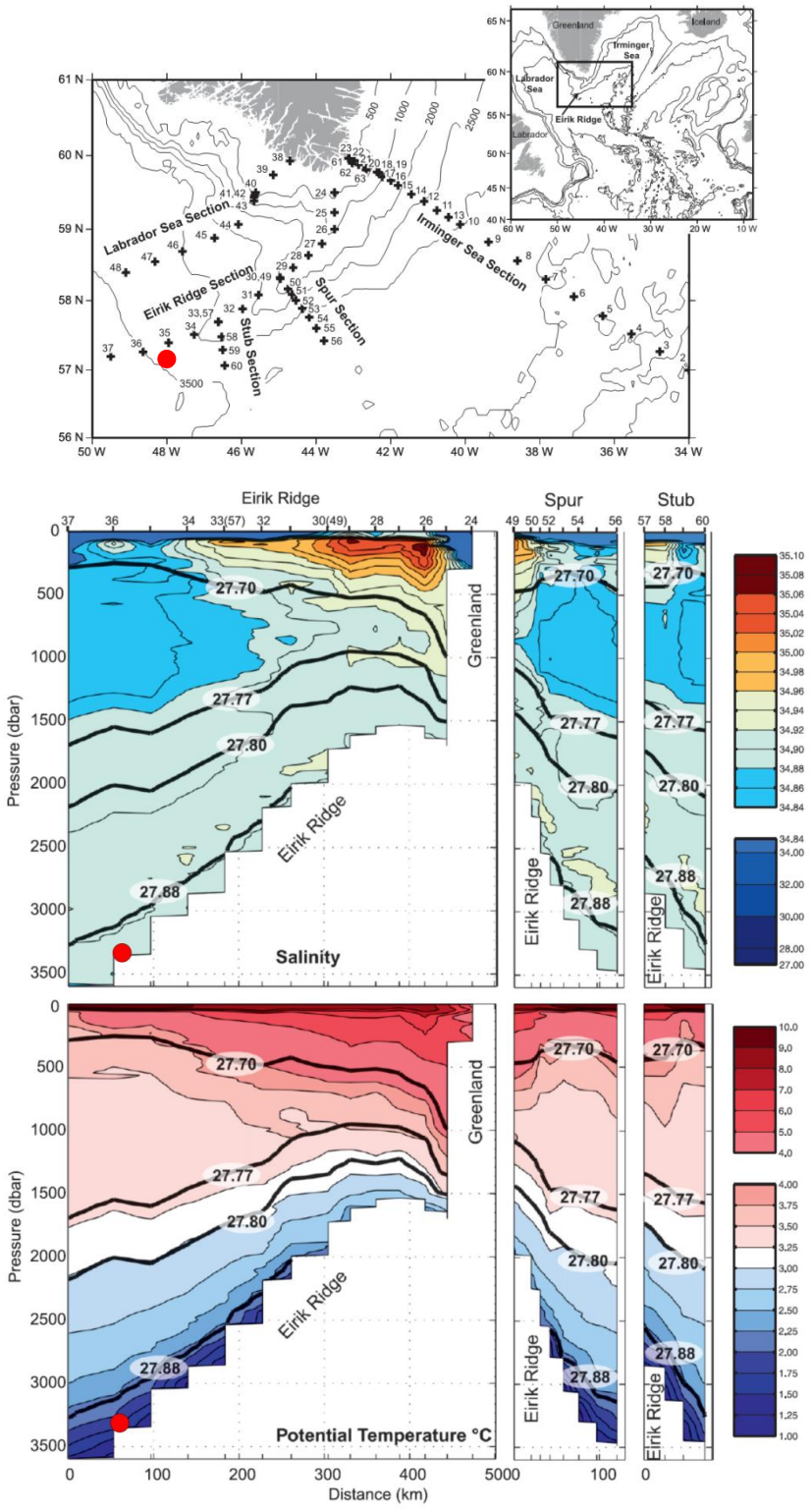

Figure 3.2. Location map of the hydrographic transects presented in the panels below (top). Hydrographic sections across the Eirik Ridge of salinity (middle) and potential temperature (bottom) recovered from the Discovery cruise 298 (August-September 2008) (Holliday et al., 2009). The red dot indicates the core location of RAPiD-35-COM.

A hydrographic transect across the Eirik Ridge is presented in Figure 3.2. The temperature and salinity of the upper 50 m show a strong summer pycnocline which is also corroborated from CTD data recovered during the CD159 cruise from this area (see Figure 3.8), and is most likely a result of summer meltwaters. At 100-300 m depth distinct areas of salty waters are observed and are consistent with the presence of Atlantic waters reaching the Eastern Labrador Sea via the IC (Figure 3.2). The salty Atlantic waters appear to lie beneath the fresher waters, and a distinct salinity gradient is present close to the Greenland coast which may be consistent with the strong boundary current between the cold and fresh waters of the EGC and the East Greenland Coastal Current and the Atlantic waters of the IC.

3.2.2. Chronology

The age model for RAPiD-35-COM was constructed based on fourteen AMS ^{14}C dates measured from monospecific planktonic foraminiferal samples (Table 3.1). Between 1000-2500 individuals of *Neogloboquadrina pachyderma (sinistral)* (*Nps* hereinafter) were picked from the >150μm size fraction. To avoid age biases from reworking and bioturbation effects care was taken to select the cleanest individuals and intervals avoiding troughs in %CF and relative percentage abundance of *Nps* (*%Nps*). A cleaning step was introduced to minimise any potential contamination in the samples before submitting the samples for analysis. This step involved adding 500 μl of MilliQ water to the sample, ultrasonicating for 3 seconds and removing the supernatant. This was repeated twice and the samples were left to dry in the oven at ~38^{o}C. Measurements were made at NOSAMS and NERC Radiocarbon Facility (Table 3.1).

Radiocarbon ages were corrected for a standard reservoir effect of 400 years and converted into calendar years using MarineCal 09 (Reimer et al., 2009) in CALIB6.03 (Stuiver et al.,11), calendar ages are presented as the average of the 1σ ranges (Table 3.1). Despite the assumption for a ΔR of 0 years, events such as deep winter convection and/or a greater influence of polar waters via the EGC in the Labrador Sea could have contributed to a variable ΔR and consequently likely apparent older ages (see below).

Core	Code*	Depth (cm)	Radiocarbon Age ±1σ (Yrs BP)	Calibrated Age 1σ average
RAPiD-35-25B	OS-82608	0.25	285±30	>1950 yrs AD
RAPiD-35-25B	SUERC-35759	6.25	720±37	1589 yrs AD
RAPiD-35-25B	OS-86418	16.75	895±25	1444 yrs AD
RAPiD-35-25B	SUERC-35760	22.75	1145±35	1261 yrs AD
RAPiD-35-25B	OS-86417	28.75	1270±25	1130 yrs AD
RAPiD-35-25B	SUERC-35761	36.25	1437±37	972 yrs AD
RAPiD-35-25B	OS-82607	43.5	1610±35	768 yrs AD
RAPiD-35-14P	SUERC-13088	2.5	714±35	355 yrs BP
RAPiD-35-14P	SUERC-35762	30	1680±37	1243 yrs BP
RAPiD-35-14P	OS-82609	39.5	1920±30	1463 yrs BP
RAPiD-35-14P	SUERC-35763	53.5	2317±35	1998.5 yrs BP
RAPiD-35-14P	SUERC-35764	65.5	2500±37	2165 yrs BP
RAPiD-35-14P	OS-82610	79.5	2830±30	2607 yrs BP
RAPiD-35-14P	SUERC-35765	99.5	3218±37	3028.5 yrs BP
RAPiD-35-14P	OS-82611	120.5	3470±20	3340.5 yrs BP
RAPiD-35-14P	OS-82612	160.5	3850±30	3810 yrs BP
RAPiD-35-14P	OS-82613	200.5	4290±40	4425.5yrs BP

Table 3.1. Radiocarbon dates obtained for RAPiD-35-COM. *OS: NOSAMS, SUERC: NERC Radiocarbon Facility

3.2.2.1. RAPiD-35-25B

- Radiocarbon dating and ΔR

Seven ^{14}C AMS dates were obtained to construct the age-model in RAPiD-35-25B. The apparent sedimentation rate appears to have remained relatively constant, with an average of 41 cm/kyr and 36 cm/kyr (by linear interpolation and polynomial fit, respectively), which approximates to a sample integration of 14 years for every 0.5 cm sampling interval (Figure 3.3a). The AMS ^{14}C date at 6.25 cm depth appears 140 years older than expected from a linear fit (Figure 3.3a). This could have resulted from reworking processes, an abrupt change in sedimentation rate or a change in the regional difference from the average global marine reservoir correction (referred to as ΔR) of the waters bathing the Eastern Labrador Sea during the LIA.

Polar waters deriving from the Arctic within the EGC have a larger ΔR than those of tropical origin (Figure 2.6). During the LIA an increase of polar waters reaching the North Atlantic via the EGC was initially suggested from IRD counts (Bond et al., 2001). Additionally, recent studies have used radiocarbon measurements on absolutely dated marine archives such as tephra counting on sediment cores or annual banding counting in long-lived bivalves to calculate the radiocarbon reservoir changes of the waters reaching North of Iceland during the Late Holocene (Eiríksson et al., 2011, Wanamaker et al., 2012). These studies found an increase in ΔR to approximately 150 years during

the LIA which confirms an increase in the influence of polar waters north of Iceland and most likely reaching the Labrador Sea. The larger influence of Arctic waters at the core site at this depth interval is supported by the proxy work presented in this chapter, such as the increase in % *Nps* at around 15 cm depth.

To provide a first order estimation of the potential impacts of changes in ΔR with time, ages were estimated assuming that the sedimentation rate was invariant throughout the record (as defined by the linear regression through the full suite of ^{14}C AMS dates-black line in Figure 3.3a) and the local ΔR was calculated as the deviation in years from the linear fit through the seven ^{14}C AMS dates. The assumption of a linear sedimentation rate is not unreasonable bearing in mind that the top 100 cm of the piston core present linear sedimentation rate for the last 3000 years (Figure 3.3b). The results showed that for all of the dates the deviation was less than ±30 years, hence smaller than the average dating error (±32), except for the date at 6.25 cm depth, which showed a deviation from the linear sedimentation rate of 140 years. Unless the 140 year deviation is due to an abrupt change in sedimentation rate deriving from changes in overflow strength or changes in the input of ice drafted debris, the magnitude is very similar to the expected ΔR from the surface waters of the EGC (150-200 years) (14C CHRONO marine database and Figure 2.6). Based on the above reasoning, this point was excluded from the age-model. Furthermore, when doing so not only was the implied sedimentation rate brought into agreement with the piston-core but the R^2 value was improved to 0.999 (Figure 3.3b).

- Top age for RAPiD-35-25B

In the 1950s and 1960s nuclear weapons testing approximately doubled the amount of radiocarbon in the atmosphere and has been registered in many natural archives. The amount of 'bomb' radiocarbon in a sample is often reported as Δ^{14}C ‰ or % Fraction Modern. For example a sample of FM>1 would indicate that it contains bomb radiocarbon and therefore it has a date of >1950 years AD (for full mathematical definition see Stuiver and Pollack (1977)). The ^{14}C AMS measurement from the top 0.5 cm of RAPiD-35-25B had a FM of 0.96. Although this by definition means that the top is not of modern age (since its FM<1) the radiocarbon date from 0.5 cm depth was negative (355 ^{14}C years), and therefore confirms that the top of the core contains some bomb radiocarbon. However, even if bioturbation effects are taken into account

(Keigwin and Guilderson, 2009, Barker et al., 2007) there is not sufficient bomb-radiocarbon in this sample for it to be of the predicted collection date (2004) which would reflect an age of >1990 years AD. By calculating the decay of the top radiocarbon date and comparing it to the modeled mixed layer ^{14}C ‰ in Reimer et al. (2009) (using an ocean mean reservoir correction of 400 years) an age of 1960 was assigned for the top of RAPiD-35-25B. The final age-model was produced using a cubic spline through six radiocarbon dates (Figure 3.3a).

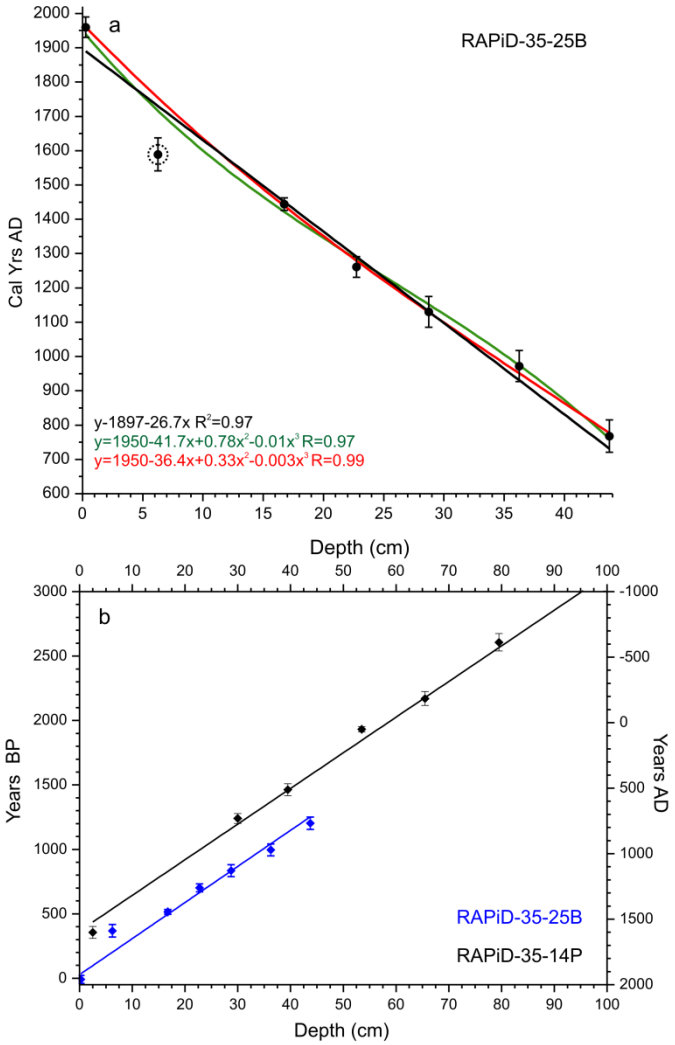

Figure 3.3. (a) Calibrated radiocarbon ages for RAPiD-35-25B shown by black points with error bars of 1σ. Black, green, red line correspond to a linear, cubic and cubic excluding the data point at 6.25cm depth (highlighted by a dotted circle), (b) Linear fit to the calibrated radiocarbon ages for RAPiD-35-25B (blue) and RAPiD-35-14P (black).

Additional ^{210}Pb dating was carried out in the fine fraction of RAPiD-35-25B (for more details in ^{210}Pb-dating see Section 2.6), samples were analysed at the University of Sussex. The ^{210}Pb profile presents an exponential decay of unsupported ^{210}Pb (Figure

3.4) down to ~6 cm depth, which supports the lack of a heavily bioturbated top and a deep mixed layer and confirms the presence of the last 150 years (which is ~6 times the half life of ^{210}Pb) within the top 5 cm of the core. The data point at 10 cm depth contains some unsupported ^{210}Pb which is most certainly a result of downward mixing of the sediment due to bioturbation. This can confirmed by the radiocarbon based age models presented in Figure 3.3a which suggest that the age of the sample at 10 cm would equate to an age of 1500-1600 years AD which is 300 years beyond the ^{210}Pb life. Furthermore the exclusion of this point for the sedimentation rate estimation improves the exponential fit from 0.66 to 0.9.

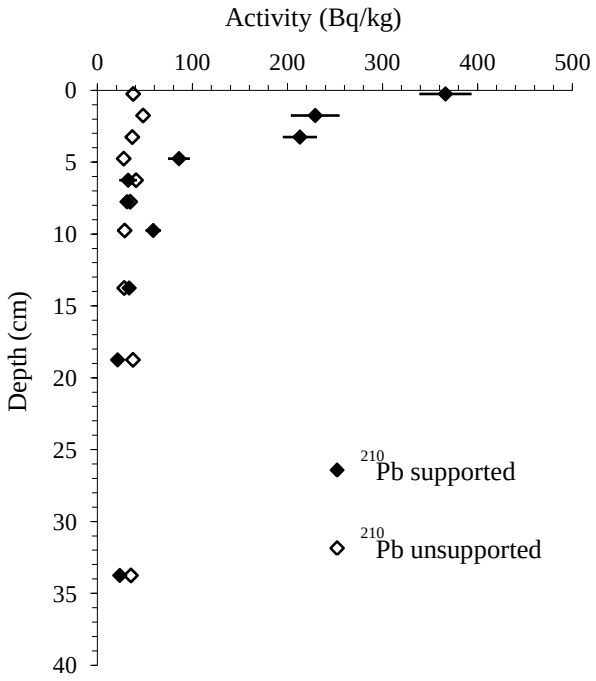

Figure 3.4. Down-core ^{210}Pb unsupported measurements on RAPiD-35-25B.

In conclusion, the sedimentation rate obtained from ^{210}Pb dating method for the top 6 cm confirms the sedimentation rates from the radiocarbon age model presented in Figure 3.3 and therefore further supports the exclusion of the radiocarbon date at 6.25 cm.

3.2.2.2. RAPiD-35-COM

The age-model for RAPiD-35-14P (0-200 cm) was constructed using a cubic spline of 10 radiocarbon dates (Table 3.1 and Figure 3.5). Based on the ^{14}C dating and further validated by the % CF (Figure 3.3 and 3.6), the splicing point between the bottom of the box-core RAPiD-35-25B and the piston core RAPiD-35-14P, was assigned at 30 cm

depth of RAPiD-35-14P. This spliced record will be referred to as RAPiD-35-COM hereinafter.

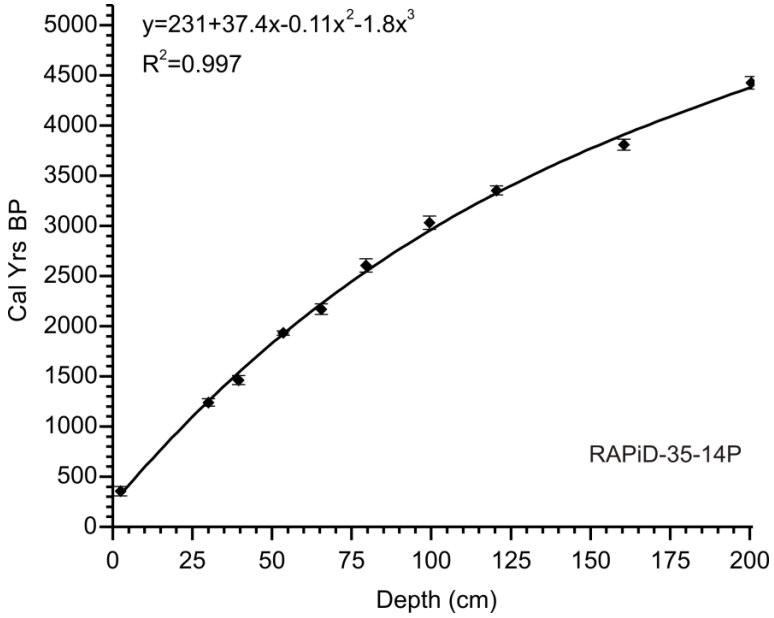

Figure 3.5. Age model for RAPiD-35-14P based on a cubic spline of 10 radiocarbon dates, 1σ error on the calibrated dates is illustrated by the error bars.

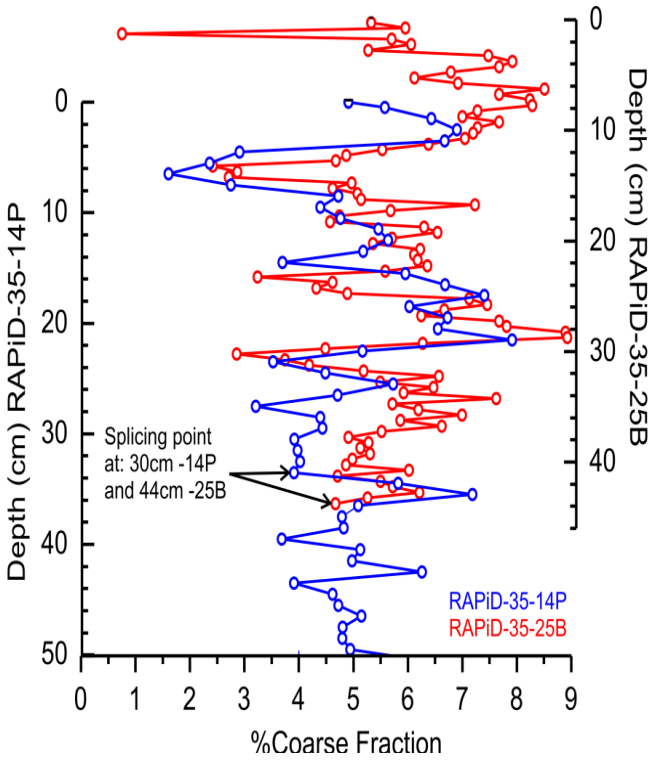

Figure 3.6. RAPiD-35-25B and RAPiD-35-14P %CF against core depth (red and blue, respectively). Splicing point is indicated by the arrows.

3.3. Methodology

3.3.1. Stable isotopes on multi-depth planktonic foraminifera

In this chapter three planktonic foraminifera species with different calcification depths were chosen to enable the study of the surface hydrography at the site, a description of their ecological preferences are summarised below.

Turborotalita quinqueloba (Figure 3.7c) is a symbiont bearing subpolar species found in the high latitudes, it is considered to live in the photic zone mostly inhabiting the near surface waters above the summer pycnocline (Bé and Tolderlund, 1971, Carstens et al., 1997, Hemleben et al., 1989, Simstich et al., 2003).

Neogloboquadrina pachyderma (sinistral) (Figure 3.7a) is a polar species that dominates the faunal assemblage in the modern day high latitude waters. This species is found in the upper water column mostly between 50-100 m depth (Simstich et al., 2003, Stangeew, 2001) and blooms during the late spring summer (Jonkers et al., 2010). However, the addition of ontogenic calcite during the late growth stages of its life cycle takes place deeper down in the water column, complicating the interpretation of the cumulative geochemical signature in the *Nps* calcite shell. Since the degree of encrustation in *Nps* ranges between 50-86% (Kohfeld et al., 1996, Kozdon et al., 2009, Simstich et al., 2003, Stangeew, 2001), the geochemical signals from this species are often interpreted as deep subsurface 150-200 m and concentrated mainly along surfaces of constant density: isopycnals (Simstich et al., 2003).

The temperate to subpolar species *Globigerina bulloides* (Figure 3.7b) predominantly inhabits the near-surface and it blooms in the summer. It shows a preference for waters with temperatures that exceed 7^{o}C (Hilbrecht, 1996). These temperature conditions are very abnormal in the Eastern Labrador Sea and are reflected by the low abundance of *G. bulloides* at the site (<4% of the assemblage) (Figure 2.5). Despite its small representation of the oceanographic conditions in the Eastern Labrador Sea we can utilise its ecological preferences for particular hydrographic conditions in order to explore the properties of the Atlantic waters reaching the site.

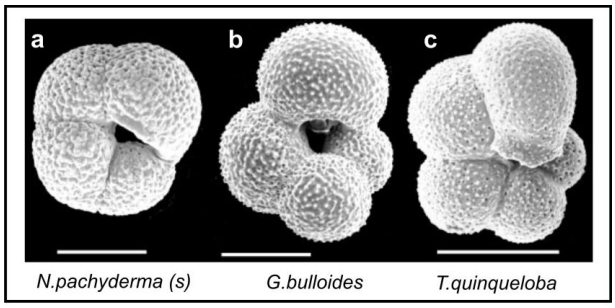

Figure 3.7. Photographs of the planktonic foraminifera (a) *Neogloboquadrina pachyderma (sinistral)*, (b) *Globigerina bulloides*, (c) *Turborotalita quinqueloba* adapted from (Norris and de Vargas, 2000). Scale bars are 100 µm.

Foraminifera were picked from the narrowest size fraction possible to avoid size effects on stable isotopes and Mg/Ca measurements (Elderfield et al., 2002). Individuals were picked with care by visually screening and selecting the best preserved and apparently cleanest tests. For *G. bulloides* 30-40 individuals were picked in the 300-355 µm where available, the size fraction was widened to 250-355 µm in intervals where not enough individuals were present. The samples which contained a wider size fraction did not lie outside the trends in the $\delta^{18}O$ record from the narrow size fraction. The observed lack of size effect on *G. bulloides* $\delta^{18}O$ is consistent with a study from the Eastern Labrador Sea (Hillaire-Marcel et al., 2001), in which the authors suggest a limited vertical migration during their growth stages. In fact, it is possible that the lack of vertical migration of *G. bulloides* in this region stems from its environmental restriction to a specific water mass at this site, in this case the IC. In contrast, the high abundance of *Nps* allowed the selection of 150-200 individuals from the 150-212 µm size fraction (See Section 3.3.2.4). Between 40-70 specimens of *T. quinqueloba* were selected from the 150-212 µm size-fraction and as a result of their light test weight (~1 µg/test) this species was solely used for stable isotope analysis. For a detailed description of the preparation and analysis of stable isotope measurements see Section 2.4.2.

Using stable isotope measurements on these three distinct planktonic foraminifera species with different depth and preferred water mass habitats can help us reconstruct the structure of the water column through time. Equilibrium calcification for *T. quinqueloba* and *Nps* was assumed (see Section 3.4.1.1 for discussion), and a vital effect correction of -0.68‰ was applied for *G. bulloides* according to temperatures of 7°C (Bemis et al., 1998). A comparison of the vertical profile of the predicted $\delta^{18}O$ of the calcite ($\delta^{18}O_{eq}$) with the ranges of $\delta^{18}O$ values obtained and presented in this chapter

for the three species (Figure 3.8) are consistent with the habitat depths reported by other studies and summarised above.

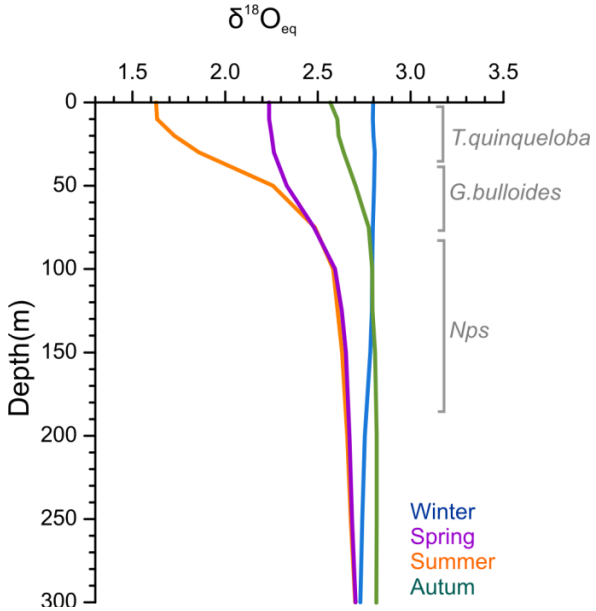

Figure 3.8. Predicted $\delta^{18}O$ of the calcite assuming equilibrium fractionation from seawater ($\delta^{18}O_{eq}$) calculated based on monthly temperature and salinity measurements from Ocean Data View (ODV). The grey brackets represent an estimated habitat depth for the planktonic foraminifera species used in this study based on the comparison of the $\delta^{18}O_{eq}$ and the $\delta^{18}O$ values obtained and presented in Section 3.4 and assuming a late spring summer growth season.

3.3.2. Paired $\delta^{18}O$ and Mg/Ca

Paired $\delta^{18}O$ and Mg/Ca measurements on *G. bulloides* and *Nps* were performed for RAPiD-35-25B, whereas only *G. bulloides* was analysed in RAPiD-35-14P. For a detailed description of the preparation and analysis of planktonic foraminifera Mg/Ca see Section 2.4.3.

3.3.2.1. Secondary effects on foraminifera Mg/Ca values

As described in Section 2.4.3, secondary effects on foraminifera Mg/Ca values such as partial post-depositional dissolution and the presence of contaminant phases such as clays, organic matter, and Fe-Mn coatings could affect the Mg/Ca values and thus its interpretation as a temperature signal (e.g. Rosenthal, 2007).

The potential impacts of partial post-depositional dissolution were monitored using average shell weights. If the foraminiferal calcite had suffered partial post-depositional dissolution, a positive correlation between Mg/Ca and the average shell weights would

be expected. A comparison of the average shell weights from *Nps* and *G. bulloides* and the Mg/Ca values down-core reveals no correlation (Figure 3.9), indicating no significant post-depositional dissolution of the calcite tests. Twenty *Nps* duplicates were picked and weighed and were used to test the natural variability of the shell weights and revealed an average relative standard deviation (1σ) of 7% which is probably a result of the large error associated with the large size range used as opposed to individual shell size measurements. Additionally the large intrasample variability of the shell weight may also arise from the environmental control on foraminiferal shell weights, which might hinder its application as a post-depositional dissolution parameter.

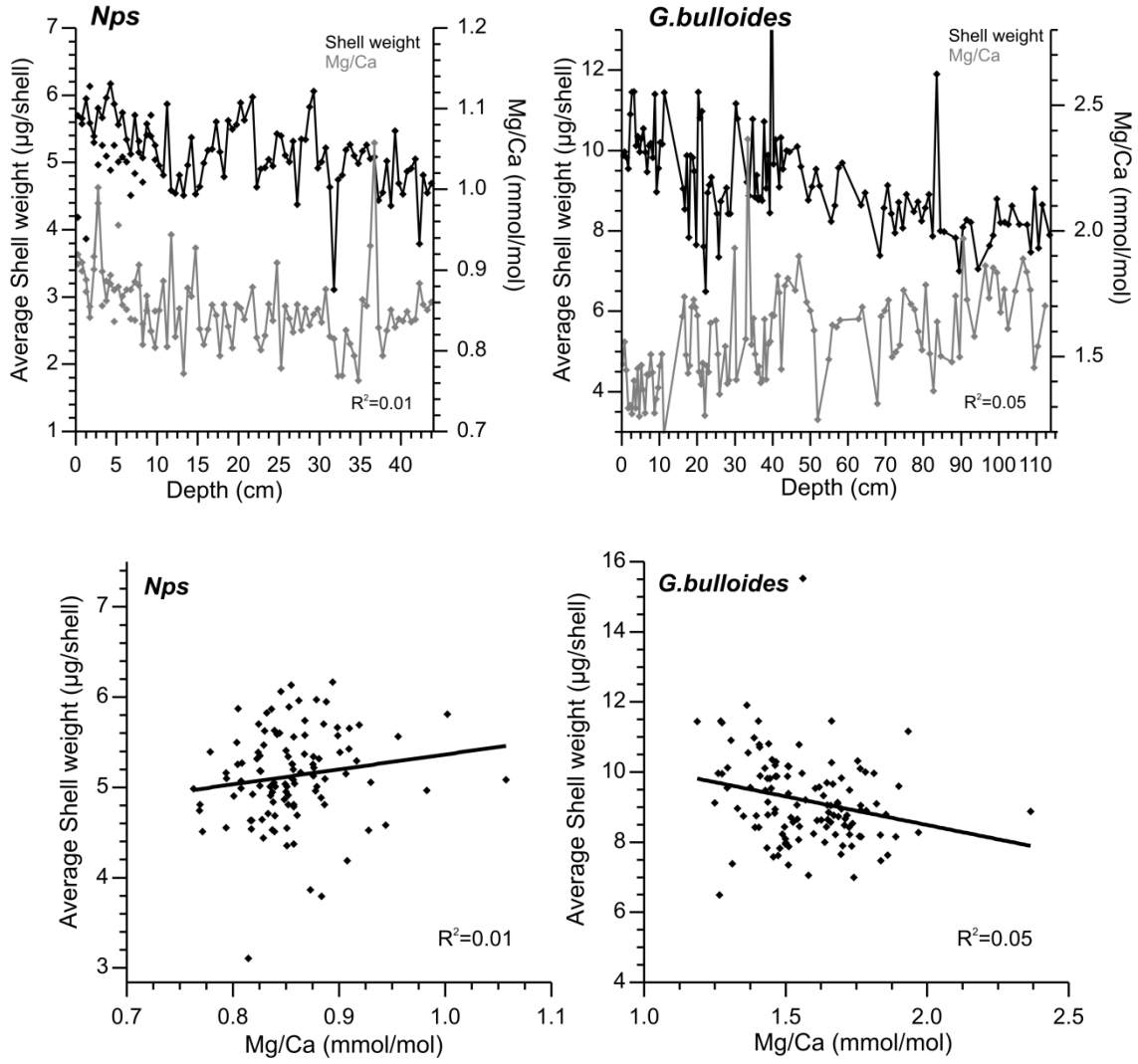

Figure 3.9. Upper panels: Downcore Mg/Ca and average shell weights for *Nps* (left) and *G. bulloides* (right). Isolated data points in the left hand panel represent the 20 *Nps* duplicates. Lower panels: Cross-plots of shell weights versus Mg/Ca concentration.

To investigate the potential contribution of Mg from contaminant phases such as clays and Fe-Mn oxides to the primary Mg/Ca temperature signal we studied down-core co-variability of minor elements such as Fe, Mn and Al with Mg/Ca.

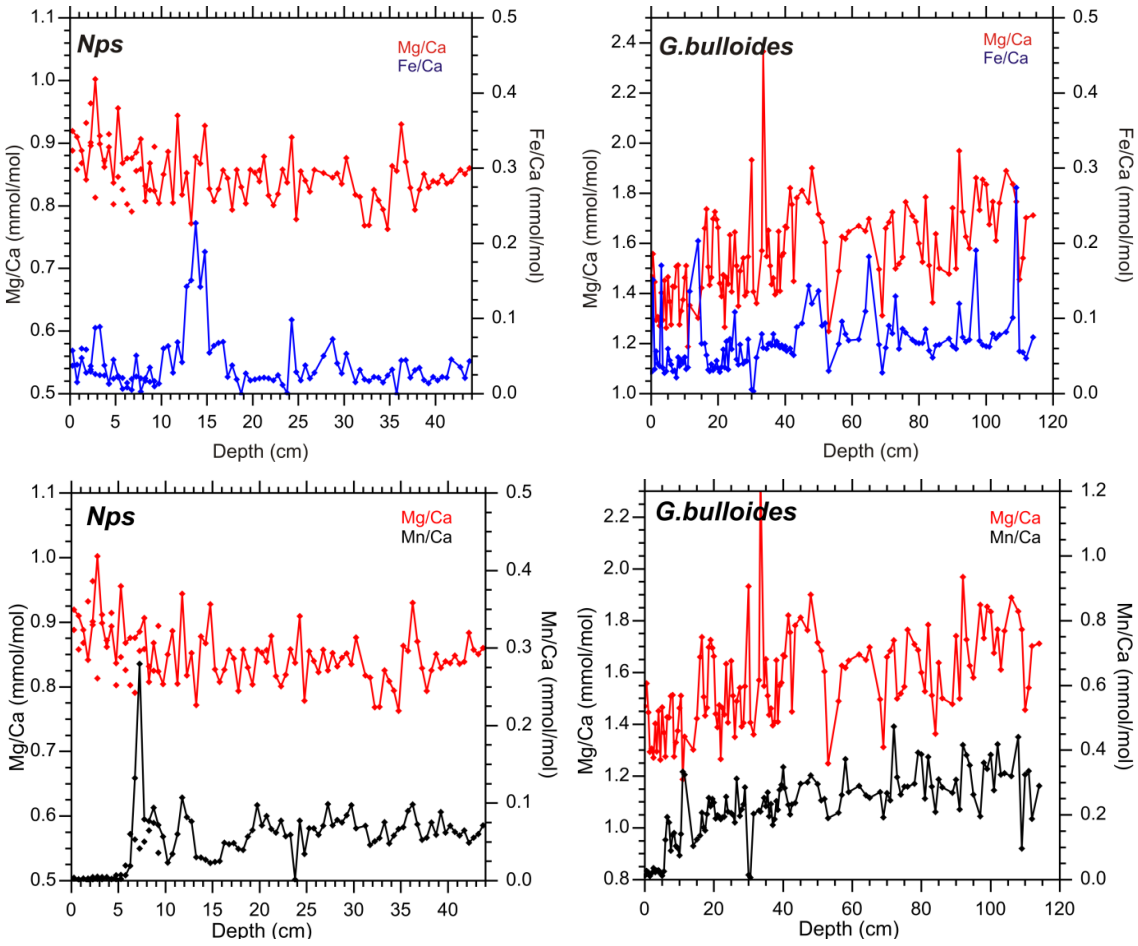

Figure 3.10. Down core Mg/Ca data versus Fe/Ca (top) and Mn/Ca (bottom) in *Nps* (left) and *G.bulloides* (right). Isolated data points represent the data from the replicates.

The Fe/Ca and Al/Ca in the *Nps* and *G. bulloides* samples were mostly found to be below the recommended threshold values by Barker et al. (2003), of 0.1 mmol/mol and 0.1 mmol/mol, respectively, indicating minimal presence of clays in the measured samples (Figure 3.10). High Fe/Ca values were found at 10-15 cm depth (Figure 3.10) mainly caused by the presence of pyrite, which was recorded by visual inspection during picking and was further supported by the low Al/Ca values (<0.1 mmol/mol).

The presence of authigenic Mn-rich coatings was monitored by examining Mn/Ca values. Low values of Mn/Ca (<0.1 mmol/mol) were found in *Nps*. However, higher values of Mn/Ca were found in *G. bulloides* (>0.4 mmol/mol) suggesting the presence

of authigenic Mn-rich phases (Figure 3.10). There are at least two potential types of Mn-coatings on foraminiferal tests (e.g. Barker et al., 2003, Wei et al., 2009): Mn-rich oxides which are generally formed from oxic water column conditions and act as a primary oxidant during early diagenesis and, Mn-rich carbonate overgrowths which are formed in extreme reductive environments such as the Panama Basin (Boyle, 1983, Pena et al., 2005). However, the Mg/Mn composition of any type of Mn-rich coating has been shown to be approximately 0.1 mmol/mmol (between 10-15%) (Barker et al., 2003, Pena et al., 2005 and references herein). This implies that for Mn/Ca values of 0.4 mmol/mol obtained for *G. bulloides*, the expected contribution to the Mg/Ca signal from Mn-rich coatings would be ~0.04 mmol/mol, which is ~2.8 % of the Mg/Ca values and lies within the analytical and procedural errors (see section below). From the evidence presented in this section it was considered that secondary effects on the foraminiferal calcite Mg/Ca measurements would not have significantly altered the primary temperature signal and hence no Mg/Ca data points were excluded from the record.

3.3.2.2. Temperature and salinity estimates

Different Mg/Ca temperature calibration equations were considered for the conversion of the Mg/Ca values to calcification temperatures for *Nps* (Elderfield and Ganssen, 2000, Nurnberg, 1995, Kozdon et al., 2009) and *G. bulloides* (Cléroux et al., 2008, Elderfield and Ganssen, 2000, Lea et al., 1999, Mashiotta et al., 1999, McConnell and Thunell, 2005) (Figure 3.11).

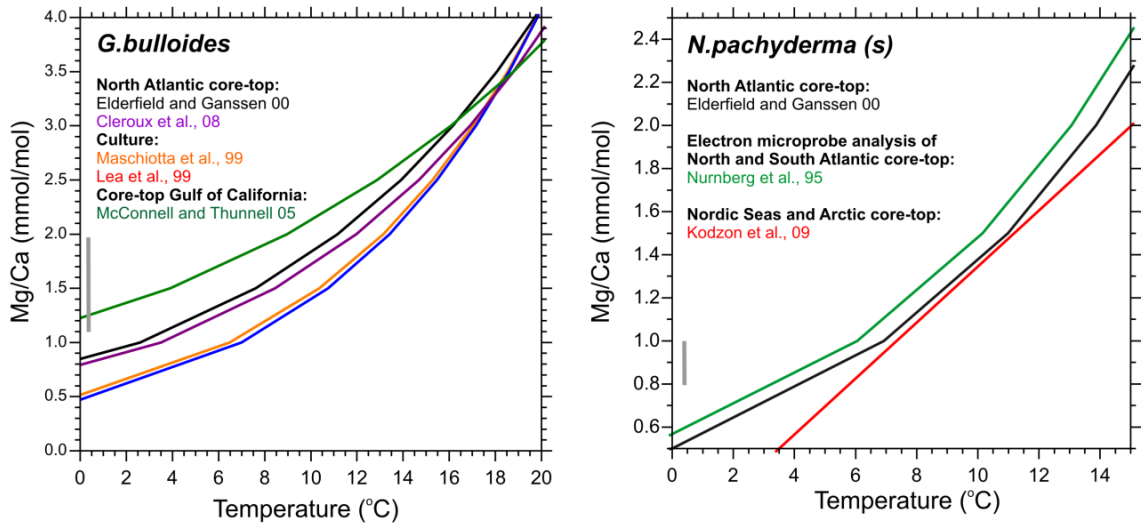

Figure 3.11. Comparison and description of the different Mg/Ca temperature calibrations for *G. bulloides* (left) and *Nps* (right). Vertical grey bars indicate the range of values obtained in the Mg/Ca records in RAPiD-35-25B.

Based on the geographical location, the methodology and the type of calibration (i.e. core-top preferentially) as summarised in Figure 3.11, the calibration equations based on the North Atlantic core-top calibration study by Elderfield and Ganssen (2000) with the form of: Mg/Ca=0.5 exp(0.1T) and Mg/Ca=0.8 exp(0.081T) for *Nps* and *G. bulloides*, respectively, were used. These calibrations were able to produce values that are comparable to spring summer modern temperature at the predicted calcification depths for both species (Figure 3.11).

The derived calcification temperatures, based on Mg/Ca ratios, were used to extract the temperature component from planktonic $\delta^{18}O$, allowing determination of the oxygen isotopic composition of seawater ($\delta^{18}O_{sw}$) (see Section 2.4.3 for more details).

Assuming that the freshwater end-member $\delta^{18}O$ was similar throughout the late Holocene, salinity was determined following the modern Labrador Sea relationship from LeGrande and Schmidt (2006):

$$\text{Salinity} = (\delta^{18}O_{sw} - 32.45)/ 0.94$$

3.3.2.3. Error analysis

Over the course of this study the long-term precision of the HR-ICP MS for Mg/Ca was better than ±2.5% (1σ). The analytical precision during the runs was better than ±2% (1σ). An estimate of ±3.7% (1σ) was used for the natural variability for Mg/Ca for *G. bulloides* following the findings presented by Barker et al. (2003) based on 30 *G. ruber* individuals. Duplicates of twenty *Nps* Mg/Ca samples were measured and an average error of ±4% (1σ) was obtained. This error includes the analytical and natural variability errors mentioned above and therefore was used in the error propagation. The combination of the analytical and natural variability errors add to an average temperature error of ±0.4°C and ±0.45°C for *Nps* and *G. bulloides*, respectively. However, analytical errors are minimal compared to the errors in the temperature calibrations, yet the latter are systematic and hence of less importance.

In order to calculate error estimates on the reconstructions of calcification temperature, $\delta^{18}O_{sw}$ a standard error propagation calculation for a quadratic paleotemperature equation was followed. Error estimates for paleotemperature and $\delta^{18}O_{sw}$ for *Nps* and *G.*

bulloides are ±0.8 °C, ±0.2 ‰, and ±0.98°C, ±0.35 ‰, respectively. Following Schmidt et al., (1999) salinity error calculations based on the uncertainties in the relationship between $\delta^{18}O_{sw}$ and salinity, estimate a salinity error of ±0.8.

3.3.2.4. Natural variability of Mg/Ca in N. pachyderma(s)

Picking monospecific samples of foraminifera within a sediment core interval is often the first step in producing palaeoceagraphic time-series. It necessarily involves the selection of a subset of individuals from within a population preserved in a particular sample (which in this case, is restricted to a particular species and size in that sediment core interval) with the intention of yielding information that is representative of the population as a whole. However, statistical sampling is prone to errors which decrease with an increasing number of individual's sampled (n). To minimise and constrain the statistical sampling errors and to test that the variability of the Mg/Ca results was not an artefact of poor sampling a natural variability study was conducted. Twenty subsamples of 40 *Nps* individuals between 150-212 µm from the same interval in RAPiD-35-25B were picked, processed and analysed separately as described in Section 2.4.3. The presence of potential contaminant phases was investigated in the same way as described in Section 3.2.1.1. Fe/Ca, Mn/Ca and Al/Ca were found below 0.03 mmol/mol, 0.1 mmol/mol and 0.12 mmol/mol, respectively thereby concluding negligible alteration of the primary Mg/Ca temperature signal.

The Mg/Ca values from the 20 sub-samples showed a percent standard deviation of ±7% (Figure 3.12). These values were then re-sampled into groups of between 2 and 20 using a 'jacknife' resampling method (a statistical tool that randomly groups the values into a specified number of groups). This enabled to study the change of the variance when 40 to 800 foraminifers' are picked, that is to say, the change in % standard deviation as a function of the foraminifera individuals picked (Figure 3.12).

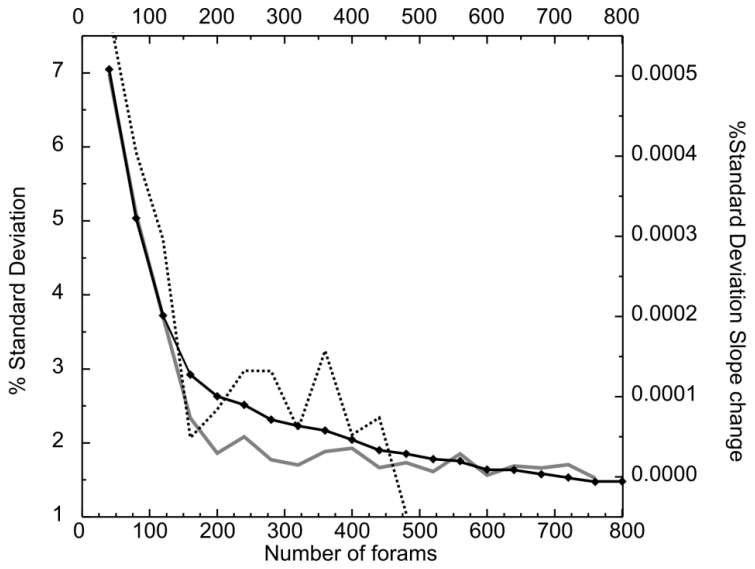

Figure 3.12. Number of *Nps* individuals picked against % standard deviation of the Mg/Ca values using a 'jacknife tool'. The slope change of the % (1σ) is shown in grey. Dotted line is the % standard deviation from the calculations obtained using a random number generator for grouping the Mg/Ca values.

A caveat with using the 'Jacknife' method is that it can repeat the values used within the same group explaining why when it groups the 20 values the standard deviation is not 0. However, as the method calculates the combination of the different values per group 100 different times, the error is small. To test the significance of the repetition of some values within the same group a random number generator was used to provide a dummy sample for re-sampling. The two grouping methods yielded very similar results. As shown in Figure 3.12, a logarithmic decrease in the % standard deviation of the Mg/Ca values with the number of foraminifera picked (or grouped) is observed. This suggests that a minimum of ~160 individuals, which is highlighted by the change in slope in Figure 3.11, should be picked in order to minimise the natural variability error to better than ±3% (1σ). In this study, 150-200 *Nps* individuals were picked for paired Mg/Ca and $\delta^{18}O$ analysis.

3.3.3. Planktonic foraminifera census data

The size fraction 150-250 μm was split repeatedly until enough (a minimum of 350 individuals) planktonic foraminifera specimens could be identified and counted in order to provide a statistically robust representation of the population.

The planktonic foraminifera assemblage 150-250 μm in RAPiD-35-COM is made up of around ~80% or above of *Nps*. The second most abundant species is *T. quinqueloba* ranging between 10-30% of the assemblage in this size fraction followed by species

such as *G. bulloides, Globorotalia truncatulinoides, Neogloboquadrina incompta, G. glutinata* and *Orbulina universa*, which were found to form <4% of the assemblage. As a result of the characteristic low species diversity assemblage in high latitudes, the assemblage counts in this size fraction were mainly dominated by the relative abundance of *Nps* versus *T. quinqueloba*.

3.4. Results and Discussion

This section is divided into two subsections: In Section 3.4.1 results obtained from the box-core RAPiD-35-25B mainly focusing on multidecadal variability during the last millennium and particularly on the onset of the LIA will be presented and discussed. Section 3.2.2 will present the results obtained from RAPiD-35-COM and centennial to millennial scale hydrographic changes during the last 3000 years will be discussed.

3.4.1. Multidecadal to centennial changes in the Eastern Labrador Sea during the last millennium

3.4.1.1. Summer surface conditions in the Eastern Labrador Sea

The shallow depth habitat of the planktonic foraminifer *T. quinqueloba* allows the surface waters above the strong and shallow summer pycnocline to be monitored (Figure 3.8) (Holliday et al., 2006). As such, it records a combination of signals indicative of summer re-stratification processes at the site. These include summer warming due to increased seasonal insolation, meltwater and influences of the fresh and cold water masses such as the EGC and the East Greenland Coastal Current (Bacon et al., 2002, Holliday et al., 2006).

The $\delta^{18}O$ record from *T. quinqueloba* shows high amplitude variations of ~0.35 ‰ between 700-1400 years AD with a long term trend towards heavier isotopic values of ~0.15 ‰ from 1400 to present (Figure 3.13c). The first half of the record shows a strong correlation with Total Solar Irradiance (TSI) (Bard et al., 2000) (Figure 3.13b) with a Pearson coefficient value of 0.56 (>95% Confidence Level) with a time-lag of 19 years, possibly indicative of irradiance driven summer melting. The Pearson coefficient was obtained by employing the PearsonT program (Mudelsee, 2003) on the equal time spaced Gaussian smoothed two time-dependent variables (TSI and $\delta^{18}O$). This relationship breaks down and no correlation is found beyond 1400 years AD, when the trend to heavier $\delta^{18}O$ commences. This heavy trend continues until the present without a

transition from the end of the LIA to the present and is a common feature observed in other high-resolution subpolar North Atlantic records (Kaufman et al., 2009, Massé et al., 2008, Richter et al., 2009, Sicre et al., 2011). Some of the observed short-lived excursions to heavier $\delta^{18}O$ values coincide with the timing of large volcanic eruptions, as indicated by global stratospheric injection of sulphates (Gao et al., 2007) (Figure 3.13a), for instance, the large 13th century eruption, which has been shown in data and models to have caused cooling in the North Atlantic and increased production of sea-ice (Miller et al., 2012, Zhong et al., 2011, Sicre et al., 2011).

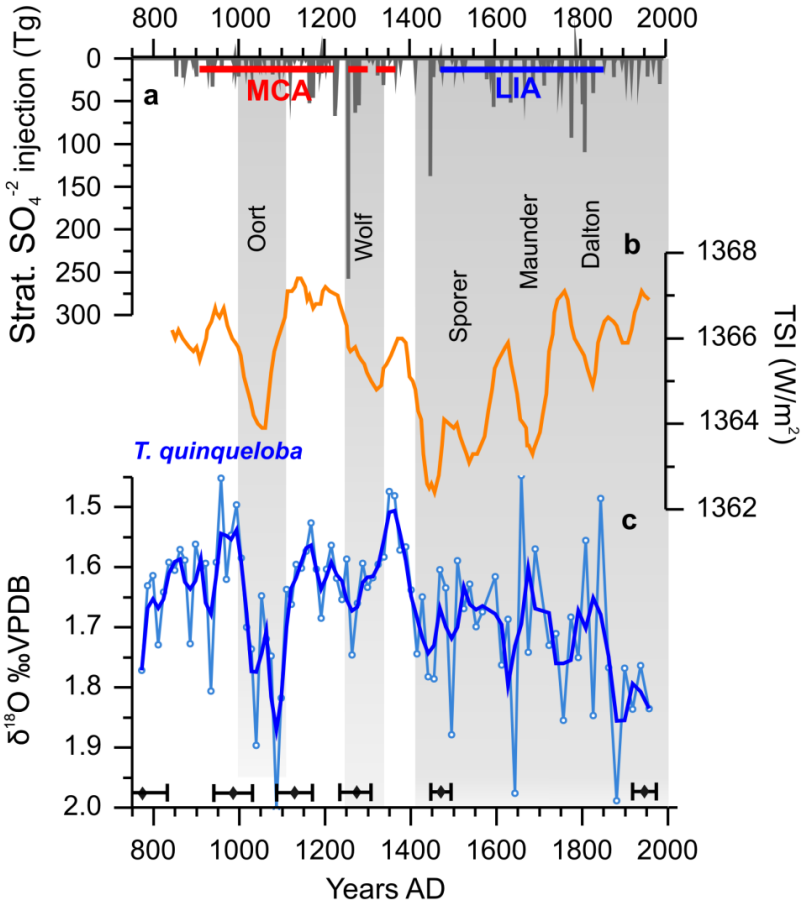

Figure 3.13. (a) Global stratospheric injection of sulphate (Tg) - proxy for volcanic forcing (Gao et al., 2007) (b) ^{10}Be based TSI (Steinhilber et al., 2009) (c) $\delta^{18}O$ *T.quinqueloba*. The shaded area marks the shift in the $\delta^{18}O$ *T.quinqueloba* which is coincident with the onset of the LIA. The two shaded bands indicate the periods of solar minima during the MCA. Diamonds indicate calibrated ^{14}C dates with 1σ error bar.

In contrast, *Nps* typically calcifies deeper down in the water column giving an approximate signal of ~200 m depth (e.g. Kozdon et al., 2009, Simstich et al., 2003). The $\delta^{18}O$ *Nps* record shows surprising stability with only very limited centennial-scale amplitude changes and a maximum variability of ~0.2 ‰ over the last 1200 years (Figure 3.14a). Similarly, paired Mg/Ca-$\delta^{18}O$ temperature (and therefore salinity) reconstructions also suggest stable calcification temperatures with a maximum variability of 2°C (and 1 psu) and a slight increase in temperature and salinities from 1550 years AD onwards (Figure 3.14b,c).

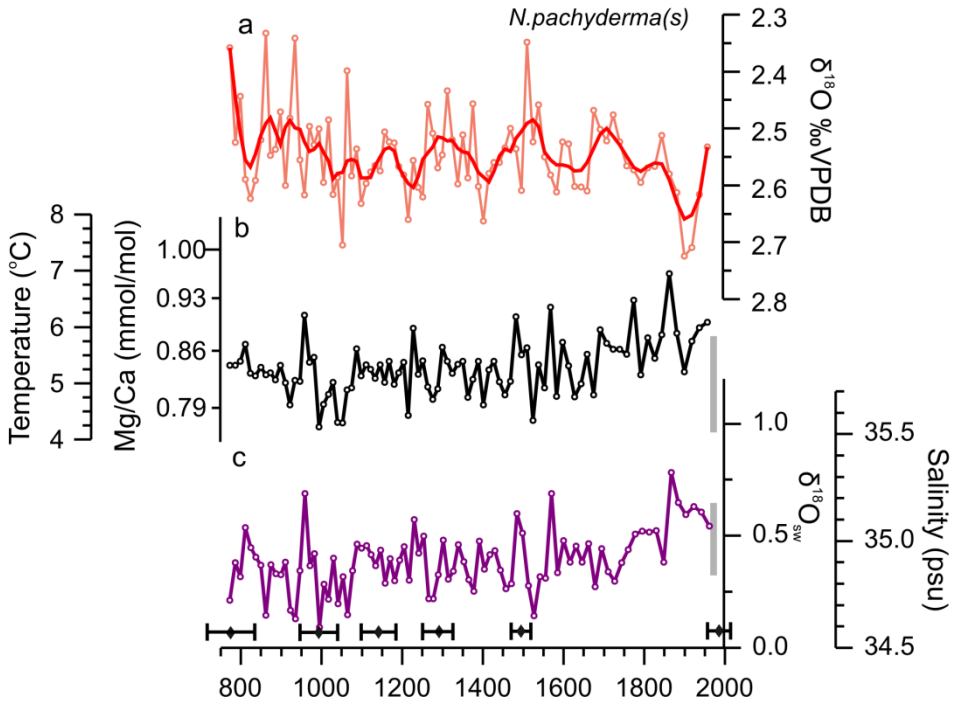

Figure 3.14. (a) $\delta^{18}O$, (b) Mg/Ca based temperature, (c) $\delta^{18}O_{sw}$ and salinity of *Nps*. Grey bars are modern temperature and salinity ranges (150-200m m depth) at the site from cruise CTD data, Holliday et al., (2009) and ODV. Diamonds indicate calibrated ^{14}C dates with 1σ error bar.

In Figure 3.15 the calcification temperatures and salinity estimates from *Nps* are plotted against modern temperature and salinity data for the North Atlantic (Key et al., 2004). This comparison shows that the *Nps* values lie approximately between the 27.5-27.8 (kg/m^3) density lines. This is in striking agreement with *Nps* plankton tow studies from the Nordic Seas (Kozdon et al., 2009, Simstich et al., 2003), in which they propose that calcification depth of this species is bound to isopycnals of potential density of 27.7 to 27.8, exactly coincident with the density range observed in Figure 3.15 on the basis of the temperature and salinity reconstructions presented here.

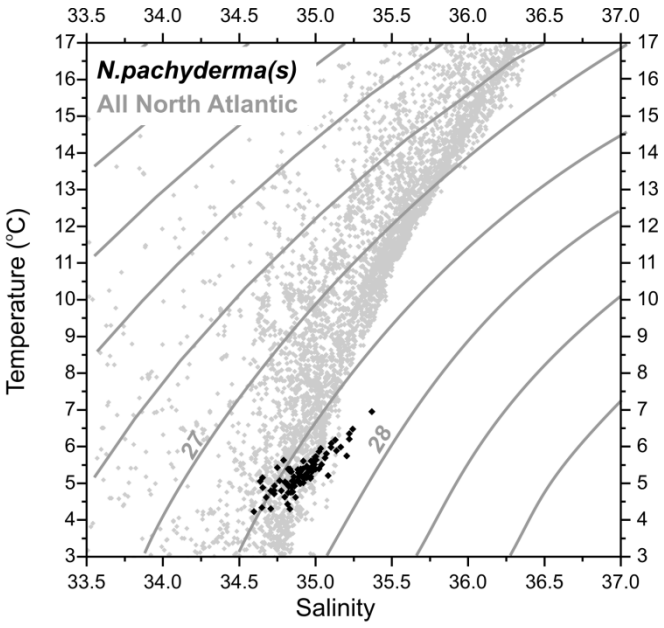

Figure 3.15. Temperature and salinity diagram. Grey lines indicate lines of same density (isopycnals). The grey points are all of the North Atlantic data from Global Ocean Data Analysis Project (GLODAP) data (Key et al., 2004). The black data points indicate the temperature and salinity values obtained from paired Mg/Ca and $\delta^{18}O$ measurements on *Nps.*

The difference between $\delta^{18}O$ values of foraminifera that live in different habitat depths is often used to provide information on the stratification of the water column (e.g. Mulitza et al., 1997, Rashid and Boyle, 2007). In particular, a study of the $\delta^{18}O$ difference between *T. quinqueloba* and *Nps* in the Nordic Seas concluded that the difference provides information on the thermal stratification of the water column (Simstich et al., 2003). A recent sediment trap study (Jonkers et al., 2010) from the Irminger Sea has challenged this application as *T. quinqueloba* and *Nps* were observed to bloom at different times during the year and thus proposed that the differences in $\delta^{18}O$ could indicate changes in the seasonal thermal contrast. Based on these data it was also suggested that both species inhabited similar depths in the water column (~50 m) and that there was a vital effect of +0.85 ‰ for the $\delta^{18}O$ of *T. quinqueloba* (Jonkers et al., 2010). However, the range of $\delta^{18}O$ values in *T. quinqueloba* obtained in this study are on average 1‰ lighter than those found by Jonkers et al. (2010). This magnitude of difference between data is hard to explain in terms of water property given the proximity of the two locations. One potential reason for the discrepancy could be genotypic differences within the same morphospecies of *T. quinqueloba* which may be adapted to different habitats and have distinct ecological preferences (Darling et al., 2000). In the Sub-Arctic North Atlantic two genotypes of *T. quinqueloba* have been

found to coexist in the water column (Stewart et al., 2001), the possibility of different ecological niches for each genotype could potentially create biases in palaeoceanographic reconstructions.

An east-west plankton tow and sediment trap study in the Nordic Seas showed that the largest offset in $\delta^{18}O$ between the two species was when there is an increased thermal stratification between the IC (Simstich et al., 2003) and the deeper waters of up to 1.5 ‰. Nevertheless, at the RAPiD-35-25B site the water column structure during the summer is very different to the one observed in the Nordic Seas. Here, a very pronounced shallow pycnocline develops during the summer (Figure 3.8) and the deeper calcification depth of *Nps* precludes the geochemical signal of this foraminifera species from being affected by re-stratification processes that take place at shallower depth in the water column. Although we observe a larger difference between *T.quinqueloba* and *Nps* during the first half of the record, probably indicating increased upper column thermal stratification, what are the effects of summer thermal re-stratification on deep water convection?

3.4.1.2. Reduction in LSW formation: Thermal versus salinity stratification

The strong salinity effect on seawater density makes salinity stratification critical for deep water convection. An increase in freshwater export to the Labrador Sea makes the surface waters fresher and therefore less dense. Due to the positive buoyancy provided by the freshwater, in spite of strong winter cooling, the upper layer will still remain less dense than the underlying waters, reducing convection and thus LSW formation. Modern examples of this process are the Great Salinity Anomalies.

The shallow habitat depth of *T. quinqueloba* allows monitoring past changes in the surface hydrography in the Eastern Labrador Sea and thus its geochemical signature can potentially provide information on freshwater discharge events that might have led to a reduction in LSW formation during the last millennium. However, the light shell weights of this species (1 µg/test) prevented the obtainment of paired $\delta^{18}O$ and Mg/Ca measurements and only $\delta^{18}O$ measurements were performed. The $\delta^{18}O$ composition of planktonic foraminifera contain a temperature and salinity component, for instance heavier $\delta^{18}O$ can either be colder and/or saltier. Unfortunately, it is hard to disentangle the contribution of both properties to this signal without any additional independent

temperature proxy. In order to tackle this issue hydrographic temperature and salinity measurements from the central Labrador Sea for the last 70 years (provided by I. Yashayaev) (Figure 3.16a and 3.16b) were used to calculate the predicted $\delta^{18}O$ of the calcite ($\delta^{18}O_{predicted}$) for this same time period (Figure 3.16c).

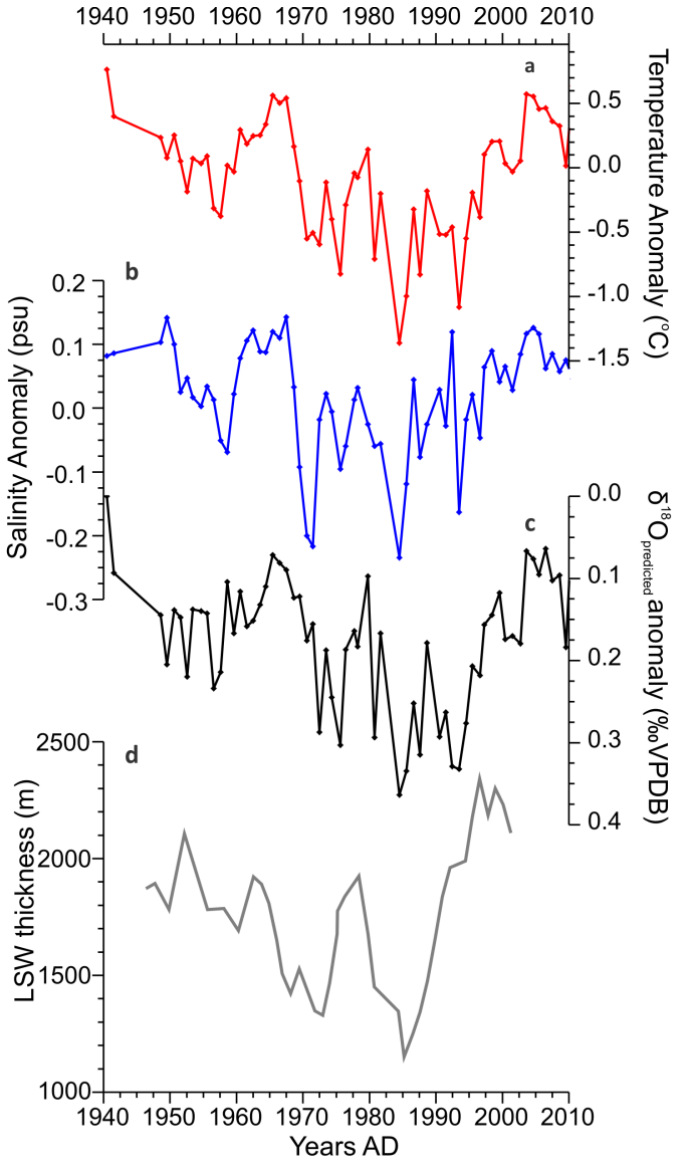

Figure 3.16. Annual hydrographic time-series of (a) temperature and (b) salinity anomalies from the central Labrador Sea (courtesy of I. Yashayaev), (c) anomalies of the predicted $\delta^{18}O$ of the foraminiferal calcite, based on the temperature (a) and salinity (b) hydrographic measurements, (d) thickness of LSW density between 27.74-27-79 kg/m^3 (Curry et al., 1998). Anomalies are calculated by subtraction from the long-term mean, except in (c) where the anomaly was calculated as the deviation from the minimum $\delta^{18}O$ value.

The predicted $\delta^{18}O_{predicted}$ shows a strong co-variability with temperature indicating that temperature dominates the $\delta^{18}O_{predicted}$ signal in the top 75 m of the water column (Figure 3.16c). Furthermore, we observe that heavier $\delta^{18}O_{predicted}$ values correspond to periods of fresher and colder waters during the salinity anomalies in the central Labrador Sea which in turn caused a decrease in LSW convection and therefore thickness of this water mass (Figure 3.16).

The ability of the $\delta^{18}O_{predicted}$ signal to record freshwater discharge events into the Labrador Sea during the Great Salinity Anomalies suggests that despite the temperature and salinity contribution to the $\delta^{18}O$ signal, the temperature dominance in the $\delta^{18}O$ in *T. quinqueloba* from RAPiD-35-25B (Figure 3.16c) can be used to monitor the past influence of cold (and fresh) Arctic waters to the site. In light of these findings and assuming that $\delta^{18}O_{sw}$-salinity relationship in the Labrador Sea remained the same during the last millennium, the 1.5-2 ‰ shift recorded in the *T. quinqueloba* $\delta^{18}O$ at the onset of the LIA (Figure 3.13c) can be explained by a temperature and salinity decrease of 1.5^{o}C and 0.2, respectively due to freshwater discharges.

Furthermore, the colder temperatures after 1400 years AD are also corroborated by the faunal assemblage changes, which are an independent quantitative ecological parameter. The relative percentage of the polar species *Nps* can be used to monitor past temperatures at the site (Hilbrecht, 1997). Assemblage counts on RAPiD-35-25B reveal abrupt shifts in the dominant species of ~35% during the period between 700-1400 years AD. There is a shift at ~1400 years AD from a mean of ~60% *Nps* to an increased presence of *Nps* to about ~80-95% which continues until the present (Figure 3.17g). Using transfer function and modern *Nps* distribution studies (Eynaud, 2011, Hilbrecht, 1996, Hilbrecht, 1997, Kucera, 2007), this shift in %*Nps* approximately equates to a temperature shift of ~2.5^{o}C, similar to the estimated temperature changes contributing to the predicted $\delta^{18}O$ values (Figure 3.16a,c). The $\delta^{18}O$ from *T. quinqueloba* and the %*Nps* record similar variability and particularly agree on the timing of this shift in surface water mass properties at ~1400 years AD, occurring at the transition from the MCA into the LIA (Figure 3.17f,g).

3.4.1.3. The onset of the Little Ice Age: a shift in atmosphere-ocean feedbacks

Documentary sources suggest that during periods of the MCA parts of Greenland were ice-free, aiding the colonisation and the establishment of Norse settlements. Conversely, during many decades of the LIA, the Icelandic shelf was documented to have been surrounded by sea ice (Koch, 1945). However, sea ice does not currently form around Iceland. As observed during the GSA, it only appears when there is a large export of sea ice from the Arctic Ocean (Andrews, 2009). Therefore, the increased presence of drift ice and cooling north of Iceland is symptomatic of a southeastward advance of the polar front and therefore an increased southward transport of Arctic waters by the EGC and the East Icelandic Current (EIC) (a branch of the EGC) into the North Atlantic.

Recurrent invasions of drift ice were documented to have reached the North Icelandic Shelf between 1500-1900 years AD i.e. during the LIA (Koch, 1945, Ogilvie and Jónsson, 2001) (Figure 3.17d). The main concern with the use of documentary sources to monitor polar front advances is that they are inherently biased as they only detect extreme southern advances which delivered Arctic drift ice to the Icelandic Shelf, under-representing intermediate advances. Furthermore, the documentary evidence of Icelandic sea ice is more fragmentary before 1600 years AD (Figure 3.17d), and therefore these reconstructions have to be interpreted cautiously. The timing and magnitude of a southward shift of the polar front and the greater influence of polar waters reaching the Denmark Strait and therefore the Labrador Sea over the last millennium has also been recorded in a wealth of proxies. The organic geochemistry sea ice proxy IP25 (Massé et al., 2008) records similar fluctuations of the presence of sea ice north of Iceland which are very comparable to the observations from Ogilvie and Jónsson (2001) (Figure 3.17d,e). The presence of quartz in the Icelandic shelf sediments has been interpreted as a proxy for allochthonous drift ice transported by the EIC (e.g. Andrews, 2009). These data suggest a steady increase in drift ice reaching the coast of North Iceland during the last millennium (Moros et al., 2006) (Figure 3.17c). Furthermore, diatom assemblages and sea surface temperature reconstructions based on alkenones from North of Iceland show a transition to colder conditions at ~1400 years AD (Jiang et al., 2005, Sicre et al., 2008b). Also, foraminifera assemblages from the east coast of Greenland in the Denmark Strait show an increased influence of polar waters at the site (Jennings and Weiner, 1996) (Figure 3.17c).

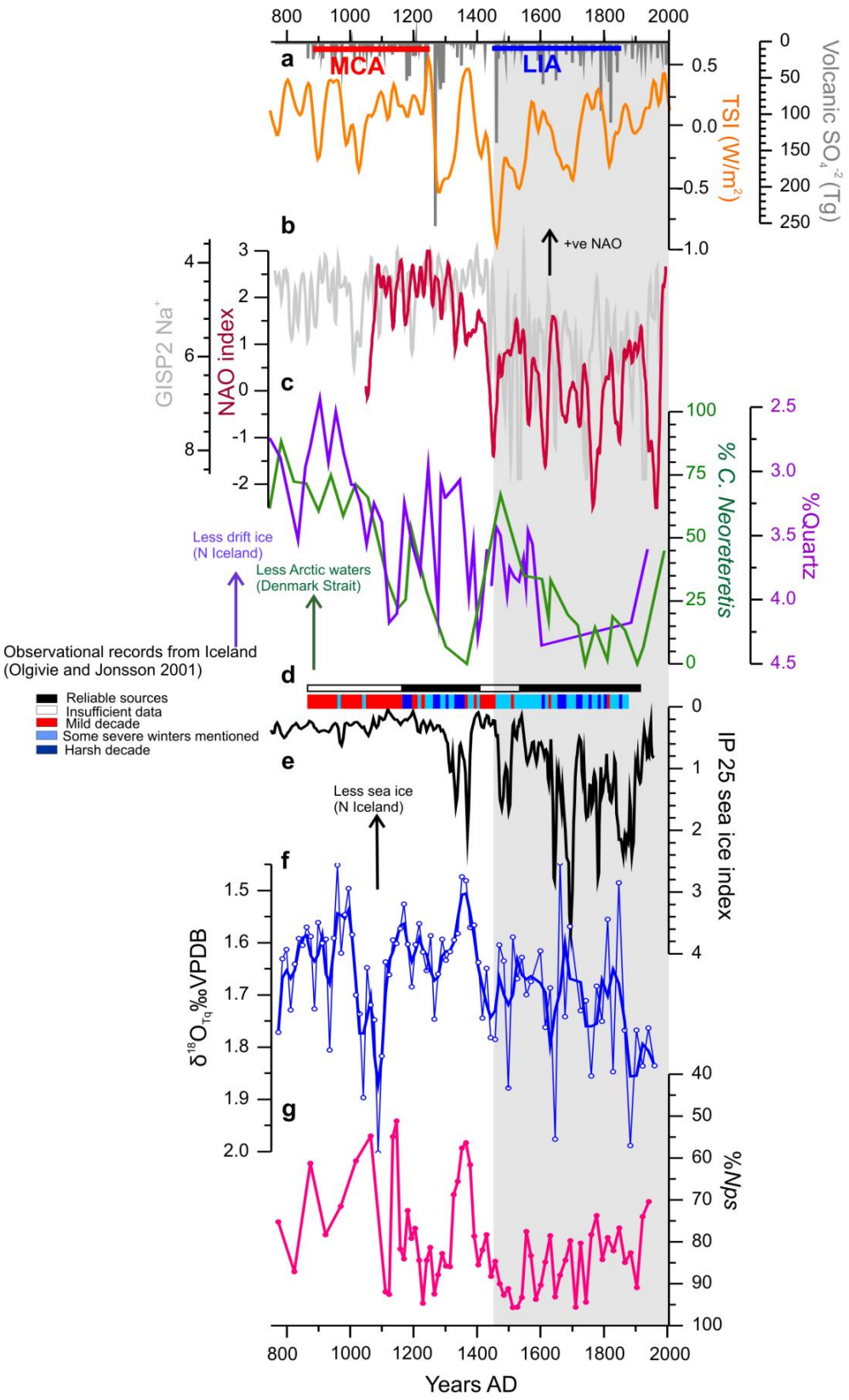

Figure 3.17. (a) External forcings: volcanic (Gao et al., 2007) (grey) and TSI forcing (Steinhilber et al., 2009) (orange) (b) Atmospheric forcing: Na^+ concentration in GISP2 (Mayewski et al., 1997) (light grey) and NAO proxy reconstruction (Trouet et al., 2009) (red) (c) % quartz reaching the North Icelandic Shelf (Moros et al., 2006) (purple), *% C. Neoteretis* in the East Greenland Continental Shelf on the Denmark Strait (Jennings and Weiner, 1996) (green) (d) Observational historical records around the Iceland coast (Ogilvie and Jónsson, 2001), (e) IP25 sea ice proxy (Massé et al., 2008), (f) and (g) $\delta^{18}O$ from *T. quinqueloba* and *%Nps*, respectively from RAPiD-35-25B (this study). The grey shaded area marks the shift at ~1450 years AD observed in the majority of the proxies.

All of the proxies records summarised above and presented in Figure 3.17c-g suggest a greater presence of polar waters and drift ice being transported southwards from the Arctic into the North Atlantic via the EGC at the onset of the LIA.

Based on modern observations, freshwater export from the Arctic to the North Atlantic has often been associated with a change in atmospheric pattern (Dickson et al., 1988). North Atlantic high-resolution atmospheric records that span the entirety of the last millennium are scarce. The two main reconstructions available are (i) a NAO reconstruction based on a tree-ring drought record from Morocco and a speleotherm precipitation record from Scotland (Trouet et al., 2009) and (ii) the sea salt concentration (Na^+) record in Greenland ice cores (GISP2), which is indicative of storminess south of Greenland (Mayewski et al., 1997, Meeker and Mayewski, 2002). Although initially, calibration studies of Na^+ in GISP2 against modern atmospheric conditions interpreted increased in the concentration of Na^+ as being indicative of a positive NAO (Mayewski et al., 1997, Meeker and Mayewski, 2002) recent re-analysis of this data has suggested that increased storminess south of Greenland (indicated by an increase in Na^+) is a very characteristic feature of negative NAO atmospheric regime (Trouet et al., 2012), thus making the two atmospheric reconstructions consistent.

Both atmospheric reconstructions present a marked shift in the North Atlantic atmospheric circulation pattern at ~1450 years from a prevalent positive to negative NAO state (Figure 3.17b). Such a shift in atmospheric conditions would have presumably enhanced the northerly winds and promoted the transport of drift ice and polar waters southwards into the Labrador Sea and caused the surface cooling and freshening observed in the Eastern Labrador Sea, probably also affecting the wind-stress curl and the westerly positioning over the Labrador Sea, like during the GSA.

The external trigger for the onset of the LIA atmospheric-ocean feedbacks remains highly debated. Solar irradiance has often been put forward as the driver for changes in the patterns of atmospheric circulation over the North Atlantic, such as the NAO, mostly through tropospheric ozone feedbacks (Shindell et al., 2001). Studies of solar irradiance forcing and frequency of blocking events (see Section 1.2.2 and 1.2.3 for details) across the Atlantic have also shown significant positive correlation (Barriopedro et al., 2008, Lockwood et al., 2011) with potential effects on the oceanic conditions in

the subpolar North Atlantic specifically the SPG (Häkkinen et al., 2011). The transition between the MCA and the LIA at around 1400 years AD was a transition to a higher frequency of solar minima periods and hence probably a more prevalent negative NAO state with increased frequency of blockings (Lockwood et al., 2011, Shindell et al., 2001). Additionally, explosive volcanism has immediate impacts on global surface climate as it exerts a negative radiative forcing, inducing surface cooling (Bradley, 1988, Robock, 2000). Despite the short residence time of aerosols in the stratosphere, volcanic eruptions can have longer-lived climatic impacts through sustained ocean-atmospheric feedbacks (Schneider et al., 2009) such as sea ice (Miller et al., 2012).
Another potential mechanism responsible for this abrupt shift in North Atlantic atmospheric circulation involves teleconnection processes between the Pacific Ocean and the North Atlantic. Model and observational studies have suggested that the differing East-West Pacific sea surface temperature response to radiative forcing at the onset of the LIA may have resulted in a transition from La Niña to El Niño states at the onset of the LIA. This, likely propagated to the North Atlantic via tropospheric dynamics and possibly tropical temperature differences between the Pacific and Atlantic, likely affecting the NAO state (Graham et al., 2007, Hoerling et al., 2001).

3.4.1.4. Changes in $\delta^{13}C$ at the onset of the LIA: changes in air-sea exchange?

Air-sea exchange is mostly influenced by wind-speed and the difference in the concentration of gasses between the atmosphere and the ocean (referred to as air-sea partial pressure difference, in the case of CO_2: $\Delta\rho CO_2$). The study of past air-sea exchange in the surface ocean could be indicative of a more or less isolated water column. For instance, a highly stratified Labrador Sea would limit the invasion of atmospheric CO_2 into the upper waters, and vice versa during periods of active deep water formation.

To gain first-order insight into changes in air-sea exchange across the MCA-LIA transition in the Eastern Labrador Sea we use the stable carbon isotopic composition ($\delta^{13}C$) values of three planktonic foraminifera species: *T. quinqueloba, G. bulloides* and *Nps*. The $\delta^{13}C$ of foraminiferal shells mainly reflects the carbon isotopic composition of the Dissolved Inorganic Carbon (DIC) of the ambient seawater in which they calcified in and $\delta^{13}C_{DIC}$ at these time-scales is affected by local changes such as the relative mixture of water masses, air-sea exchange, productivity and balance between

photosynthesis and respiration (Ravelo and Hillaire-Marcel, 2007). The interplay of all these factors and the additional kinetic and vital fractionation (which can be considerable, see Figure 3.18) complicates the interpretation of $\delta^{13}C$ in planktonic foraminiferal calcite.

Thus, the study of past air-sea exchange from the $\delta^{13}C$ in planktonic foraminifera may indicate the degree of isolation of the upper water column. For instance, if the water column in the Labrador Sea was highly stratified a reduced mixing with deeper waters will lower $\Delta\rho CO_2$ limiting the invasion of light carbon deriving from atmospheric CO_2 beyond the surface waters. Although this will increase isotopic equilibration of the $\delta^{13}C$ in the uppermost layer (leaving a lighter $\delta^{13}C_{DIC}$ signal at the surface), the underlying waters will present a heavier $\delta^{13}C$ relative to times of well-mixed upper water column.
The $\delta^{13}C$ data from the three planktonic species (Figure 3.18) shows a shift towards heavier $\delta^{13}C$ at ~1400 years AD which is consistent with a decrease in air-sea exchange (decreasing atmospheric ^{12}C flux into the ocean) at the site. The timing of this shift coincides with the transition to colder and fresher surface ocean conditions recorded by *T. quinqueloba* $\delta^{18}O$ and %*Nps*. This suggests that the strengthening freshwater stratification and/or the presence of sea ice in the upper water column may have reduced convection in the Labrador Sea and in turn decreased the invasion of light $\delta^{13}C$ atmospheric from CO_2.

Alternatively, the thermodynamic dependency of equilibration between the ocean and the atmosphere (equilibrium fractionation increases with decreasing temperature (0.1‰ per 1^{o}C temperature shift), could explain most of the observed shift in the $\delta^{13}C$ (up to 0.3‰) (Lynch-Stieglitz et al., 1995). Other complications for the interpretation of the $\delta^{13}C$ arise from the species-specific fractionation. For example the lighter $\delta^{13}C$ in *T. quinqueloba* might be a result of the symbiont-photosynthesis activity, as it causes a deviation from $\delta^{13}C_{DIC}$ by calcifying from the carbon of its internal pool and typically has a strong size-dependence probably due to differing rates of photosynthesis (Spero and Williams, 1988, Stangeew, 2001, Zeebe et al., 1999). On the other hand, *G.bulloides* has ontogenic, nutrient and carbonate ion complications (Ganssen and Kroon, 2000, Peeters et al., 2002, Spero et al., 1997). In this regard, the $\delta^{13}C$ in *Nps* might be slightly more reliable. Firstly, the deeper calcification depth of this species allows monitoring of the influx of light $\delta^{13}C_{DIC}$ deriving from atmospheric CO_2

reaching intermediate depths. Secondly, $\delta^{13}C$ in *Nps* has previously been used to monitor DIC in the North Atlantic surface waters where it was found to have a constant fractionation from the $\delta^{13}C_{DIC}$ of the ambient waters (Labeyrie and Duplessy, 1985).

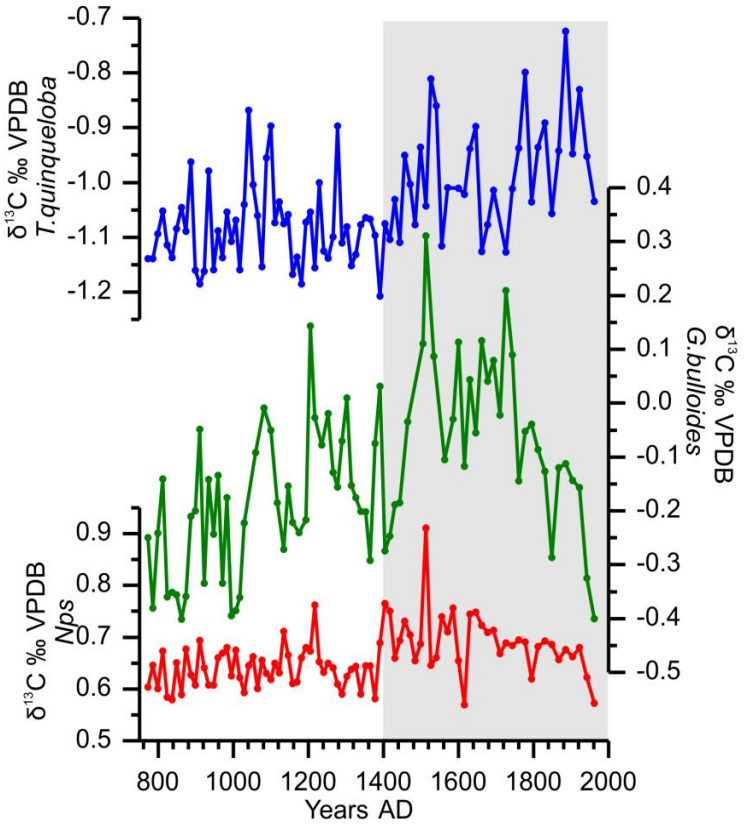

Figure 3.18. $\delta^{13}C$ *T. quinqueloba* (blue), *G. bulloides* (green), *Nps* (red), respectively. Shaded grey area marks the shift in the other proxies and therefore the onset of the LIA.

In summary, the application of $\delta^{13}C$ as a proxy for $\delta^{13}C_{DIC}$ is not straightforward and the caveats outlined above hinder the application of it as a robust proxy for air-sea exchange; yet it is noted that the data is consistent with the notion of reduced air-sea exchange in the Eastern Labrador Sea during the LIA.

Additionally, a short-lived trend towards lighter $\delta^{13}C$ in *G. bulloides* and *Nps* is observed from the 1900s to the present (Figure 3.18) and was possibly caused by the injection of isotopically light fossil fuel CO_2 into the atmosphere, a phenomenon known as the Suess effect.

3.4.1.5. Changes in the properties of the Irminger Current at the onset of the LIA

Despite the limited representation of *G. bulloides* at the RAPiD-35-COM site we make use of its ecological preferences for particular hydrographic conditions (described in Section 3.3.1) in order to explore the properties of the Atlantic waters reaching the core site. It is therefore interpreted that the temperature and salinity conditions recorded in *G. bulloides* as indicative of the properties of the IC (a branch of the North Atlantic Current) that is known to reach the site today (Holliday et al., 2009) (Figure 3.1 and 3.2). The IC is an important source of heat and salt to the Labrador Sea, balancing its annual mean surface heat loss and the addition of freshwater from boundary currents (Straneo, 2006), and it is therefore key in the restratification processes that take part in the summer and may be representative of SPG dynamics.

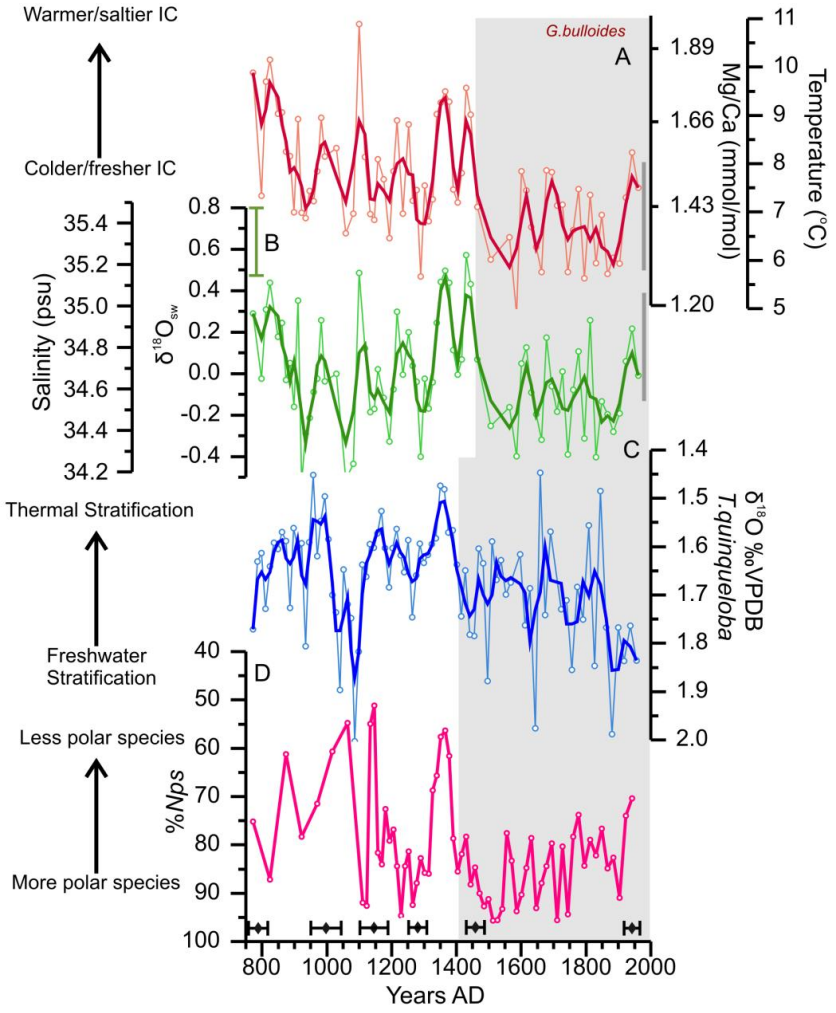

Figure 3.19. RAPiD-35-25B (a) and (b) Paired Mg/Ca-$\delta^{18}O$ based temperature and salinity reconstructions from *G.bulloides*, (c) $\delta^{18}O$ *T .quinqueloba*, (d) *%Nps.*

G. bulloides Mg/Ca-based temperature reconstructions from RAPiD-35-25B for the last millennium show warmer conditions during the first half of the record and a transition into cooler conditions after ~1450 years AD, with a prominent warm event between 1350-1450 years AD coincident with a solar maximum and a minimum in volcanic forcing period (Gao et al., 2007) (Figure 3.19). Unexpectedly, the major temperature shift occurred approximately 50 years later than the shift observed in the oceanographic changes from the $\delta^{18}O$ *T. quinqueloba* and %*Nps* reconstructions (Figure 3.19). A smaller lag of ~30 years is also observed for the beginning of the warm event ~1350 yrs AD.

The absolute lag between the Mg/Ca temperature record from *G. bulloides* and the rest of the other proxies from the site cannot be accurately quantified considering the dating errors. Nevertheless, the lag is robust as the signals are co-registered in the same samples obtained from a single core interval. Ignoring the possibility that the warm short-lived temperature peak at 1400-1450 years AD present in *G. bulloides* is an anomalous event implying that the temperature shift started at 1400 years AD and hence concomitant with the rest of the proxy records, there are other plausible explanations for this offset. Differential bioturbation effects on different sized foraminifera 150-212 µm versus 250-315 µm could have had an upward pumping effect on the larger size fraction (e.g. Hall et al., 2010). A highly likely possibility is that due to the reduced abundance of *G. bulloides* at this site (1-3% of the total assemblage) bioturbation effects on a high abundance peak prior to the MCA-LIA transition might have resulted in older foraminifera within the peak being mixed into younger intervals (approximately 2 cm) where a very reduced number of *G. bulloides* individuals were present, thereby biasing the record and creating this apparent lag. Additionally, it is also speculated that this time lag may reflect the advection time that the freshwater anomaly recorded in the Labrador Sea took to propagate around the SPG until it reached the Irminger branch of the Atlantic Inflow. The GSA took around 15 years to complete that same pathway (Dickson et al., 1988), although studies of the different 20th century salinity anomalies have revealed a considerable variability of the propagation time-scales, which has been shown to be dependent in the nature, magnitude and persistence of some of these salinity anomalies (Belkin, 2004).

The temperature and salinity reconstructions from *G. bulloides* present good similarities with the hydrographic reconstructions of the NAC presented in Chapter 4. This not only supports the argument that the geochemical signal recorded in *G. bulloides* is monitoring Atlantic Inflow waters reaching the Labrador Sea via the IC but it also means that the processes and mechanisms described in Chapter 4 for the explanation of the hydrographic shifts of the NAC waters are also applicable for the record presented in Figure 3.19.

3.4.2. Centennial to millennial variability in the Eastern Labrador Sea during the Late Holocene

Although the LIA was one of the most pronounced Holocene cold intervals recorded in the North Atlantic region it was not a unique event; and other abrupt centennial climatic events have been recorded in a wealth of palaeoproxies during the Late Holocene (e.g. Mayewski et al., 2004). In order to explore the presence of these centennial oscillations and the millennial trends of the surface water variability in the Labrador Sea and to further understand the causes, mechanisms and frequencies that governed centennial to millennial Late Holocene climatic variability, an extension of the hydrographic records back to 3000 years BP is presented below.

3.4.2.1. Upper water column reconstructions during the last 3000 years

Similar to Section 3.4.1.1, the $\delta^{18}O$ of a surface and deeper-dweller planktonic foraminifera species *T. quinqueloba* and *Nps,* respectively, is used in order to investigate changes in the structure of the upper water column at the site during the Late Holocene. In this section all of the ages will be presented in years Before Present (Present being 1950 years AD).

On longer-time scales, during the last 3000 years, $\delta^{18}O$ measurements from *T. quinqueloba* present high frequency variability up to 0.5‰ without a discernible long-term trend aside the one over the last 600 years (Figure 3.20). Recurrent short-lived events of anomalously heavy isotopic composition are recorded at 2900, 2400, 1900, 1500, 1200, 900, 500 years BP, respectively (Figure 3.20). Single spectrum analysis and wavelet analysis performed on the 20 year Gaussian interpolated record (with a 60 year window) present frequencies at periodicities of 200-400 years between 600-1700 years BP above 90% Confidence Level (CL) (Figure 3.21). Although these

cyclicities are found in the deVries solar cycles at ~210 years the short length of the record and the concentration of these periodicities in a 1000 year window of the record prevents confident conclusions to be drawn from them. Particularly as some of these cycles could be a distortion of the expected spectrum by the single-point outliers within the dataset (Weedon, 2003).

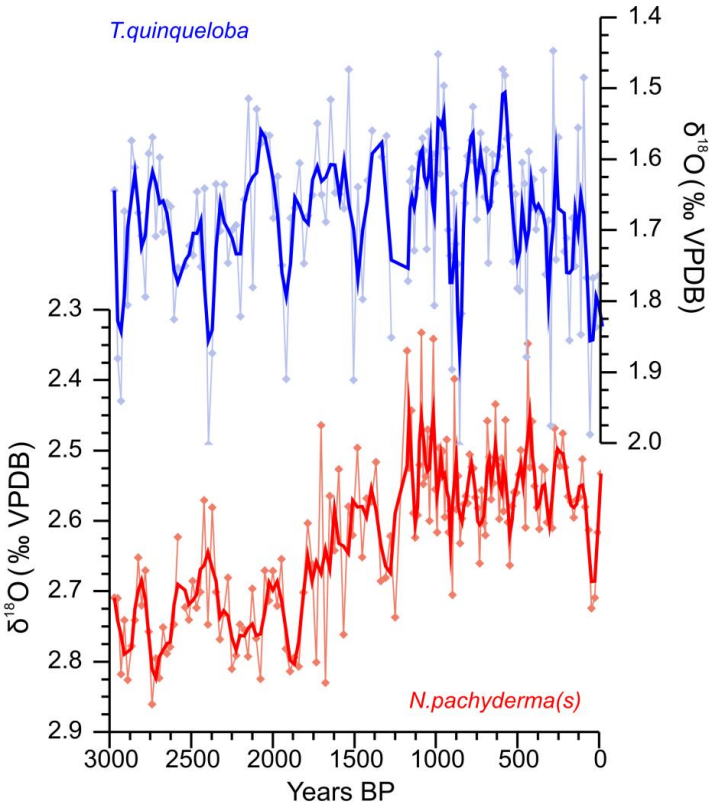

Figure 3.20. $\delta^{18}O$ *T. quinqueloba* and *Nps* from RAPiD-35-COM.

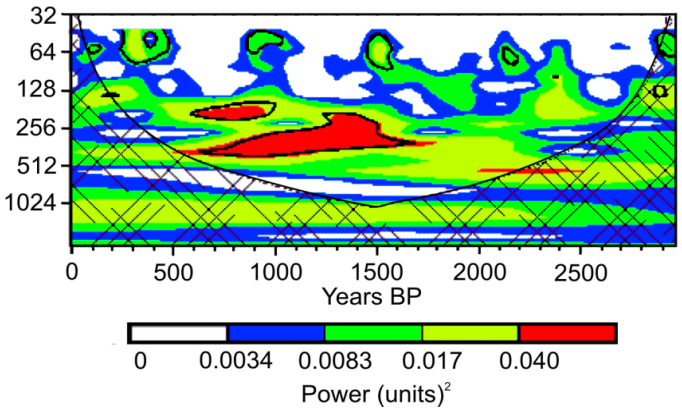

Figure 3.21. Wavelet analysis on the gaussian interpolated *T. quinqueloba* $\delta^{18}O$. Red areas indicate >75% power over red-noise level. The black line outlines the area >90% CL.

By performing a 3-point weighted average smoothing on the *T. quinqueloba* $\delta^{18}O$ it is noted that aside from the multicentennial heavy $\delta^{18}O$ excursion during the LIA (400 years BP), there is a similar broad $\delta^{18}O$ event between 2600-2200 years BP which lies below the average of the record (Figure 3.20). Contrary to expectation from Section 3.4.1.1., during the Late Holocene the deeper $\delta^{18}O$ *Nps* signal presents a slow but steady transition to lighter $\delta^{18}O$ values of a magnitude of ~0.2‰ between 1900-1200 years BP, and then remaining stable up to the present (Figure 3.20). This transition is interpreted to perhaps be related to gradual changes in the water column structure during the Late Holocene maybe due to the climatic reorganization of the Neoglacial. To this end, we use the difference in $\delta^{18}O$ between the two foraminifera species with different habitat depths ($\Delta\delta^{18}O_{Nps\text{-}Tq}$), which, as discussed in Section 3.4.1.1, can be indicative of thermal stratification of the water column. The results reveal a decrease in $\Delta\delta^{18}O_{Nps\text{-}Tq}$ through the Holocene, which is punctuated by distinct centennial-scale cooling events at 2800-2300 years BP, at 1300-1200 years BP and during the LIA (500-0 years BP) (Figure 3.22).

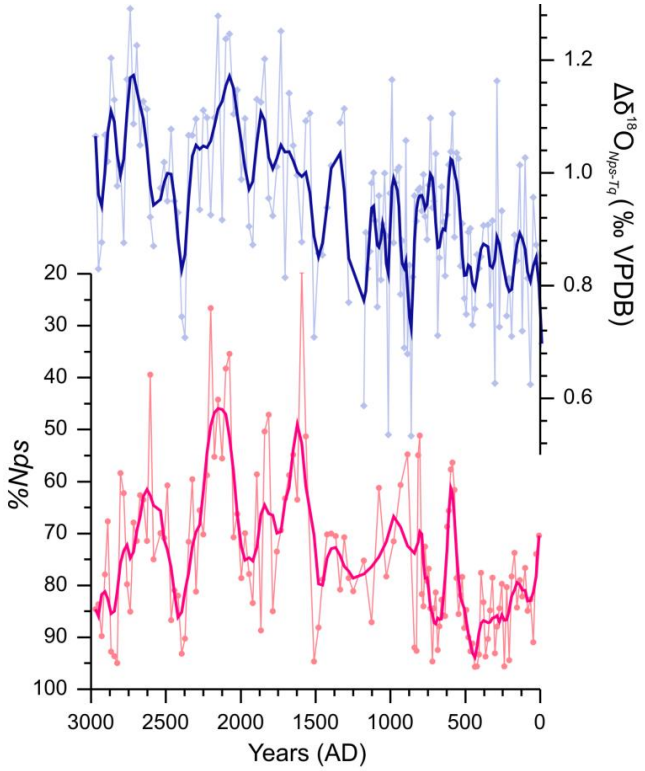

Figure 3.22. $\Delta\delta^{18}O_{Nps\text{-}Tq}$ and %*Nps* from RAPiD-35-COM.

However, the $\Delta\delta^{18}O_{Nps\text{-}Tq}$ interpretation as a stratification proxy needs to be applied with caution, particularly as changes in orbital precession during the Neoglacial resulted in Northern Hemisphere summer insolation changes which would have modified the length of the seasons. Slight seasonal variability maybe have led to changes in the blooming time of each species and resulted in changes in the seasonal thermocline temperatures at the site potentially leaving a seasonality imprint in the $\Delta\delta^{18}O_{Nps\text{-}Tq}$ signal.

Periods of $\Delta\delta^{18}O_{Nps\text{-}Tq}$ variability are also mirrored by the %*Nps* assemblage counts. For example, a decrease in the $\Delta\delta^{18}O_{Nps\text{-}Tq}$ typically corresponds to an increase in the number of polar species - %*Nps* (Figure 3.22). In the long-term, the two records show a trend towards lower $\Delta\delta^{18}O_{Nps\text{-}Tq}$ and increase %*Nps*. Centennial-scale shifts to an increase in %*Nps* and reduced $\Delta\delta^{18}O_{Nps\text{-}Tq}$ are observed on both records at 3000-2800 years BP, 2600-2300 years BP, 1500-1100 years BP and, most noticeably during the LIA at 500 years BP. Additionally a period of maximum $\Delta\delta^{18}O_{Nps\text{-}Tq}$ and minimum in %*Nps* is recorded between 1500-2300 years BP. The co-variability of these two independent variables during this period favours the application of $\Delta\delta^{18}O_{Nps\text{-}Tq}$ as a thermal stratification index.

3.4.2.2. Ocean changes in the Eastern Labrador Sea during the Neoglacial

The last 3000-4000 years of the Holocene, termed the Neoglacial period, is characterized by gradual glacial advances, experienced in most of the Northern Hemisphere, and culminating in the LIA (Bakke et al., 2010, Denton and Karlén, 1973, Nesje and Dahl, 2001). This cooling trend was preceded by the warm Holocene Thermal Maximum and was a period of climate reorganisation probably driven by the reduction in Northern Hemisphere summer insolation. The Neoglacial was not merely limited to the terrestrial realm and has been recorded in numerous North Atlantic records suggesting that the ocean may have played a crucial role in this millennial-scale cooling (Andersson et al., 2003, de Vernal and Hillaire-Marcel, 2006, Jennings et al., 2011, Jennings et al., 2002, Ólafsdóttir et al., 2010, Risebrobakken et al., 2003, Moros et al., 2006). On a wider scale the redistribution of incoming energy due to the inter-hemispheric difference in summer insolation forced the ITCZ to migrate southwards (Haug et al., 2001, Wanner et al., 2008) causing climatic changes further afield in

Africa and Asia through the alteration of the monsoon systems (deMenocal, 2001, Mayewski et al., 2004, Wanner et al., 2008).

The main characteristics of the long-term change in the North Atlantic hydrography was a gradual increase around 4000 years ago in the southward advection of cold ice-bearing Arctic waters as demonstrated by an increase in ice-rafted debris along the East Greenland Margin from Fram Strait to the North Icelandic Shelf (Andrews et al., 1997, Jennings et al., 2002, Moros et al., 2006, Müller et al., 2012) (Figure 3.23c) and reaching the Denmark Strait (Jennings et al., 2011). The results from RAPiD-35-COM also show a long-term decrease in thermal stratification ($\Delta\delta^{18}O_{Nps\text{-}Tq}$) and increase in polar species starting at ~2200 years BP which interpreted as in Section 3.4.1.2 are in agreement with the suggested increase in southward advection of polar waters and verify that these reached the Eastern Labrador Sea (Figure 3.23d,e). These results are also consistent with a foraminiferal assemblage study from Disko Bugt (West Greenland) which revealed a millennial-scale increase in the contribution of Arctic versus Atlantic waters in the WGC (Perner et al., 2011). From the evidence described above it is clear that the Neoglacial cooling was accompanied by a gradual increase in polar waters into the North Atlantic and a decrease in Atlantic Inflow waters reaching the North Iceland Shelf and the East Labrador Sea (as shown in Section 3.5.2.5). The cause for this alteration in the transport of polar waters may have been due to an insolation driven increase in the production of Arctic sea ice and/or a southward enhancement of the Arctic sea ice transport within the EGC by a gradual shift in the atmospheric circulation towards an increase in the meridional circulation over the Nordic Seas as demonstrated by several proxy records (Jong et al., 2006, Rimbu et al., 2003, Rosqvist et al., 2007, Wilson et al., 2004). Moreover, a pollen record from Newfoundland and West Greenland show a gradual trend towards a predominant meridional circulation (equivalent to a negative NAO state) over the Labrador Sea at the onset of the Neoglacial starting between 2500-2200 years BP (Jessen et al., 2011).

Based on the evidence presented above, a Neoglacial increase in freshwater forcing and a decrease in the strength of the westerlies in the Labrador Sea most likely led to a reduction in LSW convection during the Neoglacial.

3.4.2.3. Centennial-scale ocean variability in the Eastern Labrador Sea

Superimposed onto the millennial scale cooling of the Neoglacial, the North Atlantic experienced abrupt centennial climate variability (Mayewski et al., 2004). Cold events such as the 2.7 kyr event, a minor and short lived at around 1300 years BP and the LIA, have been recorded as periods of marked glacial advances in Scandinavia, Baffin Island, Iceland and the Eastern Alps (Bakke et al., 2010, Denton and Karlén, 1973, Nesje and Dahl, 2001). The results from RAPiD-35-COM (Section 3.4.2.1) reveal shifts towards cold surface conditions in the Eastern Labrador Sea recorded by decreased thermal stratification and increased presence of polar species, with a similar timing to the glacial advances (Figure 3.23). Some of these cold events have also been registered in the North Atlantic as times of increased drift ice (Bond et al., 2001) and changes in the hydrography of some of the main AMOC components (Bianchi and McCave, 1999, Hall et al., 2004, Marchitto and DeMenocal, 2003, Oppo et al., 2003, Thornalley et al., 2009). However, in comparison to previously published records, the fine temporal resolution of the proxy reconstructions obtained from RAPiD-35-COM allows and facilitates the comparison and therefore investigation of the mechanisms that might have led to the Late Holocene centennial climatic oscillations.

To test if the nature of the centennial scale climate shifts was the same as for the LIA, following the conclusions from Section 3.4.1.3, a comparison of TSI forcing, Greenland storminess, drift ice reaching north of Iceland and surface proxies from RAPiD-35-COM is presented in Figure 3.23. The cold events identified by Denton and Kárlen (1973) from glacial advances correspond broadly with the cold periods recorded in the surface Eastern Labrador Sea (Figure 3.23d,e) and generally match higher concentrations of Na^+ in GISP2 (which is interpreted as a negative NAO-like atmospheric regime) (Figure 3.23b) and an increase in Arctic drift-ice reaching North Iceland (Moros et al., 2006) (Figure 3.23c). Additionally, summer temperature and winter precipitation reconstructions based on equilibrium lines of maritime glaciers from West Norway have also been used to reconstruct the strength and positioning of the westerlies (Bakke et al., 2008). This study revealed alteration in winter precipitation centred at 2800, 1200 and 400 years BP and humid phases at 2300 and 900 years BP, indicating a zonal and meridional shift of the westerlies, respectively. Thus, this tentatively suggests that the cold/warm periods recorded in RAPiD-35-COM and in other terrestrial and marine records correspond to a negative/positive NAO-like pattern,

which is broadly consistent with the Na^+ ice core-record. Moreover, during cold events the co-variability of the atmospheric and oceanic processes appears to be associated with higher frequency and/or magnitude of TSI minima (Figure 3.23a). It is therefore concluded that the long-term coupling, between shifts in the atmospheric circulation, variability in the freshwater export from the Arctic Ocean to the Labrador Sea, the upper water column structure in the Labrador Sea and ultimately LSW formation was most likely driven by the magnitude and/or frequency of solar irradiance forcing. This suggests that Late Holocene centennial-scale events recorded in the circum-North Atlantic were similar in nature and shared the forcing and feedback mechanisms as described for the onset of the LIA in Section 3.4.1.

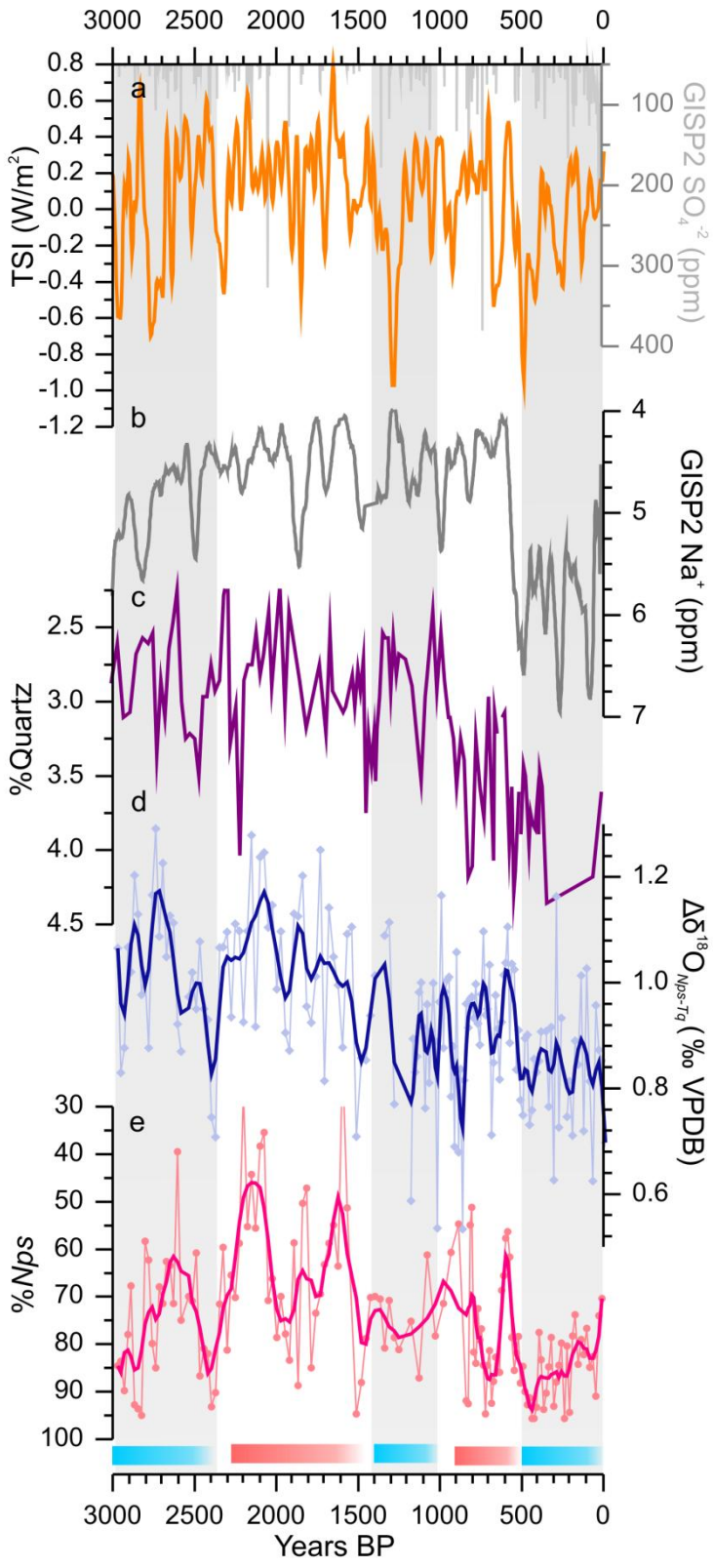

Figure 3.23. (a) Solar and volcanic forcing: TSI (W/m^2) (Steinhilber et al., 2009) and sulphate from GISP2 (Mayewski et al., 1997) , (b) Atmospheric forcing: Na^+ concentration in GISP2 (Mayewski et al., 1997), (c) %Quartz from the North Icelandic shelf (Moros et al., 2006), (d) $\Delta\delta^{18}O_{Nps\text{-}Tq}$ and (e) %*Nps* from RAPiD-35-COM. Blue and red boxes indicate glacier advances and recessions, respectively recorded in Alaska and Swedish Lapland (Denton and Karlén, 1973) and have been corroborated with other glacier advance records from the Northern Hemisphere (Bakke et al., 2010). The grey bands represent the cold rapid climate change periods identified by Mayewski et al. (2004) following the glacier extent records (Denton and Karlén, 1973).

3.4.2.4. Changes in LSW convection during the Late Holocene - A comparison to other proxy records

Proxy records of ocean changes in the Labrador Sea during the Holocene are extremely sparse. Density reconstructions of the upper water column based on dynocyst assemblages and planktonic foraminifera $\delta^{18}O$ suggest that LSW convection became established after 7 kyrs BP (Hillaire-Marcel et al., 2001). From the onset of LSW convection palaeorecords have revealed millennial scale variability in the stratification of the water column (de Vernal and Hillaire-Marcel, 2006, Solignac et al., 2004). Higher resolution Holocene proxy records have shown indirect centennial-scale variability in LSW formation linked to climatic oscillations recorded in the North Atlantic realm such as the 2700, 1500 and 500 year BP events tentatively suggesting that changes in LSW formation played a role in these oscillations (Marchitto and DeMenocal, 2003, Oppo et al., 2003, Thornalley et al., 2009).

The above mentioned cooling events were recorded as periods of distinctive warm and saline surface conditions South Iceland Basin (Thornalley et al., 2009). Hydrographic changes at this site are indicative of shifts of the subpolar front as a result of expansion and contraction of the SPG. Thus, salty/fresh and warm/cold surface conditions in the Iceland Basin have been previously interpreted as contracted/expanded SPG (Hatún et al., 2005) (See Figure 4.15 for a summary diagram). Saline events recorded south of Iceland during the last 3000 years correspond to periods of increased %*Nps* and decrease in $\Delta\delta^{18}O_{Nps\text{-}Tq}$ recorded in RAPiD-35-COM (Figure 3.24a-c), similarly suggesting that these periods were associated with increased flux of Arctic freshwater and hence a reduction in LSW formation and a contraction of the SPG.

Further support for this hypothesis is given by high resolution near-bottom relative flow speed proxy, sortable silt mean grain size ($\overline{SS}$) from core RAPiD-21-COM (57° 27, 27° 54, 2630 m) recovered from the Gardar Drift. Previous work on the top 40 cm of this core spanning the last 230 years suggested that the $\overline{SS}$ at this location is significantly influenced by LSW thickness (Boessenkool et al., 2007). For instance, during a positive NAO the increase in LSW density in the Iceland Basin causes a reduction in the flow speeds at the site.

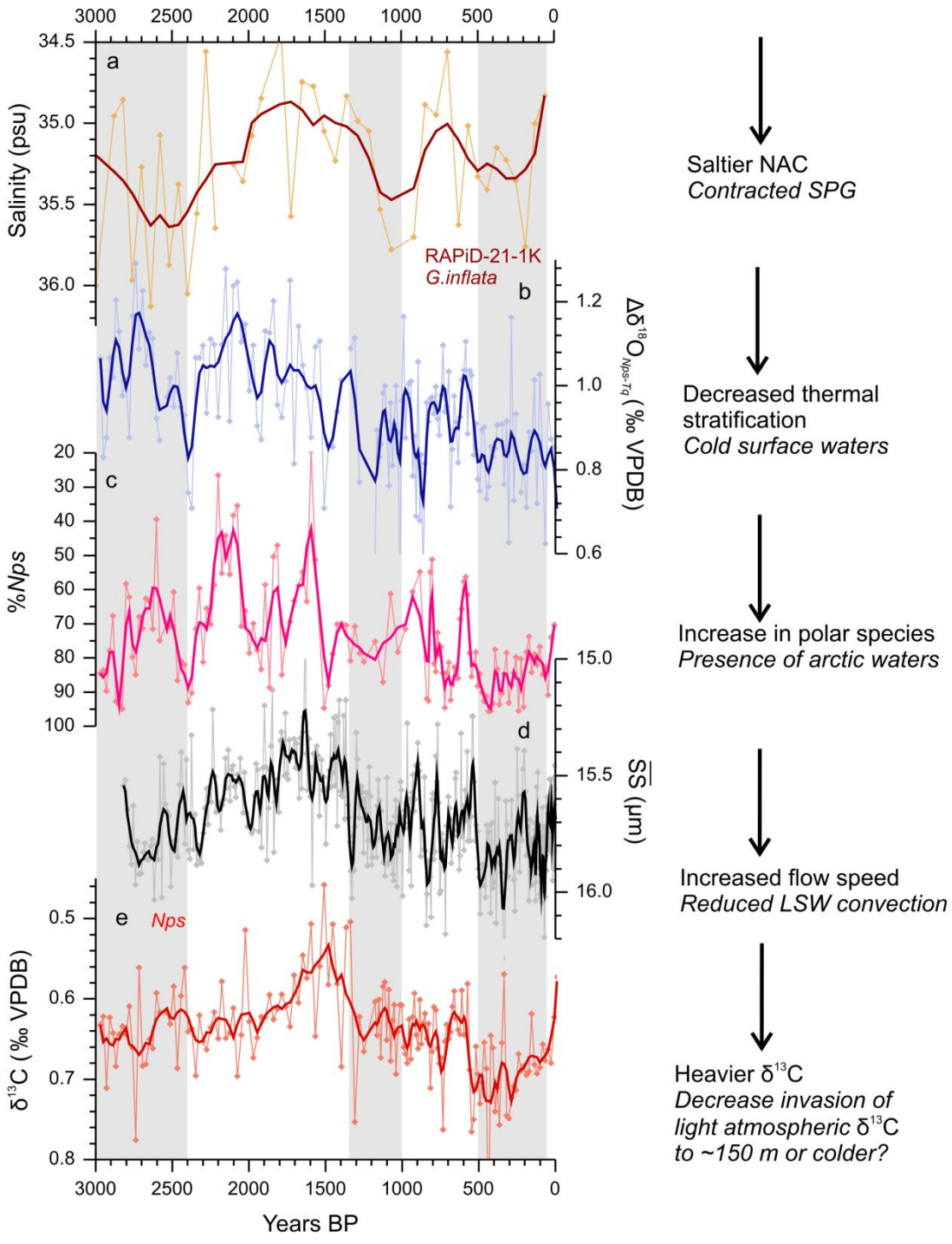

Figure 3.24. (a) Iceland Basin salinity from *G.inflata* (Thornalley et al., 09), (b) and (c) $\Delta\delta^{18}O_{Nps\text{-}Tq}$ and (e) %*Nps* from RAPiD-35-COM, (d) $\overline{SS}$ from RAPiD-21-COM Gardar Drift *(unpublished)*, (e) *Nps* $\delta^{13}C$ RAPiD-35-COM. Annotations on the right hand side in italics indicate interpretations. Grey bands correspond to the glacial advance time periods (Denton and Karlén, 1973).

Using the $\overline{SS}$ measurements from the extended Gardar Drift record RAPiD-21-COM as an indicator for the volume of the LSW it is concluded that cold conditions in the upper water column shown by increased %*Nps* (Figure 3.24c) and reduced $\Delta\delta^{18}O_{Nps\text{-}Tq}$ (Figure 3.24b) correspond to high $\overline{SS}$ in the Gardar Drift (Figure 3.24d), suggesting decreased LSW volume and hence convection. Additionally, bearing in mind the caveats presented in Section 3.3.1.4 in the interpretation of $\delta^{13}C$ of planktonic foraminifera as a proxy for air-sea exchange, comparison of the $\delta^{13}C$ record from *Nps* with the records mentioned above reveal coherent variability, either related to air-sea exchange or temperature.

3.4.2.5. Changes in the properties of the Irminger Current during the Neoglacial

The *G. bulloides* Mg/Ca-based temperature reconstruction from RAPiD-35-COM shows a millennial-scale gradual cooling of ~4°C over the last 3000 years (Figure 3.25) with centennial fluctuations in the temperature and $\delta^{18}O_{sw}$ of ~2 °C and ~0.8‰, respectively. Statistical analysis of the record does not reveal any significant cyclicities.

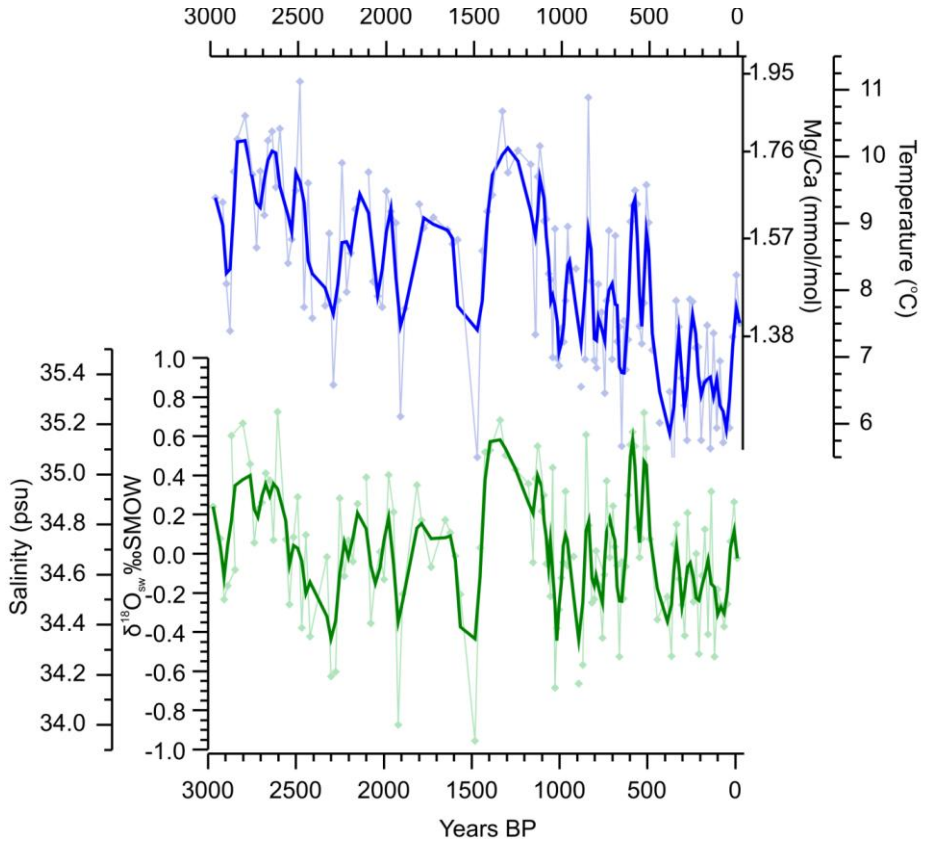

Figure 3.25. RAPiD-35-COM *G. bulloides* paired Mg/Ca-$\delta^{18}O$ based temperature and salinity reconstructions.

Following the reasoning outlined in Section 3.4.1.5, the geochemical signature of *G. bulloides* is interpreted as an indicator of the hydrographic properties of the IC reaching south of Greenland. During the last 3000 years a gradual transition to colder temperatures and/or a reduced influence of the Atlantic waters reaching the Nordic Seas has previously been recorded in different branches of the Atlantic Inflow such as the main NAC (Richter et al., 2009, Thornalley et al., 2009), North Atlantic Central Waters (Morley et al., 2011), the North Icelandic Irminger Current (Jennings et al., 2011, Ólafsdóttir et al., 2010, Bendle and Rosell-Mele, 2007) and the Atlantic waters within the WGC (Perner et al., 2011). Thus, the millennial-scale cooling recorded in *G.bulloides* and representing the IC is consistent with previous published data (Figure 3.26).

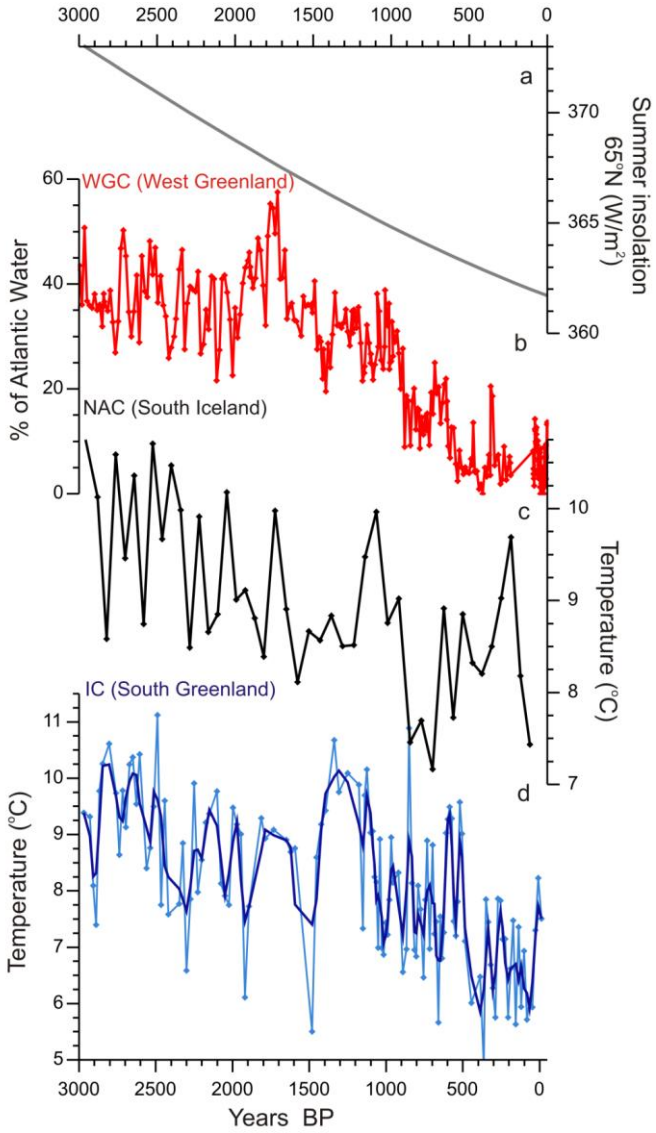

Figure 3.26. Gradual cooling trend of the NAC and reduced influence of warm and salty Atlantic waters reaching the higher latitudes potentially as a response to the decrease in summer insolation during the Neoglacial. (a) Summer insolation at 65°N (Berger, 1978), (b) Foraminifera indicators of Atlantic waters within the WGC recorded in Disko Bugt (West Greenland) (Perner et al., 11), Mg/Ca-based reconstructions of the (c) NAC south of Iceland (*G. inflata*), (d) IC from RAPiD-35-COM (*G. bulloides*).

As discussed in Section 3.4.2.2. the insolation driven Neoglacial climate re-organisation was characterized by in an increase in freshwater export into the North Atlantic and a transition towards a more meridional atmospheric circulation as shown from different proxy records (e.g. Jennings et al., 2002, Jessen et al., 2011). Several hypotheses can therefore be proposed in order to explain the recorded cooling trend from the western branches of the NAC. According to previous interpretations, a cold and fresh NAC in the Iceland Basin may have been linked to a strengthening of the SPG typically governed by the strength of LSW convection (Thornalley et al., 2009). Alternatively, the cooling of the NAC could have resulted from a potential increase in heat loss via air-sea exchange within the NAC maybe as a consequence of an increase in atmospheric forcing promoting formation of SPMW south of Iceland. However, given the mechanisms presented in Chapter 4 in conjunction with the Neoglacial atmospheric evolution, it seems likely that the cooling of the NAC (Figure 3.26) was a consequence of a weakening of the SPG mainly forced by atmospheric changes towards a more negative NAO-like state (see Chapter 4 for a detailed discussion). However, this appears to be at odds with the Neoglacial warming trends recorded in the pathway of the NAC reaching the Norwegian Sea (Moros et al., 2006 and references herein) which has recurrently been discussed in the literature (Andersen et al., 2004). The differing trends between the eastern and western Atlantic Inflow branches may suggest different regional oceanic-atmospheric responses to insolation forcing.

On centennial time-scales temperature and salinity are observed to co-vary, however, on multi-centennial to millennial time-scales the temperature changes are not mimicked by the salinity reconstructions (Figure 3.27). Thus, the relationship between these two variables appears to have changed at ~800 years BP and again around 400 years BP (Figure 3.27), to higher salinities relative to temperature. This Late Holocene temperature and salinity decoupling is a characteristic feature of other Atlantic Inflow records from the North Atlantic (Morley et al., 2011, Richter et al., 2009, Thornalley et al., 2009, Came et al., 2007) and will be discussed in more detail in Section 4.4.4.

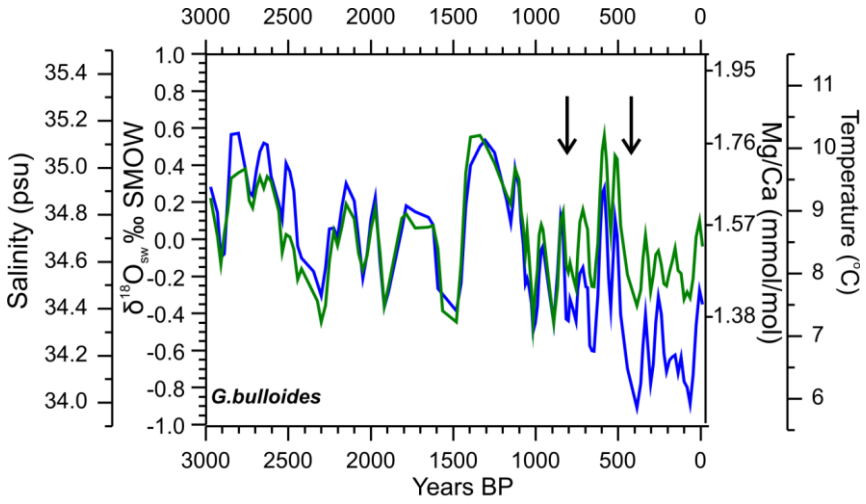

Figure 3.27. Timing of temperature (blue) and salinity (green) decoupling in the Irminger Current during the last 3000 years indicated by arrows.

3.5. Summary and Conclusions

In this chapter, multi-proxy reconstructions of the surface ocean conditions from the Eastern Labrador Sea have been shown to be highly dynamic at a variety of time-scales during the last 3000 years.

On millennial time-scales, the records reveal a long-term cooling trend associated with the Neoglacial increase in the southward advection of polar waters and a transition to a more predominant meridional atmospheric circulation over the Labrador Sea. The combination of the buoyancy and wind-stress forcing over the Labrador Sea likely altered the formation of LSW. The most accepted forcing for the cooling within the North Atlantic realm is that it was driven by a reduction in Northern Hemisphere summer insolation which caused a reduction in the Arctic sea ice melting.

At multi-centennial to centennial time-scales the multi-proxy surface records show three main abrupt cooling periods centred at 2600 and 1500 and 500 years BP (the LIA). These cold events have also been recorded in a range of palaeoproxies in the circum-North Atlantic, ranging from widespread glacial advances to abrupt shifts in the North Atlantic hydrography. From the results presented in this chapter it is concluded that despite the difference in magnitude of these cold events they probably shared a common causality. The cold events recorded in the Eastern Labrador Sea have been linked to an increase in the southward advection of polar waters, which accompanied by a simultaneous shift in the atmospheric regime towards a prevailing negative NAO-like

pattern, likely caused a reduction in LSW convection, potentially affecting the AMOC vigour. Although the external forcing that triggered these events it is still highly debated, the results from this chapter reveal that the timing of the cold events is concomitant with more pronounced and frequent solar minima. Modelling studies suggest that a decrease in TSI would have led to atmospheric changes such as the NAO state or blocking events through tropospheric ozone feedbacks. Shifts in atmospheric regimes would have had a direct effect in the North Atlantic hydrography, probably triggering ocean feedbacks that would have potentially amplified and sustained the small TSI signal. Furthermore, some of the multidecadal to centennial cold events present in RAPiD-35-25B correspond temporally with some of the most explosive volcanic eruptions (such as the one at 1250 years AD), which would have contributed towards the recorded North Atlantic cooling by triggering important sea-ice feedbacks. Additionally, some of the pronounced atmospheric shifts recorded in the North Atlantic might have been forced via teleconnections from the Pacific involving ENSO.

Indeed it is highly unlikely that there is a simple linear relationship between the forcing and the climatic response, as the latter is largely dependent on the state of the internal climate dynamics at any given time, which makes showing causality between the oceanic and atmospheric change and the external forcings complicated.

4. Changes in the Atlantic Inflow Properties During the Last 1200 years

4.1. Introduction

The North Atlantic Current (NAC) carries ~20 Sv of warm salty subtropical waters in a north eastward direction across the North Atlantic, approximately 9 Sv of which reach the Nordic Seas as the Atlantic Inflow (Rossby, 1996). These waters cross the GSR through three different pathways (Rossby and Flagg, 2012, Østerhus et al., 2005) (Figure 4.1) and are driven by direct wind forcing, estuarine forcing and pressure gradients established by deep and intermediate water formation north of the GSR, the latter being the predominant driver (Hansen and Østerhus, 2000, Dickson et al., 2008). The northward transport of heat via this current to the high latitudes contributes towards ameliorating the climate of western Europe (Seager et al., 2002). Of greater climatic importance is the import of salt to the Nordic Seas, which contributes to maintaining the high density of the surface waters, a pre-requisite for deep water formation and thus crucial for the AMOC. It is for these reasons that it is of paramount importance to study past hydrographic changes of the NAC and its potential impacts on regional and global climate.

The NAC - Subpolar front system separates the wind stress-driven diverging and converging Subpolar and Subtropical Gyres (SPG and STG, respectively). As the NAC travels northwards it draws in different water masses with its final product comprising a mixture of modified tropical waters originating from the Gulf Stream and mode waters from the SPG and STG, with a minor contribution from the Mediterranean Outflow Water (McCartney and Mauritzen, 2001, McCartney and Talley, 1982). Changes in the hydrographic properties of the Atlantic Inflow during the last thirty years have been successfully explained by changes in the cross frontal mixing of cold and fresh SPG and warm and salty STG waters due to subpolar frontal migrations as a result of the changes in strength and extent of the SPG (Hátún et al., 2005, Pérez-Brunius et al., 2004). The strength of the SPG is thought to be intimately tied to LSW convection and hence driven by buoyancy and wind-stress changes, which have mainly been attributed to the state of the NAO (Bersch, 2002, Bersch et al., 2007, Flatau et al., 2003, Curry and McCartney, 2001). During periods of strong LSW convection, doming of the isopycnals

in the central Labrador Sea and changes in sea surface height drive baroclinic circulation of the SPG. However, an increasing number of studies suggest that the driving mechanisms of the SPG are not as straightforward as previously thought, with components such as the density of the relatively light boundary (Born and Mignot, 2011), local wind stress forcing such as frequency of blocking events (Häkkinen et al., 2011), effects of the deep overflows reaching the Atlantic Basin (Eden and Willebrand, 2001, Born et al., 2009), and local effects that are propagated into the subpolar region (Häkkinen and Rhines, 2004) also playing a role.

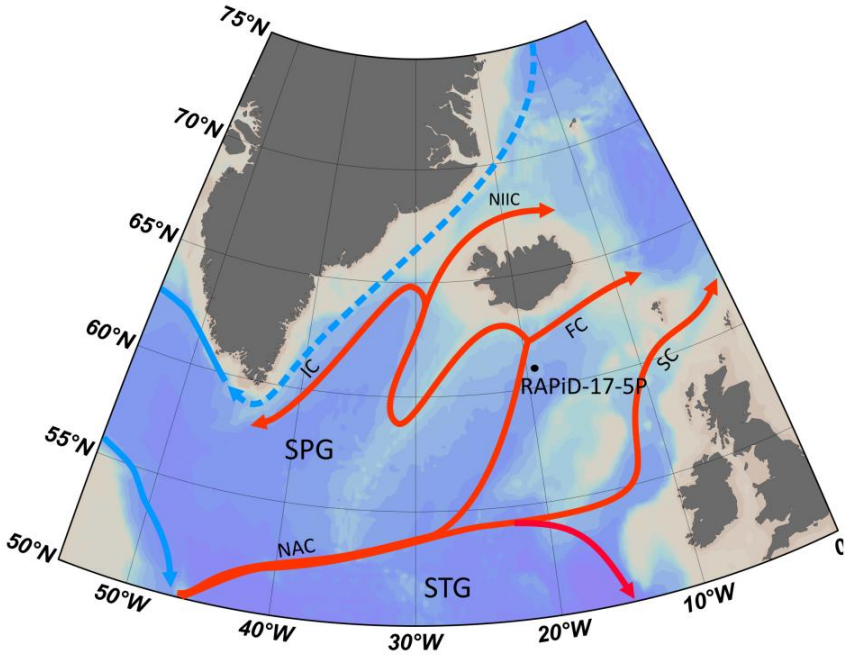

Figure 4.1. Bathymetric map outlining the schematic surface circulation in the subpolar North Atlantic. The red arrows indicate the NAC and the Atlantic Inflow branches carrying warm and salty subtropical waters such as the Faroe Current (FC), Shetland Current SC), IC (Irminger Current) and North Icelandic Irminger Current (NIIC). The blue arrows depict the cold and fresh currents originating from the Arctic which bind the SPG to the north.

Holocene centennial to millennial oscillations in the hydrographic properties of the Atlantic Inflow (South Iceland) have been inferred to correspond with the timing of rapid climate change events documented in the North Atlantic region (Bond et al., 2001, deMenocal, 2001, Mayewski et al., 2004) and have been interpreted to reflect changes in SPG dynamics (Thornalley et al., 2009). During cold events of the Holocene, a potential increase in freshwater discharge in the form of drift-ice into the North Atlantic (Bond et al., 2001), perhaps linked to a shift in the atmospheric regime (Lamb, 1979), may have caused a decrease in LSW formation (Solignac et al., 2004) and a weakening

and contraction of the SPG (Thornalley et al., 2009). In order to further understand the forcings and mechanisms governing hydrographic variability of the Atlantic Inflow and its potential link to Late Holocene climate variability, temperature and salinity reconstructions from a high-resolution sediment core recovered from the Iceland Basin are presented in this Chapter. Surface water depths in the Iceland Basin are bathed by the NAC, and feed the Iceland-Faroe and Irminger branch of the Atlantic Inflow (which are responsible for ~60% of the volume transport of Atlantic waters into the Nordic Seas (Østerhus et al., 2005); Figure 4.1). It is essential to investigate decadal to centennial variability of the hydrographic properties of the Atlantic Inflow and SPG dynamics during the last millennium to better understand the potential climatic effects of changes in the heat and salt transport to higher latitudes at these time-scales.

4.2. Materials and Methodology

RAPiD-17-5P was recovered from the Iceland Basin (for more details on the sedimentary setting see Chapter 2). The uppermost 80 cm of the piston core were sampled and processed continuously at 0.5 cm resolution.

4.2.1. Ocean setting

Hydrographic measurements from south of Iceland show the presence of a homogeneous upper water column down to approximately 600 m depth with temperatures and salinities in the range of 8.5-10^{o}C and 35.27-35.33 psu, and summer warming of the uppermost ~50 m up to 12^{o}C (Figure 4.2) (CTD cruise data from 59˚50'N 36˚42'W and WOCE09). The warm and salty hydrographic properties of this well-mixed upper layer at the RAPiD-17-5P site correspond to NAC waters of the Atlantic Inflow (Østerhus et al., 2005, Rossby and Flagg, 2012, Orvik and Niiler, 2002).

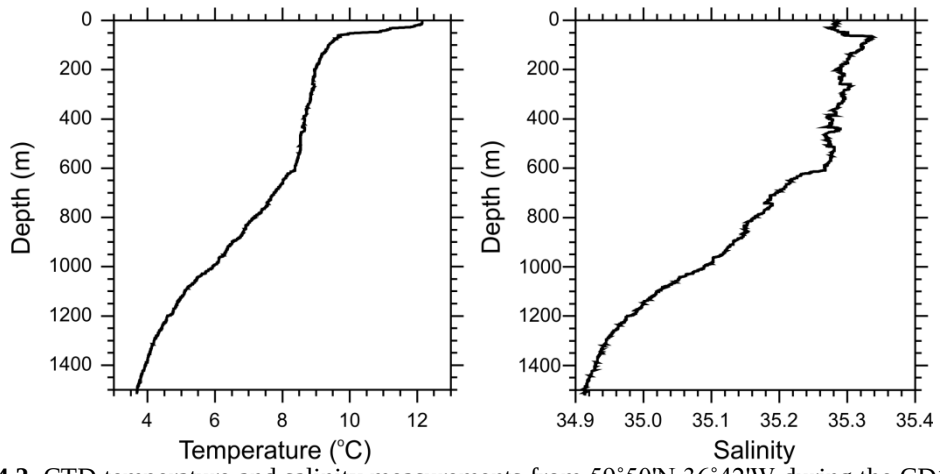

Figure 4.2. CTD temperature and salinity measurements from 59˚50'N 36˚42'W during the CD159 cruise (August 2004) (McCave, 2004).

4.2.2. Chronology

The age model for RAPiD-17-5P was constructed using seven ^{14}C AMS dates measured from monospecific samples of *G. bulloides* (>250μm) (Table 4.1), a mass of approximately 12 mg per sample was picked (equivalent to ~1000 individuals). Care was taken to select the cleanest foraminiferal tests avoiding discoloured shells to prevent age biases from reworking and bioturbation. Measurements were made at the NERC-Radiocarbon Facility

Core	Code	Depth (cm)	Radiocarbon Age ±1σ (Yrs BP)	Calibrated Age (Yrs AD)
RAPiD-17-5P	SUERC-15709*	0.5	591±35	1737
RAPiD-17-5P	SUERC-35766	34.5	874±35	1457
RAPiD-17-5P	SUERC-35769	67.25	1416±37	985
RAPiD-17-5P	SUERC-15710*	96.5	1738±37	658
RAPiD-17-5P	SUERC-15713*	200.5	2852±37	-658
RAPiD-17-5P	SUERC-14101*	750	8823±35	-7536

Table 4.1. Radiocarbon ages from RAPiD-17-5P. Calibrated ages were calculated as the average between the 1σ and 2σ averages.* Radiocarbon dates provided by D. Thornalley (unpublished).

The radiocarbon ages were corrected for marine reservoir effect using the mean marine reservoir correction of 400 years and converted to calendar years using MarineCal09 (Reimer et al., 2009) in CALIB 6.3. The ΔR of 0 is justified as the waters bathing the site are of tropical origin and have therefore been in touch with the atmosphere since their formation. Additionally, modelled reservoir correction ages based on data (Figure 2.6) show that the site lays approximately within a 400 year reservoir correction.

The age model was constructed based on a cubic spline fit to the four radiocarbon dates which deviates only slightly from a linear fit between these dates (Figure 4.3). The top four dates lie within the linear sedimentation rate shown by the radiocarbon dates obtained for the top 10 m of the piston-core, which indicate a constant sedimentation rate of approximately 100 cm/kyr for the last 9000 years (R^2=0.999) (Figure 4.3) and thus demonstrate the robustness of the age-model and the probable lack of abrupt changes in the rate of the sediment deposition during the time interval studied. The core was sampled at 0.5 cm intervals and thus each data point represents an integrated time of 5.5-5.8 years. The core-top of RAPiD-17-5P was lost as the piston core over penetrated (McCave, 2004); the top 1 cm has a calibrated age of ~1737 years AD.

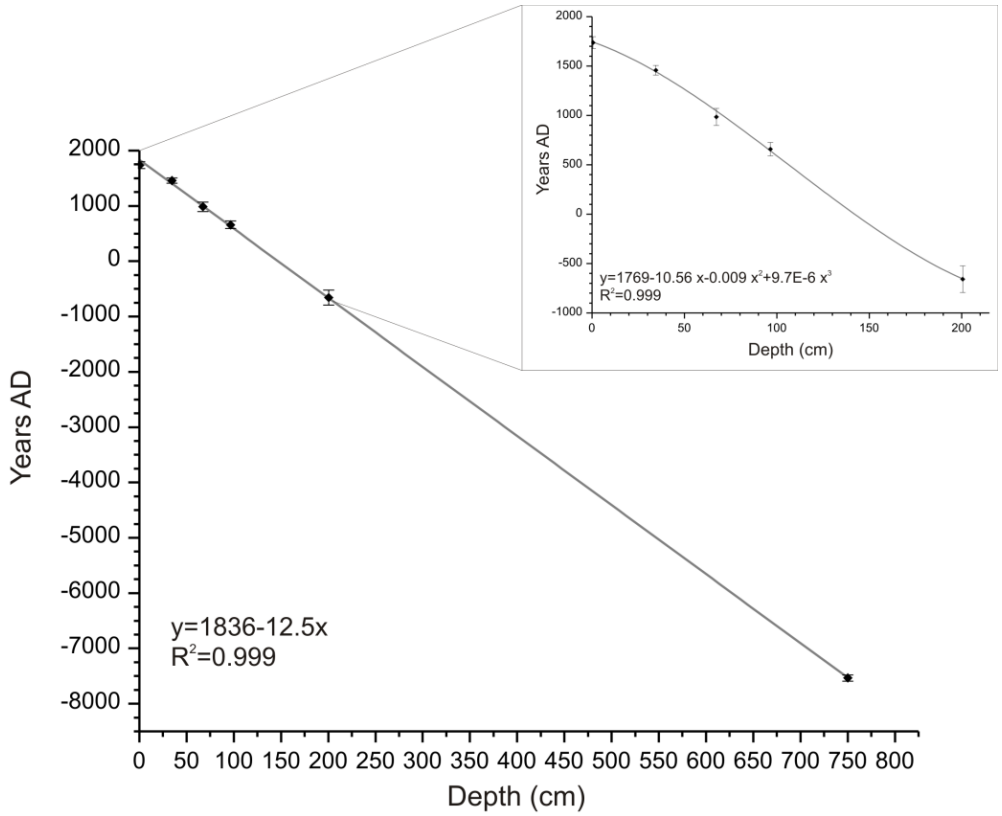

Figure 4.3. Linear fit through the calibrated radiocarbon dates from RAPiD-17-5P shown in Table 4.1. The top 8 m display a good linear fit with an R^2 value of 0.99. The inset graph presents the age-model used for the section of RAPiD-17-5P used in this study, which consists of the cubic spline through the top five dates, which display a R^2 =0.99.

4.2.3. $\delta^{18}O$ and Mg/Ca in *Globorotalia inflata*

Globorotalia inflata is a deep-dwelling planktonic foraminifera species that lives in transitional to subpolar conditions in the North Atlantic and it is most abundant in temperate waters often bathed by the NAC, ranging from 8-18^{o}C (Bé and Tolderlund, 1971, Farmer et al., 2010). North of 57^{o}N, *G. inflata* lives at 100-200 m depth, close to the seasonal thermocline (Cléroux et al., 2008), and due to the limited seasonal variation at this depth it mostly follows mean annual temperatures (Ganssen and Kroon, 2000). In the Iceland Basin, the near-thermocline habitat of *G. inflata* has been useful in providing information about the thermal stratification of the NAC in the past (Thornalley et al., 2009).

Between 6-20 individuals were picked from the 300-355 µm size fraction for paired $\delta^{18}O$ and Mg/Ca measurements. Care was taken to pick similar morphotypes and right-coiling specimens only. The specimens were crushed, cleaned and analysed following the protocol described in Section 2.4.3.

4.2.3.1.A study of potential biases in the Mg/Ca signal from Globorotalia inflata

The surface wall structure of *G. inflata* varies substantially (Hemleben et al., 1989), two different types were observed in the samples: (i) translucent and (ii) opaque white. Because encrustation of the shells could heavily bias the temperature signal towards colder temperatures (Groeneveld and Chiessi, 2011), this possibility was explored by calculating the average shell weights of the two shell types in 10 different intervals of the core. Contrary to expectation, the white opaque tests did not show consistently heavier shell weights, if anything they appeared to be lighter (Figure 4.4), indicating that these shells had probably not undergone encrustation. The lack of encrusted shells is further supported by the lack of correlation between Mg/Ca measurements and average shell weights (Figure 4.6).

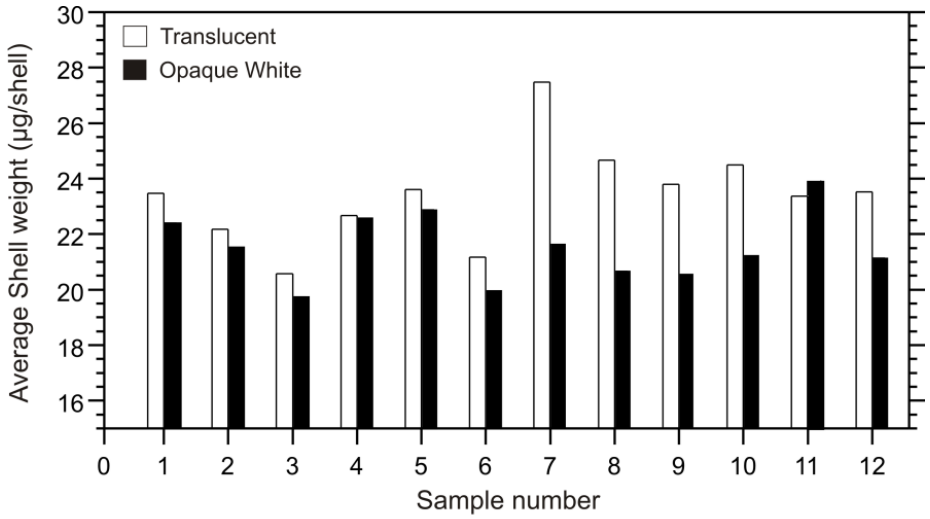

Figure 4.4. Average shell weights of 12 samples from RAPiD-17-5P of two types of *G. inflata* surface wall structure: translucent and opaque white.

A recent study on intra-test trace element variability in *G. inflata* concluded that the smaller tests record anomalously high Mg/Ca ratio which may misrepresent the true calcification temperature (Hathorne et al., 2009). However, during the present study the small *G. inflata* morphotype (3-chambers) was selected due to its continuous presence in sufficient abundance for Mg/Ca measurements. The potential issue of shell growth stage morphology on Mg/Ca thermometry was investigated by separating the individuals into 3 chambers and 3.5-4 chambers in seven different samples, which were then processed and measured independently. The results of this experiment showed no systematic (positive) offset of the smaller individuals (3 chambered tests) (Figure 4.5).

Furthermore, although the intra-sample variability in Mg/Ca was up to 0.25 mmol/mol, the inter-sample trends are the same for the two different morphotypes.

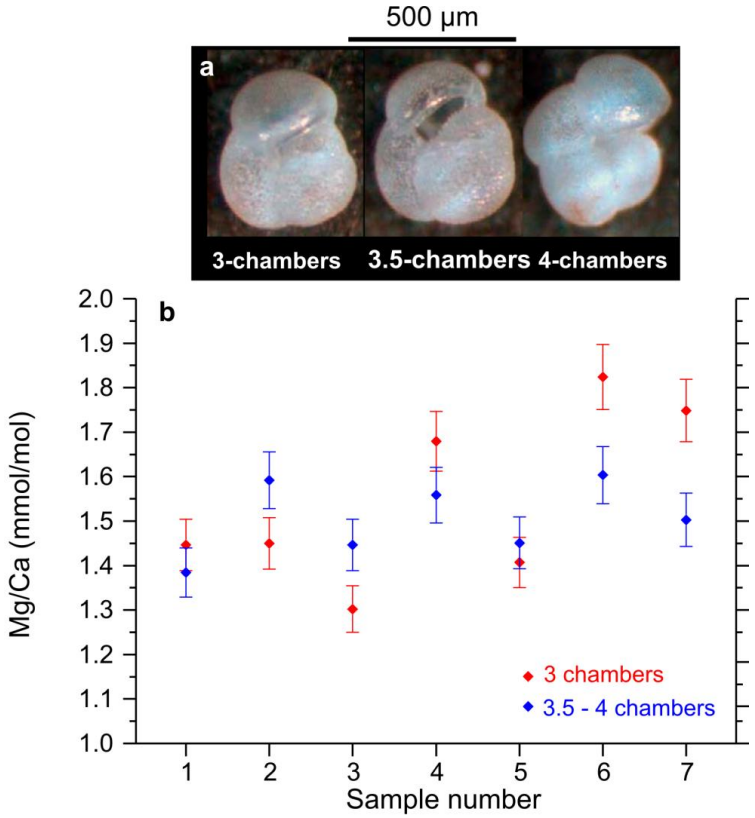

Figure 4.5. (a) Three morphotoypes of *G. inflata* adapted from Hathorne et al., (2009), (b) Mg/Ca measurements from 3 versus 3.5 and 4 chambered *G. inflata* specimens. Error bars indicate analytical errors.

4.2.3.2. Secondary influences on Mg/Ca signal

As explained in Section 3.2.1 the effects of partial dissolution and the presence of contaminant phases in the samples were explored by studying the shell weights and the concentration and co-variability of certain elements versus Mg/Ca.

The shell weights do not show any correlation with the Mg/Ca values, indicating that post depositional dissolution did not significantly affect the Mg/Ca values (Figure 4.6). This is probably because the site lies at 2303 m water depth and has thus remained significantly above the regional calcite compensation depth (currently ~4 km) throughout the interval of interest.

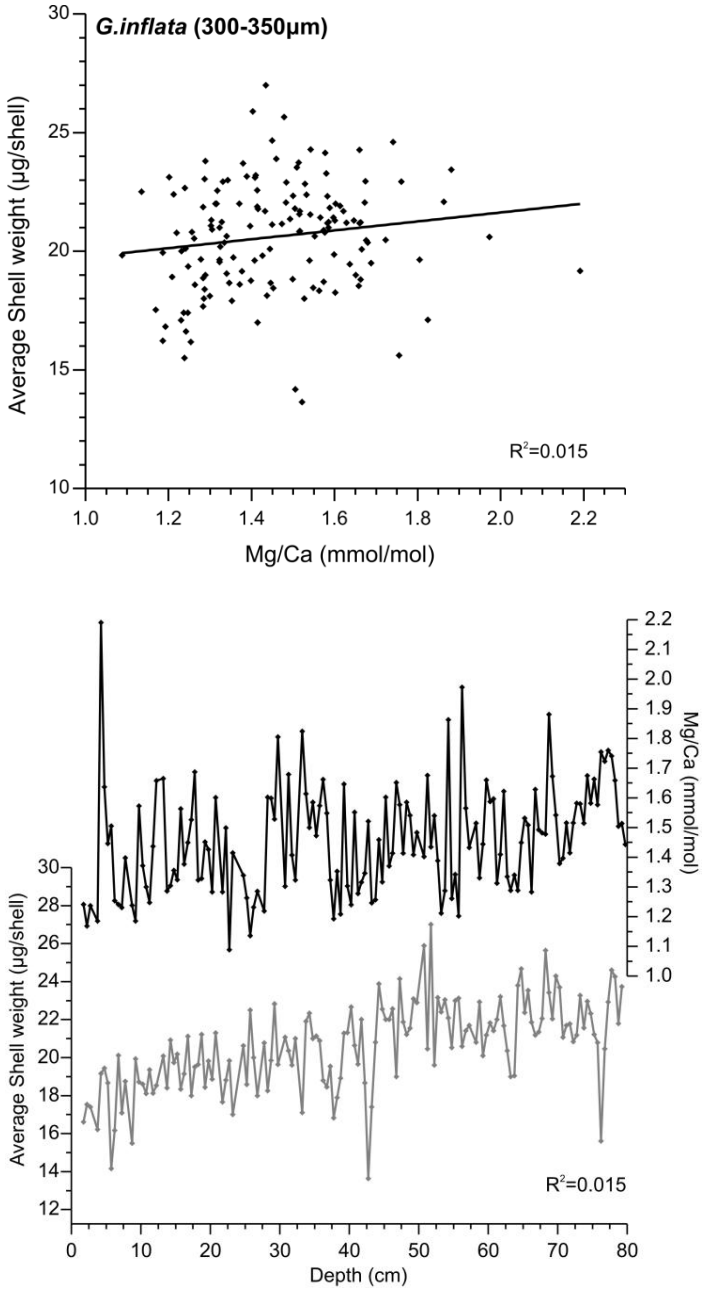

Figure 4.6. Average shell weights versus Mg/Ca on the *G. inflata* (300-350 µm) samples from RAPiD-17-5P. Cross-plot (upper graph) and down-core (lower graph)

A lack of variability between Mg/Ca and potential contaminant elements such as Fe, Mn and Al was observed. Fe/Ca did not present values > ~0.1 mmol/mol (Figure 4.7). Similarly, Mn/Ca values did not exceed concentrations of 0.1 mmol/mol (Figure 4.7). The data point at 53.75 cm depth presented high Fe/Ca and Al/Ca values of 0.25 mmol/mmol and 2 mmol/mol, which correspond to the high Mg/Ca measurement at that depth, and was therefore excluded. Regardless of the lack of co-variability with potential contaminants data points at 4.25 cm and 56.25 cm that lay outside the 2σ envelope were considered outliers and were excluded.

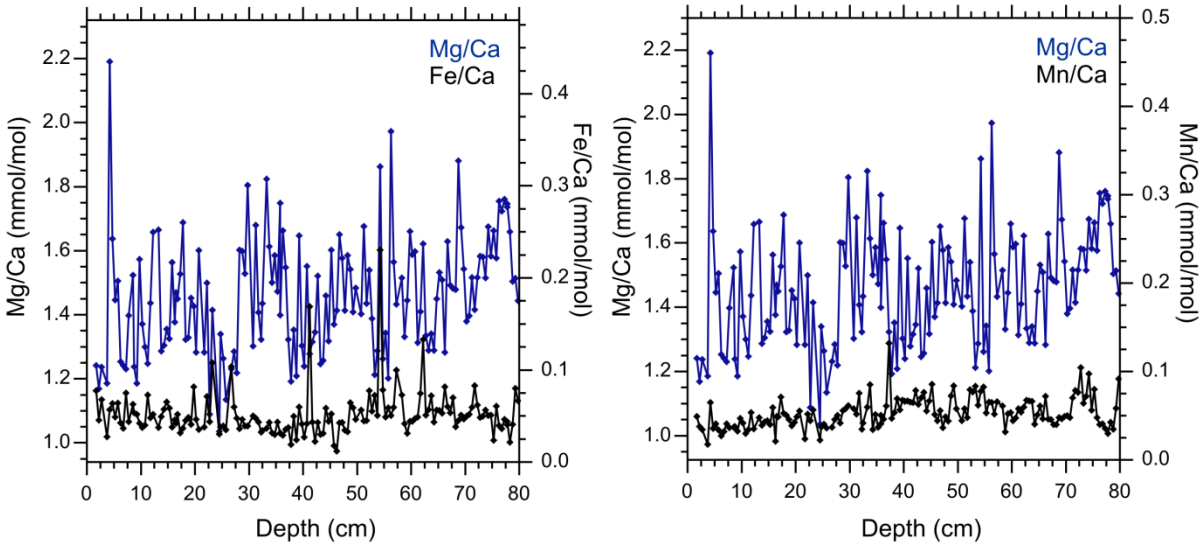

Figure 4.7. Down-core *G. inflata* Mg/Ca, Fe/Ca, Mn/Ca measurements.

4.2.3.3. Globorotalia inflata calibrations of Mg/Ca thermometry

Mg/Ca temperature calibration studies for *G. inflata* in the Atlantic show significant differences from one another and can be broadly divided into two types: Calibrations from Cléroux et al. (2007), Farmer et al. (2010) and Annand et al. (2003) suggest a higher sensitivity of temperature to Mg/Ca than calibrations from Elderfield and Ganssen (2000), Thornalley et al. (2009) and Groeneveld and Chiessi (2011) (Figure 4.8). This discrepancy is probably related to the pre-exponential constant being either set or calculated to be 0.1 or close to it. Setting the pre-exponent to 0.1 follows the multi-species calibration results of Elderfield and Ganssen (2000) in which it was suggested that this relationship was common in the calibration equations of all of the foraminferal species.

Using the lower sensitivity calibrations, the temperatures shifts recorded in the Mg/Ca from RAPiD-17-5P appear more realistic, for example the range of Mg/Ca values obtained would equate to temperature shifts of 3.5-4.5^{o}C as opposed to 6-9 ^{o}C when using the higher sensitivity calibrations. A recent sediment trap study from the western coast of Africa also yielded better temperature estimates compared to the monthly water column temperatures when using the low temperature sensitivity calibrations for Mg/Ca in *G. inflata* (Haarmann et al., 2011).

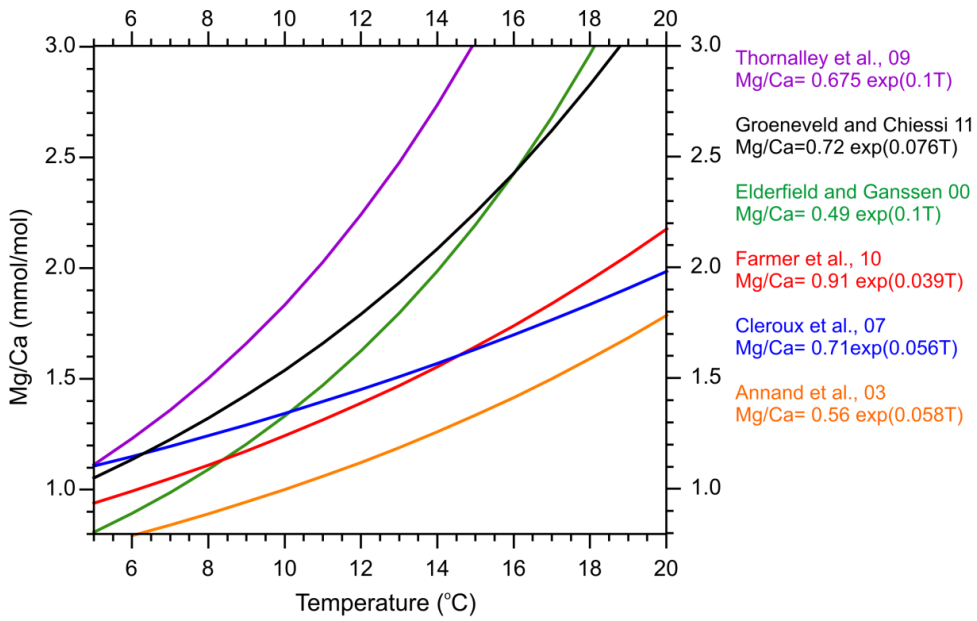

Figure 4.8. Comparison of *G. inflata* Mg/Ca temperature calibration curves from different studies.

Addition of ontogenic calcite crust at a greater depth in the water column in *G. inflata* has been recorded to heavily bias the Mg/Ca signal towards lower temperatures (Groeneveld and Chiessi, 2011). Accordingly, the studies of Thornalley et al. (2009), Groeneveld and Chiessi (2011), Haarmann et al. (2001) as well as this study, used the following strict criteria: special care was taken to select non-encrusted juvenile (3-chambered) specimens from a narrow size fraction. It is therefore possible that the high sensitivity calibrations obtained in other studies might have been due to the selection of encrusted *G. inflata* shells, leading to a flattening of the calibration curve. The caveat to this hypothesis is that ontogenic effects would also affect the $\delta^{18}O$ signal of the foraminiferal calcite. The $\delta^{18}O$ signal of the foraminifera is often used in calibration studies for the allocation of the species habitat depth in order to calculate the calcification temperatures. Therefore, if the $\delta^{18}O$ signal had suffered encrustation due to its vertical migration then the Mg/Ca calibration would reflect this same depth and not necessarily result in a lower sensitivity calibration.

On the basis of the geographical proximity of RAPiD-17-5P to RAPiD-12-1K (Thornalley et al., 2009), the identical criteria followed in the selection of the *G. inflata* individuals such as size fraction (300-355 μm), morphology (small morphotypes) and lack of encrustation (predominantly picked the individuals with translucent wall structure) and the similarity of the Mg/Ca values obtained, the Thornalley et al. (2009) palaeotemperature calibration curve with the form of Mg/Ca= 0.675 exp (0.1T) was

used. Calcification temperature estimates range between 6-9^{o}C, which are very comparable to the seasonal thermocline temperatures at the site ~8-9^{o}C (cruise CTD and WOCE09) assuming a calcification depth for *G. inflata* of 100-200 m (Cléroux et al., 2007) (Figure 4.2).

4.3. Results

4.3.1. Temperature and salinity variability

During the last millennium, Mg/Ca measurements of *G. inflata* yield values between 1.1-1.8 mmol/mol. This range in Mg/Ca values equates to a range of approximately 3.5^{o}C when using the Thornalley et al. (2009) calibration. High frequency (subdecadal to decadal) variability in the Mg/Ca record is in the range of 0.2 and 0.3 mmol/mol (equivalent to approximately 1^{o}C) (Figure 4.9b). In order to facilitate the study of the multidecadal variability a 1:2:1 weighted three-point average smoothing was applied. It is worth noting that values from the early part of the record display smaller deviations from the 3-point smoothing curve, possibly as a result of the increased number of individuals available in that core section. During the last millennium the record shows abrupt shifts in temperature of approximately 3^{o}C and lasting almost a century, with a broad long-term cooling of ~2^{o}C from 800 years AD to1750 years AD (Figure 4.9b).

The record of $\delta^{18}O$ from *G. inflata* displays a long-term trend of 0.3‰ towards heavier values over the same period. A record of $\delta^{18}O_{sw}$ was calculated following equation 2 in Section 2.4.3, by combining the $\delta^{18}O$ and Mg/Ca-based temperature values. Values of $\delta^{18}O_{sw}$ oscillate between -0.1 and 0.7‰. Salinities were then determined using the modern $\delta^{18}O_{sw}$-Salinity relationship in the North Atlantic from LeGrande and Schmidt (2006). This relationship is assumed to have remained constant when calculating salinities down-core. The salinity reconstruction shows rapid shifts of ~1.5, which mirror the temperature variability; although the long-term trend observed in the temperature record is absent.

The average error in the temperature estimates is ±1.14^{o}C including analytical (±3%) and calibration (±1.1^{o}C) errors. $\delta^{18}O_{sw}$ measurement error of ±0.08‰ and the temperature error effects on the $\delta^{18}O_{sw}$ calculation result in a $\delta^{18}O_{sw}$ error of ±0.29‰. Based on calculations of the uncertainties in the relationship between $\delta^{18}O_{sw}$ and salinity from Schmidt et al. (1999), a salinity error of ±0.8 is used.

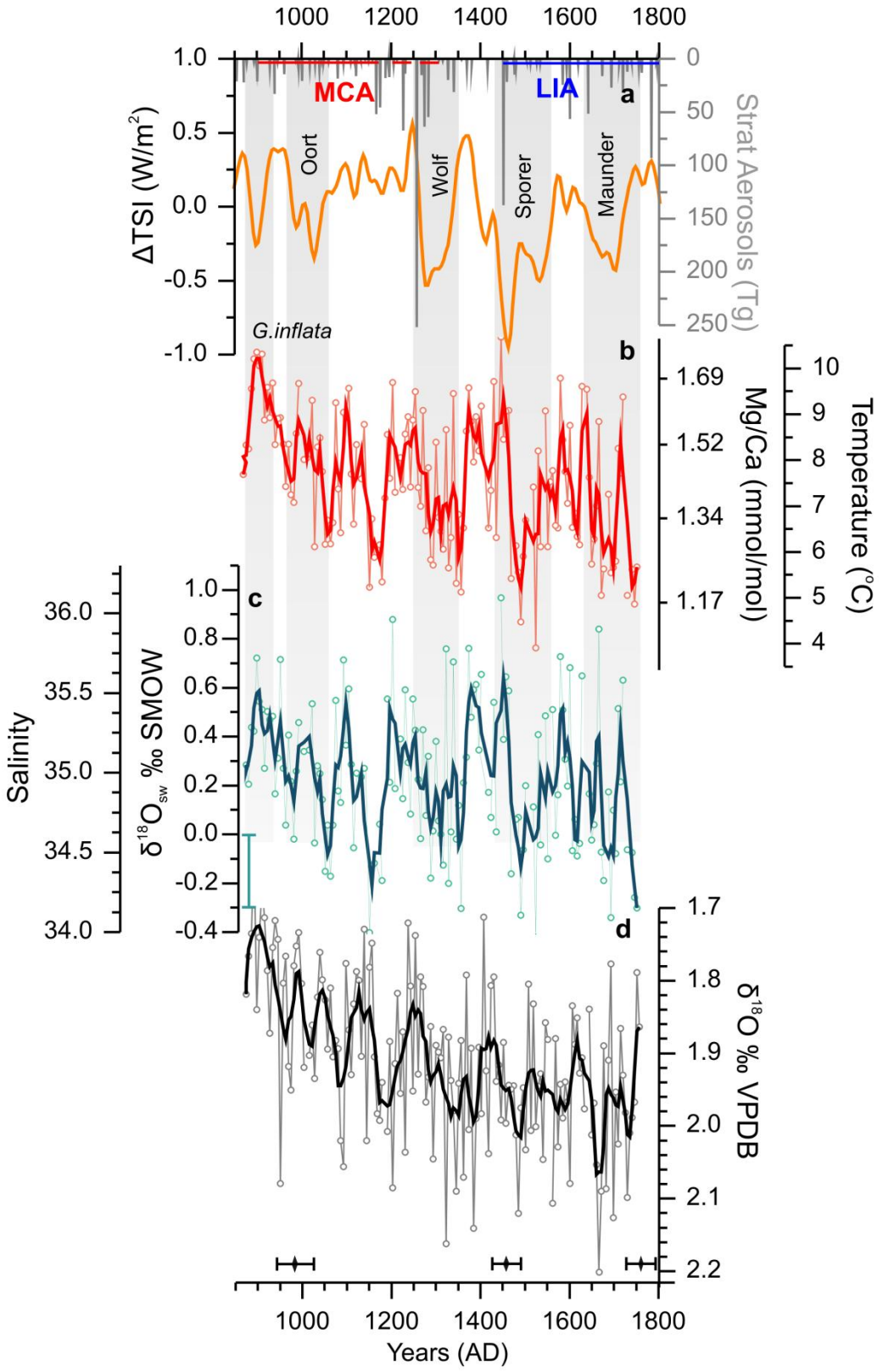

Figure 4.9. (a) Total solar irradiance forcing (W/m^2) (Steinhilber et al., 2009) and global volcanic stratospheric aerosol (Gao et al., 2007), *G. inflata* Mg/Ca and temperature (b) $\delta^{18}O_{sw}$ and salinity (c) and $\delta^{18}O_{calcite}$ (d) reconstructions from RAPiD-17-5P. Blue and red bars at the top of the graph indicate the MCA and the LIA climatic periods. Radiocarbon dates and the 1σ range are indicated by the diamonds and error bars. Shaded areas indicate periods of solar minima.

4.3.2. Salinity influence on Mg/Ca

The seemingly large magnitude of the Mg/Ca variability throughout the last millennium could be an artefact resulting from salinity effects on Mg/Ca. Both culture and core-top studies have shown evidence for a salinity effect on Mg/Ca in planktonic foraminiferal calcite (Lea et al., 1999, Nürnberg et al., 1996), yet, the magnitude of this effect still remains disputed. Culturing experiments have suggested a Mg/Ca-salinity dependency of ~9-15% (Lea et al., 1999, Nürnberg et al., 1996, Kısakürek et al., 2008), whereas core-top studies indicate larger sensitivity ranging between 15-59% (Ferguson et al., 2008). However, recent findings explain the upper end of the sensitivity values as a result of Mg-rich overgrowths found in settings such as the Mediterranean and the Red Sea (Boussetta et al., 2011, Kontakiotis et al., 2011, Hoogakker et al., 2009). Once diagenetic alteration is accounted for, the revised core-top studies suggest an Mg/Ca-salinity dependency of 27-15% (Arbuszewski et al., 2010, Sabbatini et al., 2011).

Recent re-examination of Mg/Ca core-tops from a latitudinal section through the Atlantic basin reveals minimal Mg/Ca-salinity dependency in higher latitudes with salinities <35psu on *G. ruber* (Arbuszewski et al., 2010). Furthermore, coupled core-top and plankton tow studies on *G. inflata* in the Mediterranean do not present any salinity effects on Mg/Ca excess (Mathien-Blard and Bassinot, 2009). Both these pieces of evidence suggest that the influence of salinity in the *G. inflata* Mg/Ca in this study is probably minimal. Nevertheless, assuming an extreme salinity change of 1 in the Atlantic Inflow as a result of increased influence of subptropical mode waters (salinity ~36) versus subpolar mode waters (salinity ~35) during cross frontal mixing and using a maximum Mg/Ca sensitivity to salinity effects of 27%, the temperature signal could potentially be amplified by a maximum of ~0.6^{o}C. This is considerably smaller than the variability observed in the RAPiD-17-5P record and therefore strongly suggests that a salinity bias in Mg/Ca thermometry has not significantly affected the primary temperature signal.

4.3.3. Statistical analysis and link to external forcing

Centennial to multidecadal temperature and salinity changes of the Atlantic Inflow in the Iceland Basin are found to be highly correlated with solar forcing (Steinhilber et al., 2009) (Figure 4.9a). In order to quantify the relationship between solar irradiance and the recorded oceanographic shifts, both time-series (temperature and TSI) were

Gaussian smoothed at equal time-intervals (6 years with an 18 year window) and a pearson coefficient (Pt) was estimated employing the programme PearsonT (Mudelsee, 2003). A minimum positive correlation of Pt=0.3 with a bootstrap error of 0.16; 0.46 n=142 at >95% CL was obtained with a time-lag of 30 years (the solar irradiance leading the temperature) (Figure 4.10a), which is within the combined dating uncertainty. However, this coefficient is augmented when increasing the filter width of the Gaussian interpolation of the two variables, mainly as this process eliminates the high-frequency (subdecadal to multidecadal) variability which is not at the frequency that these variables correlate. For example, at a 16 year time step the Pt coefficient between the two variables increases to 0.48 (0.209; 0.685) n=52 >95% CL.

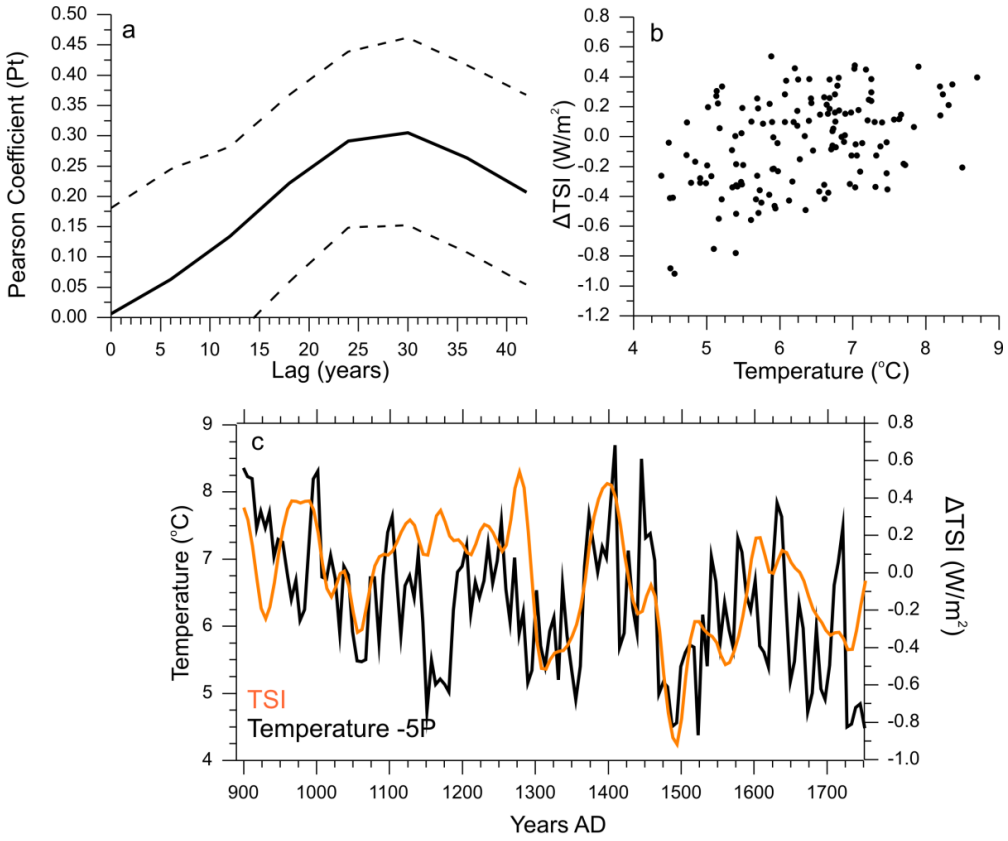

Figure 4.10. (a) Pearson coefficient at >95% CL of the correlation between the RAPiD-17-5P temperature reconstruction and ΔTSI at different time-lags. Dashed lines indicate the confidence interval. (b) Temperature from RAPiD-17-5P versus ΔTSI with a 30 year lag. (c) Time-series of RAPiD-17-5P temperature and ΔTSI with a 30 year lag.

Furthermore, a strong correlation between the start of the cold and fresh events at 1250 and 1450 years AD is also coincident with two of the largest inputs of aerosols into the stratosphere by volcanic eruptions (Gao et al., 2007) (Figure 4.9a). The association of these volcanic eruptions with the onset of the solar minima makes it difficult to disentangle the relative contribution of the external forcings to these temperature shifts.

Spectral analysis on the 6 year Gaussian interpolated temperature record exhibit frequencies centred at 192 and 44 years at above 90% CL (Figure 4.11a). The peak at ~192 years was also present in the irregularly-spaced spectral analysis, and centred at ~177 years (which is within the bandwidth). The ~192 year cyclicity between 1250-1650 years AD observed in the temperature record is similar to the periodicities from the deVries solar cycles (200-210 years) (e.g. Braun et al., 2005) and it is thus coherent and reiterates the temperature-TSI correlation. Wavelet analysis was also performed on the 6 year Gaussian smoothed zero-padded (256 point) temperature record, using *Wavelet* by Torrence and Compo (1998). Periodicities centred around 192 (135-225 years) were found to stand out over the background noise with significant power (>75%) at above 90 CL but were limited to 1250-1650 years AD (Figure 4.11b), albeit extending into the 'cone of influence' where possible edge effects may be increasingly important. To further support the linkage between solar irradiance and the Atlantic Inflow temperature, wavelet analysis was carried out on the ^{10}Be –based TSI reconstruction. The results display a very similar temporal and spatial distribution of the power and >90% CL envelope to that of the temperature reconstruction at periodicities centred at 200 years between 1200-1750 years AD (Figure 4.11b,c).

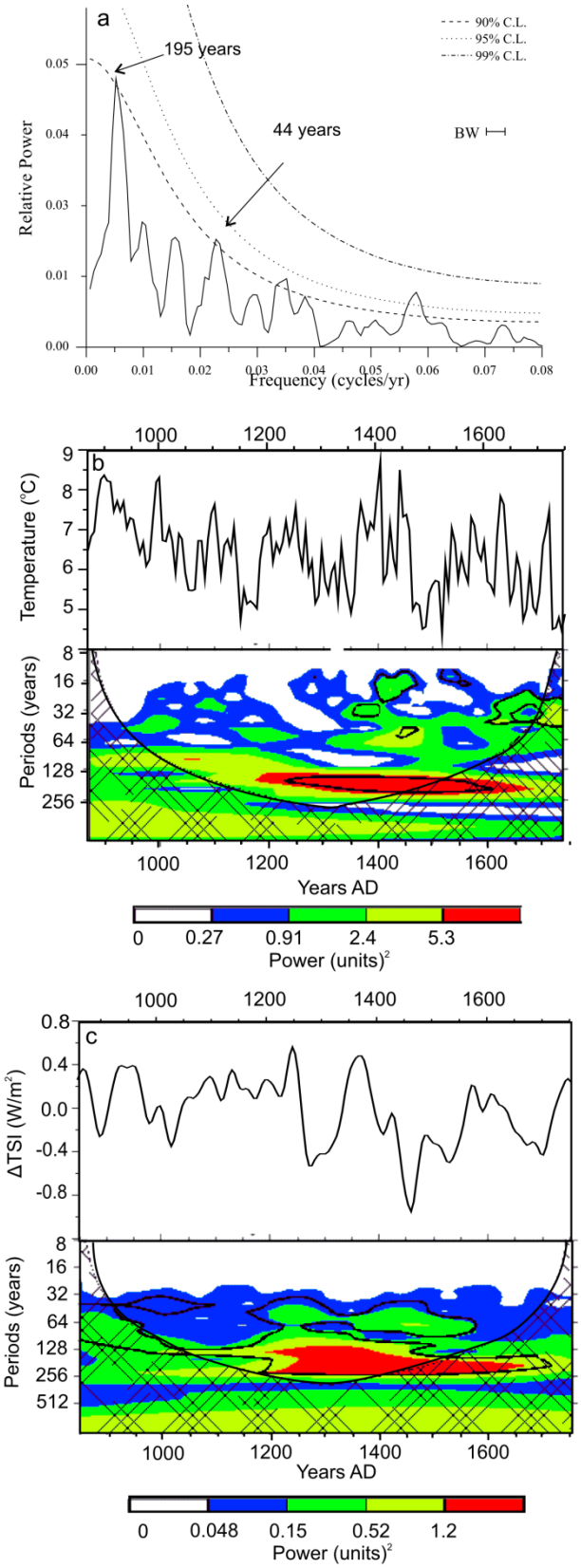

Figure 4.11. (a) Single spectral analysis of temperature reconstruction from RAPiD-17-5P. Two peaks are found (above 90% confidence level) at periodicities of 192 and 44 years. (b) Wavelet analysis on the 6 year interpolated temperature record from RAPiD-17-5P using *Wavelet* by Torrence and Compo (1998). (c) Wavelet analysis on TSI forcing from Steinhilber et al. 2009. White, blue, green, yellow and red colours denote power above red-noise of 0, 15, 25, 50 and 75% respectively. The black outline indicates confidence level of 90% assuming a red-noise model.

An interesting feature in Figure 4.11c is that the 90% CL envelope transitions from periodicities ranging between 100-60 years to periodicities between 128-200 years at around 1200 years AD. The lower power during the early period tentatively suggests that there was a muted solar signal which would explain the lack of power in the temperature record before 1200 years AD.

Additionally, Gaussian band-pass filtering of the temperature record from RAPiD-17-5P centred at 192 years (spanning the bandwidth 146-277 years) and the TSI record (Steinhilber et al., 2010) centred at the deVries periodicities of 200 years (175-230 years) was performed. The results highlight the good correspondence between the external forcing and ocean response at ~200 year frequencies (Figure 4.12).

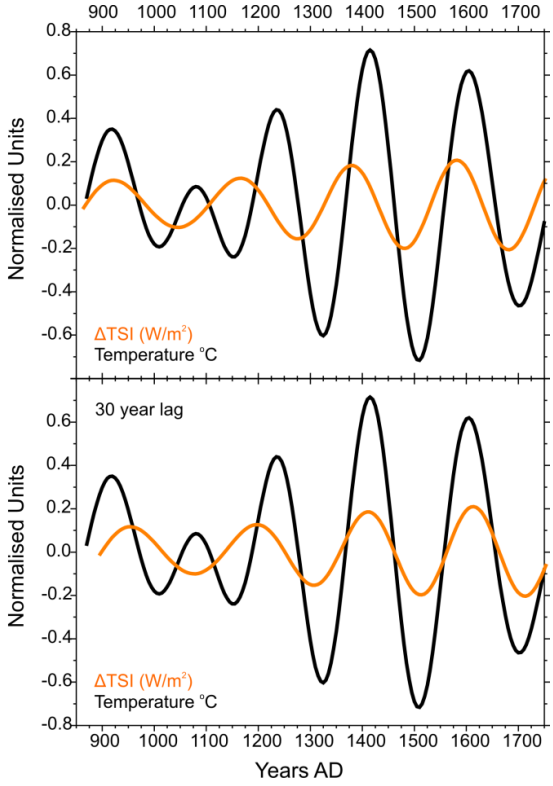

Figure 4.12. Band-pass filtered temperature record from RAPiD-17-5P (black) and Steinhilber et al., (2009) ^{10}Be-based TSI forcing (orange) at 170-250 years. The lower panel presents the record with an imposed 30 year lag on the ΔTSI forcing.

4.4. Discussion

4.4.1. Variability of the properties of the Atlantic Inflow during the Late Holocene: A comparison with other studies

A comparison of the reconstructed temperature and salinity in the Iceland Basin for the last millennium (this study) versus the last 8000 years (Thornalley et al., 2009) reveals similarities in the magnitude and range of values at multidecadal and millennial time-scales (Figure 4.13). This suggests, not only an equally highly dynamic variability of the Atlantic Inflow properties at these very different time-scales, but also emphasizes that these changes did not simply oscillate between states of fresh/cold versus warm/salty conditions at millennial time scales but were highly dynamic at multidecadal time-scales.

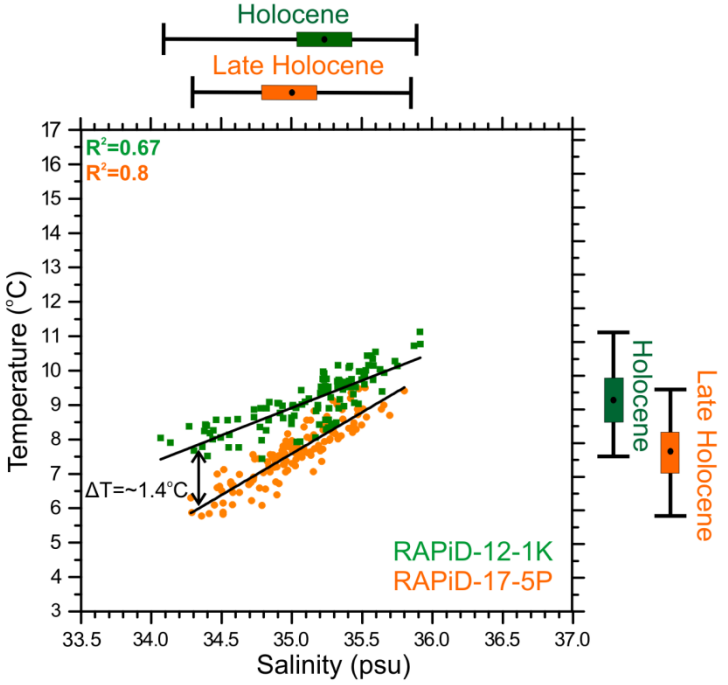

Figure 4.13. Late Holocene (this study) versus whole Holocene (Thornalley et al., 2009) 3-point smoothed temperature and salinity reconstructions from the Iceland Basin. The chart ranges indicate the magnitude of change and the average values are shown by a dot.

Comparison of high-resolution foraminiferal temperature records from waters deriving from the NAC during the last millennium show comparable trends (Figure 4.14). However, high resolution alkenone-based sea surface temperatures from the Gardar Drift (Sicre et al., 2011) or North of Iceland (Sicre et al., 2008b) do not display similarities with the Mg/Ca temperature reconstructions presented in this study, this is likely due to the preferred habitat depth and season in which the different organisms live, a discrepancy that has been reviewed by Leduc et al. (2010).

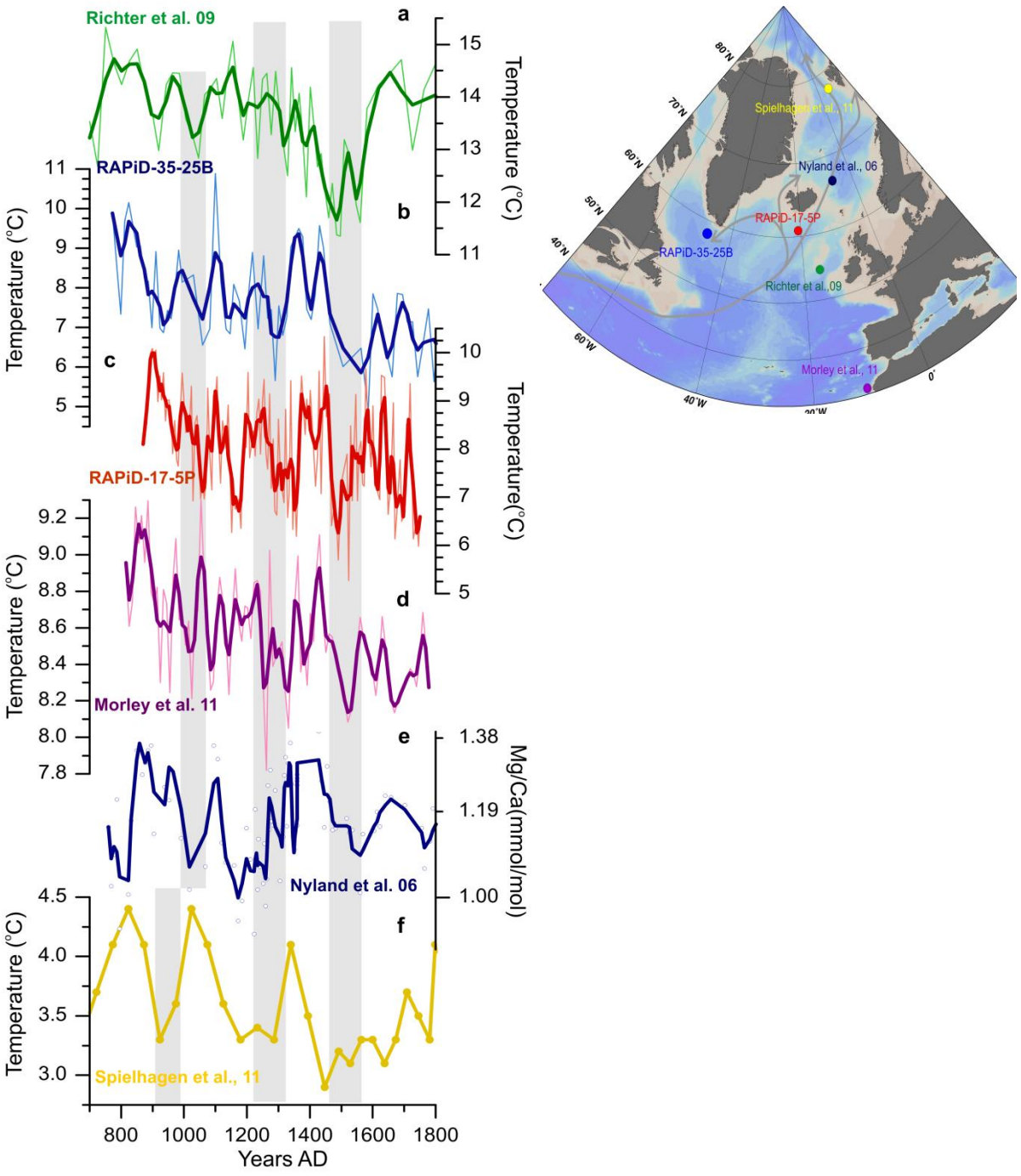

Figure 4.14. Foraminifera Mg/Ca-based temperature reconstructions from sites that are bathed by the Atlantic Inflow. (a) Richter et al. (2009), (b) RAPiD-35-25B presented in Chapter 3, (c) RAPiD-17-5P (this Chapter), (d) Morley et al. (2010), (e) Nyland et al. (2006), (f) Spielhagen et al. (2011). Grey shading shows some of the temperature minima. Map shows the colour-coded locations of the temperature reconstructions, grey arrows are schematic pathway of the Atlantic Inflow.

4.4.2. Mechanisms for the variability in the properties of the Atlantic Inflow

The Atlantic Inflow originates in the tropical Atlantic as the Gulf Stream. As it travels north it draws its waters from the SPG and STG. Following the reasoning of Hatún et al. (2005), the variability in temperature, and salinity in particular, observed in the Iceland Basin could be a result of changes originating in (i) the source waters of the Gulf Stream and STG, or (ii) the SPG, (iii) dynamic changes in the relative contribution of the two gyres, or (iv) local air-sea exchanges (precipitation-evaporation). The aim of this section is to review the proxy records that could eliminate some options and thus indicate the origin of the abrupt changes observed in the hydrograhic properties of the Atlantic Inflow in the Iceland Basin during the last millennium.

4.4.2.1. Changes in the hydrography of the Gulf Stream and the Subtropical Gyre

The Atlantic Warm Pool (AWP) is a large volume of warm water (defined as the area of >28.5^{o}C isotherm) which develops during the boreal summer in the region of the Gulf of Mexico, the Caribbean Sea and the western tropical North Atlantic. The AWP contains the source waters for the Gulf Stream. These will eventually be modified as they are transported northwards to become the NAC. A number of geochemical temperature proxy reconstructions from foraminifera, sclerosponges and corals from this region reveal a consistent 1-2^{o}C cooling at the onset of the LIA at around 1450 years AD with some colder periods tentatively coincident with solar minima (Haase-Schramm et al., 2003, Haase-Schramm et al., 2005, Black et al., 2007, Kilbourne et al., 2010, Richey et al., 2009, Lund and Curry, 2004, Saenger et al., 2009). Salinity estimates based on paired Mg/Ca-δ^{18}O measurements on planktonic foraminifera from the Florida Current and the Gulf of Mexico show an increase in $\delta^{18}O_{sw}$ of 0.4 and 0.3‰, respectively (equivalent to a salinity increase of ~1.5) at the onset of the LIA, which is not unexpected as it is probably connected to the southward migration of the ITCZ as recorded in the Cariaco Basin (Haug et al., 2001), the Yucatán Peninsula (Hodell et al., 2005) and in the Pacific region (Sachs et al., 2009).

The propagation of the temperature and salinity anomalies from the AWP into the Gulf Stream during the LIA are corroborated by surface ocean reconstructions from the Carolina Slope (Saenger et al., 2011). Furthermore, cross-current density gradient and current shear estimates of the Gulf Stream (at Florida Strait) reveal that the volume

transport during the LIA was approximately 10% lower than at present, implying a reduction in the northward heat transport towards the higher latitudes and a southward displacement of the Gulf Stream (Lund et al., 2006) which could have resulted in a decreased influence of this water mass on the slope waters of the East coast of the United States and Canada (Cronin et al., 2010, Marchitto and DeMenocal, 2003, Sachs, 2007).

Since the NAC draws part of its waters from the STG, hydrographic changes in the gyre mode waters will influence the variability of the properties of the NAC. Temperature reconstructions based on corals and foraminifera from the Eastern Caribbean (Saenger et al., 2008), Sargasso Sea (Keigwin, 1996), the Equatorial Current (a current that bounds the south of the STG) (Nyberg et al., 2002), and the eastern STG (deMenocal, 2001, Kuhnert and Mulitza, 2011) indicate a consistent cooling of the STG at the onset of the LIA with an uncertain magnitude ranging from 1-3^{o}C. However, due to the lack of salinity reconstructions it remains equivocal if this cooling was accompanied by a salinity decrease in the STG.

In summary, during the LIA a cooling has been recorded in the tropics and subtropical regions of the North Atlantic. It is yet unclear what the changes were at multidecadal to centennial resolution during the last millennium and, specific to the STG, if the cooling was also linked to salinity changes.

4.4.2.2. Changes in the hydrography of the Subpolar Gyre

High resolution (multidecadal to centennial) palaeoceanographic reconstructions from the SPG are scarce and mostly concentrated along its boundary currents such as the NAC (Section 4.4.1) or the Labrador Current (Keigwin and Pickart, 1999, Keigwin et al., 2003). However, in Chapter 3, high-resolution palaeoceanographic reconstructions revealed a cooling and potential freshening in the Eastern Labrador Sea but it is hard to assess if this was widespread throughout the SPG.

4.4.2.3. Changes in the relative contribution of Subpolar and Subtropical gyre

Previous studies in the area (Hátún et al., 2005, Thornalley et al., 2009) have suggested that changes in the temperature and particularly the salinity of the Atlantic Inflow in the Iceland Basin are controlled by subpolar front migrations. East-West shifts of the

subpolar front are associated with the spatial extent of the SPG and affect the relative contribution of the subpolar versus suptropical waters to the NAC. Observational studies have proposed that the extent of the SPG is governed by the strength of the SPG which is in turn largely driven by the intensity of deep convection in the Labrador Sea (see Figure 4.15 for a summary diagram of this mechanism).

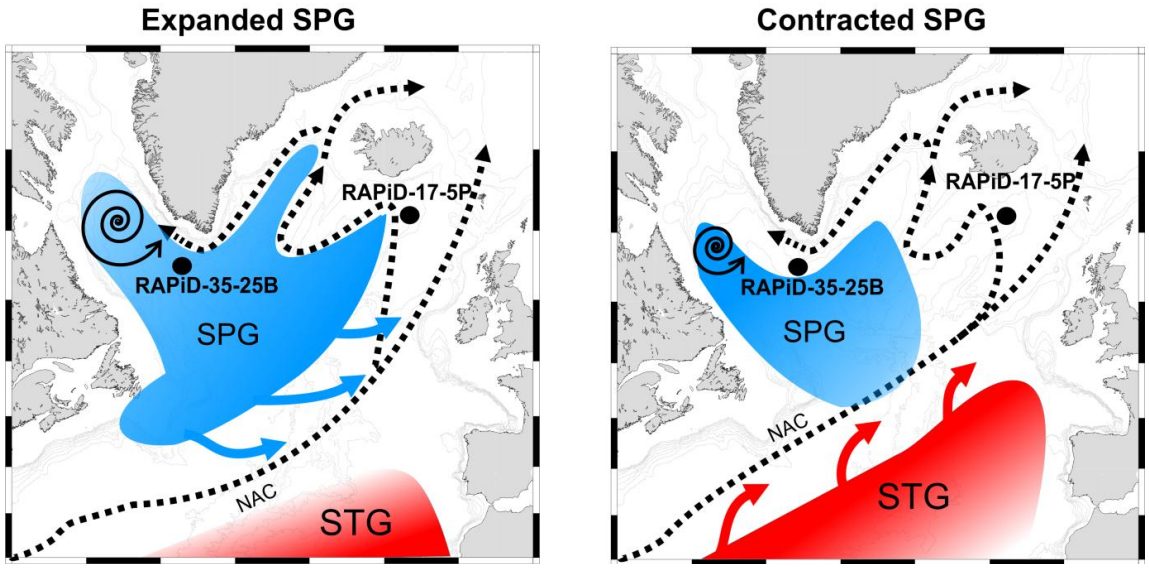

Figure 4.15. Simplified diagram of expanded/contracted SPG during strong/weak SPG driven by increased/decreased deep water formation in the Labrador Sea (indicated by the size of the asymmetrical spirals) and its effects on temperature and salinity South Iceland as interpreted in previous studies (Hátún et al., 2005, Thornalley et al., 2009). Blue indicates the cold and fresh SPG and the red represents the warm and salty STG.

Proxy reconstructions inferred as being indicative of LSW convection changes (presented in Chapter 3) are compared to the temperature record of the Iceland Basin (Figure 4.16). The temperature record from the Iceland Basin and the LSW proxy records do not reveal any coherency in their trends (Figure 4.16). Therefore, aside from SPG dynamics being dictated by LSW convection as suggested in previous studies in this area (Hátún et al., 2005, Thornalley et al., 2009), additional mechanisms must have governed the hydrographic conditions in the Iceland Basin at multidecadal time-scales.

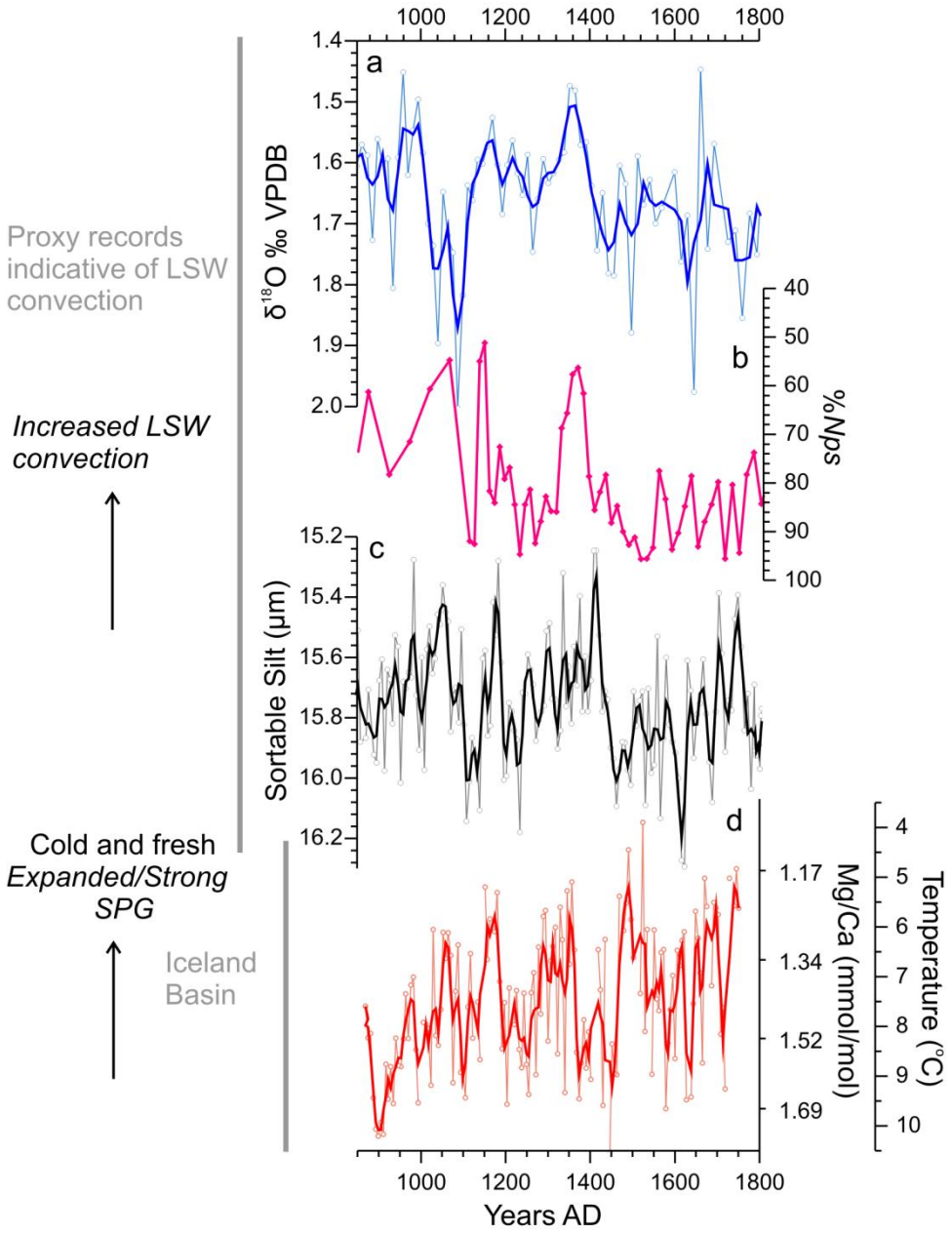

Figure 4.16. Comparison of Eastern Labrador Sea surface proxies inferred to indicate LSW convection presented in Chapter 3 and the Iceland Basin temperature reconstruction from RAPiD-17-5P. (a) $\delta^{18}O$ *T. quinqueloba* and (b) *%Nps* from RAPiD-35-25B (Eastern Labrador Sea), (c) Grain size sortable silt proxy from RAPiD-21-COM (Gardar Drift), (d) Temperature record from RAPiD-17-5P (Iceland Basin).

4.4.2.4. Changes in heat and freshwater via air-sea exchange in the Atlantic Inflow

The NAC is modified along its pathway, becoming colder and fresher as a consequence of air sea exchange. Modern studies (Hansen and Østerhus, 2000) have suggested that an annual heat loss of 60 W/m^2 and freshwater input of 25 cm with a homogenisation down to 500 m depth would decrease the temperature by 1^{o}C and salinity by 0.02. To account for the magnitude of the hydrographic changes recorded in the Iceland Basin over the last millennium (3.5^{o}C and 1.5 psu), the NAC waters would have needed 3.5 years and 75 years to explain the temperature and salinity changes, respectively. Considering that the advection velocity of the NAC is approximately 5^o of latitude a year (Bower et al., 2002) even if the 10% reduction in the volume transport of the Gulf Stream during the LIA was taken into account (Lund et al., 2006), the NAC would have not had sufficient time to cool but particularly freshen to explain the results.

4.4.2.5. Summary

The interpretation for the hydrographic changes in the Atlantic Inflow is not a straightforward. From the evidence presented above it is concluded that the entire North Atlantic underwent a general cooling at the onset of the LIA. However, it is difficult to constrain the mechanisms that influenced the multidecadal hydrographic changes recorded in the Iceland Basin (particularly the ones concerning changes in the hydrographic properties of the gyre mode waters) mostly due to the scarcity of high-resolution records spanning this time period.

4.4.3. Changes in the properties of the Atlantic Inflow in CCSM4

To explore the sensitivity of SPG dynamics to solar forcing and gain a wider picture of the amplifying mechanisms involved in the hydrographic changes observed in the Iceland Basin, model experiments were run in the National Centre of Atmospheric Research (NCAR) and analysed by A. Born at the University of Bern as part of collaborative work. The model Community Climate System Model v.4.0 (CCSM4) is a fully coupled climate model (composed of four separate and simultaneous models: land, atmosphere, ocean and sea-ice) which has been used to simulate the Earth's climate system (Gent et al., 2011). Changes in solar irradiance are prescribed using the TSI reconstructions from Vieria et al. (2011) for the last millennium. The modelling results reveal a strong positive correlation of the temperature and salinities in the Atlantic Inflow (south of Iceland) and the TSI forcing with a correlation coefficient above ~0.5

(Figure 4.17), findings that are in striking agreement with the proxy records presented in this chapter.

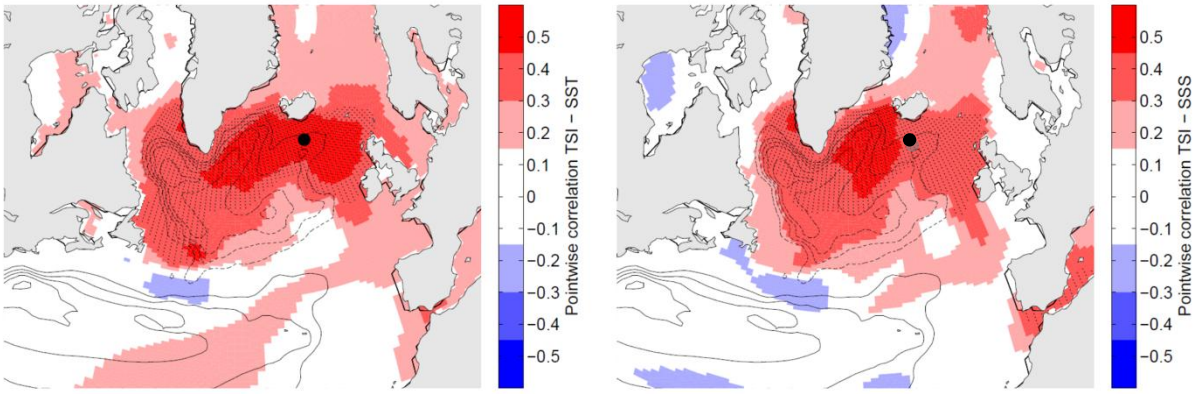

Figure 4.17. Pointwise correlation of sea surface temperature (left) and salinity (right) with total solar irradiance. Time-series have been filtered with a 50-year low-pass filter. Contours show the time-average depth-integrated stream function. Correlations above the confidence threshold are dotted. Highest correlations are found in the path of the Irminger Current due to an increase in heat and salt transport with a stronger SPG. The location of RAPiD-17-5P is marked with a black dot (*Courtesy of A. Born*).

Furthermore, volume transport analysis of the SPG suggests that contrary to previous interpretations warmer and saltier temperatures south of Iceland are indicative of increased heat and salt transport and hence correspond to periods of stronger SPG circulation (Figure 4.18) (Note that negative stream function indicates anticlockwise circulation).

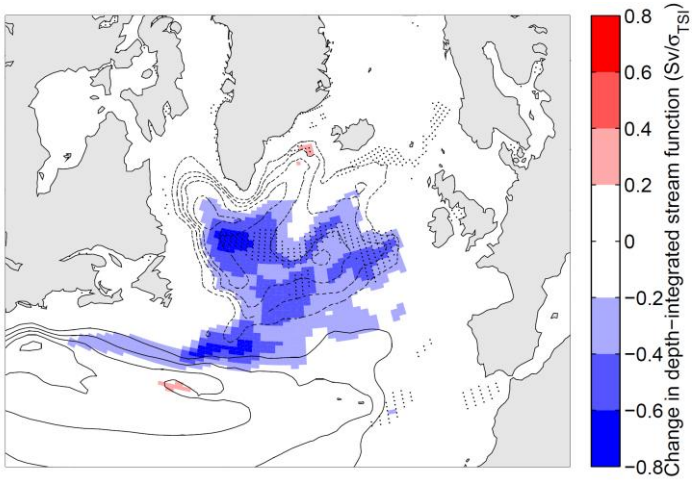

Figure 4.18. Regression of the depth-integrated stream function onto the total solar irradiance, filtered with a 50-year low-pass filter (colours). Significant areas are dotted. Contours show the time-average depth integrated stream function (*Courtesy of A. Born*).

In order to investigate the feedback mechanisms that were triggered by solar forcing, Sea Level Pressure (SLP) changes during solar irradiance maxima and minima were analysed in the model. The results indicate that during periods of solar minima the dominant atmospheric regime was characterised by an anomalous high-pressure system off West Europe (Figure 4.19). This would have created an anomalous blocking regime displacing and weakening the westerlies in the eastern SPG (similarly to Häkkinen et al., 2011) diminishing the wind stress curl eventually leading to slowing down of the SPG by buoyancy feedbacks (Figure 4.21 for a summary of the mechanism).

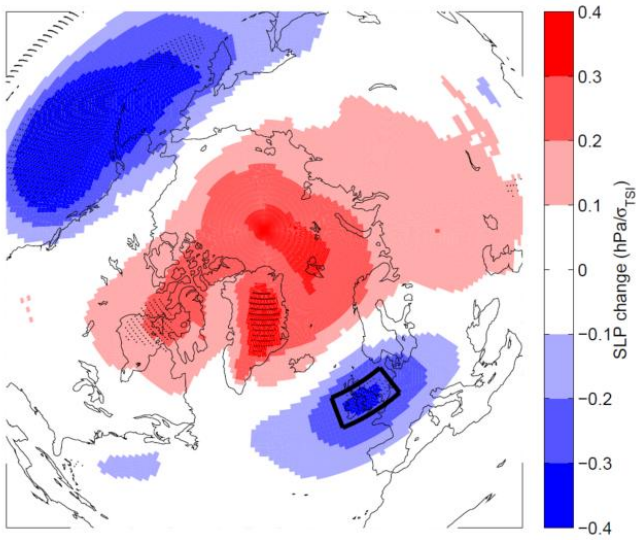

Figure 4.19. Regression of winter SLP on TSI. Time-series have been filtered with a 50 year low-pass filter. Areas above 95% confidence threshold are marked with dots. SLP analysis of CCSM4 reveals a high pressure system during low TSI off Europe marked with a black box (i.e. increased winter blocking) (*Courtesy of A. Born*).

Periods of increased atmospheric blocking during the LIA were first suggested by Lamb (1979) as an explanation for the severe winters experienced in Europe during the Maunder Minimum. Blocking events in the eastern North Atlantic derive from instabilities of the jet stream and are typically associated with a negative NAO state (Shabbar et al., 2001, Woollings et al., 2010a, Häkkinen et al., 2011, Luo, 2005). In an attempt to validate the SLP changes driven by solar irradiance observed in the model, high resolution NAO reconstructions obtained from very diverse archives have been compiled and are presented in Figure 4.20. This comparison reveals that pre-industrial proxy NAO reconstructions extending back to 1400 years AD are highly variable and often in considerable disagreement with each other (Pinto and Raible, 2012). Studies of

the robustness of the NAO proxy reconstructions have suggested that these discrepancies arise from the spatial complexity of the NAO and the inability of proxy reconstructions to monitor these (Schmutz et al., 2000, Lehner et al., 2012). Therefore, the lack of a consistent picture prevents a confident interpretation of the NAO state at centennial to multidecadal time-scales during the last millennium. Despite this, an increasing number of meteorological studies have investigated the potential links between blocking events and solar irradiance for the last 350 years and have shown a good correlation between the recorded winter Central England Temperatures (which are mainly dominated by the frequency of winter blocking) and the recorded solar activity (Barriopedro et al., 2008, Lockwood et al., 2011, Lockwood et al., 2010, Woollings et al., 2010b). Similarly, a number of modelling studies predict a negative NAO state during solar minima, specifically the Maunder Minimum (Swingedouw et al., 2011, Zorita et al., 2004, Shindell et al., 2001, Raible et al., 2007). The relationship between solar activity and atmospheric circulation has frequently been explained by complex feedbacks that take place in the upper stratosphere, as a response from ozone formation to changes in ultra violet radiation (Gray et al., 2010, Shindell et al., 2001, Woollings et al., 2010b). Nonetheless, modelling studies with a simplified representation of the upper atmosphere, like CCSM4, find a similar response to solar forcing suggesting that other feedbacks such as internal climate dynamics, teleconnections and ocean-atmosphere feedbacks must also play an important role (Swingedouw et al., 2011, Zorita et al., 2004, Spangehl et al., 2010).

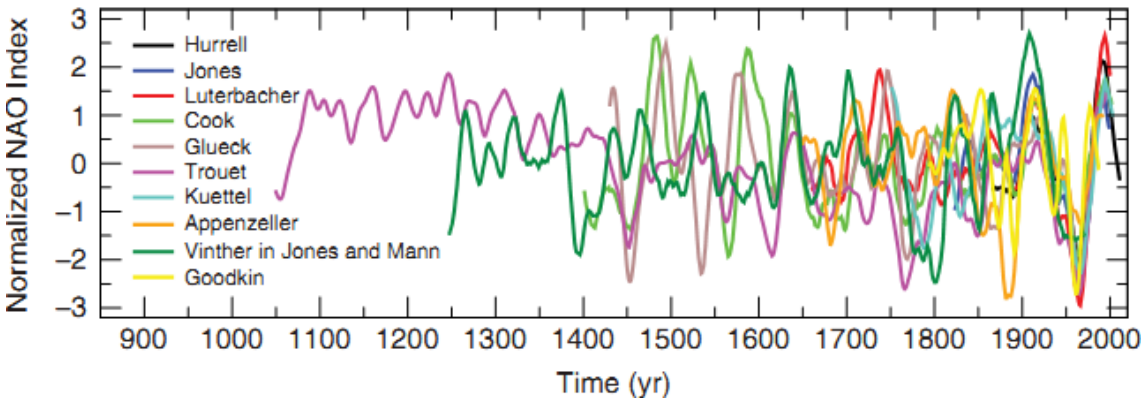

Figure 4.20. Compilation of proxy-based normalized NAO reconstructions (Pinto and Raible, 2012 and references therein).

The interpretation of the hydrographic conditions in the Iceland Basin based on the model study is schematically summarized in Figure 4.21.

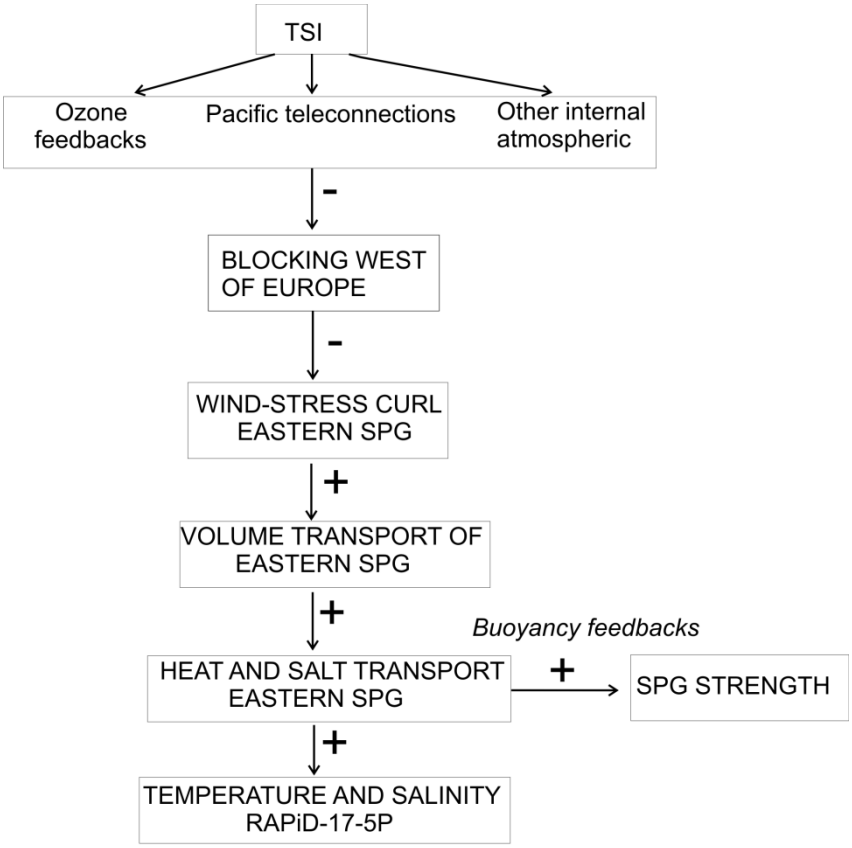

Figure 4.21. Summary diagram of the forcing and feedback mechanisms highlighted from the CCSM4 model run to explain the reconstructed hydrographic changes of the Atlantic Inflow from RAPiD-17-5P during the last millennium. Negative and positive signs indicate negative and positive feedbacks, respectively.

It is possible to reconcile the interpretation outlined in this section with the studies from Thornalley et al., (2009) because hydrographic changes at different time-scales are likely to have been dominated by different mechanisms. Millennial scale variability in the properties of the Atlantic Inflow were suggested to be controlled by SPG dynamics forced by changes in LSW formation (Thornalley et al., 2009). This may potentially have over-printed the multidecadal hydrographic changes driven by localised atmospheric forcing in the eastern SPG resulting from anomalous blocking events.

4.4.4. Changes in the temperature and salinity relationship of the Atlantic Inflow during the last millennium

As mentioned in Section 3.4.1.5 and 3.4.2.5, a long-term change in the relationship between temperature and salinity at approximately 1400 years AD has been recorded in all high-resolution Atlantic Inflow reconstructions. The temperatures present a long-term cooling trend that is not mirrored by the salinity (Figure 4.22).

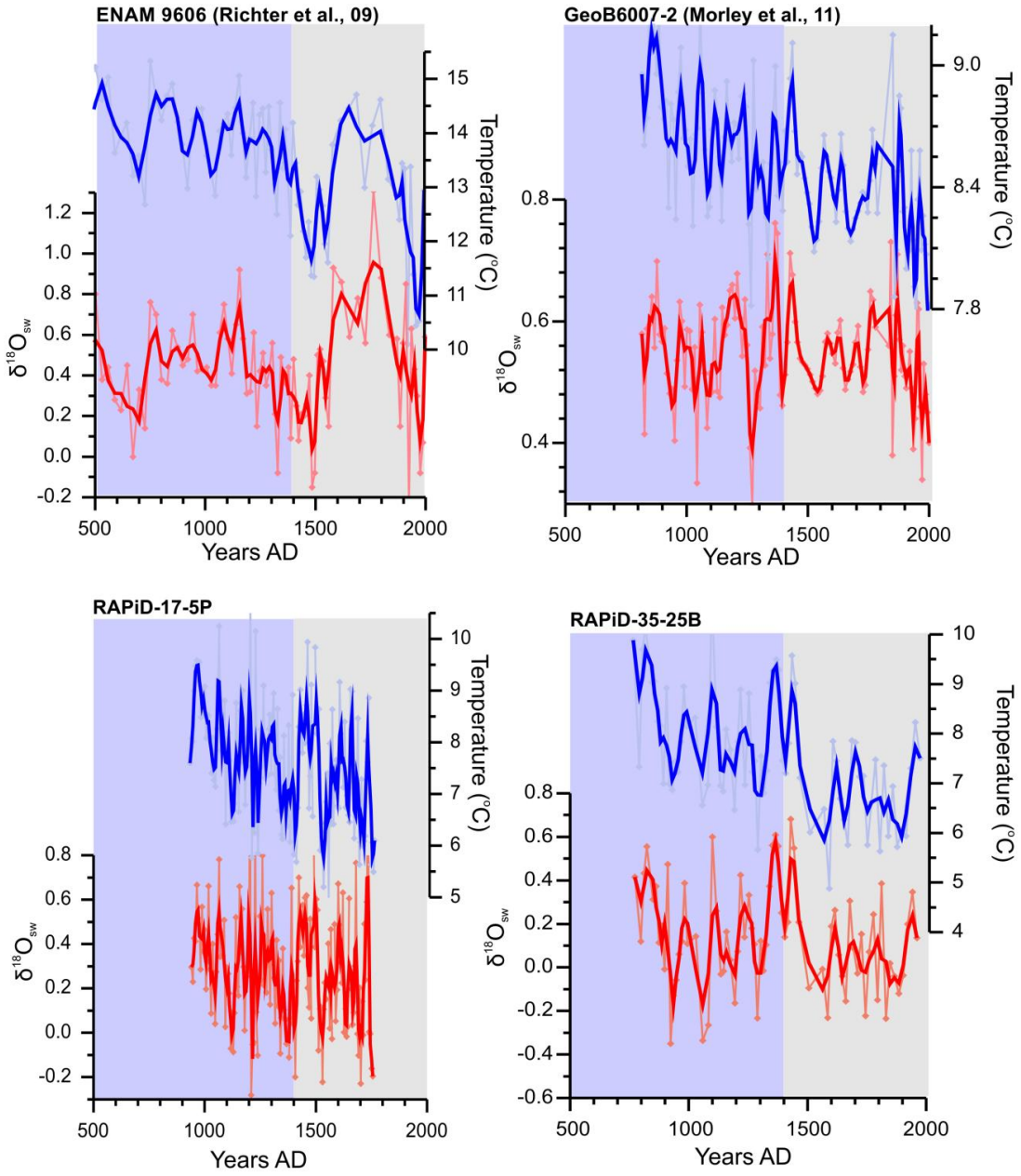

Figure 4.22. Temperature (blue) and $\delta^{18}O_{sw}$ (red) reconstructions from ENAM9606 (Feni Drift, 55°39N 13°59, 2543 m water depth) (Richter et al., 2009), GeoB6007- (West Africa: 30.85°N, 10.27°W at 899 m water depth) (Morley et al., 2011), RAPiD-17-5P (Iceland Basin) and RAPiD-35-25B (Chapter 3). Light and dark grey shading highlight pre and post 1400 years AD, respectively.

This is visually more apparent when temperature is plotted versus salinity (Figure 4.23) for the two time periods (before and after 1400 years AD). Post 1400 years AD the data show a consistent shift of the linear relationship towards lower temperatures and/or higher salinities.

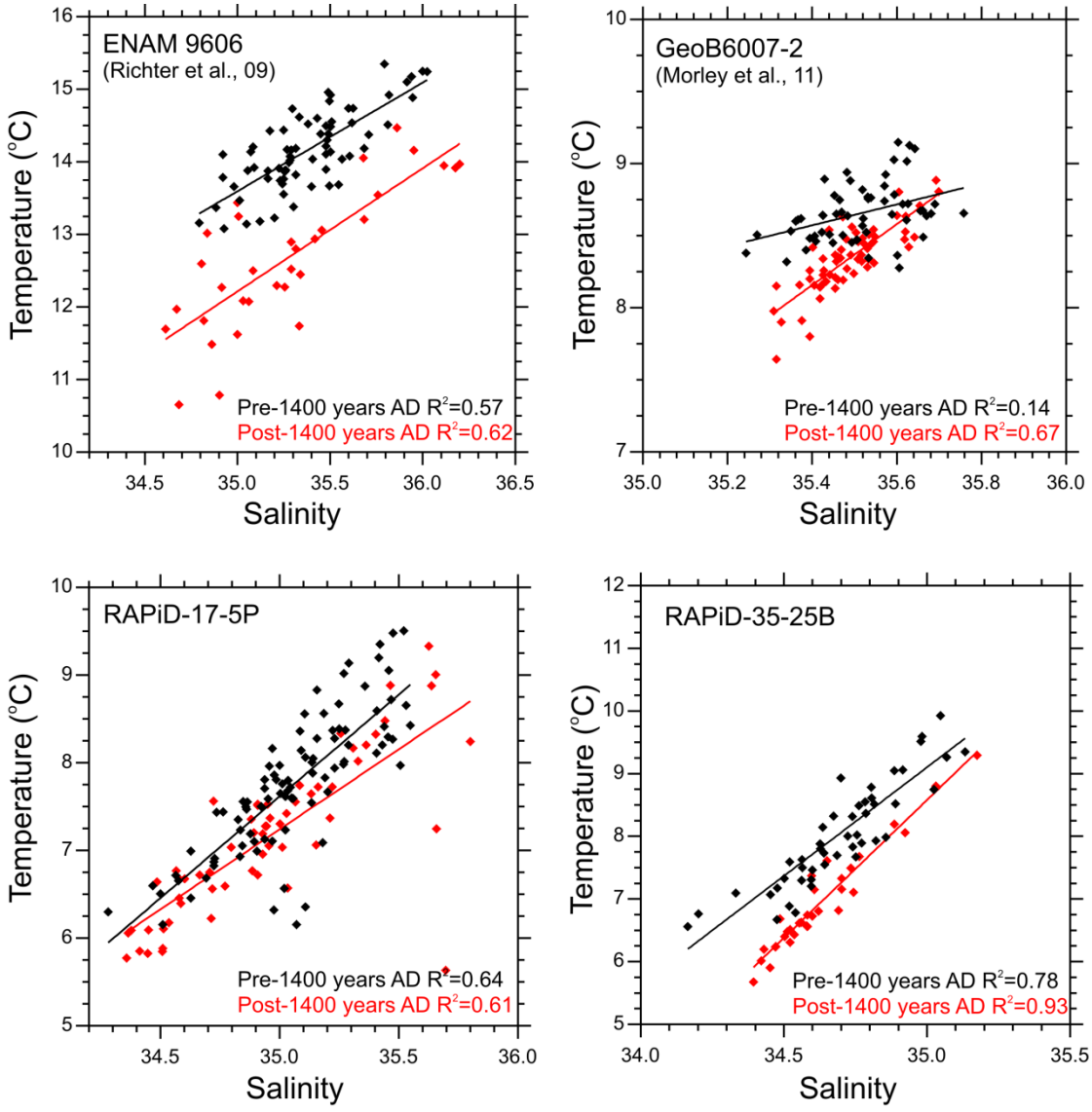

Figure 4.23. Temperature and salinity plots before 1400 years AD and after years AD (black and red, respectively), with the linear trends of this data.

First of all, it is hard to ascertain if this offset of the linear relationship between temperature and salinity before and after 1400 years AD is a feature resulting from an anomalous temperature or salinity.

Assuming it was a salinity change it can be argued that anomalous high salinity in the Atlantic Inflow after 1400 years could have resulted from the abrupt southward migration of the ITCZ at the onset of the LIA (Haug et al., 2001, Sachs et al., 2009). A southern shift in the rain belt is thought to have decreased the freshwater input into the AWP causing an increase in salinity that has been recorded in numerous records of the AWP (Lund et al., 2006, Richey et al., 2009, Saenger et al., 2011). This anomaly may have then propagated northwards into the higher latitudes within the NAC. Although some of the salinity changes observed in the $\delta^{18}O_{sw}$ would have been compensated for by the cooling recorded in the entire North Atlantic and described in Section 4.4.2.1, the ITCZ shift at this time was abrupt and large, and therefore there is a possibility for uncompensated salinity changes in the NAC waters that were transported northwards. Alternative mechanisms include, an alteration in the hydrological cycle along the pathway of the NAC, changes in the predominance of different water masses taking place during cross frontal mixing in the NAC, or an increase in sea-ice formation during the LIA making the surface waters more saline due to brine rejection processes and leading to a change in the slope of the salinity- $\delta^{18}O_{sw}$ relationship.

Conversely, the change in the temperature and salinity relationship could be due to anomalously cold temperatures as a result of an increased air-sea exchange during the abrupt Northern Hemisphere cooling at ~1400 years AD. A change in the prevailing atmospheric pattern over the North Atlantic from zonal (positive NAO-like state) to more meridional (negative NAO-like state) at the onset of the LIA might have enhanced winter convection south of Iceland leading to a reduction in temperatures with respect to the MCA.

The timing of the change of the intercept of the linear relationship between the temperature and salinity is coincident with the transition from the MCA to the LIA that is present in a lot of the North Atlantic records. Furthermore, this event is not unique, and a similar feature is observed at 800 years AD in Came et al. (2007), Thornalley et al. (2009) and the Late Holocene record presented in Section 3.4.2.5, Figure 3.23. Despite the remarkable consistency of these findings across the Atlantic Inflow records

over the last two millennia, it is very hard to discern the dominant cause for this relationship change between these two hydrographic properties. Further work from different sites might eliminate some of these possibilities, for instance, the changes in cross-frontal mixing or the northward propagation of the anomalies from the tropics.

4.5. Summary and Conclusions

In this chapter, Mg/Ca-$\delta^{18}O$ measurements on the planktonic foraminifera species *G. inflata* are used to reconstruct the hydrographic conditions of the seasonal thermocline in the Iceland Basin during the last millennium. The results reveal centennial temperature and salinity shifts in the Atlantic Inflow of 3.5^{o}C and 1.5 psu, which present a strong correlation with TSI forcing (Pearson T=0.48). Periods of solar minima correspond to marked shifts towards colder and fresher conditions south of Iceland. Comparison with other records is complicated due to their lower temporal resolution. However, the results obtained here are coherent with other Late Holocene foraminifera-based temperature reconstructions of the Atlantic Inflow including that of *G. bulloides* monitoring the temperature and salinity from the IC (presented in Chapter 3).

The interpretation of the hydrographic changes found in this study is not straightforward and this may be a result of the limited number of North Atlantic palaeoceanographic records at this resolution. In this chapter, two different possible mechanisms are explored in order to explain the recorded abrupt temperature and salinity shifts.

Following the reasoning from Hatún et al., (2005), the temperature and in particular the salinity variability observed in the Iceland Basin could be a result of changes in (i) the Gulf Stream source waters or those of the STG, (ii) the SPG source waters, (iii) the relative contribution of the two gyres, or (iv) local heat and freshwater air-sea exchanges. Through a process of elimination, previous studies have interpreted changes in salinity in the mixing region south of Iceland to be indicative of changes in the cross frontal mixing due to SPG dynamics (option (iii)) and thus warm and salty waters resulted from the contraction (E-W displacement) as an effect of weakening of the SPG. In this chapter, the same elimination process is followed, albeit inconclusively. Comparison of the hydrographic changes in the Iceland Basin with proxies indicative of LSW formation does not show a clear relationship, suggesting that temperature and

salinity changes in the Iceland Basin at multidecadal to centennial time-scales were probably not dominated exclusively by changes in SPG dynamics.

Modelling experiments using CCSM4 reveal a significant positive correlation between TSI, surface temperature and salinities in the Iceland and Irminger Basins during the last millennium, coherent with the results obtained from RAPiD-17-5P and RAPiD-35-25B. This positive relationship is also observed in the volume transport of the SPG, which is decreased during low solar irradiance. Periods of solar minima correspond to a decrease in the heat and salt transport around the SPG. Winter SLP analysis in the model reveals the presence of an anticyclone system west of Europe during periods of low solar irradiance. This atmospheric feature is characteristic of blocking events, which lead to diversion of the westerlies, thereby decreasing the wind-stress curl over the eastern part of the SPG and effectively weakening the Eastern SPG. Such an anomaly is then propagated around the gyre by buoyancy driven feedbacks specifically through enhanced salt transport in the boundary current of the SPG.

Certainly, other possibilities cannot be ruled out, such as propagation of freshwater export events into the North Atlantic originating from the Canadian or Central Arctic which would have eventually advected around the SPG reaching the Iceland Basin, changes in the subpolar mode water formation as a result of changes in the stratification of the upper water column and/or simply artefacts recorded within foraminiferal calcite.

5. Late Holocene Changes in the Vigour of the Nordic Overflows

5.1. Introduction

The Nordic Seas and Arctic Ocean are the final destination of the warm salty waters originating from the tropics which are transported to the higher latitudes within the NAC. On their northward travel into the Nordic Seas and beyond, the Atlantic Inflow waters lose heat via air-sea exchange, increase their density and eventually sink to form intermediate and deep water masses in the Nordic Seas. The newly formed water masses and other dense waters originating from the Arctic Ocean are constrained to the north of the Nordic Seas by a submarine ridge that lies between Greenland and Scotland, known as the Greenland Scotland Ridge (GSR) (Figure 5.1). This topographic feature forms a physical barrier that controls the exchange of dense waters between the Nordic Seas and the open Atlantic Ocean.

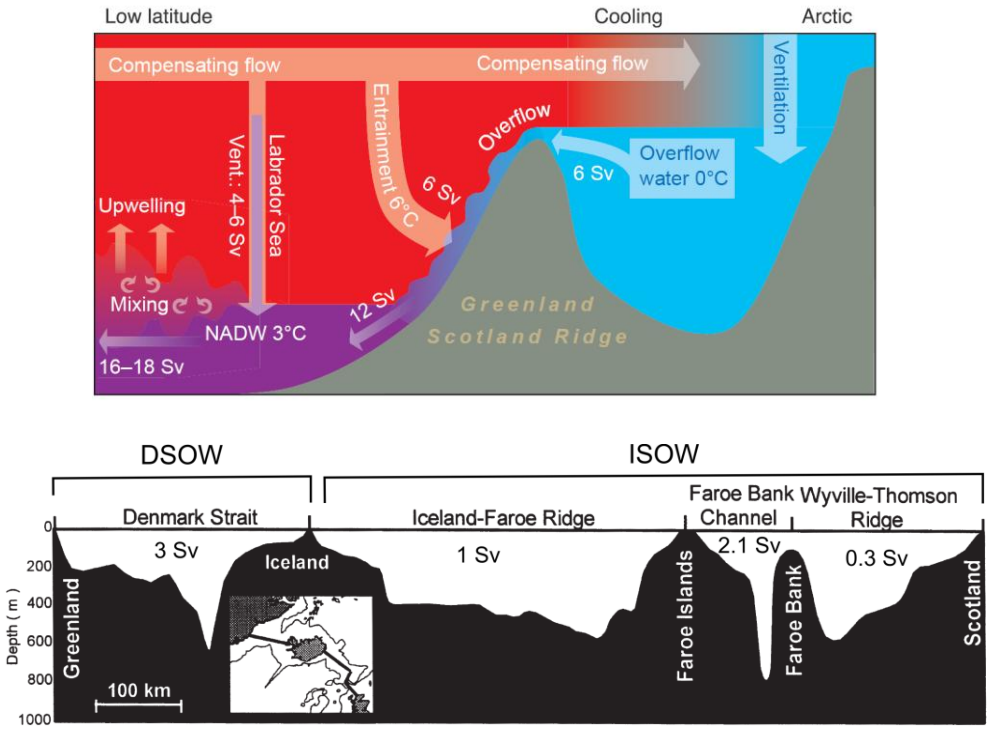

Figure 5.1. Schematic diagram of the key meridional overturning processes that take place in the Nordic Seas and the North Atlantic Basin (Hansen et al., 2004) (top). Bathymetric profile across the GSR, section outlined in the inset map (Hansen and Østerhus, 2000). Approximate volume transport of each of the overflows according to the summary of Olsen et al., (2008) (bottom).

Deep water formation in the Nordic Seas sets a horizontal density gradient across the GSR which drives the drainage of these dense waters over the sill as the Nordic Overflows (Hansen et al., 2001). The rate of dense water export by the overflows into the North Atlantic Basin is hydraulically controlled and is proportional to the cross-sill density difference ($\Delta \rho = \rho_1 - \rho_2$) and to the square of the upstream reservoir height (ΔH) (Whitehead, 1998) (Figure 5.2). Alteration of these two factors will therefore drive changes in the vigour of the overflows reaching the Atlantic Basin.

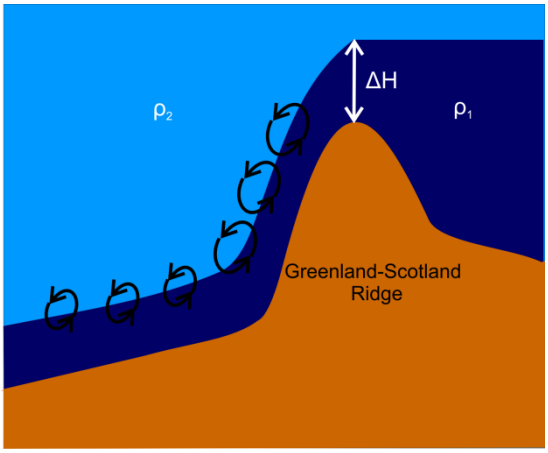

$$Q = \frac{g' h_u^2}{2f}$$

$$g' = g\Delta\rho/\rho$$

Figure 5.2. Schematic diagram of the factors influencing the hydraulically controlled transport of the Nordic Overflows into the North Atlantic Basin. ΔH: reservoir height, which is normally defined to be the height of the interface level (normally isopycnal σ_θ > 28 kg/m^3) above the sill (Hansen et al., 2001); ρ_1: density of the upstream overflow waters; ρ_2: density of downstream water masses. The equation defines the volume flux across a sill as presented in Whitehead (1998) (Q) (h_u: reservoir height; g: gravity; ρ: density of motionless layer (ρ_2); $\Delta\rho$: density contrast across the sill; *f:* Coriolis parameter.

The densest overflow waters pass through the deepest passages of the GSR, the Denmark Strait and the Faroe Bank Channel. As such, the Nordic Overflows are divided into two major branches east and west of Iceland: the Iceland Scotland Overflow Water (ISOW) and the Denmark Strait Overflow Water (DSOW), respectively (Figure 5.1). While the nature of the two overflows is different primarily because of the differing sill geometries and the physical properties of their upstream source waters, both overflows contribute approximately equally (~3 Sv each) to the total volume flux of dense waters ventilating the subpolar North Atlantic (Olsen et al., 2008 and references therein). Once the overflows cross the ridge, they descend over the sill subsequently entraining intermediate waters found in the Irminger and Iceland Basins (mostly LSW and SPMW). This downstream entrainment process contributes to at least a two-fold increase in the overflow volume transport (Price and Baringer, 1994, Hansen et al.,

2004) (Figure 5.1). Thereafter, the overflows continue as density-driven bottom currents following the bathymetry whilst undergoing mixing with the overlying waters (note that 'entrainment' is used to denote turbulent mixing created by topographic instabilities and 'mixing' is used to express small-scale diffusive processes). The intensive downstream entrainment and mixing not only modify the initial volume transport but also significantly alter the hydrographic properties of the overflow waters (Price and Baringer, 1994) (Figure 5.1). The two overflows ISOW and DSOW merge south of the Denmark Strait forming the upper and lower branches of the DWBC on reaching Cape Farewell. The DWBC subsequently flows around the Labrador Basin and in combination with LSW eventually forms NADW when reaching Newfoundland Basin (Figure 5.3).

The Nordic Overflows are of pivotal importance to the climate system as they are the densest component contributing to the production of NADW, and therefore provide ~30% of the volume transport of the abyssal limb of the AMOC (Hansen et al., 2004). Furthermore, the flow of deep waters into the North Atlantic Basin sets a pressure gradient at the surface which contributes significantly to the inflow of warm waters into the Nordic Seas (Hansen and Østerhus, 2000). As discussed in Chapter 4, the advection of salt and heat to the high latitudes via the Atlantic Inflow is not only important for shaping the climate in Western Europe (Seager et al., 2002) but also crucial for promoting deep water formation. Additionally, modelling studies have suggested that the density of the overflows and their transport can also influence the oceanographic conditions south of the GSR, for instance the SPG circulation (Born et al., 2009, Zhang et al., 2011).

Future climate predictions under increasing atmospheric CO_2 levels anticipate a change in the freshwater budget in the Arctic Ocean and Nordic Seas as a result of a decline in Arctic sea ice cover, melting of the Greenland Ice Sheet and increase in circum-Arctic river run-off (IPCC, 2007). The addition of freshwater into the high latitudes may lower the salinity and reduce the formation of dense waters in the Nordic Seas which would potentially weaken the overflow transport across the ridge possibly affecting the AMOC (e.g. Wilkenskjeld and Quadfasel, 2005, Hansen et al., 2004).

Between 1965-2000, the subpolar North Atlantic experienced a gradual freshening which has been mainly attributed to the effects of a shift between extremes of the NAO towards a positive state (Dickson et al., 2003). During this time, the freshening of the upper ~1000 m in the Nordic Seas and the overflows was initially suggested to have reduced the overflow transport and potentially the AMOC (Dickson et al., 2002, Hansen et al., 2001, Bryden et al., 2005). However, recent re-analysis of the direct measurements from Hansen et al. (2001) and additional overflow transport measurements have concluded that in spite of the freshwater forcing the transport of the overflows and the AMOC were not significantly altered during this period (Olsen et al., 2008, Cunningham et al., 2007).

Furthermore internannual and decadal variability of ISOW and DSOW have been monitored using direct measurements and indirect transport calculations from hydrographic transects for the last 60 years and have shown 10-30% variability in the transport of the two overflows (Macrander et al., 2005, Olsen et al., 2008, Dickson et al., 1999, Bacon, 1998, Sarafanov et al., 2009). The relationship between the vigour of the two overflows has not yet been established. Some modelling studies have suggested the presence of an out-of-phase relationship between strength of ISOW and DSOW (Biastoch et al., 2003, Kohl, 2010, Serra et al., 2010) whereas recent transport calculations of the two overflows reaching Cape Farewell have been shown to not only be in-phase but also negatively correlated to LSW thickness (Sarafanov et al., 2009).

Prior to reaching any conclusion on the anthropogenic climate change and its effect on the freshening and weakening of the overflows and the AMOC, it is necessary to extend the instrumental overflows record back in time to enable differentiation between natural and anthropogenic variability of these key AMOC water masses. On centennial time-scales, proxy reconstructions have revealed abrupt changes in the strength and/or depth of the overflow boundary currents at times corresponding to well-known millennial-centennial scale climatic oscillations, such as the 8.2 kyr event (Ellison et al., 2006), the 2.7 kyr event (Hall et al., 2004) and the LIA (Bianchi and McCave, 1999). This ocean-climate link potentially implicates the Nordic Overflows and hence the alteration of the AMOC during these climatic events.

This chapter will present Late Holocene near-bottom flow speed reconstructions obtained using the palaeocurrent proxy sortable silt mean grain size ($\overline{SS}$) from two sediment cores strategically located in the path of the ISOW and DSOW. Potential mechanisms explaining the millennial-scale overflow strength variability throughout the Late Holocene will be discussed.

5.2. Materials and Methodology

5.2.1. Ocean Setting

The regional surface oceanographic setting of marine sediment cores RAPiD-35-COM and RAPiD-17-5P have previously been described in Section 3.2.1 and Section 4.1, respectively. However, the focus of this chapter is the study of the deep ocean circulation at these sites (Figure 5.3).

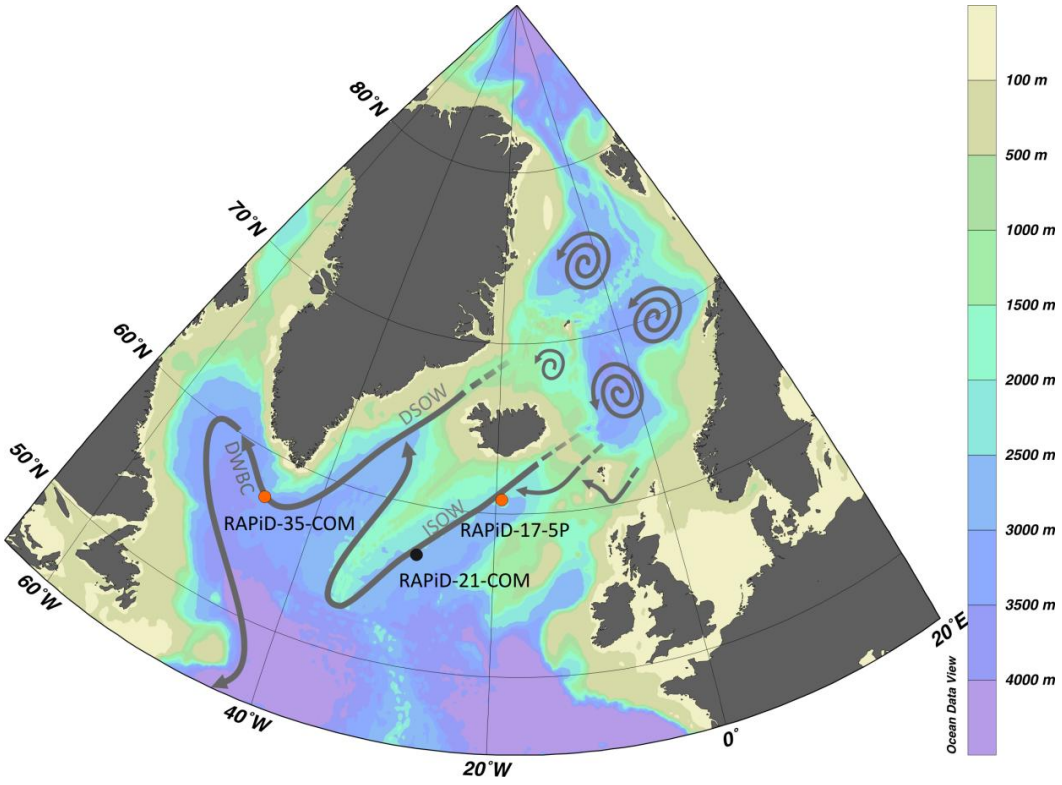

Figure 5.3. Bathymetric map of the Nordic Seas and the North Atlantic, indicating the location for RAPiD-17-5P, RAPiD-35-COM and RAPiD-21-COM (red dots indicate the core locations used in this study). Arrows represent the simplified deep ocean circulation of the Nordic Overflows. Spirals indicate the sites of open ocean convection in the Nordic Seas which produce the main source waters for the Nordic Overflows.

Sediment core RAPiD-35-COM was recovered from the Eirik Ridge (as described in Section 2.2.1 and presented in Figure 5.3). CTD transects on the Eirik Ridge, show a temperature of <2^{o}C and salinity of 34.9 at the core location (3500 m water depth) (Holliday et al., 2009) (Figure 5.4). CTD measurements obtained during the CD159 cruise at two neighbouring locations (58° 14N, 47°W and 56° 45N, 52° 27W) in the Labrador Basin show temperatures and salinities of 1.6-1.75 ^{o}C and 34.86-34.89 respectively (>3000 water depth) (CD159 Cruise Report). Both lines of evidence indicate that currently the core location lies in the pathway of the DSOW (defined as >27.88 kg/m^{3}) (Hunter et al., 2007a) (Figure 5.4). The width of the overflow plume at the site is of approximately 150 km (Bacon and Saunders, 2009), similarly to that predicted from numerical studies of the overflow plume at >700 km downstream of the GSR (Price and Baringer, 1994).

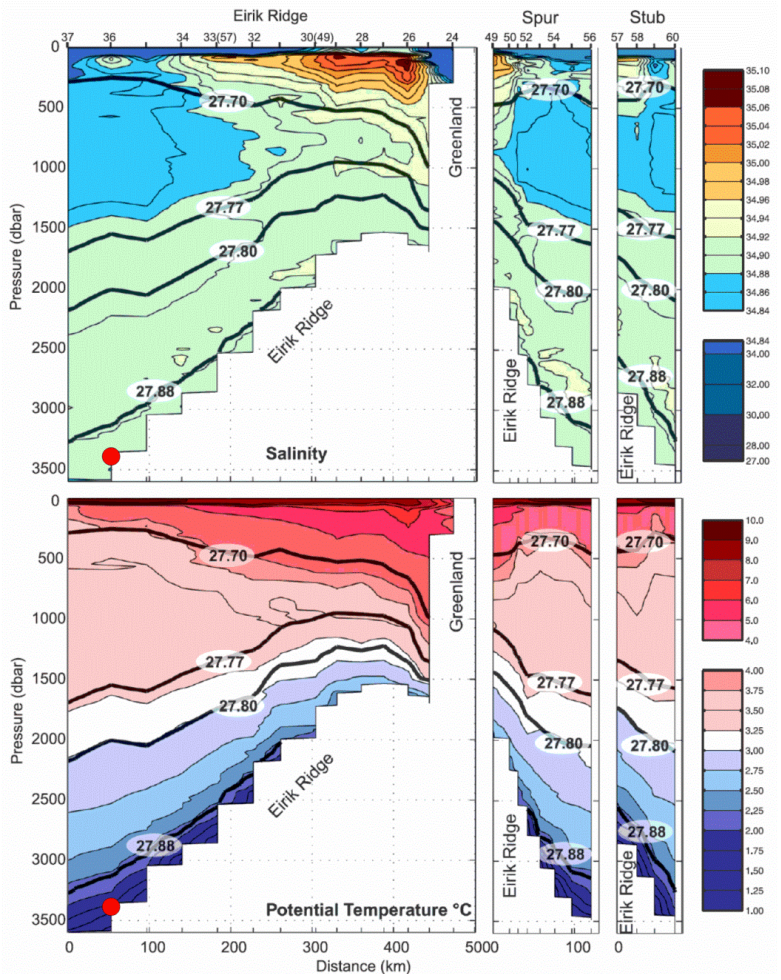

Figure 5.4- Salinity (top) and potential temperature (bottom) from the Eirik Ridge hydrographic section recovered from the Discovery cruise 298 (August-September 2008). The thick lines denote the isopycnals which divide specific water masses: NEADW (σ_θ = 27.70-27.80 kg/m^{3}); DSOW (σ_θ > 27.88 kg/m^{3}); DWBC (σ_θ >27.80 kg/m^{3}; T<3^{o}C) (Holliday et al., 2009). The red dot denotes the core location of RAPiD-35-COM. For a map of the CTD transect refer to Figure 3.2.

RAPiD-17-5P was recovered from the Iceland Basin (as described in Section 2.2.2 and presented in Figure 5.3). Numerous hydrographic studies focusing on the deep circulation in the Iceland Basin (Bianchi and McCave, 2000, Van Aken, 1995, van Aken and Becker, 1996) and the CTD data obtained during the CD159 cruise (McCave, 2004) show temperatures and salinities of ~2.8-3 ^{o}C and ~34.97 respectively at the core site, which confirm that RAPiD-17-5P lies directly in the pathway of the ISOW (Figure 5.5).

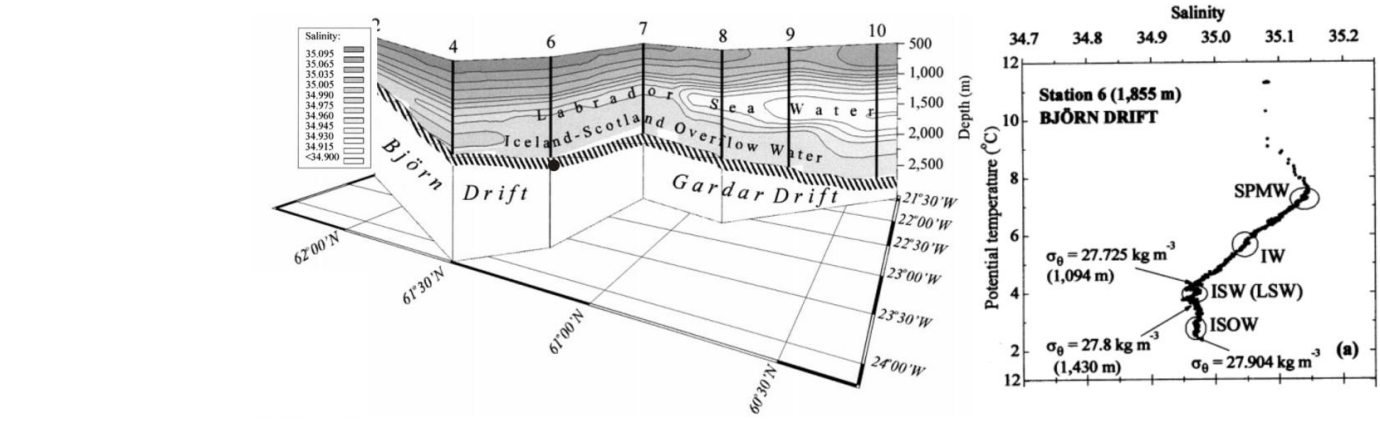

Figure 5.5. Salinity distribution in the Iceland Basin obtained from a hydrographic transect. The location of RAPiD-17-5P is marked with a black dot (left). Temperature and salinity plot of CTD cast from the deep Bjorn Drift closely located to RAPiD-17-5P (right) (Bianchi and McCave, 2000).

5.2.2. Chronology

Sediment processing and chronologies for RAPiD-35-COM and RAPiD-17-5P have been presented and described in Section 3.2.2 and Section 4.2.2, respectively.

5.2.3. Sortable Silt

The use of the sortable silt mean grain size ($\overline{SS}$) allows the reconstruction of past relative speed of the near-bottom speed current from sedimentary cores (e.g. McCave and Hall, 2006) (Section 2.4.1).

The preparation for $\overline{SS}$ measurements is described in Chapter 2 (Section 2.4.1). After the carbonate and opal removal steps, the samples which were contained in 65 ml nalgene bottles were ultrasonicated for 3 minutes, before shaking and pipetting twice 150 µl into the beaker. The repetition of the pipetting was adopted as a measure to minimise the

procedural error attached to pipetting. The grain size measurements were obtained using a *Beckman Multisizer Coulter Counter III*. The samples were run with a concentration of <4% and generally between 1- 2.5%. The particles from RAPiD-17-5P were particularly coarse and dense, and initial analysis showed poor precision (up to 3 μm), which was caused by the settling of the particles from the sample suspension over the period of the analyses. This was overcome by elevating the speed of the stirrer (54) to stop particle deposition. Additionally, the volume of electrolyte (Isoton^{TM}) used to suspend the sample was increased in order to avoid turbulence and drawdown of bubbles into the sample at the higher stirrer speed. The sample blank under the higher stirrer speed did not present significant background noise. Each sample was run a minimum of two times in an arbitrary order and over several days. The average standard deviation error from the duplicate or triplicate runs was ±0.6 μm which is approximately the 1.8% precision error quoted by Bianchi et al. (1999).

5.3. Results

5.3.1. RAPiD-17-5P

The subdecadal $\overline{SS}$ near-bottom flow speed reconstruction of the overflow east of Iceland, shows a particle size variability ranging from 6-8 μm for the last 2000 years (Figure 5.6). The $\overline{SS}$ record presents a trough in $\overline{SS}$ between 2000-1450 years BP with a low centred at 1700 years BP followed by a gradual decrease of approximately 4.5 μm in grain size from ~1450 years BP to 200 years BP. The $\overline{SS}$ record exhibits very defined and clear centennial to multidecadal oscillations but do not present a systematic relationship with the traditionally known intervals of climate variability identified and recorded in a multitude of proxy reconstructions within the North Atlantic and described and reviewed by Mayewski et al. (2004) (Figure 5.6).

Single spectrum and wavelet analyses were performed on the linearly detrended 6 year Gaussian smoothed RAPiD-17-5P $\overline{SS}$ record with an 18 year window (using the same methodology as described in Section 2.6). Single spectrum analysis revealed a peak above 90% CL at 380 years (Figure 5.7a), which could potentially relate to the Holocene 400 year cycles observed in other ISOW $\overline{SS}$ records (Hall et al., 2004). However, using the wavelet analysis and band-pass filtering it is clear that the 400 year cycle is not present throughout the record and only appears between 1700-1200 years

BP at >80% CL (Figure 5.7b,c) and is also present within the cone of influence. This suggests that this frequency cycle is not a pervasive feature of the flow speed record of ISOW.

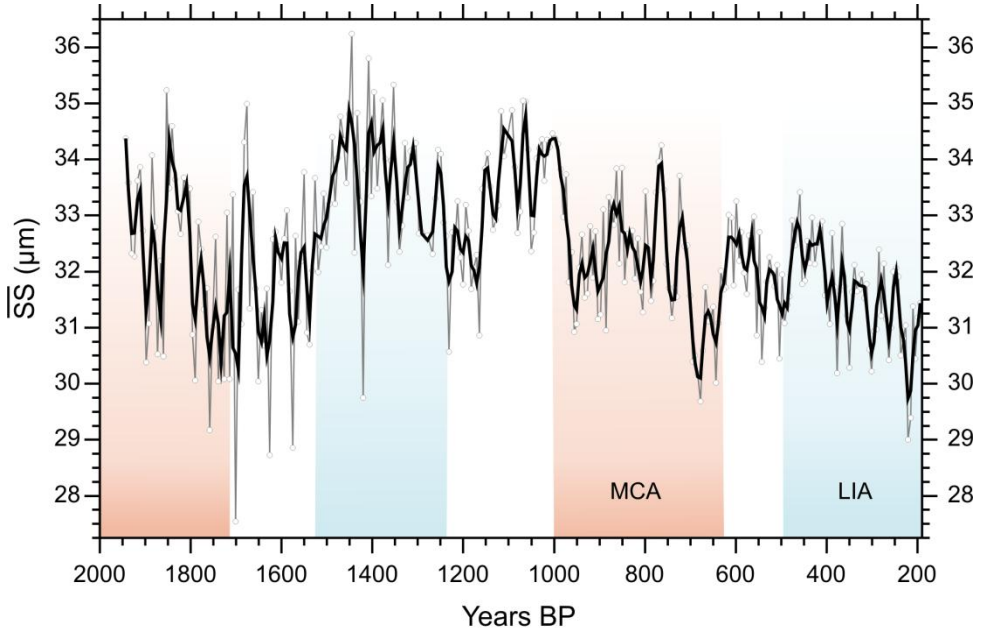

Figure 5.6. Sortable silt mean grain size measurements from RAPiD-17-5P. Blue and red shading represent cold and warm centennial-scale climate oscillations that have been established based on advances or retreats of alpine glaciers (Denton and Karlén, 1973) and have been recorded in a number of proxies records recovered from the North Atlantic region (Mayewski et al., 2004).

Other frequencies in the 40-60 year domain are also statistically significant at above 90% CL on the single spectrum analysis. These periodicities could potentially be related to the so-called Atlantic Multidecadal Oscillation (AMO). The AMO is defined as the interannual variability of sea surface temperatures in the North Atlantic between 0-70^{o}N, which have been observed to oscillate with periodicities of 50-88 years (Schlesinger and Ramankutty, 1994). Modelling studies have suggested that the AMO arises from internal variability in the strength of AMOC (Knight et al., 2005, Sutton and Hodson, 2005), mostly via northward salt transport feedbacks (Vellinga and Wu, 2004). During a strong AMOC an enhanced transport of heat and salt to the higher latitudes creates a cross-equatorial sea surface temperature gradient which will drives a northward migration of the ITCZ. This shift of the tropical rain belt will eventually freshen the tropical Atlantic and this freshwater anomaly will travel northwards and slowdown the AMOC, according to modelling work this process takes approximately 50-60 years (Vellinga and Wu, 2004). While the short length of the proxy reconstructions of the AMO (1600 and 1300 years AD, Gray et al., 2004, Mann et al.,

2009, respectively) precludes a confident comparison with the RAPiD-17-5P ISOW overflow vigour, the potential for such a relationship suggested by the spectral characteristics is very encouraging. Especially, as if correct this would be the first evidence of the link between the deep limb of the AMOC and the AMO. Nevertheless, the interpretation of the multidecadal cyclicities found in the $\overline{SS}$ of RAPiD-17-5P any further is difficult particularly as the cyclicity is 8-10 times the sampling interval and thus the reliability of this peak may be questioned and therefore further detailed discussion is not included in Section 5.4.

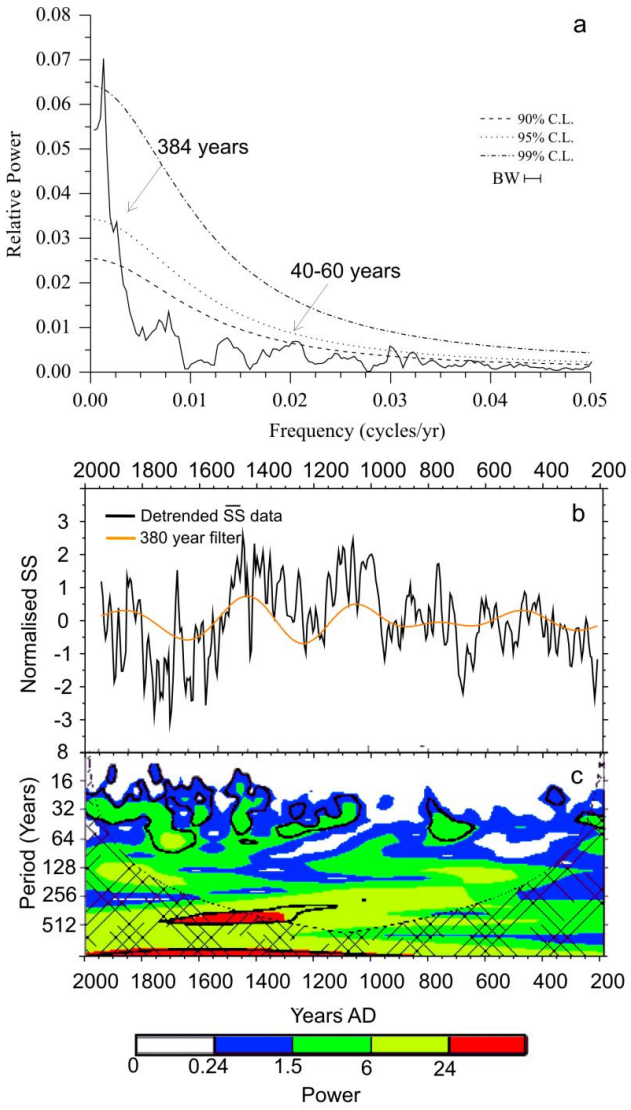

Figure 5.7. (a) Single spectral analysis (BW= Bandwidth) (b) Band-pass filter at 380 years (c) Wavelet analysis on the linearly detrended 6 year Gaussian smoothed $\overline{ss}$ from RAPiD-17-5P. White, blue, green, yellow and red colours denote power above red-noise of 0, 15, 25, 50 and 75%, respectively. The black outline indicates a confidence level of 80% assuming a red-noise model.

5.3.2. RAPiD-35-COM

Sortable silt mean grain size measurements from RAPiD-35-COM show fluctuations in the particle sizes of 5-7 μm over the last 4000 years (Figure 5.8). The flow speed record is punctuated by centennial oscillations which shift to higher amplitudes at ~2500 years BP with faster flow speeds becoming more prevalent towards the present (Figure 5.8). This transition is also marked by a millennial-scale trend towards higher flow speeds. Similarly to RAPiD-17-5P, the centennial shifts do not show any clear pattern with respect to the well-known cold and warm periods that have been recorded in numerous palaeorecords from the circum-North Atlantic and are indicated in Figure 5.8 (see Mayewski et al., 2004 for a review). Although it is tempting to comment on the suggestive correspondence of cold/warm intervals with slower/faster flow speeds respectively, it is particularly hard to reconcile this putative correlation with the flow speed increase found within the LIA without invoking significant age uncertainty for the last 500 years of the record.

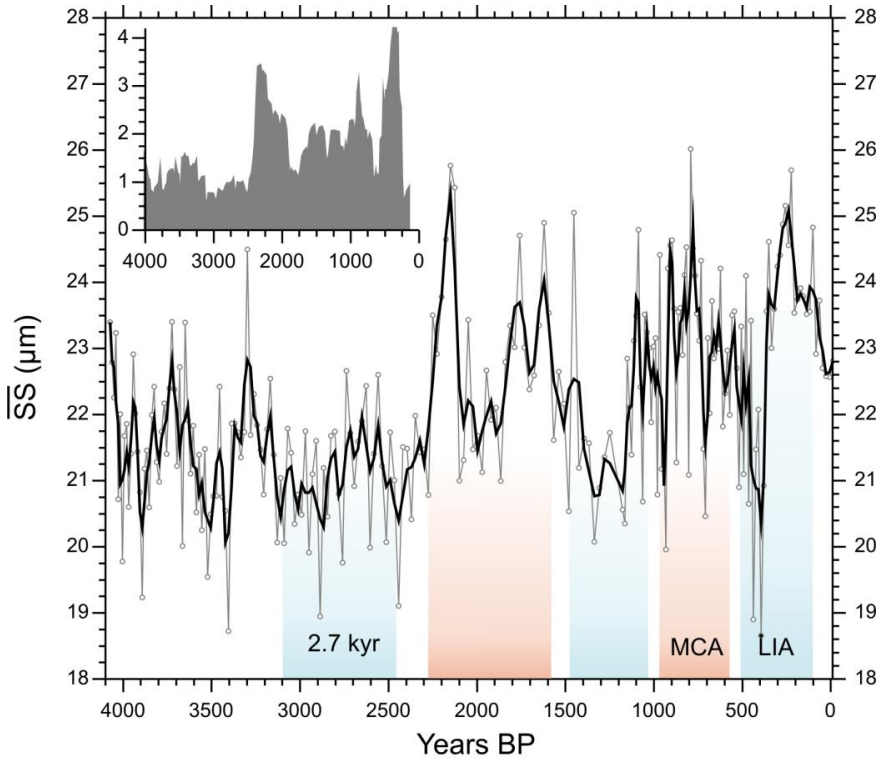

Figure 5.8. Sortable silt mean grain size measurements from RAPiD-35-COM. Blue and red shading represent cold and warm centennial-scale climate oscillations that have been established based or advances of retreats of alpine glaciers (Denton and Karlén, 1973) and have been recorded in a wealth of proxies in the North Atlantic realm. Inset diagram denotes the variance performed on a 300-year window of the $\overline{SS}$ and illustrates the increase in variance from 2500 years BP towards the present.

In order to investigate the multi-centennial scale variability of the near-bottom flow speeds of DSOW in more detail, the $\overline{SS}$ record was Gaussian smoothed at the average time step of the record;18 years (with a 54 year window) and detrended by removing the linear trend towards higher relative speed of DSOW. Single spectrum analysis (using the same method as described in 2.6.2) reveals two spectral power peaks centred between 570-460 years and at 177 years (>95% confidence level) (Figure 5.9a). The time-evolution of these periodicities can be observed in the wavelet analysis (Figure 5.9c), which was carried out as described in Section 2.6.3. The high power at >90% CL extends between 2750 years BP to 300 years BP (albeit extending into the cone of influence with potential edge effects) at periodicities of 550-460 years with a marked transition from ~450 year to ~550 year cycles at ~1500 years AD (Figure 5.9c). This is further demonstrated in the band-pass filtered record at these particular frequencies (Figure 5.9b).

Holocene cyclicities of 400-550 years (or 900 years) have previously been reported to be present in different Holocene proxy reconstructions such as ice cores (Grootes et al., 1993, Stuiver and Braziunas, 1993a), marine records (Chapman and Shackleton, 2000, Hall et al., 2004) and other palaeorecords (Schulz and Paul, 2002). The absence of these cyclicities within solar variability has led to the proposed explanation for them as a possible product of stochastic resonance in the internal modes within the climate system (Schulz and Paul, 2002). Although an external trigger cannot be ruled out as it is possible that variability at these frequencies may arise from the multiple combination of deVries and Gleissberg solar cycles (210 and 70 years) (Braun et al., 2005).

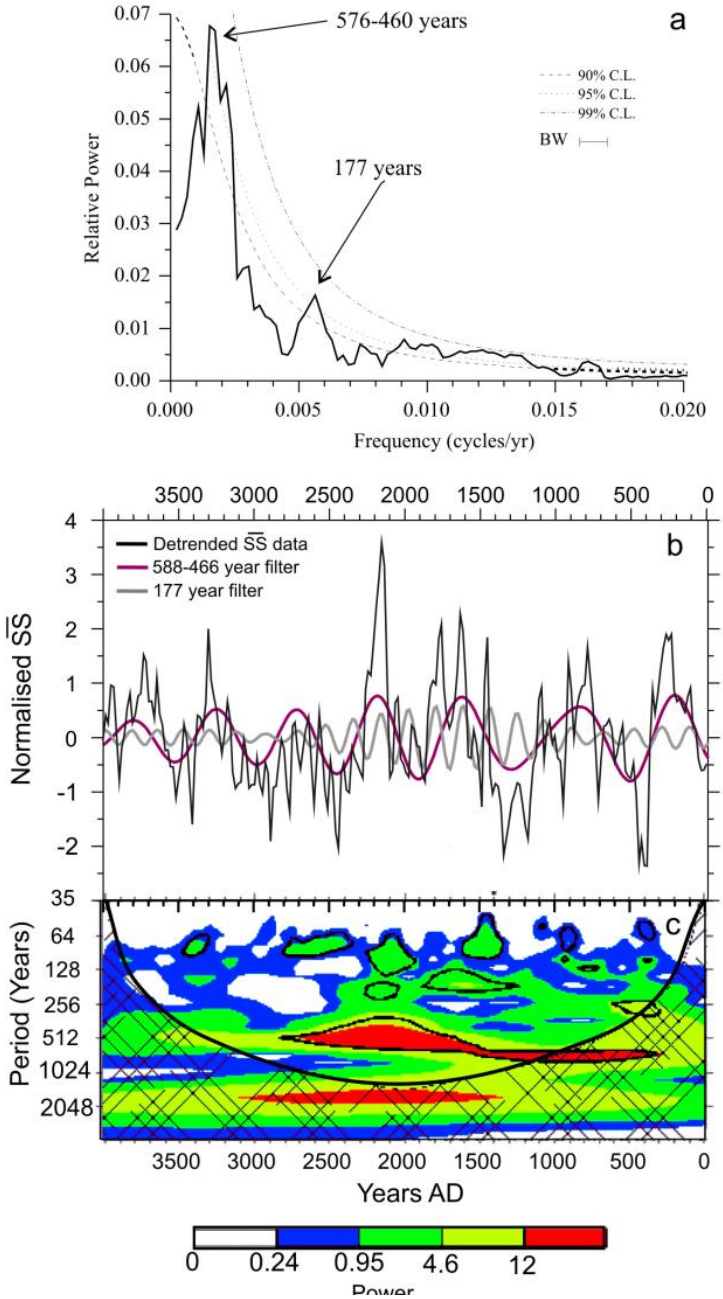

Figure 5.9. (a) Single spectral analysis (BW= Bandwidth) (b) Band-pass filter of at 588-466 years and 177 year (c) Wavelet analysis on the linearly detrended 18 year Gaussian smoothed $\overline{ss}$ from RAPiD-35-COM. White, blue, green, yellow and red colours denote power above red-noise model of 0, 15, 25, 50 and 75% respectively. The black outline indicates confidence level of 90% assuming a red-noise model.

5.4. Discussion

The main focus of this section is to investigate the mechanisms that governed the millennial-scale changes in the vigour of the Nordic Overflows recorded in the $\overline{SS}$ measurements from RAPiD-17-5P and RAPiD-35-COM for ISOW and DSOW, respectively.

Considering the physical mechanisms that drive the transport of the overflows (Figure 5.2), variability in the vigour of the overflows could result from: (i) upstream changes in the production and/or hydrographic character of the source waters supplying the overflows (which would lead to changes in the density of the overflows (ρ_1) and the reservoir height (ΔH)) an/or (ii) hydrographic characteristics of the waters south of the GSR such as LSW and SPMW (which would change the density (ρ_2)) (Figure 5.2). Following this reasoning, the potential upstream and downstream changes that might have led to the millennial scale variability in the vigour of the Nordic Overflows will be investigated in this section.

5.4.1. Late Holocene changes in the vigour of the ISOW

Recent unpublished Holocene bottom flow speed $\overline{SS}$ reconstructions from a depth transect of 13 cores from nearby locations on the Iceland Rise indicate that there have been no substantial changes in the depth of the ISOW during the last 2000 years (Thornalley et al., in prep). This information allows confidence in the interpretation of the $\overline{SS}$ reconstruction presented from this core-location as being representative of the variability in the near-bottom flow speed of ISOW.

5.4.1.1. Upstream mechanisms for the variability of Iceland Scotland Overflow vigour

Unlike DSOW, the origin of the waters supplying ISOW is better established, and its main constituent has been proposed to be the Norwegian Sea Deep Waters (NSDW) (Mauritzen, 1996, Swift, 1984). The NSDW comprises a mixture of intermediate waters formed in the Norwegian Sea mostly as a consequence of the transformation of the Norwegian Atlantic Current (NwAC) and the deep waters formed by the densification of Atlantic-origin waters along the cyclonic-loop into the Arctic Ocean and around the Nordic Seas which eventually flow through the Fram Strait and continue southwards to

the Norwegian Sea and eventually flow through the Faroe Bank Channel (Eldevik et al., 2009, Mauritzen, 1996) (Figure 5.10).

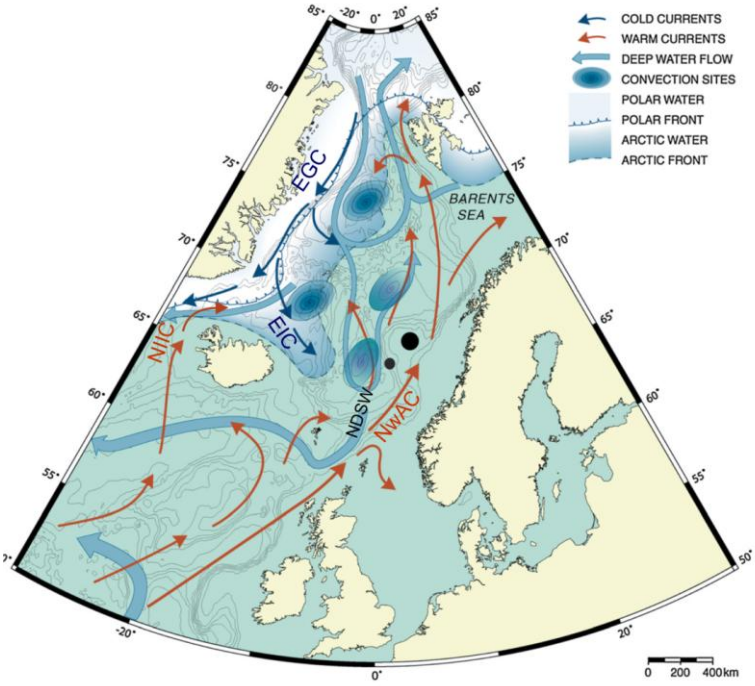

Figure 5.10. Schematic surface and deep ocean circulation of the Nordic Seas. Adapted from Nyland et al. (2006). EGC: East Greenland Current; EIC: East Icelandic Current; NDSW: Norwegian Deep Sea Water; NIIC: North Icelandic Irminger Current; NwAC: Norwegian Atlantic Current.

The surface hydrography of the Nordic Seas broadly consists of the south flowing EGC in the east of the basin, which transports low-salinity Arctic waters along the East Greenland margin and on the western side of the basin, warm salty Atlantic Inflow waters flow northwards as the NwAC (Figure 5.10). As previously suggested, the transformation of these waters via winter cooling and convection is a key process for deep water formation in the Nordic Seas, and particularly for the formation of NDSW and hence ISOW. A number of Holocene surface proxy reconstructions of the NwAC (from the Norwegian Sea, along the Norwegian continental margin and the Barents Sea) present discrepancies in the long term trends for the last 2000 years: some authors have suggested a warming (Risebrobakken et al., 2003, Moros et al., 2004), whereas other records have shown a cooling trend (Calvo et al., 2002, Sejrup et al., 2011, Risebrobakken et al., 2010, Nyland et al., 2006). Furthermore, the limited number of records of the NwAC with a similar resolution to the $\overline{SS}$ record from RAPiD-17-5P, hinders the ability to precisely constrain the role of surface ocean changes on ISOW flow speed over the last 2000 years. It is therefore not yet possible to determine if the

inflow of Atlantic waters into the Nordic Seas was reduced during the Neoglacial and if this might have decreased the formation of dense waters in the Norwegian Sea that supply the ISOW.

Ample evidence exists for a Late Holocene trend towards a cold and sea ice laden EGC and an increase in the influence of polar waters reaching North of Iceland via the EIC (a branch of the EGC) (Figure 5.10 and Figure 5.11a,b) (Andrews et al., 1997, Jennings et al., 2002, Moros et al., 2006, Müller et al., 2012). This oceanographic regime was probably associated with an increase in the volume of Arctic drift ice and freshwater being transported southwards via the EGC as a consequence of an enhanced Arctic sea-ice production due to a decline in summer insolation at these latitudes. It is likely that an increase in the freshwater content of the EGC and EIC may have fed into the Norwegian Sea and consequently decreased the formation of the intermediate waters which contribute to NSDW. However, attention should be drawn to the fact that the lateral extent of the surface currents within the Nordic Seas (i.e. the EGC and NwAC) is very sensitive to atmospheric forcing. For instance, a more meridional circulation with strengthened northerlies over the Nordic Seas (equivalent to a negative NAO-like state), leads to a decrease in the eastward influence of the Arctic waters deriving from the EGC and a widening of the NwAC in the Norwegian Sea (Blindheim et al., 2000).

Several high-resolution reconstructions indicative of Neoglacial atmospheric circulation changes such as: storminess records based on dune development in Northern Ireland (Wilson et al., 2004) and peat bogs from Scandinavia (Jong et al., 2006, De Jong et al., 2009), precipitation reconstructions from lacustrine sediments from Sweden (Rosqvist et al., 2007), pollen reconstructions from the West Greenland and Newfoundland (Jessen et al., 2011) and alkenone-derived sea surface trends (Rimbu et al., 2003) all present consistent long term trends that are suggestive of a gradual Neoglacial transition towards a more meridional atmospheric circulation over the North Atlantic. Thus, following Blindheim et al. (2000), a Neoglacial atmospheric shift to a more meridional circulation over the Nordic Seas may have limited the ability of freshwater within the EGC to extend eastwards and influence the convection sites of NSDW. Nevertheless, the Neoglacial climate boundary conditions were not the same as today. On long timescales (multicentennial to millennial), it is possible that alterations to the

freshwater budget of the Nordic Seas may have overridden the effects of atmospheric forcing in the Norwegian Sea as described by Blindheim et al. (2000). A Neoglacial increase in the amount of Arctic freshwater being delivered to the Norwegian Seas would have probably inhibited intermediate water formation. A reduction in NSDW would have lowered the density and/or the reservoir height of the ISOW source waters driving a decrease in ISOW vigour, as shown in the RAPiD-17-5P $\overline{SS}$ near-bottom flow speed reconstruction from 1400 years BP onwards (Figure 5.11c). This hypothesis is in agreement with modelling studies which have predicted a reduction in the intermediate water formation feeding the Nordic Overflows as a response to the insolation driven sea ice production and export into the Nordic Seas during the Late Holocene (Renssen et al., 2006).

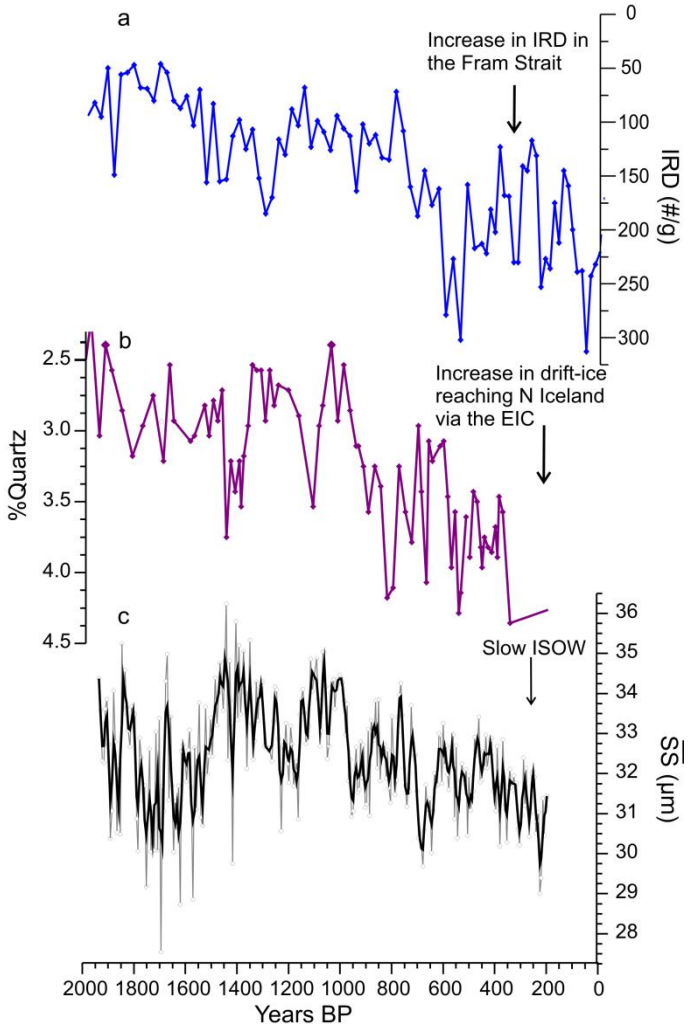

Figure 5.11. (a) Ice Rafted Debris (IRD) counts from Fram Strait (Werner et al., 2011), (b) % Quartz recorded from the North Icelandic shelf (Moros et al., 2006), (c) $\overline{ss}$ measurements from RAPiD-17-5P (this study).

5.4.1.2. Downstream mechanisms for the variability and evolution of the of Iceland Scotland Overflow vigour

The downstream entrainment of ISOW takes place primarily with SPMW in the Iceland Basin because of the shallower and broader ridge (compared to the Denmark Strait) and also because there is little variation in LSW thickness between strong/weak LSW formation in the far north of the Iceland Basin (Van Aken et al., 2011, Yashayaev et al., 2007). Therefore the temperatures of SPMW or the Atlantic waters of the NAC play a dominant role in entrainment processes. The potential co-variability of the density of the SPMW and the ISOW vigour, was explored using the NAC Mg/Ca-based temperature reconstructions from the Iceland Basin: a high resolution record from the same core (RAPiD-17-5P) which was presented in Chapter 4 (Figure 5.12b) and the lower resolution temperature record from Thornalley et al. (2009) (Figure 5.12c). A similar broad long term cooling from 1200 to 200 years BP, corresponding to a slower ISOW during colder NAC/SPMW is observed. However, if the downstream processes were the dominant control on the $\overline{SS}$ record, a better agreement between these two co-registered signals from the same core (RAPiD-17-5P) would clearly be expected. It can therefore concluded that the density of the SPMW/NAC waters was not the main cause for the variability of ISOW vigour recorded in the Iceland Basin.

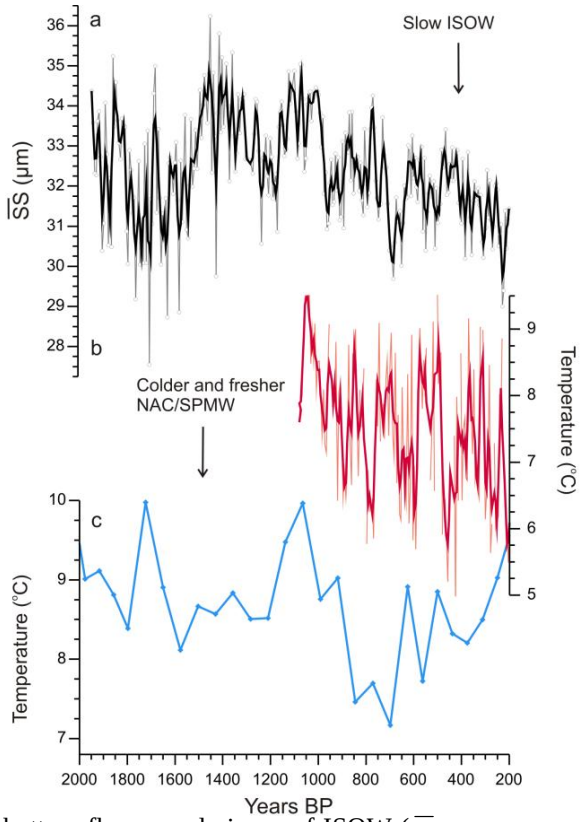

Figure 5.12. (a) Near-bottom flow speed vigour of ISOW ($\overline{ss}$ measurements from RAPiD-17-5P - this study). Temperature reconstructions of the NAC waters in the Iceland Basin from (b) RAPiD-17-5P (presented in Chapter 4) and (c) RAPiD-12-1K (Thornalley et al., 2009).

5.4.1.3. Downstream evolution of the ISOW vigour

RAPiD-17-5P is located very close to the GSR and it therefore monitors the hydraulically controlled transport of ISOW entering the Atlantic Basin. This signal is then further modified via downstream mixing processes that take place along the flow path of ISOW. In an attempt to study the Late Holocene downstream mixing processes of ISOW within the Iceland Basin, the $\overline{SS}$ record from RAPiD-17-5P (Figure 5.13a) is compared to a $\overline{SS}$ record from RAPiD-21-COM (Figure 5.13b) located in the Gardar Drift (~700 km downstream of RAPiD-17-5P) (see Figure 5.3 for location). The $\overline{SS}$ records from the two localities reveal no resemblance in their individual flow speed reconstructions of ISOW (Figure 5.13a,b). This finding is remarkable since it illustrates the regional variability that $\overline{SS}$ records can present as a result of the complexity of the processes that govern the density driven bottom flow speeds of the overflows.

The difference between these records should theoretically be indicative of the downstream modification in the ISOW vigour. The sortable silt datasets were normalised by subtracting the average of the whole record to each individual data point and dividing it by the standard deviation of the entire $\overline{SS}$ record. In Figure 5.13c the difference between the two normalised flow speed records is plotted, revealing a gradual trend towards increased speed at Gardar Drift in comparison to the Iceland Basin starting at 1400 years, perhaps as a response to an increase in the downstream mixing and/or the density gradient between ISOW and the overlying waters (which drives the geostrophic flow).

The strength of convection in the Labrador Sea determines the density and thickness of the LSW found at intermediate depths in the Iceland Basin and overlying the ISOW (Van Aken et al., 2011, Yashayaev, 2007b, Yashayaev et al., 2007). A gradual change in the strength of the LSW convection since 1400 years BP may have therefore affected the downstream ISOW vigour either by entrainment or by the density contrast between the two water masses. A comparison of the Late Holocene proxy reconstructions from the Labrador Sea and the downstream speed of ISOW (Figure 5.14) shows that a decrease in the inferred LSW formation corresponds to an increase in the difference in ISOW speeds between the two sites.

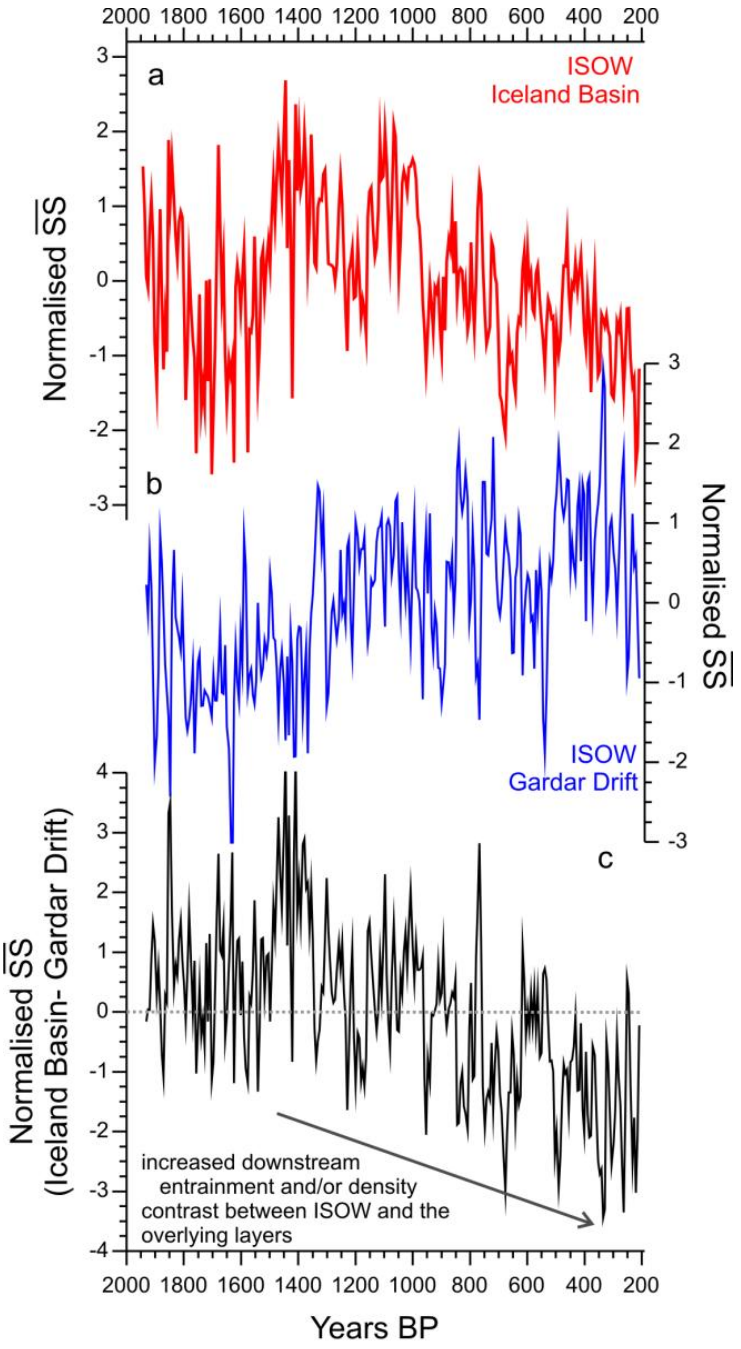

Figure 5.13. (a) $\overline{ss}$ measurements from RAPiD-17-5P in the Iceland Basin (this study), (b) $\overline{ss}$ measurements from Gardar Drift (RAPiD-21-COM - unpublished data, courtesy of I. Hall), (c) difference between the 6 year Gaussian smoothed normalised $\overline{ss}$ measurements from the Iceland Basin and the Gardar Drift.

The strong influence of the LSW hydrography on the ISOW vigour further downstream of the GSR has previously been shown in a subdecadally resolved $\overline{SS}$ record from the Gardar Drift for the last 230 years (Boessenkool et al., 2007). Additionally in this study, hydrographic transects of the Iceland Basin between a strong/weak LSW convection during positive/negative NAO in 1994 and 1960, respectively lend support to this

inverse relationship between the ISOW flow speed and LSW state. As suggested by Boessenkool et al. (2007) the dominance of the state of the LSW on the ISOW vigour at Gardar Drift can be explained as a consequence of changes in (i) the density of LSW (as that would affect the geostrophic flow of ISOW), (ii) the density gradient in the Iceland Basin and (iii) the density of LSW in the Labrador and Irminger Basins which would have increased hydrostatic pressure on ISOW, affecting its vigour.

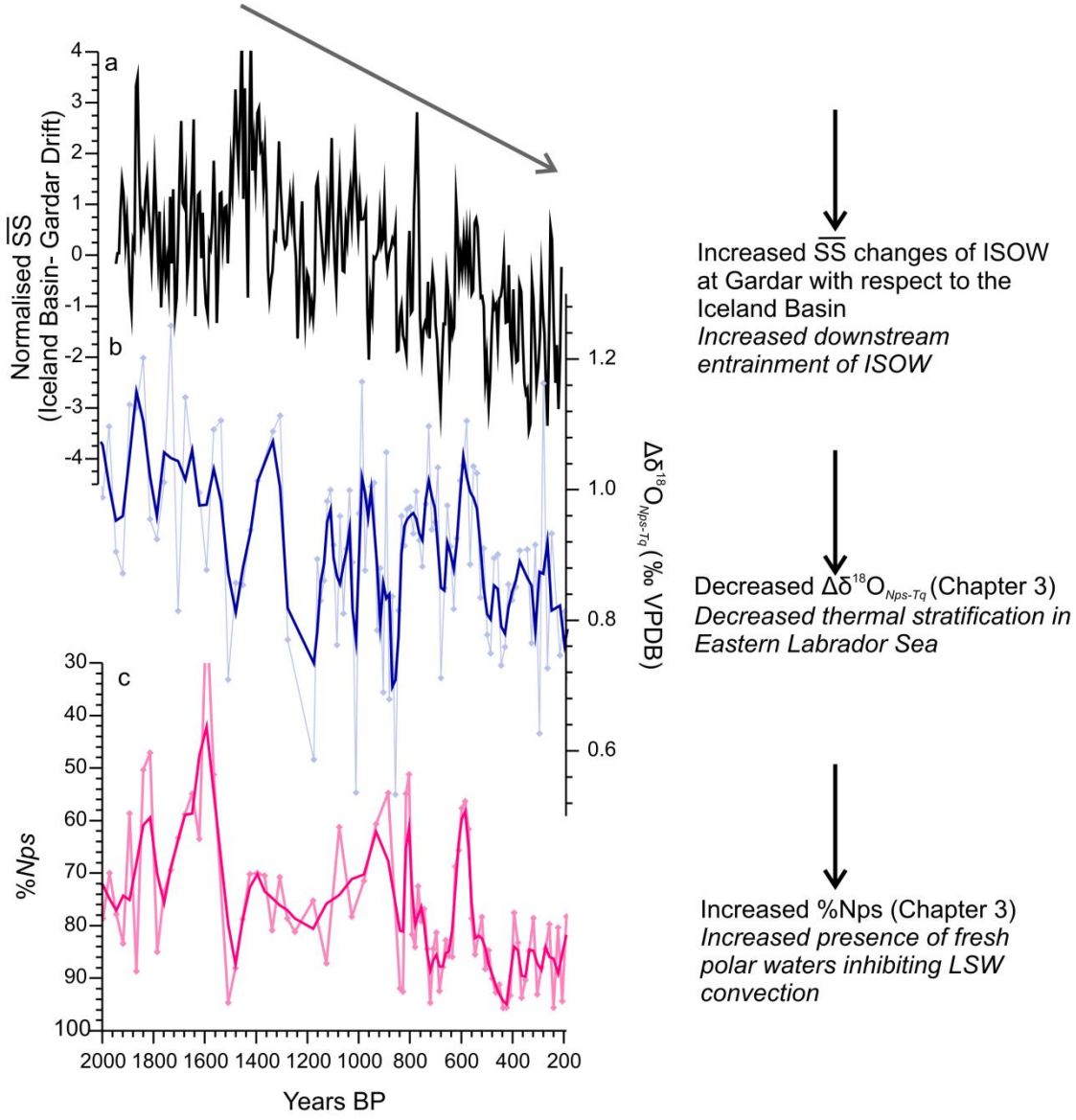

Figure 5.14. (a) Difference between the normalised $\overline{SS}$ measurements from the Iceland Basin and the Gardar Drift, (b) $\Delta\delta^{18}O_{Nps-Tq}$ and (c) *%Nps* from RAPiD-35-COM (presented in Chapter 3).

5.4.2. Late Holocene variability of the Denmark Strait Overflow vigour

5.4.2.1. Changes in the upstream source waters supplying DSOW: East Greenland Current versus North Icelandic Jet

The DSOW is formed by a complex and varied mixture of water masses deriving from the Arctic, intermediate waters formed in the Nordic Seas, re-circulating Atlantic waters and other minor water masses (Tanhua et al., 2005, Dickson et al., 2008 for a review) Consequently, the variability of DSOW vigour can arise from changes in the relative contribution of its source waters and/or in the hydrographic properties of these. For the last five decades many hydrographic and tracer studies have been undertaken to investigate the composition of DSOW, yet, it remains unclear as to which water masses are the primary contributors to DSOW. Some studies have suggested that the DSOW is exclusively supplied by the EGC, which comprises a mixture of re-circulating Atlantic waters (Atlantic waters that have suffered transformation and densification via heat loss in and around the Nordic Seas) and polar waters formed in the Arctic and/or in the Greenland Sea (Eldevik et al., 2009, Jeansson et al., 2008, Mauritzen, 1996, Rudels et al., 2002, Swift and Aagaard, 1981, Strass et al., 1993). Others have proposed intermediate waters formed in the Iceland Sea as a result of winter cooling as the dominant constituent of DSOW (Jonsson, 1999, Jonsson and Valdimarsson, 2004, Swift et al., 1980, Vage et al., 2011). These two contrasting proposed sources for the DSOW have often been referred to as Atlantic and Polar, respectively (Eldevik et al., 2009).

The $\overline{SS}$ record from RAPiD-35-COM presents a gradual trend towards higher near-bottom flow speeds of DSOW from ~2500 years BP to present (Figure 5.15a). Proxy records based on Ice Rafted Debris (IRD) counts, benthic foraminiferal assemblages and organic geochemistry along the East Greenland Slope show a consistent picture indicating a progressive increase in sea ice and colder EGC for the last 3000-4000 years (Figure 5.15b) (Andrews et al., 1997, Andersen et al., 2004, Jennings et al., 2002, Müller et al., 2012). A gradual increase in the southern influence of polar waters reaching North Iceland has also been suggested by an increase in terrigenous allochtonous quartz transported by drift ice by the EIC (Andrews, 2009, Moros et al., 2006) (Figure 5.15c). The increase in the southern advection of polar waters, suggests either a gradual eastern shift of the polar front and/or an increase in the southward transport of polar waters within the EGC throughout the Late Holocene. If we assume

the latter, a concomitant increase in the volume transport of the EGC and DSOW vigour (Figure 5.15a,b) would be in agreement with the concept of the EGC as a dominant water mass source of DSOW (e.g. Rudels et al., 2002). Moreover, bearing in mind the Neoglacial atmospheric circulation evolution (discussed in Section 5.4.1.1) it is unlikely that the increased presence of drift ice North of Iceland was the result of a south eastward shift of the polar front mainly as more meridional atmospheric circulation over the Nordic Seas would have led to a narrowing of the EGC and hence a westward shift in the polar front.

Deep ocean mooring studies have identified that the seasonal variability of the EGC upstream of the Denmark Strait differs from that found in DSOW (Jonsson, 1999, Jonsson and Valdimarsson, 2004). As initially suggested by Swift et al. (1980), recent evidence strongly supports the importance of intermediate waters formed by winter convection in the Iceland Sea as important contributors (~50%) to the DSOW transports (Vage et al., 2011). The recently discovered North Icelandic Jet (NIJ), is a narrow 15-20 km-wide barotropic jet that flows from the Iceland Sea to the Denmark Strait along the Iceland Slope beneath the Atlantic Inflow branch with a mean speed velocity of 40 cm/sec following the 600 m isobath (Jonsson and Valdimarsson, 2004). As demonstrated in model simulations, the transport and transformation of the warm salty waters from the North Iceland Irminger Current (NIIC) (a branch of the Atlantic Inflow, Figure 5.10) into the Iceland Basin, plays a critical role in the formation of the NIJ (Vage et al., 2011). However, Late Holocene reconstructions, based on foraminiferal and coccolithophore assemblages (Jennings et al., 2011, Ólafsdóttir et al., 2010, Giraudeau et al., 2004) show a decrease of the influence NIIC reaching North Iceland for the last 4000 years. This is further supported by alkenone and diatom-based temperature reconstructions from North Iceland (Bendle and Rosell-Mele, 2007, Sicre et al., 2008a, Jiang et al., 2002) (Figure 5.15d). Taking together this evidence, these studies consistently suggest a gradual increase in the influence of polar waters relative to Atlantic waters reaching the North Icelandic shelf for the last 3000 years. It is therefore difficult to reconcile that an increased influence of polar waters in the Iceland Sea would have promoted winter convection, especially since modelling studies have demonstrated the key role of the inflow of Atlantic waters in the preconditioning for open convection in the Iceland Sea (Vage et al., 2011).

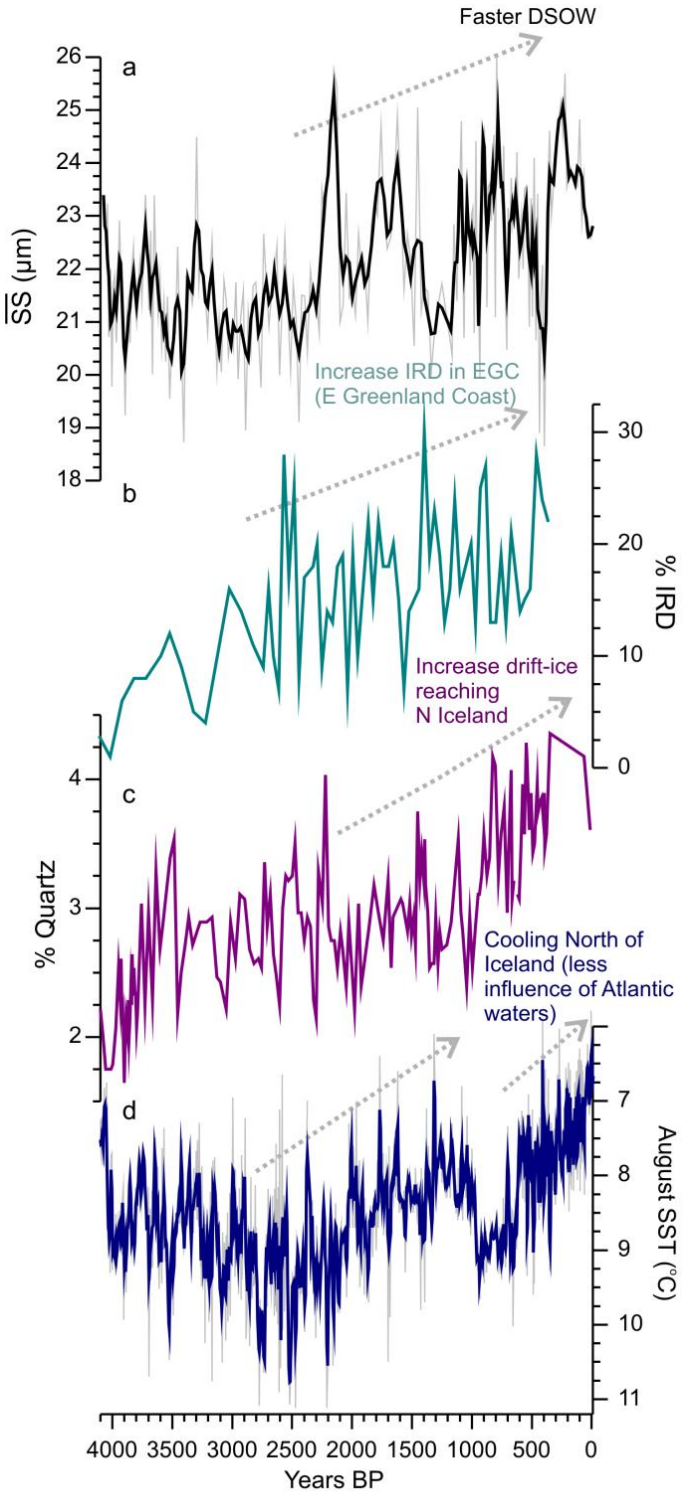

Figure 5.15. (a) Near-bottom flow speed vigour of DSOW ($\overline{SS}$ measurements from RAPiD-35-COM-this study) (b) % IRD from the East Greenland Coast (Jennings et al., 2002), % quartz from the North Icelandic shelf (Moros et al., 2006), alkenone-based August Sea Surface Temperatures (SST) from North Iceland (Sicre et al., 2008b, Sicre et al., 2008a). Arrows highlight the millennial-scale trends.

5.4.2.2. Potential effects of atmospheric forcing on the source waters supplying DSOW

The atmospheric regime over the Nordic Seas (which is mainly related to the NAO-state) also strongly affects the hydrographic conditions and inevitably the overflow formation (Blindheim et al., 2000). For instance, changes in atmospheric circulation can potentially modify the formation and transport of the overflow waters by changes in the regional windstress-curl (e.g. Biastoch et al., 2003, Kohl, 2010), the heat flux in the locations of deep convection (Dickson et al., 1996, Dickson et al., 2000) and the inflow of Atlantic warm waters into the Nordic Seas (Orvik and Skagseth, 2003, Blindheim et al., 2000).

Two competing theories for the effects of the atmospheric circulation on the source waters for DSOW have been proposed, each implicitly supporting one of the proposed source waters explored in the previous section. Modern observations have shown that a negative NAO-like state leads to strengthened northerlies (meridional circulation) which promotes the southward transport of polar waters within the EGC into the North Atlantic (Dickson et al., 1996). Therefore, the observed Late Holocene increase in sea-ice in the EGC (Andrews et al., 1997, Andersen et al., 2004, Jennings et al., 2002, Müller et al., 2012) may have plausibly resulted from the combined effects of stronger northerlies promoting enhanced transport of the EGC (as suggested by Dickson et al., 1996) and/or an increase in the production and transport of sea ice from the Arctic. Such changes in the EGC, may have affected the DSOW via an increase in southward transport of its source waters and an increase in the contribution of the upper deep polar waters within the EGC (Rudels et al., 2002).

Alternatively, modelling studies predict that a decrease in wind-stress curl around Iceland and the Nordic Seas (during a negative NAO state) leads to an increased supply of the overflow waters from the Iceland Sea (Kaese et al., 2009, Kohl, 2010). It is therefore possible that a Neoglacial transition towards a more a negative NAO-like atmospheric circulation over the Nordic Seas, potentially increased production and transport of waters from the Iceland Sea towards the Denmark Strait via an enhanced NIJ. Nonetheless, observational data shows that strengthening of the northerlies during a negative NAO-like state result in an increase leakage of EGC waters (Malmberg and Jonsson, 1997) and reduced influence of NIIC waters (Blindheim, 1968) reaching the

Iceland Sea. These modern oceanic processes appear to be consistent with the proxy records presented in Figure 3.15 and described in Section 5.4.2 that suggest that a Neoglacial atmospheric evolution towards more meridional circulation may have been accompanied by a decrease in the influence of NIIC versus EGC waters reaching the Iceland Sea (Figure 5.15). It is therefore somewhat difficult to reconcile a putative intensification in deep water formation within the Iceland Sea with an increase in the influence of polar versus Atlantic waters reaching the Iceland Sea as previously mentioned (Figure 5.15c,d).

From this analysis, it is concluded that an enhanced supply and/or density of the EGC waters to the DSOW is the most plausible explanation for the upstream changes that might have led to a Neoglacial increase in the DSOW vigour recorded in RAPiD-35-COM. It is hypothesised that the Arctic increase in sea ice formation and cover during the Neoglacial as a response to the decrease in summer insolation at high latitudes would have led to an increase in the formation of dense Arctic waters via brine rejection processes. Furthermore, the Neoglacial transition towards a strengthened meridional circulation would have enhanced the southward transport of the EGC waters. Nevertheless, the mechanism remains equivocal and has yet to be observed in the modern. Alternatively, the increase in the vigour of DSOW may have instead been caused by downstream processes.

5.4.2.3. Downstream entrainment processes of DSOW

The overflows are also driven by the cross-sill density gradient. Consequently, past changes in the density of the downstream water masses such as SPMW but mostly LSW would have affected the vigour of DSOW. Hydrographic transects show that, during periods of reduced (enhanced) LSW formation, the density and volume of this water mass in the Irminger Basin is thus decreased (increased) (Yashayaev, 2007b). A comparison of the millennial-scale variability of the surface conditions in the Eastern Labrador Sea (presented in Chapter 3 and obtained from the same core RAPiD-35-COM) highlight a millennial-scale reduction in the formation of LSW (Figure 5.16c,d) which was accompanied by a cooling of the IC perhaps indicating (as interpreted in Chapter 4) a weakening in the SPG circulation (Figure 5.16b) during the last 2250-3000 years BP. This trend is similar to the one recorded in the DSOW vigour towards higher

speeds. Such a coeval relationship is consistent with a Late Holocene decrease in LSW formation (and hence density) leading to an increase in the cross- ridge density gradient, thereby driving a faster transport of DSOW into the Atlantic Basin, which in turn would also promote entrainment and therefore a greater volume of DSOW. Similarities in the long-term trends between these co-registered surface and deep records from 2500 years BP onwards (Figure 5.16a-c), suggests that millennial-scale variability in the transport of dense waters through the Denmark Strait into the North Atlantic was potentially governed by the state and therefore density of the LSW.

Moreover, this finding may partly be in agreement with observational data (Dickson et al., 1996) that have suggested the presence of an antiphased 'see-saw' of deep water formation between the convection centres of the Labrador and Greenland Sea. The relationship has been explained to occur through the opposing impacts of atmospheric circulation in each of the convective centres (Dickson et al., 1996). This seminal work by Dickson et al. (1996) concluded that during a positive NAO-like state the strengthening of the westerlies (more zonal atmospheric circulation) over the North Atlantic promoted heat loss and deep convection in the Labrador Sea. Conversely, during a negative NAO state the enhanced northerlies (more meridional atmospheric circulation) aided the delivery of polar waters via the EGC into the SPG, thereby inhibiting convection in the Labrador Sea but enhancing it in the Greenland Sea. However, during the Neoglacial, proxy work from the Fram Strait has suggested an expansion of the sea ice into the Greenland Sea (Müller et al., 2012, Werner et al., 2011), which means that freshwater forcing deriving from an increase in Arctic sea ice export might have been a more dominant control (compared to atmospheric forcing) on convection in the Greenland Sea.

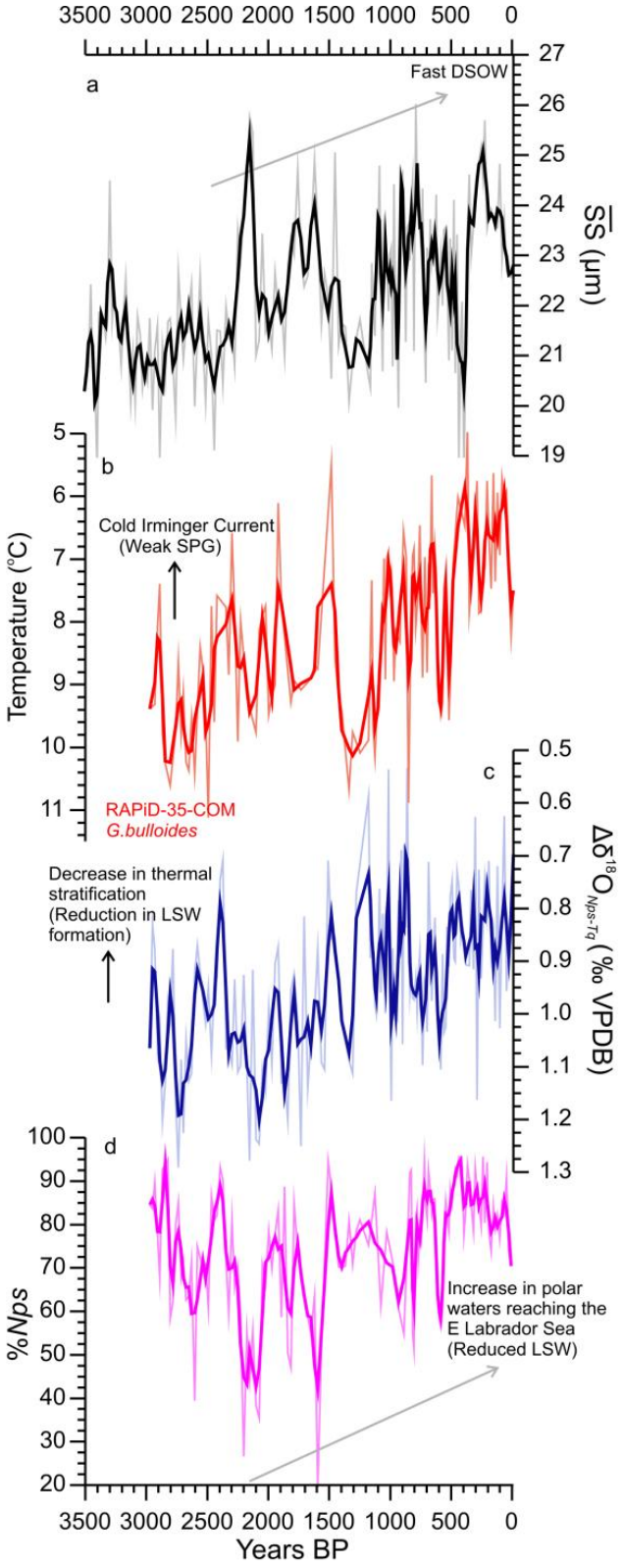

Figure 5.16. a) Near-bottom flow speed vigour of DSOW ($\overline{SS}$ measurements from RAPiD-35-COM-this study), (b) *G.bulloides* Mg/Ca-based temperature from the Irminger Current (presented in Section 3.4.2.4), (c) $\Delta\delta^{18}O_{Nps\text{-}Tq}$ and (d) %*Nps* from RAPiD-35-COM (Chapter 3).

5.4.2.4. Summary of DSOW flow variability and further work

As illustrated above, our current knowledge on the causes of the transport variability of DSOW is still very limited, an issue which complicates our interpretation of the near-bottom flow speed of DSOW in the past. From the options outlined above it is hard to discern which one was the dominant mechanism in governing this millennial trend towards an increased vigour of DSOW that started at ~2500 years BP. From the evidence presented in the last few sections, it is concluded that upstream changes in the transport and constituents of the EGC and/or a reduction in the LSW formation were the most likely candidates for the Late Holocene strengthening of DSOW. The proposed changes in the Neoglacial ocean conditions were chiefly governed by the insolation driven atmospheric re-organisation and high latitude sea ice production.

5.4.3. Coupling in the vigour of the Nordic Overflows

The relationship between the vigour of ISOW and DSOW is yet to be fully established. Modelling studies have repeatedly proposed an antiphasing behaviour in the transport between these overflows over the GSR caused by the differing effects of atmospheric forcing on the deep water formation at different convection sites in the Nordic Seas which supply the overflows. However, recent baroclinic calculations based on hydrographic sections for the last 30 years have revealed in-phase multidecadal variability of the modified ISOW and DSOW reaching Cape Farewell, which furthermore seem to be negatively correlated to the thickness and therefore convection strength of LSW.

In Section 5.4.2 two alternative processes were proposed to explain the recorded variability of the DSOW vigour: (i) an upstream mechanism influenced by the density of the source waters and (ii) a downstream mechanism dependent on the LSW state (see Figure 3.20 for a summary diagram). Assuming that the $\overline{SS}$ record from RAPiD-35-COM contains an upstream signal, then comparison between ISOW (Iceland Basin) and DSOW (Eirik Ridge) can test the relationship of the overflows which is set by ocean-atmospheric processes north of the GSR. Alternatively, if we assume that RAPiD-35-COM $\overline{SS}$ is mostly governed by downstream processes, similar to the downstream ISOW signal from Gardar Drift then according to modern observations (Sarafanov et

al., 2009) an in-phase relationship of the modified overflows strength (RAPiD-21-COM and RAPiD-35-COM) might be expected.

A comparison of the normalised $\overline{SS}$ records from ISOW (RAPiD-17-5P) and DSOW (RAPiD-35-COM) tentatively suggests millennial-scale anti-phased behaviour in the vigour of the overflows east and west of Iceland (Figure 3.17). Although it is not possible to investigate the potential compensation in the cross-ridge transport of the overflows caused by this antiphasing (particularly since there is no universal calibration for $\overline{SS}$ with flow speed) these results are in close agreement with a number of modelling studies. It was initially suggested that an increase in wind-stress curl North of Iceland steers the circulation of waters to the west of Iceland enhancing DSOW transport while decreasing the outflow through the Faroe Bank Channel (Biastoch et al., 2003). However, recent modelling studies propose that this anti-correlated behaviour of the overflows stems from a switch between different source water masses supplying the overflows as a response to wind-stress curl changes around Iceland and in the Nordic Seas (which is closely dependent on the NAO state) (Kohl, 2010, Serra et al., 2010) (Figure 3.18). The mechanism invoking the re-direction of the surface waters east and west of Iceland via wind-stress forcing is probably of more relevance to DSOW variability on annual to shorter time-scales whereas upstream changes in the site of overflow formation are more likely the causes for longer time-scale variability (Kohl et al., 2007). Nonetheless, this relationship has not yet been clearly observed in the instrumental record. The weakening and strengthening of DSOW (Macrander et al., 2005) and ISOW (Hansen and Osterhus, 2007), respectively in 2000 has been used as evidence for this relationship (Kohl et al., 2007). Other authors have been more hesitant about this statement and still hold that there is no convincing observational evidence for this co-variance of the overflows (Dickson et al., 2008).

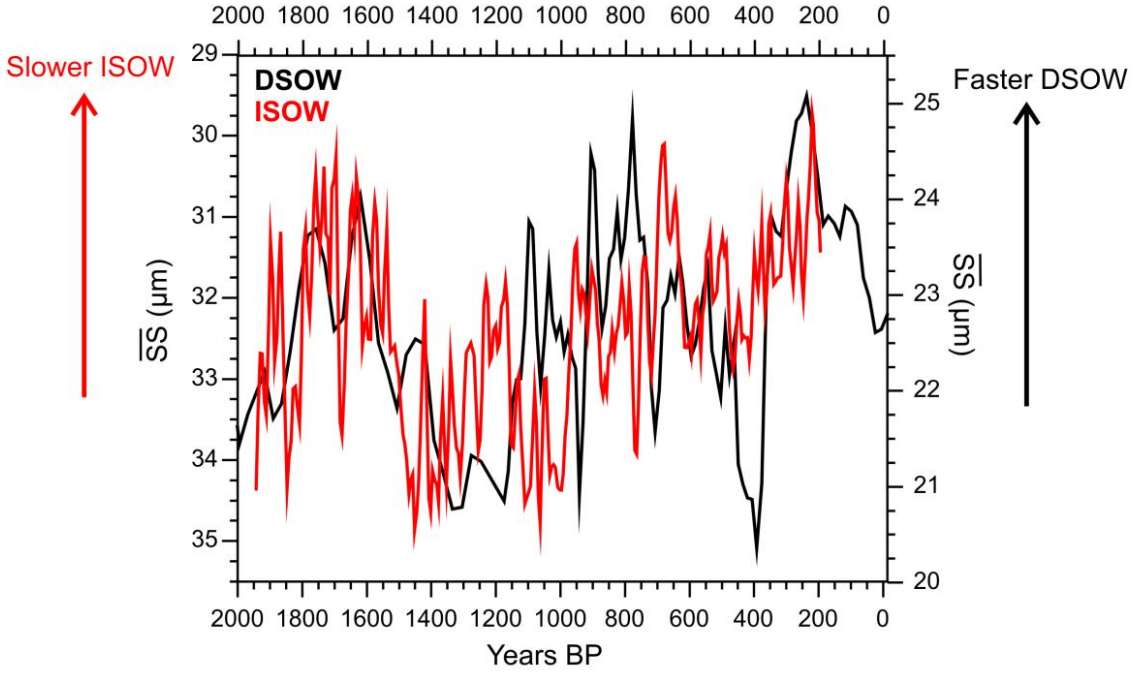

Figure 5.17. Comparison between the $\overline{ss}$ from DSOW (RAPiD-35-COM) and ISOW (RAPiD-17-5P) in black and red respectively, for the last 2000 years.

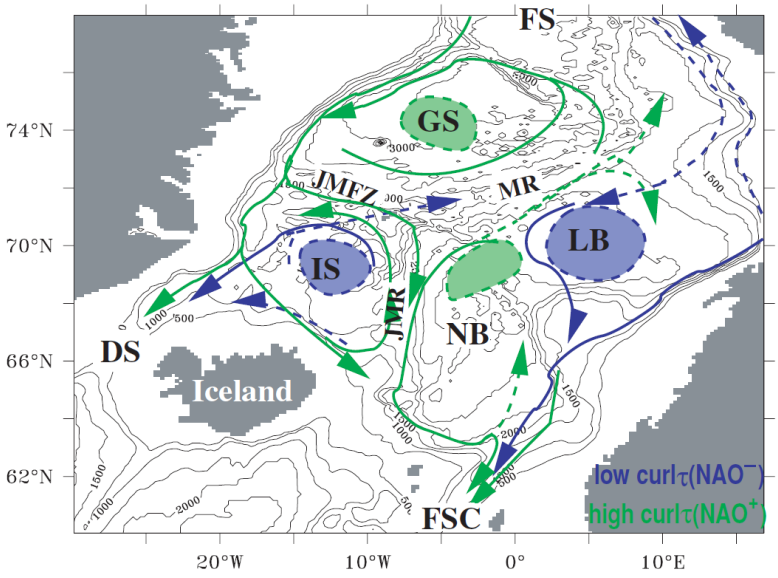

Figure 5.18. Schematic map of the circulation of waters supplying the DSOW (DS) and ISOW (FSC) overflows during high (green) and low (blue) wind stress curl around Iceland, which is related to a positive and a negative NAO-like state (Kohl, 2010). The coloured shaded areas indicate larger pools of water that potentially contribute to the overflows. The four major basins are the Lofoten Basin (LB) and the Norwegian Basin (NB) in the east and the Greenland Sea (GS) and the Iceland Sea (IS) in the west separated by the Mohn Ridge (MR) which continues to the south as Jan Mayen Ridge (JMR). Dashed lines indicate pathways of overflow water mass types that contribute only indirectly (e.g. through enhancing reservoirs) to the overflows.

Instead, if the $\overline{SS}$ record from RAPiD-35-COM contained a downstream signal then according to Sarafanov (2009), the strength of modified DSOW and modified ISOW should present an in-phase relationship. Comparison of the $\overline{SS}$ records from Cape Farewell (RAPiD-35-COM) and Gardar Drift (RAPiD-21-COM) does not show a clear in-phase relationship of the strength of the modified overflows as suggested by the hydrographic studies obtained from Cape Farewell (Sarafanov et al., 2009).

5.5. Summary and Conclusions

In this study, we present two high-resolution Late Holocene near-bottom flow speed reconstructions using the $\overline{SS}$ proxy from two sediment cores located in the pathway of the two Nordic Overflows. The results reveal that the vigour of the Nordic Overflows has been highly variable at multidecadal to centennial time-scales during the Late Holocene, as well as indicating Late Holocene millennial-scale trends towards an increase and decrease of the DSOW and ISOW vigour, respectively.

Following the hydraulic laws that control the transport of the overflow waters across the GSR, several mechanisms were explored in order to explain the recorded millennial scale variability in the vigour of the overflows. The mechanisms examined comprised: the study of upstream changes in the sources and production of water masses supplying the overflow and/or the density from the downstream water masses.

The ISOW is mainly supplied by the NDSW a water mass that is chiefly formed as a result of the transformation of NwAC via heat loss. The study of the surface conditions from proxy data in the Norwegian Sea does not show a consistent picture. According to current observations an increase in Atlantic water influence in the Norwegian Sea should be expected from the Neoglacial atmospheric trend towards a negative NAO-like state. However atmospheric forcing of the Norwegian Sea surface hydrography might have played a minor role compared to the insolation driven increase in Arctic sea-ice production and export which has been recorded in the Eastern Greenland Margin and the Iceland Sea. This scenario would have led to a reduction in convection at this site and a subsequent slowdown of ISOW as shown in the $\overline{SS}$ record.

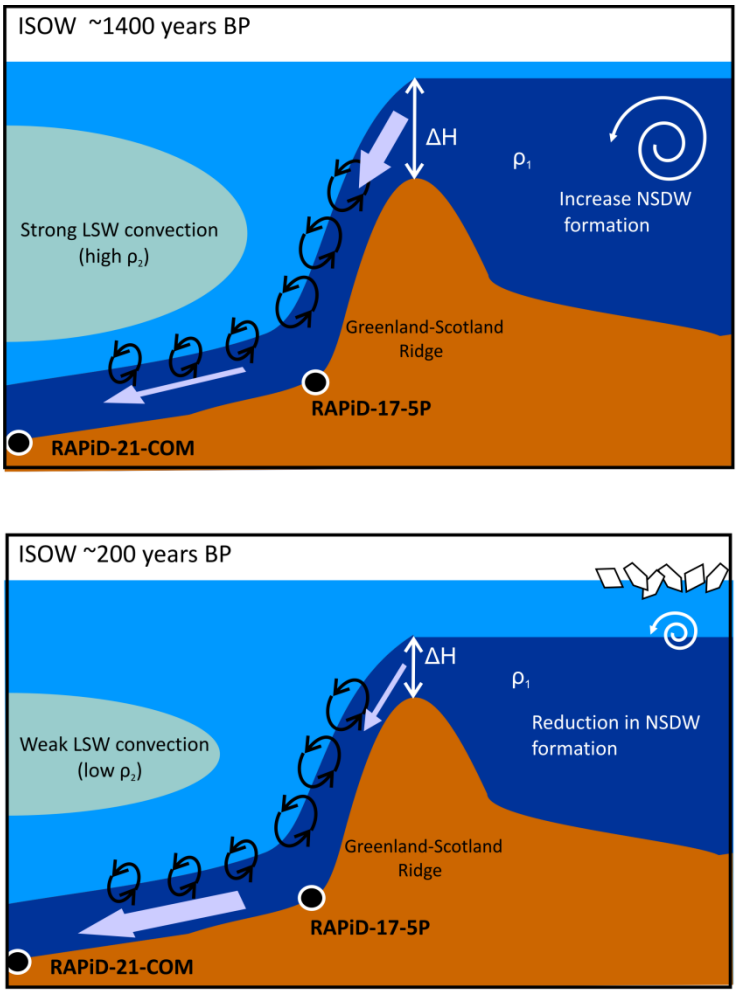

Figure 5.19. Simplified diagram of the interpretation of the ISOW dynamics as inferred from the SS measurements from RAPiD-17-5P and RAPiD-21-COM between 1400-200 years BP. Top diagram- Around 1400 years BP increased NSDW formation in the Norwegian Sea enhanced the transport of ISOW to the Iceland Basin (RAPiD-17-5P). The presence of expanded and dense LSW in the Iceland Basin most likely reduced the transport between RAPiD-17-5P and RAPiD-21-COM. Bottom diagram - Around 200 years AD the alteration of the freshwater budget in the Nordic Seas by the increase in Arctic sea-ice and freshwater export reduced formation of NSDW and therefore a decrease in the ISOW vigour reaching RAPiD-17-5P. However, a concomitant reduction in LSW formation led to an increase in the vigour of ISOW between RAPiD-17-5P and RAPiD-21-COM.

The downstream evolution of the ISOW vigour in the Iceland Basin was studied using a novel approach which consisted of studying the difference in flow speed records from two cores located at different distances downstream of the GSR (one located ~700 km downstream of the other). The results of this comparison revealed an increase in the downstream vigour of the ISOW in the Iceland Basin for the last 1500 years, not recorded in the site closest to the ridge. This could have either resulted from an increase in the density contrast between ISOW and the overlying waters and/or an increase in the

downstream mixing of ISOW, probably related to the decrease in the LSW formation during the Late Holocene. This finding highlights the important role of the LSW in the modification of ISOW flow and consequently the lower limb of the AMOC.

Careful investigation of the upstream source waters of DSOW has led to the conclusion that the most plausible mechanism for the Late Holocene increase in DSOW vigour was an insolation-driven atmospheric and Arctic freshwater budget re-organisation that increased the density and/or production of the waters within the EGC. Additionally, we find a concomitant increase in DSOW bottom flow speeds with a reduction in LSW convection. A decrease in the density of the LSW in the Irminger Basin would have increased the cross-ridge density gradient promoting the overflow transport.

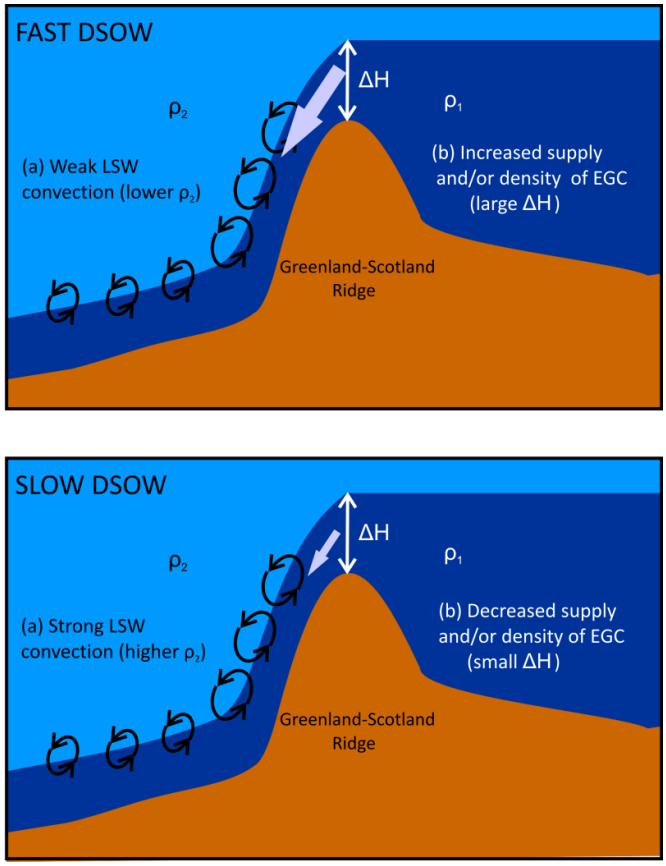

Figure 5.20. Schematic cartoon of the possible downstream (a) and upstream (b) mechanisms by which a fast versus slow DSOW as recorded in $\overline{SS}$ from RAPiD-35-COM and interpreted in this Chapter may be explained.

Comparison of the near-bottom flow speeds from ISOW and DSOW for the Late Holocene, shows a potential inverse relationship of the cross-ridge overflow strength east and west of Iceland at millennial time-scales. According to modelling experiments this is perhaps a product of long-term switches between sources supplying the overflows governed by atmospheric changes (such as NAO-like patterns). However, it is not possible to quantify the temporal changes in the volume transport of ISOW and DSOW on the two records alone (particularly since there is no universal calibration for $\overline{SS}$ with flow speed). Therefore the potential compensation in the cross-ridge transport of the overflows caused by a possible antiphasing cannot be investigated.

6. Conclusions and Further Work

6.1. Surface Ocean Changes in the Eastern Labrador Sea During the Last 3000 years

Model and observational studies have shown that buoyancy and wind stress forcing can severely impact winter convection in the Labrador Sea with consequences for the AMOC and climate. The results presented in this thesis, based on upper water column reconstructions from multi-species planktonic foraminifera $\delta^{18}O$, Mg/Ca and %*Nps*, record centennial to millennial variability in the influence of polar waters reaching the Labrador Sea for the past 3000 years. The recorded incursions of low-salinity polar waters are interpreted in terms of their potential effects on deep water convection in the Labrador Sea.

At the MCA-LIA transition (~1400 years AD), a strengthening of the northerlies is likely to have promoted the southward transport of freshwater within the EGC into the Eastern Labrador Sea as indicated by the increase in %*Nps* and the inferred sea surface cooling of 2-3^{o}C from $\delta^{18}O$ of *T. quinqueloba*. A concomitant increase in the influence of polar waters reaching the LSW and a weakening of the westerlies in response to a shift towards a prevalent negative-NAO state most likely led to a reduction in LSW formation. The trigger for the atmospheric shift at the onset of the LIA remains equivocal but was probably a consequence of internal atmospheric feedback mechanisms or teleconnections arising from an increase in the frequency and magnitude of solar minima and/or explosive volcanism during the LIA.

An extension of the surface ocean reconstructions over the last 3000 years, demonstrates centennial-scale oscillations in the incursions of polar waters reaching the Labrador Sea at 0-500, 1000-1250 and 2200-3000 years BP, with periods of relative warm surface conditions (less influence of polar waters) from 600-900 and 1500-2200 years BP. The timing of these events corresponds to periods of globally recognised climatic oscillations, which were mainly centred in the North Atlantic region. Since the centennial-scale cold events are synchronous with periods of low TSI, similar external forcings and oceanic-atmospheric responses to that of the onset of the LIA are proposed. However, the Late Holocene relationship between the ocean and atmospheric changes is

slightly more unclear mainly as a consequence of the limited high resolution atmospheric and ocean reconstructions presently available.

The millennial-scale variability in the surface ocean conditions of the Eastern Labrador Sea reveals a cooling trend from 2200 years BP to the present. The combined effects of a Neoglacial insolation-driven increase in Arctic sea ice production and gradual shift towards a more meridional atmospheric circulation may have increased the southward transport of polar waters resulting in a potential reduction in LSW formation.

6.2. Hydrographic Changes in the Atlantic Inflow During the Last Millennium

Temperature and salinity reconstructions of the Atlantic Inflow based on paired Mg/Ca and $\delta^{18}O$ measurements on the near-thermocline planktonic foraminifera *G. inflata* show centennial oscillations of 3.5^{o}C and 1.5 psu during the last millennium. The temperature variability shows a positive correlation with TSI (Pearson T= 0.48). Marked shifts towards colder and fresher conditions of the NAC correspond to periods of solar minima. This relationship is further supported by the presence of 200 year cycles within the temperature record, which is similar to the 210-year deVries solar cycles.

In the past, modelling studies based on observational data from the Iceland Basin have suggested that temperature but particularly salinity changes in the Atlantic Inflow predominantly arise from the relative contribution of waters from the STG or SPG governed by the changes in the strength and spatial extent of the SPG. This mechanism is explored by comparing the hydrographic variability of the NAC with the surface conditions in the Labrador Sea inferred to represent changes in LSW convection but no similarities are observed. This suggests that SPG dynamics was not the dominant mechanism for the hydrographic changes found in the NAC during the last millennium.

Modelling experiments as part of a collaborative project have shown significant positive correlation between TSI and surface temperature and salinities in the Iceland and Irminger Basins during the last millennium. This is consistent with the hydrographic proxy reconstructions of the NAC and the IC during the last millennium, presented in this thesis. A positive relationship is also found between TSI and volume transport of the SPG with periods of solar minima corresponding to weakening of the SPG. Winter SLP analyses in the model reveal the presence of atmospheric blocking patterns in the

Eastern North Atlantic during periods of solar minima which is supported by a number of observational studies. Atmospheric blocking would have caused diversion of the westerlies and reduction of the wind-stress curl over the eastern part of the SPG which would have initially weakened the Eastern SPG and then propagated around the gyre by other feedback mechanisms.

6.3. Changes in the Temperature and Salinity of the Irminger Current

The ecological preferences for particular hydrographic conditions of *G. bulloides* are used to explore the temperature and salinity of the IC reaching the Labrador Sea from paired $\delta^{18}O$ and Mg/Ca measurements.

The temperature of the IC reveals a shift towards colder temperatures at the onset of the LIA. The temperature reconstruction of this branch of the NAC shows multicentennial similarities with the subdecadally resolved reconstruction of the NAC confirming that it is monitoring the IC and therefore consistent with the mechanism summarized in 6.2
A gradual temperature decrease in the IC of ~4^{o}C for the last 3000 years has been recorded. The Neoglacial cooling trend is consistent with temperature records in other NAC branches. Assuming the temperature of the NAC waters is indicative of the heat transport and hence SPG strength (as proposed in Chapter 4 from the modelling studies), the cooling of the IC for the last 3000 years may be suggestive of a weakening of the SPG perhaps driven by the inferred reduction in LSW. However there are other possibilities that could also explain this cooling such as severe cooling of the NAC due to air-sea exchange and/or an increase in the winter SPMW formation south of Iceland.

6.4. Late Holocene Changes in the Vigour of the Nordic Overflows

Sortable silt mean grain size measurements on two sediment cores that lie in the pathway of ISOW and DSOW reveal significant variability in the vigour of the Nordic Overflows at multidecadal to millennial time-scales during the Late Holocene.

A decline in northern summer insolation and a transition towards a more meridional atmospheric circulation during the Neoglacial, probably led to an increase in the production and southward export of sea ice and freshwater from the Arctic into the

Nordic Seas. The gradual alteration of the freshwater budget of the Nordic Seas possibly reduced the open ocean convection in the Norwegian Sea, which led to a slowdown of ISOW as recorded from the $\overline{SS}$ measurements from the Iceland Basin from 1400 years BP onwards. However, ISOW vigour reconstructions from a site ~700 km further downstream records an increase in flow speed of ISOW from ~1400 years BP. The difference between the two $\overline{SS}$ records (closer and further downstream of the GSR) highlights the importance of downstream processes in the modification of the overflow vigour. Downstream processes are mainly affected by the density of the overlying waters in the Iceland Basin, which is mainly dominated by the properties and therefore the strength of LSW convection. A Neoglacial reduction in the deep water convection in the Labrador Sea (as inferred from the surface proxy reconstructions from the Eastern Labrador Sea) would have decreased the density of the intermediate water masses extending into the Iceland and Atlantic Basins. The reduction in LSW formation could have modified the ISOW transport by (i) the increase in the density contrast between the overflow and overlying waters, (ii) the larger horizontal density gradient in the Iceland Basin and/or (iii) the decrease in hydrostatic pressure from the overlying waters.

DSOW near-bottom flow speed records present an increase in the amplitude of the variability towards predominant higher flow speeds starting at ~2500 years BP. The millennial-scale changes in the vigour of this overflow can be explained by two different mechanisms involving upstream and/or downstream processes. The EGC has been proposed to be one of the main sources supplying DSOW. During the Neoglacial proxy records have recorded an increase in the southward transport of drift ice within the EGC. An insolation-driven Neoglacial increase in Arctic sea ice production would have promoted the formation of dense polar waters by brine rejection processes eventually feeding into the EGC. In addition, strengthening of the northerlies might have also enhanced the southward transport of the EGC through the Denmark Strait, perhaps also affecting the DSOW. Alternatively, an inferred Neoglacial decrease in open winter convection in the Labrador Sea from the freshwater forcing deriving from the Arctic would have resulted in a decrease in the density of the intermediate waters in the Irminger Basin, chiefly LSW. This would have increased the cross-ridge density gradient promoting DSOW transport over the GSR during the Neoglacial.

The near bottom flow speed records from ISOW (Iceland Basin) and DSOW (Cape Farewell) show a weak antiphased relationship between the vigour of the overflows. This antiphasing has been proposed numerous times from models as being a consequence of the differing effects of wind-stress forcing on the deep water formation sites in the Nordic Seas or surface steering of the overflow waters.

6.5. Summary of Findings

	Eastern Labrador Sea		**Iceland Basin**		**Cape Farewell**
	Surface summer Restratification %*Nps*, $\delta^{18}O_{Tq}$ and $\Delta\delta^{18}O_{Tq\text{-}Nps}$	**Irminger Current T/S** Mg/Ca and $\delta^{18}O$ *G. bulloides*	**North Atlantic Current T/S** Mg/Ca and $\delta^{18}O$ *G. inflata*	**ISOW vigour** $\overline{SS}$	**DSOW vigour** $\overline{SS}$
Multidecadal to centennial ocean variability	Not present	Not present	200 year cyclicities potentially linked to changes in solar irradiance	Potential 40-60 year cyclicities	400-500 and 177 year cyclicities
MCA-LIA transition	Marked MCA-LIA transition towards increase in cold polar waters	Transition from cold/fresh to salty/warm IC at the onset of the LIA	Not present	Not present	Not present
Late Holocene centennial climatic oscillations (e.g. cold events such as LIA, DACP, 2.7 kyrs)	Shifts to more polar waters reaching the E Labrador Sea during the abrupt climate cold events	Not present	Not applicable	Not present	Not present
Neoglacial	Cooling trend (decrease in thermal stratification and increase in polar waters)	Cooling for the last 3000 years	Gradual cooling over the last ~1200 years	Slowing down for the last ~1400 years BP	Increase in the vigour for the last ~2500 years

Table 6.1. Summary of the findings presented in this thesis are subdivided into location and water masses (columns) and climate intervals and oscillations (rows).

6.6. Further Work

Having proven in this study the value of these marine sediment cores for high-resolution palaeoceanographic reconstructions, the obvious future work would be to either extend these records back in time to cover the entire Holocene at this highest resolution or to get snapshots of the ocean changes at particular intervals of interest such as the Holocene Climatic Optimum, the 8.2 kyr event, the Early Holocene or even the last interglacial. The aim should be firstly to either prove or disprove some of the hypotheses and relationships presented here and secondly to gain further insight into the variability of these water masses at different time-scales.

In this study, a suite of proxy reconstructions of some key AMOC water masses have shown highly dynamic ocean variability at multidecadal to millennial time-scales during the past 3000 years. Some of these ocean changes are coincident with climatic oscillations recorded in the North Atlantic region. However, it is difficult to ascertain if these ocean-climate events were associated with changes in the strength of the AMOC as no consistent variability especially within the water masses that supply the deep limb of the AMOC has been found. It is of paramount importance to complement all of the data presented in this thesis with a modelling component since this will be the only way to quantify the possible changes in the strength of the AMOC and to test the proposed driving mechanism for the ocean changes presented here.

Additional proxy work will enable validation of the hypothesis and mechanisms highlighted during this study. For example, IRD counts on RAPiD-35-COM would enable to relate the temperature changes recorded in the surface of the Labrador Sea to an increase in drift ice being transported by the EGC and reaching the Labrador Sea,

Further developments on the DSOW vigour work could include analysing $\overline{SS}$ in additional cores. A common assumption for single-site $\overline{SS}$ reconstructions is that the site lay in the core of the deep current during the time-period studied. In order to improve our confidence in the interpretation of the $\overline{SS}$ record from RAPiD-35-COM and to monitor past vertical and horizontal migrations of the overflow plume, additional $\overline{SS}$ records should be produced along a depth-transect from the Eirik Ridge. Future work could also comprise a series of depth transects on the Greenland Slope between the Denmark Strait and Cape Farewell to enable the study of the downstream modification

of DSOW which would help elucidate the cause for the change in its vigour presented here. Additionally, the millennial variability in the $\overline{SS}$ reconstructions of the two overflows could be further strengthened by trace metal or stable isotope analysis in benthic forminifera from the same cores.

References

AAGAARD, K. & CARMACK, E. C. 1989. The Role of Sea Ice and Other Fresh Water in the Arctic Circulation. *Journal of Geophysical Research,* 94, 14485-14498.

AAGAARD, K. & COACHMAN, L. K. 1968. EAST GREENLAND CURRENT NORTH OF DENMARK STRAIT .2. *Arctic,* 21, 267-&.

AMMANN, C. M., JOOS, F., SCHIMEL, D. S., OTTO-BLIESNER, B. L. & TOMAS, R. A. 2007. Solar influence on climate during the past millennium: Results from transient simulations with the NCAR Climate System Model. *Proceedings of the National Academy of Sciences of the United States of America,* 104, 3713-3718.

ANAND, P., ELDERFIELD, H. & CONTE, M. H. 2003. Calibration of Mg/Ca thermometry in planktonic foraminifera from a sediment trap time series. *Paleoceanography,* 18, 1050.

ANDERSEN, C., KOÇ, N., JENNINGS, A. & ANDREWS, J. T. 2004. Nonuniform response of the major surface currents in the Nordic Seas to insolation forcing: Implications for the Holocene climate variability. *Paleoceanography,* 19, PA2003.

ANDERSSON, C., RISEBROBAKKEN, B., JANSEN, E. & DAHL, S. O. 2003. Late Holocene surface ocean conditions of the Norwegian Sea (Vøring Plateau). *Paleoceanography,* 18, 22-1.

ANDREWS, J. T. 2009. Seeking a Holocene drift ice proxy: Non-clay mineral variations from the SW to N-central Iceland shelf: Trends, regime shifts, and periodicities. *Journal of Quaternary Science,* 24, 664-676.

ANDREWS, J. T., SMITH, L. M., PRESTON, R., COOPER, T. & JENNINGS, A. E. 1997. Spatial and temporal patterns of iceberg rafting (IRD) along the East Greenland margin, ca. 68°N, over the last 14 cal.ka. *Journal of Quaternary Science,* 12, 1-13.

APPLEBY, P. G. & OLDFIELD, F. 1978. The calculation of lead-210 dates assuming a constant rate of supply of unsupported 210Pb to the sediment. *CATENA,* 5, 1-8.

ARBUSZEWSKI, J., DEMENOCAL, P., KAPLAN, A. & FARMER, E. C. 2010. On the fidelity of shell-derived δ^{18}Oseawater estimates. *Earth and Planetary Science Letters,* 300, 185-196.

BACON, S. 1998. Decadal variability in the outflow from the Nordic seas to the deep Atlantic Ocean. *Nature,* 394, 871-874.

BACON, S., GOULD, W. J. & JIA, Y. 2003. Open-ocean convection in the Irminger Sea. *Geophysical Research Letters,* 30, 50-1.

BACON, S., REVERDIN, G., RIGOR, I. G. & SNAITH, H. M. 2002. A freshwater jet on the East Greenland shelf. *Journal of Geophysical Research,* 107, 5-1.

BACON, S. & SAUNDERS, P. M. 2009. The Deep Western Boundary Current at Cape Farewell: Results from a Moored Current Meter Array. *Journal of Physical Oceanography,* 40, 815-829.

BAKKE, J., DAHL, S. O., PAASCHE, Ø., RIIS SIMONSEN, J., KVISVIK, B., BAKKE, K. & NESJE, A. 2010. A complete record of Holocene glacier variability at Austre Okstindbreen, northern Norway: an integrated approach. *Quaternary Science Reviews,* 29, 1246-1262.

BARD, E., RAISBECK, G., YIOU, F. & JOUZEL, J. 2000. Solar irradiance during the last 1200 years based on cosmogenic nuclides. *Tellus, Series B: Chemical and Physical Meteorology,* 52, 985-992.

BARKER, S., BROECKER, W., CLARK, E. & HAJDAS, I. 2007. Radiocarbon age offsets of foraminifera resulting from differential dissolution and fragmentation within the sedidmentary bioturbated zone. *Paleoceanography,* 22.

BARKER, S., GREAVES, M. & ELDERFIELD, H. 2003. A study of cleaning procedures used for foraminiferal Mg/Ca paleothermometry. *Geochemistry Geophysics Geosystems,* 4, 8407.

BARLOW, L. K., SADLER, J. P., OGILVIE, A. E. J., BUCKLAND, P. C., AMOROSI, T., INGIMUNDARSON, J. H., SKIDMORE, P., DUGMORE, A. J. & MCGOVERN, T. H. 1997. Interdisciplinary investigations of the end of the Norse western settlement in Greenland. *Holocene,* 7, 489-499.

BARRIOPEDRO, D., GARCÍA-HERRERA, R. & HUTH, R. 2008. Solar modulation of Northern Hemisphere winter blocking. *Journal of Geophysical Research* 113.
BÉ, A. W. H. & TOLDERLUND, D. S. 1971. *Distribution and ecology of planktonic foraminifera* Cambridge University Press, New York.

BELKIN, I. M. 2004. Propagation of the Great Salinity Anomaly of the 1990s around the northern North Atlantic. *Geophys. Res. Lett.,* 31, L08306.

BELKIN, I. M., LEVITUS, S., ANTONOV, J. & MALMBERG, S. A. 1998. 'Great Salinity Anomalies' in the North Atlantic. *Progress In Oceanography,* 41, 1-68.

BEMIS, B. E., SPERO, H. J., BIJMA, J. & LEA, D. W. 1998. Reevaluation of the Oxygen Isotopic Composition of Planktonic Foraminifera: Experimental Results and Revised Paleotemperature Equations. *Paleoceanography,* 13, 150-160.

BENDLE, J. A. P. & ROSELL-MELE, A. 2007. High-resolution alkenone sea surface temperature variability on the North Icelandic Shelf: implications for Nordic Seas palaeoclimatic development during the Holocene. *Holocene,* 17, 9-24.

BERGER, A. 1978. Long-term variations of caloric insolation resulting from the earth's orbital elements. *Quaternary Research,* 9, 139-167.

BERSCH, M. 2002. North Atlantic Oscillation-induced changes of the upper layer circulation in the northern North Atlantic Ocean. *Journal of Geophysical Research* 107, 20-1.

BERSCH, M., YASHAYAEV, I. & KOLTERMANN, K. P. 2007. Recent changes of the thermohaline circulation in the subpolar North Atlantic. *Ocean Dynamics,* 57, 223-235.

BIANCHI, G. G., HALL, I. R., MCCAVE, I. N. & JOSEPH, L. 1999. Measurement of the sortable silt current speed proxy using the Sedigraph 5100 and Coulter Multisizer IIe: Precision and accuracy. *Sedimentology,* 46, 1001-1014.

BIANCHI, G. G. & MCCAVE, I. N. 1999. Holocene periodicity in North Atlantic climate and deep-ocean flow south of Iceland. *Nature,* 397, 515-517.

BIANCHI, G. G. & MCCAVE, I. N. 2000. Hydrography and sedimentation under the deep western boundary current on Björn and Gardar Drifts, Iceland Basin. *Marine Geology,* 165,
137-169.

BIASTOCH, A., KASE, R. H. & STAMMER, D. B. 2003. The sensitivity of the Greenland-Scotland Ridge overflow to forcing changes. *Journal of Physical Oceanography,* 33, 2307-2319.

BLACK, D. E., ABAHAZI, M. A., THUNELL, R. C., KAPLAN, A., TAPPA, E. J. & PETERSON, L. C. 2007. An 8-century tropical Atlantic SST record from the Cariaco Basin: Baseline variability, twentieth-century warming, and Atlantic hurricane frequency. *Paleoceanography,* 22.

BLINDHEIM, J. 1968. Hydrographic investigations in the Irminger Sea in the years 1954-1964. *Fiskeridirek-toratets Skrifter,* 14, 72-97.

BLINDHEIM, J., BOROVKOV, V., HANSEN, B., MALMBERG, S. A., TURRELL, W. R. & OSTERHUS, S. 2000. Upper layer cooling and freshening in the Norwegian Sea in relation to atmospheric forcing. *Deep-Sea Research Part I-Oceanographic Research Papers,* 47, 655-680.

BOESSENKOOL, K. P., HALL, I. R., ELDERFIELD, H. & YASHAYAEV, I. 2007. North Atlantic climate and deep-ocean flow speed changes during the last 230 years. *Geophysical Research Letters,* 34, L13614.

BOND, G., KROMER, B., BEER, J., MUSCHELER, R., EVANS, M. N., SHOWERS, W., HOFFMANN, S., LOTTI-BOND, R., HAJDAS, I. & BONANI, G. 2001. Persistent Solar Influence on North Atlantic Climate During the Holocene. *Science,* 294, 2130-2136.

BOND, G., SHOWERS, W., CHESEBY, M., LOTTI, R., ALMASI, P., DEMENOCAL, P., PRIORE, P., CULLEN, H., HAJDAS, I. & BONANI, G. 1997. A Pervasive Millennial-Scale Cycle in North Atlantic Holocene and Glacial Climates. *Science,* 278, 1257-1266.

BORN, A., LEVERMANN, A. & MIGNOT, J. 2009. Sensitivity of the Atlantic Ocean circulation to a hydraulic overflow parameterisation in a coarse resolution model: Response of the subpolar gyre. *Ocean Modelling,* 27, 130-142.

BORN, A. & MIGNOT, J. 2011. Dynamics of decadal variability in the Atlantic subpolar gyre: a stochastically forced oscillator. *Climate Dynamics*, 1-14.

BOUSSETTA, S., BASSINOT, F., SABBATINI, A., CAILLON, N., NOUET, J., KALLEL, N., REBAUBIER, H., KLINKHAMMER, G. & LABEYRIE, L. 2011. Diagenetic Mg-rich calcite in Mediterranean sediments: Quantification and impact on foraminiferal Mg/Ca thermometry. *Marine Geology,* 280, 195-204.

BOWER, A., LOZIER, S. & GARY, S. 2011. Export of Labrador Sea Water from the subpolar North Atlantic: A Lagrangian perspective. *Deep-Sea Research Part II: Topical Studies in Oceanography,* 58, 1798-1818.

BOWER, A. S., LE CANN, B., ROSSBY, T., ZENK, W., GOULD, J., SPEER, K., RICHARDSON, P. L., PRATER, M. D. & ZHANG, H. M. 2002. Directly measured mid-depth circulation in the northeastern North Atlantic Ocean. *Nature,* 419, 603-607.

BOWER, A. S., LOZIER, M. S., GARY, S. F. & BÖNING, C. W. 2009. Interior pathways of the North Atlantic meridional overturning circulation. *Nature,* 459, 243-247.

BOYLE, E. A. 1983. Manganese carbonate overgrowths on foraminifera tests. *Geochimica et Cosmochimica Acta,* 47, 1815-1819.

BOYLE, E. A. & KEIGWIN, L. D. 1985. Comparison of Atlantic and Pacific paleochemical records for the last 215,000 years: changes in deep ocean circulation and chemical inventories. *Earth and Planetary Science Letters,* 76, 135-150.

BRADLEY, R. S. 1988. The explosive volcanic eruption signal in northern hemisphere continental temperature records. *Climatic Change,* 12, 221-243.

BRADLEY, R. S., HUGHES, M. K. & DIAZ, H. F. 2003. Climate in Medieval Time. *Science,* 302, 404-405.

BRAUN, H., CHRISTL, M., RAHMSTORF, S., GANOPOLSKI, A., MANGINI, A., KUBATZKI, C., ROTH, K. & KROMER, B. 2005. Possible solar origin of the 1,470-year glacial climate cycle demonstrated in a coupled model. *Nature,* 438, 208-211.

BROECKER, W. & CLARK, E. 2011. Radiocarbon-age differences among coexisting planktic foraminifera shells: The barker effect. *Paleoceanography,* 26.

BROECKER, W. S. 1991. The Great Ocean Conveyor. *Oceanography,* 4, 10.

BROECKER, W. S. 2001. Was the Medieval Warm Period Global? *Science,* 291, 1497-1499.

BROWN, S. J. & ELDERFIELD, H. 1996. Variations in Mg/Ca and Sr/Ca ratios of planktonic foraminifera caused by postdepositional dissolution: Evidence of shallow Mg-dependent dissolution. *Paleoceanography,* 11, 543-551.

BRYDEN, H. L., LONGWORTH, H. R. & CUNNINGHAM, S. A. 2005. Slowing of the Atlantic meridional overturning circulation at 25[deg][thinsp]N. *Nature,* 438, 655-657.

BUEHLER, T., RAIBLE, C. C. & STOCKER, T. F. 2011. The relationship of winter season North Atlantic blocking frequencies to extreme cold or dry spells in the ERA-40. *Tellus A,* 63, 212-222.

BUTZIN, M., PRANGE, M. & LOHMANN, G. 2005. Radiocarbon simulations for the glacial ocean: The effects of wind stress, Southern Ocean sea ice and Heinrich events. *Earth and Planetary Science Letters,* 235, 45-61.

CALVO, E., GRIMALT, J. O. & JANSEN, E. 2002. High resolution U(37)(K) sea surface temperature reconstruction in the Norwegian Sea during the Holocene. *Quaternary Science Reviews,* 21, 1385-1394.

CAME, R. E., OPPO, D. W. & MCMANUS, J. F. 2007. Amplitude and timing of temperature and salinity variability in the subpolar North Atlantic over the past 10 k.y. *Geology,* 35, 315-318.

CARSTENS, J., HEBBELN, D. & WEFER, G. 1997. Distribution of planktic foraminifera at the ice margin in the Arctic (Fram Strait). *Marine Micropaleontology,* 29, 257-269.

CATTIAUX, J., VAUTARD, R., CASSOU, C., YIOU, P., MASSON-DELMOTTE, V. &
CODRON, F. 2010. Winter 2010 in Europe: A cold extreme in a warming climate. *Geophysical Research Letters,* 37.

CHAPMAN, M. R. & SHACKLETON, N. J. 2000. Evidence of 550-year and 1000-year cyclicities in North Atlantic circulation patterns during the Holocene. *The Holocene,* 10, 287-291.

CLARK, P. U., PISIAS, N. G., STOCKER, T. F. & WEAVER, A. J. 2002. The role of the thermohaline circulation in abrupt climate change. *Nature,* 415, 863-869.

CLÉROUX, C., CORTIJO, E., ANAND, P., LABEYRIE, L., BASSINOT, F., CAILLON, N. & DUPLESSY, J.-C. 2008. Mg/Ca and Sr/Ca ratios in planktonic foraminifera: Proxies for upper water column temperature reconstruction. *Paleoceanography,* 23, PA3214.

CLÉROUX, C., CORTIJO, E., DUPLESSY, J.-C. & ZAHN, R. 2007. Deep-dwelling foraminifera as thermocline temperature recorders. *Geochemistry Geophysics Geosystems,* 8, Q04N11.

COLE-DAI, J., MOSLEY-THOMPSON, E., WIGHT, S. P. & THOMPSON, L. G. 2000. A 4100-year record of explosive volcanism from an East Antarctica ice core. *Journal of Geophysical Research* 105, 24431-24441.

CRONIN, T. M., HAYO, K., THUNELL, R. C., DWYER, G. S., SAENGER, C. & WILLARD, D. A. 2010. The Medieval Climate Anomaly and Little Ice Age in

Chesapeake Bay and the North Atlantic Ocean. *Palaeogeography, Palaeoclimatology, Palaeoecology,* 297, 299-310.

CROWLEY, T. J. 2000. Causes of Climate Change Over the Past 1000 Years. *Science,* 289, 270-277.

CULLEN, H. M., DEMENOCAL, P. B., HEMMING, S., HEMMING, G., BROWN, F. H., GUILDERSON, T. & SIROCKO, F. 2000. Climate change and the collapse of the Akkadian empire: Evidence from the deep sea. *Geology*, 28, 379-382.

CUNDY, A. B. & CROUDACE, I. W. 1996. Sediment accretion and recent sea-level rise in the solent, Southern England: Inferences from radiometric and geochemical studies. *Estuarine Coastal and Shelf Science,* 43, 819-819.

CUNNINGHAM, S. A., KANZOW, T., RAYNER, D., BARINGER, M. O., JOHNS, W. E., MAROTZKE, J., LONGWORTH, H. R., GRANT, E. M., HIRSCHI, J. J. M., BEAL, L. M., MEINEN, C. S. & BRYDEN, H. L. 2007. Temporal Variability of the Atlantic Meridional Overturning Circulation at 26.5°N. *Science,* 317, 935-938.

CURRY, R. & MAURITZEN, C. 2005. Dilution of the Northern North Atlantic Ocean in Recent Decades. *Science,* 308, 1772-1774.

CURRY, R. G. & MCCARTNEY, M. S. 2001. Ocean gyre circulation changes associated with the North Atlantic Oscillation. *Journal of Physical Oceanography,* 31, 3374-3400.

CURRY, R. G., MCCARTNEY, M. S. & JOYCE, T. M. 1998. Oceanic transport of subpolar climate signals to mid-depth subtropical waters. *Nature,* 391, 575-577.

D'ARRIGO, R., ANCHUKAITIS, K. J., BUCKLEY, B., COOK, E. & WILSON, R. 2012. Regional climatic and North Atlantic Oscillation signatures in West Virginia red cedar over the past millennium. *Global and Planetary Change,* 84–85, 8-13.

DARLING, K. F., WADE, C. M., STEWART, I. A., KROON, D., DINGLE, R. & LEIGH BROWN, A. J. 2000. Molecular evidence for genetic mixing of Arctic and Antarctic subpolar populations of planktonic foraminifers. *Nature,* 405, 43-47.

DE JONG, R., HAMMARLUND, D. & NESJE, A. 2009. Late Holocene effective precipitation variations in the maritime regions of south-west Scandinavia. *Quaternary Science Reviews,* 28, 54-64.

DE VERNAL, A. & HILLAIRE-MARCEL, C. 2006. Provincialism in trends and high frequency changes in the northwest North Atlantic during the Holocene. *Global and Planetary Change,* 54, 263-290.

DEBRET, M., BOUT-ROUMAZEILLES, V., GROUSSET, F., DESMET, M., MCMANUS, J. F., MASSEI, N., SEBAG, D., PETIT, J. R., COPARD, Y. & TRENTESAUX, A. 2007. The origin of the 1500-year climate cycles in Holocene North-Atlantic records. *Climate of the Past Discussions,* 3, 679-692.

DEMENOCAL, P. B. 2001. Cultural Responses to Climate Change During the Late Holocene. *Science,* 292, 667-673.

DENTON, G. H. & BROECKER, W. S. 2008. Wobbly ocean conveyor circulation during the Holocene? *Quaternary Science Reviews,* 27, 1939-1950.

DENTON, G. H. & KARLÉN, W. 1973. Holocene climatic variations—Their pattern and possible cause. *Quaternary Research,* 3, 155-205.

DESER, C., WALSH, J. E. & TIMLIN, M. S. 2000. Arctic sea ice variability in the context of recent atmospheric circulation trends. *Journal of Climate,* 13, 617-633.
DICKSON, B., MEINCKE, J. & RHINES, P. (eds.) 2008. Arctic–Subarctic Ocean Fluxes Defining the Role of the Northern Seas in Climate: Springer Netherlands.

DICKSON, B., MEINCKE, J., VASSIE, I., JUNGCLAUS, J. & OSTERHUS, S. 1999. Possible predictability in overflow from the Denmark Strait. *Nature,* 397, 243-246.

DICKSON, B., YASHAYAEV, I., MEINCKE, J., TURRELL, B., DYE, S. & HOLFORT, J. 2002. Rapid freshening of the deep North Atlantic Ocean over the past four decades. *Nature,* 416, 832-837.

DICKSON, R., LAZIER, J., MEINCKE, J., RHINES, P. & SWIFT, J. 1996. Long-term coordinated changes in the convective activity of the North Atlantic. *Progress In Oceanography,* 38, 241-295.

DICKSON, R., RUDELS, B., DYE, S., KARCHER, M., MEINCKE, J. & YASHAYAEV, I. 2007. Current estimates of freshwater flux through Arctic and subarctic seas. *Progress In Oceanography,* 73, 210-230.

DICKSON, R. R., CURRY, R. & YASHAYAEV, I. 2003. Recent changes in the North Atlantic. Philosophical Transactions of the Royal Society of London Series a-Mathematical Physical and Engineering Sciences, 361, 1917-1933.

DICKSON, R. R., MEINCKE, J., MALMBERG, S. A. & LEE, A. J. 1988. The "great salinity anomaly" in the Northern North Atlantic 1968-1982. *Progress In Oceanography,* 20, 103-151.

DICKSON, R. R., OSBORN, T. J., HURRELL, J. W., MEINCKE, J., BLINDHEIM, J., ADLANDSVIK, B., VINJE, T., ALEKSEEV, G. & MASLOWSKI, W. 2000. The Arctic Ocean response to the North Atlantic oscillation. *Journal of Climate,* 13, 2671-2696.

EDDY, J. A. 1976. MAUNDER MINIMUM. *Science,* 192, 1189-1202.

EDEN, C. & WILLEBRAND, J. 2001. Mechanism of Interannual to Decadal Variability of the North Atlantic Circulation. *Journal of Climate,* 14, 2266-2280.

EIRÍKSSON, J., KNUDSEN, K. L., LARSEN, G., OLSEN, J., HEINEMEIER, J., BARTELS-JÓNSDÓTTIR, H. B., JIANG, H., RAN, L. & SÍMONARSON, L. A. 2011. Coupling of palaeoceanographic shifts and changes in marine reservoir ages off North

Iceland through the last millennium. *Palaeogeography, Palaeoclimatology, Palaeoecology,* 302, 95-108.

ELDERFIELD, H. & GANSSEN, G. 2000. Past temperature and $\delta^{18}O$ of surface ocean waters inferred from foraminiferal Mg/Ca ratios. *Nature,* 405, 442-445.

ELDERFIELD, H., VAUTRAVERS, M. & COOPER, M. 2002. The relationship between shell size and Mg/Ca, Sr/Ca, $\delta^{18}O$, and $\delta^{13}C$ of species of planktonic foraminifera. *Geochem. Geophys. Geosyst.,* 3, 1052.

ELDEVIK, T., NILSEN, J. E. O., IOVINO, D., ANDERS OLSSON, K., SANDO, A. B. & DRANGE, H. 2009. Observed sources and variability of Nordic seas overflow. *Nature Geoscience,* 2, 406-410.

ELLISON, C. R. W., CHAPMAN, M. R. & HALL, I. R. 2006. Surface and Deep Ocean Interactions During the Cold Climate Event 8200 Years Ago. *Science,* 312, 1929-1932.

EMILIANI, C. 1955. PLEISTOCENE TEMPERATURES. *Journal of Geology,* 63, 538-578.

EPSTEIN, S., R. , BUCHSBAUM, H. A., C., L. & UREY 1953. Revised carbonate-water isotopic temperature scale , . *Geological Society American Bulletin,* 64, 1315-1326.

EYNAUD, F. Planktonic foraminifera in the arctic: Potentials and issues regarding modern and quaternary populations. 2011.

FARMER, E. J., CHAPMAN, M. & ANDREWS, J. 2010. North Atlantic Globorotalia inflata coretop Mg/Ca calibrations and temperature reconstructions over Termination I *IOP Conference Series: Earth and Environmental Science,* 9

FERGUSON, J. E., HENDERSON, G. M., KUCERA, M. & RICKABY, R. E. M. 2008. Systematic change of foraminiferal Mg/Ca ratios across a strong salinity gradient. *Earth and Planetary Science Letters,* 265, 153-166.

FLATAU, MARIA, K., TALLEY, LYNNE, NIILER & PEARN, P. 2003. *The North Atlantic oscillation, surface Current velocities, and SST changes in the subpolar North Atlantic,* Boston, MA, ETATS-UNIS, American Meteorological Society.

GANSSEN, G. M. & KROON, D. 2000. The isotopic signature of planktonic foraminifera from NE Atlantic surface sediments: Implications for the reconstruction of past oceanic conditions. *Journal of the Geological Society,* 157, 693-699.

GAO, C., OMAN, L., ROBOCK, A. & STENCHIKOV, G. L. 2007. Atmospheric volcanic loading derived from bipolar ice cores: Accounting for the spatial distribution of volcanic deposition. *Journal of Geophysical Research D: Atmospheres,* 112.

GELDERLOOS, R., KATSMAN, C. A. & DRIJFHOUT, A. S. S. 2011. Assessing the roles of three eddy types in restratifying the Labrador Sea after deep convection. *Journal of Physical Oceanography,* 41, 2102-2119.

GENT, P. R., DANABASOGLU, G., DONNER, L. J., HOLLAND, M. M., HUNKE, E. C., JAYNE, S. R., LAWRENCE, D. M., NEALE, R. B., RASCH, P. J., VERTENSTEIN, M., WORLEY, P. H., YANG, Z.-L. & ZHANG, M. 2011. The Community Climate System Model Version 4. *Journal of Climate,* 24, 4973-4991.

GIRAUDEAU, J., JENNINGS, A. E. & ANDREWS, J. T. 2004. Timing and mechanisms of surface and intermediate water circulation changes in the Nordic Seas over the last 10,000 years: a view from the North Iceland shelf. *Quaternary Science Reviews,* 23, 2127-2139.

GOOSSE, H., ARZEL, O., LUTERBACHER, J., MANN, M. E., RENSSEN, H., RIEDWYL, N., TIMMERMANN, A., XOPLAKI, E. & WANNER, H. 2006. The origin of the European "Medieval Warm Period". *Climate of the Past Discussions,* 2, 285-314.

GOOSSE, H., RENSSEN, H., TIMMERMANN, A. & BRADLEY, R. S. 2005. Internal and forced climate variability during the last millennium: a model-data comparison using ensemble simulations. *Quaternary Science Reviews,* 24, 1345-1360.

GRAHAM, N. E., HUGHES, M. K., AMMANN, C. M., COBB, K. M., HOERLING, M. P., KENNETT, D. J., KENNETT, J. P., REIN, B., STOTT, L., WIGAND, P. E. & XU, T. 2007. Tropical Pacific - mid-latitude teleconnections in medieval times. *Climatic Change,* 83, 241-285.

GRAY, L. J., BEER, J., GELLER, M., HAIGH, J. D., LOCKWOOD, M., MATTHES, K., CUBASCH, U., FLEITMANN, D., HARRISON, G., HOOD, L., LUTERBACHER, J., MEEHL, G. A., SHINDELL, D., VAN GEEL, B. & WHITE, W. 2010. SOLAR INFLUENCES ON CLIMATE. *Reviews of Geophysics,* 48.

GRAY, S. T., GRAUMLICH, L. J., BETANCOURT, J. L. & PEDERSON, G. T. 2004. A tree-ring based reconstruction of the Atlantic Multidecadal Oscillation since 1567 AD. *Geophysical Research Letters,* 31.

GROENEVELD, J. & CHIESSI, C. M. 2011. Mg/Ca of Globorotalia inflata as a recorder of permanent thermocline temperatures in the South Atlantic. *Paleoceanography,* 26, PA2203.

GROOTES, P. M. & STUIVER, M. 1997. Oxygen 18/16 variability in Greenland snow and ice with 10^{-3} to 10^{5} year time resolution. *Journal of Geophysics Research,* 102, 26455-26470.

GROOTES, P. M., STUIVER, M., WHITE, J. W. C., JOHNSEN, S. & JOUZEL, J. 1993. Comparison of oxygen isotope records from the GISP2 and GRIP Greenland ice cores. *Nature,* 366, 552-554.

GROSSMANN, I. & KLOTZBACH, P. J. 2009. A review of North Atlantic modes of natural variability and their driving mechanisms. *Journal of Geophysical Research,* 114, D24107.

GROVE, J. M. 1988. *The Little Ice Age,* London, Methuen.

HAARMANN, T., HATHORNE, E. C., MOHTADI, M., GROENEVELD, J., KÖLLING, M. & BICKERT, T. 2011. Mg/Ca ratios of single planktonic foraminifer shells and the potential to reconstruct the thermal seasonality of the water column. *Paleoceanography,* 26, PA3218.

HAASE-SCHRAMM, A., BÖHM, F., EISENHAUER, A., DULLO, W.-C., JOACHIMSKI, M. M., HANSEN, B. & REITNER, J. 2003. Sr/Ca ratios and oxygen isotopes from sclerosponges: Temperature history of the Caribbean mixed layer and thermocline during the Little Ice Age. *Paleoceanography,* 18, 1073.

HAASE-SCHRAMM, A., BÖHM, F., EISENHAUER, A., GARBE-SCHÖNBERG, D., DULLO, W. C. & REITNER, J. 2005. Annual to interannual temperature variability in the Caribbean during the Maunder sunspot minimum. *Paleoceanography,* 20.

HAIGH, J. D. 1994. THE ROLE OF STRATOSPHERIC OZONE IN MODULATING THE SOLAR RADIATIVE FORCING OF CLIMATE. *Nature,* 370, 544-546.

HAIGH, J. D. 1996. The impact of solar variability on climate. *Science,* 272, 981-984.
HAIGH, J. D., WINNING, A. R., TOUMI, R. & HARDER, J. W. 2010. An influence of solar spectral variations on radiative forcing of climate. *Nature,* 467, 696-699.

HAKKINEN, S. 1993. An Arctic source for the Great Salinity Anomaly: a simulation of the Arctic ice-ocean system for 1955-1975. *Journal of Geophysical Research,* 98, 16,397-16,410.

HÄKKINEN, S. 2002. Freshening of the Labrador Sea surface waters in the 1990s: Another great salinity anomaly? *Geophysic Research Letters,* 29, 2232.

HÄKKINEN, S. & RHINES, P. B. 2004. Decline of Subpolar North Atlantic Circulation During the 1990s. *Science,* 304, 555-559.

HÄKKINEN, S., RHINES, P. B. & WORTHEN, D. L. 2011. Atmospheric Blocking and Atlantic Multidecadal Ocean Variability. *Science,* 334, 655-659.

HALL, A. & STOUFFER, R. J. 2001. An abrupt climate event in a coupled ocean-atmosphere simulation without external forcing. *Nature,* 409, 171-174.

HALL, I. R., BIANCHI, G. G. & EVANS, J. R. 2004. Centennial to millennial scale Holocene climate-deep water linkage in the North Atlantic. *Quaternary Science Reviews,* 23, 1529-1536.

HALL, I. R., BOESSENKOOL, K. P., BARKER, S., MCCAVE, I. N. & ELDERFIELD, H. 2010. Surface and deep ocean coupling in the subpolar North Atlantic during the last 230 years. *Paleoceanography,* 25.

HALL, M. M. & BRYDEN, H. L. 1982. Direct estimates and mechanisms of ocean heat transport. *Deep Sea Research Part A. Oceanographic Research Papers,* 29, 339-359.

HANSEN, B. & OSTERHUS, S. 2007. Faroe Bank Channel overflow 1995-2005. *Progress In Oceanography,* 75, 817-856.

HANSEN, B. & ØSTERHUS, S. 2000. North Atlantic–Nordic Seas exchanges. *Progress In Oceanography,* 45, 109-208.

HANSEN, B., ØSTERHUS, S., QUADFASEL, D. & TURRELL, W. 2004. Already the Day After Tomorrow? *Science,* 305, 953-954.

HANSEN, B., TURRELL, W. R. & OSTERHUS, S. 2001. Decreasing overflow from the Nordic seas into the Atlantic Ocean through the Faroe Bank channel since 1950. *Nature,* 411, 927-930.

HATHORNE, E. C., JAMES, R. H. & LAMPITT, R. S. 2009. Environmental versus biomineralization controls on the intratest variation in the trace element composition of the planktonic foraminifera G. inflata and G. scitula. *Paleoceanography,* 24, PA4204.

HÁTÚN, H., SANDØ, A. B., DRANGE, H., HANSEN, B. & VALDIMARSSON, H. 2005. Influence of the Atlantic Subpolar Gyre on the Thermohaline Circulation. *Science,* 309, 1841-1844.

HAUG, G. H., HUGHEN, K. A., SIGMAN, D. M., PETERSON, L. C. & RÖHL, U. 2001. Southward migration of the intertropical convergence zone through the holocene. *Science,* 293, 1304-1308.

HEMLEBEN, C., M. SPINDLER & ANDERSON, R. 1989. *Modern Planktonic Foraminifera,* New York Springer.

HILBRECHT, H. 1996. Extant planktic foraminifera and the physical environment in the Atlantic and Indian Oceans. *In:* MITTEILUNGEN AUS DEM GEOLOGISCHEN INSTITUT DER EIDGEN. TECHNISCHEN HOCHSCHULE UND DER UNIVERSITÄT ZÜRICH, N. F. (ed.). Zürich.

HILBRECHT, H. 1997. Morphologic gradation and ecology in Neogloboquadrina pachyderma and N. dutertrei (planktic foraminifera) from core top sediments. *Marine Micropaleontology,* 31, 31-43.

HILLAIRE-MARCEL, C., DE VERNAL, A., BILODEAU, G. & WEAVER, A. J. 2001. Absence of deep-water formation in the Labrador Sea during the last interglacial period. *Nature,* 410, 1073-1077.

HODELL, D. A., BRENNER, M., CURTIS, J. H., MEDINA-GONZÁLEZ, R., ILDEFONSO-CHAN CAN, E., ALBORNAZ-PAT, A. & GUILDERSON, T. P. 2005. Climate change on the Yucatan Peninsula during the Little Ice Age. *Quaternary Research,* 63, 109-121.

HODELL, D. A., CURTIS, J. H. & BRENNER, M. 1995. Possible role of climate in the collapse of Classic Maya civilization. *Nature,* 375, 391-394.

HOERLING, M. P., HURRELL, J. W. & XU, T. 2001. Tropical Origins for Recent North Atlantic Climate Change. *Science,* 292, 90-92.

HOFER, D., RAIBLE, C. C. & STOCKER, T. F. 2010. Variations of the Atlantic meridional overturning circulation in control and transient simulations of the last millennium. *Climate of the Past Discussions,* 6.

HOLLIDAY, N. P., BACON, S., ALLEN, J. & MCDONAGH, E. L. 2009. Circulation and transport in the western boundary currents at Cape Farewell, Greenland. *Journal of Physical Oceanography,* 39, 1854-1870.

HOLLIDAY, N. P., WANIEK, J. J., DAVIDSON, R., WILSON, D., BROWN, L., SANDERS, R., POLLARD, R. T. & ALLEN, J. T. 2006. Large-scale physical controls on phytoplankton growth in the Irminger Sea Part I: Hydrographic zones, mixing and stratification. *Journal of Marine Systems,* 59, 201-218.

HOOGAKKER, B. A. A., KLINKHAMMER, G. P., ELDERFIELD, H., ROHLING, E. J. &
HAYWARD, C. 2009. Mg/Ca paleothermometry in high salinity environments. *Earth and Planetary Science Letters,* 284, 583-589.

HU, F. S., KAUFMAN, D., YONEJI, S., NELSON, D., SHEMESH, A., HUANG, Y., TIAN, J., BOND, G., CLEGG, B. & BROWN, T. 2003. Cyclic Variation and Solar Forcing of Holocene Climate in the Alaskan Subarctic. *Science,* 301, 1890-1893.

HUGHES, M. K. & DIAZ, H. F. 1994. Was there a 'medieval warm period', and if so, where and when? *Climatic Change,* 26, 109-142.

HUNTER, S., WILKINSON, D., LOUARN, E., NICK MCCAVE, I., ROHLING, E., STOW, D. A. V. & BACON, S. 2007a. Deep western boundary current dynamics and associated sedimentation on the Eirik Drift, Southern Greenland Margin. *Deep-Sea Research Part I: Oceanographic Research Papers,* 54, 2036-2066.

HUNTER, S. E., WILKINSON, D., STANFORD, J., STOW, D. A. V., BACON, S., AKHMETZHANOV, A. M. & KENYON, N. H. 2007b. The Eirik Drift: A long-term barometer of North Atlantic deepwater flux south of Cape Farewell, Greenland.

HURRELL, J. W. 1995. Decadal Trends in the North Atlantic Oscillation: Regional Temperatures and Precipitation. *Science,* 269, 676-679.

HURRELL, J. W. & DESER, C. 2009. North Atlantic climate variability: The role of the North Atlantic Oscillation. *Journal of Marine Systems,* 78, 28-41.

HURRELL, J. W., VISBECK, M., BUSALACCHI, A., CLARKE, R. A., DELWORTH, T. L., DICKSON, R. R., JOHNS, W. E., KOLTERMANN, K. P., KUSHNIR, Y., MARSHALL, D., MAURITZEN, C., MCCARTNEY, M. S., PIOLA, A., REASON, C., REVERDIN, G., SCHOTT, F., SUTTON, R., WAINER, I. & WRIGHT, D. 2006. Atlantic climate variability and predictability: A CLIVAR perspective. *Journal of Climate,* 19, 5100-5121.

HUT, G. 1987. Stable isotope reference samples for geochemical and hydrological investigations. Report of Consultant's Group Meeting. International Atomic Energy Agency. Vienna, Austria, , p. 42.

INESON, S., SCAIFE, A. A., KNIGHT, J. R., MANNERS, J. C., DUNSTONE, N. J., GRAY, L. J. & HAIGH, J. D. 2011. Solar forcing of winter climate variability in the Northern Hemisphere. *Nature Geosci,* 4, 753-757.

IPCC 2007. Climate Change 2007: The Physical Sciene Basis. *In:* CHANGE, I. P. O. C. (ed.). Cambridge University Press.

JEANSSON, E., JUTTERSTROEM, S., RUDELS, B., ANDERSON, L. G., OLSSON, K. A., JONES, E. P., SMETHIE, W. M., JR. & SWIFT, J. H. 2008. Sources to the East Greenland Current and its contribution to the Denmark Strait Overflow. *Progress In Oceanography,* 78, 12-28.

JENNINGS, A., ANDREWS, J. & WILSON, L. 2011. Holocene environmental evolution of the SE Greenland Shelf North and South of the Denmark Strait: Irminger and East Greenland current interactions. *Quaternary Science Reviews,* 30, 980-998.

JENNINGS, A. E., KNUDSEN, K. L., HALD, M., HANSEN, C. V. & ANDREWS, J. T. 2002. A mid-Holocene shift in Arctic sea-ice variability on the East Greenland Shelf. *Holocene,* 12, 49-58.
JENNINGS, A. E. & WEINER, N. J. 1996. Environmental change in eastern Greenland during the last 1300 years: evidence from foraminifera and lithofacies in Nansen Fjord, 68°N. *The Holocene,* 6, 179-191.

JESSEN, C. A., SOLIGNAC, S., NØRGAARD-PEDERSEN, N., MIKKELSEN, N., KUIJPERS, A. & SEIDENKRANTZ, M.-S. 2011. Exotic pollen as an indicator of variable atmospheric circulation over the Labrador Sea region during the mid to late Holocene. *Journal of Quaternary Science,* 26, 286-296.

JIANG, H., EIRÍKSSON, J., SCHULZ, M., KNUDSEN, K. L. & SEIDENKRANTZ, M. S. 2005. Evidence for solar forcing of sea-surface temperature on the North Icelandic Shelf during the late Holocene. *Geology,* 33, 73-76.

JIANG, H., SEIDENKRANTZ, M. S., KNUDSEN, K. L. & EIRIKSSON, J. 2002. Late-Holocene summer sea-surface temperatures based on a diatom record from the north Icelandic shelf. *Holocene,* 12, 137-147.

JOHNSEN, S. J., DAHL-JENSEN, D., GUNDESTRUP, N., STEFFENSEN, J. P., CLAUSEN, H. B., MILLER, H., MASSON-DELMOTTE, V., SVEINBJÖRNSDOTTIR, A. E. & WHITE, J. 2001. Oxygen isotope and palaeotemperature records from six Greenland ice-core stations: Camp Century, Dye-3, GRIP, GISP2, Renland and NorthGRIP. *Journal of Quaternary Science,* 16, 299-307.

JONES, P. D., BRIFFA, K. R., OSBORN, T. J., LOUGH, J. M., VAN OMMEN, T. D., VINTHER, B. M., LUTERBACHER, J., WAHL, E. R., ZWIERS, F. W., MANN, M. E., SCHMIDT, G. A., AMMANN, C. M., BUCKLEY, B. M., COBB, K. M., ESPER, J., GOOSSE, H., GRAHAM, N., JANSEN, E., KIEFER, T., KULL, C., KÜTTEL, M., MOSLEY-THOMPSON, E., OVERPECK, J. T., RIEDWYL, N., SCHULZ, M., TUDHOPE, A. W., VILLALBA, R., WANNER, H., WOLFF, E. & XOPLAKI, E. 2009. High-resolution palaeoclimatology of the last millennium: A review of current status and future prospects. *Holocene,* 19, 3-49.

JONG, R. D., BJÖRCK, S., BJÖRKMAN, L. & CLEMMENSEN, L. B. 2006. Storminess variation during the last 6500 years as reconstructed from an ombrotrophic peat bog in Halland, southwest Sweden. *Journal of Quaternary Science,* 21, 905-919.
JONKERS, L., BRUMMER, G. J. A., PEETERS, F. J. C., VAN AKEN, H. M. & DE JONG, M. F. 2010. Seasonal stratification, shell flux, and oxygen isotope dynamics of leftcoiling N. pachyderma and T. quinqueloba in the western subpolar North Atlantic. *Paleoceanography,* 25.

JONSSON, S. 1999. The circulation in the northern part of the Denmark Strait and its variability. *CES CM,* 9.

JONSSON, S. & VALDIMARSSON, H. 2004. A new path for the Denmark Strait overflow water from the Iceland Sea to Denmark Strait. *Geophysic Research Letters,* 31, L03305.

KAESE, R. H., SERRA, N., KOEHL, A. & STAMMER, D. 2009. Mechanisms for the variability of dense water pathways in the Nordic Seas. *Journal of Geophysical Research-Oceans,* 114.
KATSMAN, C. A., SPALL, M. A. & PICKART, R. S. 2004. Boundary current eddies and their role in the restratification of the Labrador Sea. *Journal of Physical Oceanography,* 34, 1967-1983.

KATZ, A. 1973. The interaction of magnesium with calcite during crystal growth at 25–90°C and one atmosphere. *Geochimica et Cosmochimica Acta,* 37, 1563-1586.

KAUFMAN, D. S., SCHNEIDER, D. P., MCKAY, N. P., AMMANN, C. M., BRADLEY, R. S., BRIFFA, K. R., MILLER, G. H., OTTO-BLIESNER, B. L., OVERPECK, J. T., VINTHER, B. M., ABBOTT, M., AXFORD, Y., BIRD, B., BIRKS, H. J. B., BJUNE, A. E., BRINER, J., COOK, T., CHIPMAN, M., FRANCUS, P., GAJEWSKI, K., GEIRSDDTTIR, Á., HU, F. S., KUTCHKO, B., LAMOUREUX, S., LOSO, M., MACDONALD, G., PEROS, M., PORINCHU, D., SCHIFF, C., SEPPÄ, H. & THOMAS, E. 2009. Recent warming reverses long-term arctic cooling. *Science,* 325, 1236-1239.

KEIGWIN, L. D. 1996. The little ice age and medieval warm period in the Sargasso Sea. *Science,* 274, 1504-1508.

KEIGWIN, L. D. & BOYLE, E. A. 2000. Detecting Holocene changes in thermohaline circulation. *Proceedings of the National Academy of Sciences of the United States of America,* 97, 1343-1346.

KEIGWIN, L. D. & GUILDERSON, T. P. 2009. Bioturbation artifacts in zero-age sediments. *Paleoceanography,* 24.

KEIGWIN, L. D. & PICKART, R. S. 1999. Slope water current over the Laurentian Fan on interannual to millennial time scares. *Science,* 286, 520-523.

KEIGWIN, L. D., SACHS, J. P. & ROSENTHAL, Y. 2003. A 1600-year history of the Labrador Current off Nova Scotia. *Climate Dynamics,* 21, 53-62.

KEY, R. M., KOZYR, A., SABINE, C. L., LEE, K., WANNINKHOF, R., BULLISTER, J. L., FEELY, R. A., MILLERO, F. J., MORDY, C. & PENG, T. H. 2004. A global ocean carbon climatology: Results from Global Data Analysis Project (GLODAP). *Global Biogeochemical Cycles,* 18, GB4031.

KILBOURNE, K. H., QUINN, T. M., WEBB, R., GUILDERSON, T., NYBERG, J. & WINTER, A. 2010. Coral windows onto seasonal climate variability in the northern Caribbean since 1479. *Geochemistry, Geophysics, Geosystems,* 11.

KIM, S.-T. & O'NEIL, J. R. 1997. Equilibrium and nonequilibrium oxygen isotope effects in synthetic carbonates. *Geochimica et Cosmochimica Acta,* 61, 3461-3475.

KıSAKÜREK, B., EISENHAUER, A., BÖHM, F., GARBE-SCHÖNBERG, D. & EREZ, J. 2008. Controls on shell Mg/Ca and Sr/Ca in cultured planktonic foraminiferan, Globigerinoides ruber (white). *Earth and Planetary Science Letters,* 273, 260-269.

KNIGHT, J. R., ALLAN, R. J., FOLLAND, C. K., VELLINGA, M. & MANN, M. E. 2005. A signature of persistent natural thermohaline circulation cycles in observed climate. *Geophysical Research Letters,* 32.
KNUDSEN, M. F., RIISAGER, P., DONADINI, F., SNOWBALL, I., MUSCHELER, R., KORHONEN, K. & PESONEN, L. J. 2008. Variations in the geomagnetic dipole moment during the Holocene and the past 50 kyr. *Earth and Planetary Science Letters,* 272, 319-329.

KOCH, L. 1945. The east Greenland ice,. *Medd. Grønland, København,* 130, 1-374.

KOHFELD, K. E., FAIRBANKS, R. G., SMITH, S. L. & WALSH, I. D. 1996. Neogloboquadrina pachyderma (sinistral coiling) as paleoceanographic tracers in polar oceans: Evidence from Northeast Water Polynya plankton tows, sediment traps, and surface sediments. *Paleoceanography,* 11, 679-699.

KOHL, A. 2010. Variable source regions of Denmark Strait and Faroe Bank Channel overflow waters. *Tellus Series a-Dynamic Meteorology and Oceanography,* 62, 551-568.

KOHL, A., KAESE, R. H., STAMMER, D. & SERRA, N. 2007. Causes of changes in the Denmark strait overflow. *Journal of Physical Oceanography,* 37, 1678-1696.

KONTAKIOTIS, G., MORTYN, P. G., ANTONARAKOU, A., MARTÍNEZ-BOTÍ, M. A. & TRIANTAPHYLLOU, M. V. 2011. Field-based validation of a diagenetic effect on G. ruber Mg/Ca paleothermometry: Core top results from the Aegean Sea (eastern Mediterranean). *Geochemistry Geophysics Geosystems,* 12, Q09004.

KOZDON, R., EISENHAUER, A., WEINELT, M., MELAND, M. Y. & NÜRNBERG, D. 2009. Reassessing Mg/Ca temperature calibrations of Neogloboquadrina pachyderma (sinistral) using paired δ44/40Ca and Mg/Ca measurements. *Geochemistry, Geophysics, Geosystems,* 10.

KOZIOL, A. M. & NEWTON, R. C. 1995. Experimental determination of the reactions magnesite plus quartz equals enstatite plus CO2 and magnesite equals periclase plus

CO2, and enthalpies of formation of enstatite and magnesite. *American Mineralogist,* 80, 1252-1260.

KUCERA, M. 2007. Chapter Six Planktonic Foraminifera as Tracers of Past Oceanic Environments. *In:* CLAUDE, H. M. & ANNE DE, V. (eds.) *Developments in Marine Geology.* Elsevier.

KUHNERT, H. & MULITZA, S. 2011. Multidecadal variability and late medieval cooling of near-coastal sea surface temperatures in the eastern tropical North Atlantic. *Paleoceanography,* 26, PA4224.

LABEYRIE, L. D. & DUPLESSY, J. C. 1985. Changes in the oceanic 13C 12C ratio during the last 140 000 years: High-latitude surface water records. *Palaeogeography, Palaeoclimatology, Palaeoecology,* 50, 217-240.

LAMB, H. H. 1965. The early medieval warm epoch and its sequel. *Palaeogeography, Palaeoclimatology, Palaeoecology,* 1, 13-37.

LAMB, H. H. 1979. Climatic variation and changes in the wind and ocean circulation: The Little Ice Age in the northeast Atlantic. *Quaternary Research,* 11, 1-20.
LANGEHAUG, H. R., MEDHAUG, I., ELDEVIK, T. & OTTERÅ, O. H. 2012. Arctic/Atlantic Exchanges via the Subpolar Gyre*. *Journal of Climate,* 25, 2421-2439.

LAVENDER, K. L., BRECHNER OWENS, W. & DAVIS, R. E. 2005. The mid-depth circulation of the subpolar North Atlantic Ocean as measured by subsurface floats. *Deep-Sea Research Part I: Oceanographic Research Papers,* 52, 767-785.

LAVENDER, K. L., DAVIS, R. E. & OWENS, W. B. 2000. Mid-depth recirculation observed in the interior Labrador and Irminger seas by direct velocity measurements. *Nature,* 407, 66-69.

LAZIER, J., HENDRY, R., CLARKE, A., YASHAYAEV, I. & RHINES, P. 2002. Convection and restratification in the Labrador Sea, 1990-2000. *Deep-Sea Research Part I: Oceanographic Research Papers,* 49, 1819-1835.
LAZIER, J. R. N. 1980. Oceanographic conditions at Ocean Weather Ship Bravo, 1964–1974. *Atmosphere-Ocean,* 18, 227-238.

LEA, D. W., MASHIOTTA, T. A. & SPERO, H. J. 1999. Controls on magnesium and strontium uptake in planktonic foraminifera determined by live culturing. *Geochimica et Cosmochimica Acta,* 63, 2369-2379.

LEDUC, G., SCHNEIDER, R., KIM, J. H. & LOHMANN, G. 2010. Holocene and Eemian sea surface temperature trends as revealed by alkenone and Mg/Ca paleothermometry. *Quaternary Science Reviews,* 29, 989-1004.

LEGRANDE, A. N. & SCHMIDT, G. A. 2006. Global gridded data set of the oxygen isotopic composition in seawater. *Geophysical Research Letters,* 33.

LEHNER, F., RAIBLE, C. C. & STOCKER, T. F. 2012. Testing the robustness of a precipitation proxy-based North Atlantic Oscillation reconstruction. *Quaternary Science Reviews,* 45, 85-94.

LILLY, J. M. & RHINES, P. B. 2002. Coherent eddies in the Labrador Sea observed from a mooring. *Journal of Physical Oceanography,* 32, 585-598.

LOCKWOOD, M., HARRISON, R. G., OWENS, M. J., BARNARD, L., WOOLLINGS, T. & STEINHILBER, F. 2011. The solar influence on the probability of relatively cold UK winters in the future. *Environmental Research Letters,* 6.

LOCKWOOD, M., HARRISON, R. G., WOOLLINGS, T. & SOLANKI, S. K. 2010. Are cold winters in Europe associated with low solar activity? *Environmental Research Letters,* 5.

LU, Y., WRIGHT, D. G. & YASHAYAEV, I. 2007. Modelling hydrographic changes in the Labrador sea over the past five decades. *Progress In Oceanography,* 73, 406-426.

LUND, D. C. & CURRY, W. B. 2004. Late Holocene variability in Florida Current surface density: Patterns and possible causes. *Paleoceanography,* 19, 1-17.

LUND, D. C., LYNCH-STIEGLITZ, J. & CURRY, W. B. 2006. Gulf Stream density structure and transport during the past millennium. *Nature,* 444, 601-604.
LUO, D. 2005. Why is the North Atlantic block more frequent and long-lived during the negative NAO phase? *Geophys. Res. Lett.,* 32, L20804.

LYNCH-STIEGLITZ, J., STOCKER, T. F., BROECKER, W. S. & FAIRBANKS, R. G. 1995. The influence of air-sea exchange on the isotopic composition of oceanic carbon: Observations and modeling. *Global Biogeochemical Cycles,* 9, 653-665.

MACRANDER, A., SEND, U., VALDIMARSSON, H., JÓNSSON, S. & KÄSE, R. H. 2005. Interannual changes in the overflow from the Nordic Seas into the Atlantic Ocean through Denmark Strait. *Geophysical Research Letters,* 32, L06606.

MALMBERG, S. A. & JONSSON, S. 1997. Timing of deep convection in the Greenland and Iceland Seas. *Ices Journal of Marine Science,* 54, 300-309.

MANIGHETTI, B., MCCAVE, I. N., MASLIN, M. & SHACKLETON, N. J. 1995. Chronology for Climate Change: Developing Age Models for the Biogeochemical Ocean Flux Study Cores. *Paleoceanography,* 10, 513-525.

MANN, M. E. 2002a. *Little Ice Age,* Chichester, John Wiley & Sons, Ltd,.

MANN, M. E. 2002b. *Medieval Climatic Optimum,* Chichester, John Wiley & Sons, Ltd.

MANN, M. E., CANE, M. A., ZEBIAK, S. E. & CLEMENT, A. 2005. Volcanic and Solar Forcing of the Tropical Pacific over the Past 1000 Years. *Journal of Climate,* 18, 447-456.

MANN, M. E. & LEES, J. M. 1996. Robust estimation of background noise and signal detection in climatic time series. *Climatic Change,* 33, 409-445.

MANN, M. E., ZHANG, Z., RUTHERFORD, S., BRADLEY, R. S., HUGHES, M. K., SHINDELL, D., AMMANN, C., FALUVEGI, G. & NI, F. 2009. Global Signatures and Dynamical Origins of the Little Ice Age and Medieval Climate Anomaly. *Science,* 326, 1256-1260.

MARCHITTO, T. M. & DEMENOCAL, P. B. 2003. Late Holocene variability of upper North Atlantic Deep Water temperature and salinity. *Geochemistry, Geophysics, Geosystems,* 4.

MARSHALL, J., KUSHNIR, Y., BATTISTI, D., CHANG, P., CZAJA, A., DICKSON, R., HURRELL, J., MCCARTNEY, M., SARAVANAN, R. & VISBECK, M. 2001. North Atlantic climate variability: phenomena, impacts and mechanisms. *International Journal of Climatology,* 21, 1863-1898.

MARSHALL, J. & SCHOTT, F. 1999. Open-ocean convection: Observations, theory, and models. *Reviews in Geophysics,* 37, 1-64.

MASARIK, J. & BEER, J. 2009. An updated simulation of particle fluxes and cosmogenic nuclide production in the Earth's atmosphere. *J. Geophys. Res.,* 114, D11103.

MASHIOTTA, T. A., LEA, D. W. & SPERO, H. J. 1999. Glacial–interglacial changes in Subantarctic sea surface temperature and δ18O-water using foraminiferal Mg. *Earth and Planetary Science Letters,* 170, 417-432.

MASSÉ, G., ROWLAND, S. J., SICRE, M. A., JACOB, J., JANSEN, E. & BELT, S. T. 2008. Abrupt climate changes for Iceland during the last millennium: Evidence from high resolution sea ice reconstructions. *Earth and Planetary Science Letters,* 269, 564-568.

MATHIEN-BLARD, E. & BASSINOT, F. 2009. Salinity bias on the foraminifera Mg/Ca thermometry: Correction procedure and implications for past ocean hydrographic reconstructions. *Geochemistry Geophysics Geosystems,* 10, Q12011.

MAURITZEN, C. 1996. Production of dense overflow waters feeding the North Atlantic across the Greenland-Scotland Ridge. Part 1: Evidence for a revised circulation scheme. *Deep Sea Research Part I: Oceanographic Research Papers,* 43, 769-806.

MAYEWSKI, P. A., MEEKER, L. D., TWICKLER, M. S., WHITLOW, S., QINZHAO, Y., BERRY LYONS, W. & PRENTICE, M. 1997. Major features and forcing of high-latitude Northern Hemisphere atmospheric circulation using a 110 000-year-long glaciochemical series. *Journal of Geophysical Research,* 102, 26345-26366.

MAYEWSKI, P. A., ROHLING, E. E., STAGER, J. C., KARLÉN, W., MAASCH, K. A., MEEKER, L. D., MEYERSON, E. A., GASSE, F., VAN KREVELD, S., HOLMGREN, K., LEE-THORP, J., ROSQVIST, G., RACK, F., STAUBWASSER, M., SCHNEIDER, R. R. & STEIG, E. J. 2004. Holocene climate variability. *Quaternary Research,* 62, 243-255.

MCCARTNEY, M. S. & MAURITZEN, C. 2001. On the origin of the warm inflow to the Nordic Seas. *Progress In Oceanography,* 51, 125-214.

MCCARTNEY, M. S. & TALLEY, L. D. 1982. The subpolar mode water of the North Atlantic Ocean. *J. Phys. Oceanogr.*, 51, 118-1169.

MCCAVE, I. N. 2004. CD159 Cruise Report.

MCCAVE, I. N. & HALL, I. R. 2006. Size sorting in marine muds: Processes, pitfalls, and prospects for paleoflow-speed proxies. *Geochemistry Geophysics Geosystems,* 7, Q10N05.

MCCAVE, I. N., HALL, I. R. & BIANCHI, G. G. 2006. Laser vs. settling velocity differences in silt grainsize measurements: estimation of palaeocurrent vigour. *Sedimentology,* 53, 919-928.

MCCAVE, I. N., MANIGHETTI, B. & ROBINSON, S. G. 1995. Sortable Silt and Fine Sediment Size/Composition Slicing: Parameters for Palaeocurrent Speed and Palaeoceanography. *Paleoceanography,* 10, 593-610.

MCCAVE, I. N. & TUCHOLKE, B. E. 1986. *Deep Current-Controlled Sedimentation in the Western North Atlantic,* Geological Society of America.

MCCONNELL, M. C. & THUNELL, R. C. 2005. Calibration of the planktonic foraminiferal Mg/Ca paleothermometer: Sediment trap results from the Guaymas Basin, Gulf of California. *Paleoceanography,* 20, PA2016.

MEEKER, L. D. & MAYEWSKI, P. A. 2002. A 1400-year high-resolution record of atmospheric circulation over the North Atlantic and Asia. *Holocene,* 12, 257-266.

MIGNOT, J., KHODRI, M., FRANKIGNOUL, C. & SERVONNAT, J. 2011. Volcanic impact on the Atlantic Ocean over the last millennium. *Climate of the Past,* 7, 1439-1455.

MILLER, G. H., GEIRSDÓTTIR, A., ZHONG, Y., LARSEN, D. J., OTTO-BLIESNER, B. L., HOLLAND, M. M., BAILEY, D. A., REFSNIDER, K. A., LEHMAN, S. J., SOUTHON, J. R., ANDERSON, C., BJÖRNSSON, H. & THORDARSON, T. 2012. Abrupt onset of the Little Ice Age triggered by volcanism and sustained by sea-ice/ocean feedbacks. *Geophysical Research Letters,* 39.

MILLIGAN, T. G. & KRANCK, K. 1997. Electroresistance particle size analyzers. . *In:* J.P.M.SYVITSKI (ed.) *Principles, Methods, and Application of Particle Size Analysis.* Cambridge University Press, Cambridge.

MORLEY, A., SCHULZ, M., ROSENTHAL, Y., MULITZA, S., PAUL, A. & RÜHLEMANN, C. 2011. Solar modulation of North Atlantic central Water formation at multidecadal timescales during the late Holocene. *Earth and Planetary Science Letters,* 308, 161-171.

MOROS, M., ANDREWS, J. T., EBERL, D. D. & JANSEN, E. 2006. Holocene history of drift ice in the northern North Atlantic: Evidence for different spatial and temporal modes. *Paleoceanography,* 21.

MOROS, M., EMEIS, K., RISEBROBAKKEN, B., SNOWBALL, I., KUIJPERS, A., MCMANUS, J. & JANSEN, E. 2004. Sea surface temperatures and ice rafting in the Holocene North Atlantic: climate influences on northern Europe and Greenland. *Quaternary Science Reviews,* 23, 2113-2126.

MUCCI, A. 1987. Influence of temperature on the composition of magnesian calcite overgrowths precipitated from seawater. *Geochimica et Cosmochimica Acta,* 51, 1977-1984.

MUDELSEE, M. 2003. Estimating Pearson's correlation coefficient with bootstrap confidence interval from serially dependent time series. *Mathematical Geology,* 35, 651-665.

MULITZA, S., DURKOOP, A., HALE, W., WEFER, G. & NIEBLER, H. S. 1997. Planktonic foraminifera as recorders of past surface-water stratification. *Geology,* 25, 335-338.

MÜLLER, J., WERNER, K., STEIN, R., FAHL, K., MOROS, M. & JANSEN, E. 2012. Holocene cooling culminates in sea ice oscillations in Fram Strait. *Quaternary Science Reviews,* 47, 1-14.

MURRAY 1897. On the distribution of the pelagic Foraminifera at the surface and on the floor of the ocean. *Journal of Natural Sciences,* 11, 17-27.

NESJE, A. & DAHL, S. O. 2001. Late-glacial to Holocene environmental changes and climate variability: Evidence from Voldafjorden, Western Norway. *Journal of Quaternary Science,* 16, 181-198.

NORRIS, R. D. & DE VARGAS, C. 2000. Evolution all at sea. *Nature,* 405, 23-24.
NURNBERG, D. 1995. Magnesium in tests of Neogloboquadrina pachyderma sinistral from high northern and southern latitudes. *Journal of Foraminiferal Research,* 25, 350-368.

NÜRNBERG, D., BIJMA, J. & HEMLEBEN, C. 1996. Assessing the reliability of magnesium in foraminiferal calcite as a proxy for water mass temperatures. *Geochimica et Cosmochimica Acta,* 60, 803-814.

NYBERG, J., MALMGREN, B. A., KUIJPERS, A. & WINTER, A. 2002. A centennial-scale variability of tropical North Atlantic surface hydrography during the late Holocene. *Palaeogeography, Palaeoclimatology, Palaeoecology,* 183, 25-41.

NYLAND, B. F., JANSEN, E., ELDERFIELD, H. & ANDERSSON, C. 2006. Neogloboquadrina pachyderma (dex. and sin.) Mg/Ca and δ18O records from the Norwegian Sea. *Geochemistry, Geophysics, Geosystems,* 7.

OGILVIE, A. E. J. & JÓNSSON, T. 2001. "Little ice age" research: A perspective from iceland. *Climatic Change,* 48, 9-52.

ÓLAFSDÓTTIR, S., JENNINGS, A. E., GEIRSDÓTTIR, A., ANDREWS, J. & MILLER, G. H. 2010. Holocene variability of the North Atlantic Irminger current on the south- and northwest shelf of Iceland. *Marine Micropaleontology,* 77, 101-118.

OLSEN, S. M., HANSEN, B., QUADFASEL, D. & OSTERHUS, S. 2008. Observed and modelled stability of overflow across the Greenland-Scotland ridge. *Nature,* 455, 519-522.
OOMORI, T., KANESHIMA, H., MAEZATO, Y. & KITANO, Y. 1987. DISTRIBUTION COEFFICIENT OF MG-2+ IONS BETWEEN CALCITE AND SOLUTION AT 10-50-DEGREES-C. *Marine Chemistry,* 20, 327-336.

OPPO, D. W., MCMANUS, J. F. & CULLEN, J. L. 2003. Palaeo-oceanography: Deepwater variability in the Holocene epoch. *Nature,* 422, 277-277.

ORVIK, K. A. & NIILER, P. 2002. Major pathways of Atlantic water in the northern North Atlantic and Nordic Seas toward Arctic. *Geophysical Research Letters,* 29, 1896.

ORVIK, K. A. & SKAGSETH, Ø. 2003. The impact of the wind stress curl in the North Atlantic on the Atlantic inflow to the Norwegian Sea toward the Arctic. *Geophysical Research Letters,* 30, 1884.

ØSTERHUS, S., TURRELL, W. R., JÓNSSON, S. & HANSEN, B. 2005. Measured volume, heat, and salt fluxes from the Atlantic to the Arctic Mediterranean. *Geophysical Research Letters,* 32, L07603.

PARDOIGUZQUIZA, E., CHICAOLMO, M. & RODRIGUEZTOVAR, F. J. 1994. CYSTRATI - A COMPUTER-PROGRAM FOR SPECTRAL-ANALYSIS OF STRATIGRAPHIC SUCCESSIONS. *Computers & Geosciences,* 20, 511-584.
PEETERS, F. J. C., BRUMMER, G. J. A. & GANSSEN, G. 2002. The effect of upwelling on the distribution and stable isotope composition of Globigerina bulloides and Globigerinoides ruber (planktic foraminifera) in modern surface waters of the NW Arabian Sea. *Global and Planetary Change,* 34, 269-291.

PENA, L. D., CALVO, E., CACHO, I., EGGINS, S. & PELEJERO, C. 2005. Identification and removal of Mn-Mg-rich contaminant phases on foraminiferal tests: Implications for Mg/Ca past temperature reconstructions. *Geochemistry Geophysics Geosystems,* 6, Q09P02.

PÉREZ-BRUNIUS, P., ROSSBY, T. & WATTS, D. R. 2004. Absolute Transports of Mass and Temperature for the North Atlantic Current– Subpolar Front System. *Journal of Physical Oceanography,* 34, 1870-1883.

PERNER, K., MOROS, M., LLOYD, J. M., KUIJPERS, A., TELFORD, R. J. & HARFF, J. 2011. Centennial scale benthic foraminiferal record of late Holocene oceanographic variability in Disko Bugt, West Greenland. *Quaternary Science Reviews,* 30, 2815-2826.

PICKART, R. S., SPALL, M. A., RIBERGAARD, M. H., MOORE, G. W. K. & MILLIFF, R. F. 2003. Deep convection in the Irminger sea forced by the Greenland tip jet. *Nature,* 424, 152-156.

PINTO, J. G. & RAIBLE, C. C. 2012. Past and recent changes in the North Atlantic oscillation. *Wiley Interdisciplinary Reviews: Climate Change,* 3, 79-90.

PORTER, S. C. & DENTON, G. H. 1967. Chronology of neoglaciation in the North American Cordillera. *American Journal of Science,* 265, 177-210.

POZO-VÁZQUEZ, D., ESTEBAN-PARRA, M. J., RODRIGO, F. S. & CASTRO-DÍEZ, Y. 2001. The Association between ENSO and Winter Atmospheric Circulation and Temperature in the North Atlantic Region. *Journal of Climate,* 14, 3408-3420.

PRICE, J. F. & BARINGER, M. O. 1994. OUTFLOWS AND DEEP-WATER PRODUCTION BY MARGINAL SEAS. *Progress In Oceanography,* 33, 161-200.

RAHMSTORF, S. 2002. Ocean circulation and climate during the past 120,000 years. *Nature,* 419, 207-214.

RAIBLE, C., YOSHIMORI, M., STOCKER, T. & CASTY, C. 2007. Extreme midlatitude cyclones and their implications for precipitation and wind speed extremes in simulations of the Maunder Minimum versus present day conditions. *Climate Dynamics,* 28, 409-423.

RASHID, H. & BOYLE, E. A. 2007. Mixed-Layer Deepening During Heinrich Events: A Multi-Planktonic Foraminiferal $\delta^{18}O$ Approach. *Science,* 318, 439-441.

RAVELO, A. C. & HILLAIRE-MARCEL, C. 2007. Chapter Eighteen The Use of Oxygen and Carbon Isotopes of Foraminifera in Paleoceanography. *In:* CLAUDE, H. M. & ANNE DE, V. (eds.) *Developments in Marine Geology.* Elsevier.

REIMER, P, J., BAILLIE, M. G, L., BARD, E, BAYLISS, A, BECK, J, W., BLACKWELL, P, G., RAMSEY, BRONK, C., BUCK, C, E., BURR, G, S., EDWARDS, R, L., FRIEDRICH, M, GROOTES, P, M., GUILDERSON, T, P., HAJDAS, I, HEATON, T, J., HOGG, A, G., HUGHEN, K, A., KAISER, K, F., KROMER, B, MCCORMAC, F, G., MANNING, S, W., R, W., RICHARDS, D, A., SOUTHON, J, R., TALAMO, S, TURNEY, C. S, M., VAN DER, P., J & WEYHENMEYER 2009. *INTCAL09 AND MARINE09 RADIOCARBON AGE CALIBRATION CURVES, 0-50,000 YEARS CAL BP*, Tucson, AZ, ETATS-UNIS, University of Arizona.

RENSSEN, H., GOOSSE, H. & MUSCHELER, R. 2006. Coupled climate model simulation of Holocene cooling events: Solar forcing triggers oceanic feedback. *Climate of the Past Discussions,* 2, 209-232.

RENSSEN, H., SEPPA, H., HEIRI, O., ROCHE, D. M., GOOSSE, H. & FICHEFET, T. 2009. The spatial and temporal complexity of the Holocene thermal maximum. *Nature Geosciences,* 2, 411-414.

RHEIN, M., FISCHER, J., SMETHIE, W. M., SMYTHE-WRIGHT, D., WEISS, R. F., MERTENS, C., MIN, D. H., FLEISCHMANN, U. & PUTZKA, A. 2002. Labrador Sea Water: Pathways, CFC inventory, and formation rates. *Journal of Physical Oceanography,* 32, 648-665.

RICHEY, J. N., POORE, R. Z., FLOWER, B. P., QUINN, T. M. & HOLLANDER, D. J. 2009. Regionally coherent Little Ice Age cooling in the Atlantic Warm Pool. *Geophysical Research Letters,* 36.

RICHTER, T. O., PEETERS, F. J. C. & VAN WEERING, T. C. E. 2009. Late Holocene (0-2.4 ka BP) surface water temperature and salinity variability, Feni Drift, NE Atlantic Ocean. *Quaternary Science Reviews,* 28, 1941-1955.

RIMBU, N., LOHMANN, G., KIM, J. H., ARZ, H. W. & SCHNEIDER, R. 2003. Arctic/North Atlantic Oscillation signature in Holocene sea surface temperature trends as obtained from alkenone data. *Geophysical Research Letters,* 30, 1280.

RISEBROBAKKEN, B., JANSEN, E., ANDERSSON, C., MJELDE, E. & HEVRØY, K. 2003. A high-resolution study of Holocene paleoclimatic and paleoceanographic changes in the Nordic Seas. *Paleoceanography,* 18, 17-1.

RISEBROBAKKEN, B., MOROS, M., IVANOVA, E. V., CHISTYAKOVA, N. & ROSENBERG, R. 2010. Climate and oceanographic variability in the SW Barents Sea during the Holocene. *Holocene,* 20, 609-621.

ROBOCK, A. 2000. Volcanic eruptions and climate. *Reviews of Geophysics,* 38, 191-219.

RODWELL, M. J., ROWELL, D. P. & FOLLAND, C. K. 1999. Oceanic forcing of the wintertime North Atlantic Oscillation and European climate. *Nature,* 398, 320-323.

ROSENTHAL, Y. 2007. Chapter Nineteen Elemental Proxies for Reconstructing Cenozoic Seawater Paleotemperatures from Calcareous Fossils. *In:* CLAUDE, H. M. & ANNE DE, V. (eds.) *Developments in Marine Geology.* Elsevier.

ROSENTHAL, Y., LOHMANN, G. P., LOHMANN, K. C. & SHERRELL, R. M. 2000. Incorporation and Preservation of Mg in Globigerinoides sacculifer: Implications for Reconstructing the Temperature and 18O/16O of Seawater. *Paleoceanography,* 15, 135-145.

ROSQVIST, G. C., LENG, M. J. & JONSSON, C. 2007. North Atlantic region atmospheric circulation dynamics inferred from a late-Holocene lacustrine carbonate isotope record, northern Swedish Lapland. *Holocene,* 17, 867-873.

ROSSBY, T. 1996. The North Atlantic Current and surrounding waters: At the crossroads. *Reviews of Geophysics,* 34, 463-481.

ROSSBY, T. & FLAGG, C. N. 2012. Direct measurement of volume flux in the Faroe-Shetland Channel and over the Iceland-Faroe Ridge. *Geophysical Research Letters,* 39, L07602.

RUDELS, B., FAHRBACH, E., MEINCKE, J., BUDEUS, G. & ERIKSSON, P. 2002. The East Greenland Current and its contribution to the Denmark Strait overflow. *Ices Journal of Marine Science,* 59, 1133-1154.

RUSSEL, W. B. 1980. Review of the Role of Colloidal Forces in the Rheology of Suspensions. *Journal of Rheology,* 24,, 287-317.

SABBATINI, A., BASSINOT, F., BOUSSETTA, S., NEGRI, A., REBAUBIER, H., DEWILDE, F., NOUET, J., CAILLON, N. & MORIGI, C. 2011. Further constraints on

the diagenetic influences and salinity effect on Globigerinoides ruber (white) Mg/Ca thermometry: Implications in the Mediterranean Sea. *Geochemistry Geophysics Geosystems,* 12, Q10005.

SACHS, J. P. 2007. Cooling of Northwest Atlantic slope waters during the Holocene. *Geophys. Res. Lett.,* 34, L03609.

SACHS, J. P., SACHSE, D., SMITTENBERG, R. H., ZHANG, Z., BATTISTI, D. S. & GOLUBIC, S. 2009. Southward movement of the Pacific intertropical convergence zone AD[thinsp]1400-1850. *Nature Geosci,* 2, 519-525.

SAENGER, C., CAME, R. E., OPPO, D. W., KEIGWIN, L. D. & COHEN, A. L. 2011. Regional climate variability in the western subtropical North Atlantic during the past two millennia. *Paleoceanography,* 26.

SAENGER, C., COHEN, A. L., OPPO, D. W., HALLEY, R. B. & CARILLI, J. E. 2009. Surface-temperature trends and variability in the low-latitude North Atlantic since 1552. *Nature Geosci,* advanced online publication.

SAENGER, C., COHEN, A. L., OPPO, D. W. & HUBBARD, D. 2008. Interpreting sea surface temperature from strontium/calcium ratios in Montastrea corals: Link with growth rate and implications for proxy reconstructions. *Paleoceanography,* 23, PA3102.

SARAFANOV, A., FALINA, A., MERCIER, H., LHERMINIER, P. & SOKOV, A. 2009. Recent changes in the Greenland-Scotland overflow-derived water transport inferred from hydrographic observations in the southern Irminger Sea. *Geophysical Research Letters,* 36, L13606.

SCHLESINGER, M. E. & RAMANKUTTY, N. 1994. An oscillation in the global climate system of period 65-70 years. *Nature,* 367, 723-726.
SCHMIDT, G. A. 1999. Error Analysis of Paleosalinity Calculations. *Paleoceanography,* 14, 422-429.

SCHMUTZ, C., LUTERBACHER, J., GYALISTRAS, D., XOPLAKI, E. & WANNER, H. 2000. Can we trust proxy based NAO index reconstructions? *Geophysical Research Letters,* 27, 1135-1138.

SCHNEIDER, D. P., AMMANN, C. M., OTTO-BLIESNER, B. L. & KAUFMAN, D. S. 2009. Climate response to large, high-latitude and low-latitude volcanic eruptions in the community climate system model. *Journal of Geophysical Research* 114.

SCHULZ, M. & PAUL, A. 2002. Holocene climate variability on centennial-to-millennial time scales: 1. Climate records from the North-Atlantic realm.

SCHULZ, M., PRANGE, M. & KLOCKER, A. 2007. Low-frequency oscillations of the Atlantic Ocean meridional overturning circulation in a coupled climate model. *Climate of the Past,* 3, 97-107.

SEAGER, R., BATTISTI, D. S., YIN, J., GORDON, N., NAIK, N., CLEMENT, A. C. & CANE, M. A. 2002. Is the Gulf Stream responsible for Europe's mild winters? *Quarterly Journal of the Royal Meteorological Society,* 128, 2563-2586.

SEJRUP, H. P., HAFLIDASON, H. & ANDREWS, J. T. 2011. A Holocene North Atlantic SST record and regional climate variability. *Quaternary Science Reviews,* 30, 3181-3195.

SERRA, N., KÄSE, R. H., KÖHL, A., STAMMER, D. & QUADFASEL, D. 2010. On the low-frequency phase relation between the Denmark Strait and the Faroe-Bank Channel overflows. *Tellus A,* 62, 530-550.

SHABBAR, A., HUANG, J. P. & HIGUCHI, K. 2001. The relationship between the wintertime North Atlantic Oscillation and blocking episodes in the North Atlantic. *International Journal of Climatology,* 21, 355-+.

SHACKLETON, N. 1967. Oxygen Isotope Analyses and Pleistocene Temperatures Re-assessed. *Nature,* 215, 15-17.

SHINDELL, D. 1999. Solar cycle variability, ozone, and climate. *Science,* 284, 305-308.

SHINDELL, D. T., SCHMIDT, G. A., MANN, M. E., RIND, D. & WAPLE, A. 2001. Solar forcing of regional climate change during the Maunder Minimum. *Science,* 294, 2149-2152.

SHINDELL, D. T., SCHMIDT, G. A., MILLER, R. L. & MANN, M. E. 2003. Volcanic and solar forcing of climate change during the preindustrial era. *Journal of Climate,* 16, 4094-4107.

SHOR, N. A. 1974. Bottom Currents and Abyssal Sedimentation Processes South of Iceland. Degree of Doctor in Phylosophy.

SICRE, M.-A., YIOU, P., EIRIKSSON, J., EZAT, U., GUIMBAUT, E., DAHHAOUI, I.,
KNUDSEN, K.-L., JANSEN, E. & TURON, J.-L. 2008a. A 4500-year reconstruction of sea surface temperature variability at decadal time-scales off North Iceland. *Quaternary Science Reviews,* 27, 2041-2047.

SICRE, M. A., HALL, I. R., MIGNOT, J., KHODRI, M., EZAT, U., TRUONG, M. X., EIRÍKSSON, J. & KNUDSEN, K. L. 2011. Sea surface temperature variability in the subpolar Atlantic over the last two millennia. *Paleoceanography,* 26.

SICRE, M. A., JACOB, J., EZAT, U., ROUSSE, S., KISSEL, C., YIOU, P., EIRÍKSSON, J., KNUDSEN, K. L., JANSEN, E. & TURON, J. L. 2008b. Decadal variability of sea surface temperatures off North Iceland over the last 2000 years. *Earth and Planetary Science Letters,* 268, 137-142.

SIEGENTHALER, U. & SARMIENTO, J. L. 1993. Atmospheric carbon dioxide and the
ocean. *Nature,* 365, 119-125.
SIMSTICH, J., SARNTHEIN, M. & ERLENKEUSER, H. 2003. Paired δ18O signals of Neogloboquadrina pachyderma (s) and Turborotalita quinqueloba show thermal stratification structure in Nordic Seas. *Marine Micropaleontology,* 48, 107-125.

SOLIGNAC, S., DE VERNAL, A. & HILLAIRE-MARCEL, C. 2004. Holocene sea-surface conditions in the North Atlantic - Contrasted trends and regimes in the western and eastern sectors (Labrador Sea vs. Iceland Basin). *Quaternary Science Reviews,* 23, 319-334.

SOLIGNAC, S., SEIDENKRANTZ, M. S., JESSEN, C., KUIJPERS, A., GUNVALD, A. K. & OLSEN, J. 2011. Late-holocene sea-surface conditions offshore Newfoundland based on dinoflagellate cysts. *Holocene,* 21, 539-552.

SPANGEHL, T., CUBASCH, U., RAIBLE, C. C., SCHIMANKE, S., KÖRPER, J. & HOFER, D. 2010. Transient climate simulations from the Maunder Minimum to present day: Role of the stratosphere. *Journal of Geophysical Research,* 115, D00I10.

SPERO, H. J., BIJMA, J., LEA, D. W. & BERNIS, B. E. 1997. Effect of seawater carbonate concentration on foraminiferal carbon and oxygen isotopes. *Nature,* 390, 497-500.

SPERO, H. J. & WILLIAMS, D. F. 1988. Extracting environmental information from planktonic foraminiferal δ13C data. *Nature,* 335, 717-719.

SPIELHAGEN, R. F., WERNER, K., SØRENSEN, S. A., ZAMELCZYK, K., KANDIANO, E., BUDEUS, G., HUSUM, K., MARCHITTO, T. M. & HALD, M. 2011. Enhanced Modern Heat Transfer to the Arctic by Warm Atlantic Water. *Science,* 331, 450-453.

STANFORD, J. D., ROHLING, E. J., BACON, S. & HOLLIDAY, N. P. 2011. A review of the deep and surface currents around Eirik Drift, south of Greenland: Comparison of the past with the present. *Global and Planetary Change,* 79, 244-254.

STANGEEW, E. 2001. Distribution and isotopic composition of living planktonic foraminifera N. pachyderma (sinistral) and T. quinqueloba in the high latitude North Atlantic. Ph.D. dissertation, , Christian-Albrechts-Univ.

STEINHILBER, F., ABREU, J. A., BEER, J., BRUNNER, I., CHRISTL, M., FISCHER, H., HEIKKILÄ, U., KUBIK, P. W., MANN, M., MCCRACKEN, K. G., MILLER, H., MIYAHARA, H., OERTER, H. & WILHELMS, F. 2012. 9,400 years of cosmic radiation and solar activity from ice cores and tree rings. *Proceedings of the National Academy of Sciences,* 109, 5967-5971.

STEINHILBER, F., BEER, J. & FRÖHLICH, C. 2009. Total solar irradiance during the Holocene. *Geophysical Research Letters,* 36.
STEWART, I. A., DARLING, K. F., KROON, D., WADE, C. M. & TROELSTRA, S. R. 2001. Genotypic variability in subarctic Atlantic planktic foraminifera. *Marine Micropaleontology,* 43, 143-153.

STOMMEL, H. 1961. Thermohaline Convection with Two Stable Regimes of Flow. *Tellus,* 13, 224-230.

STRANEO, F. 2006. Heat and freshwater transport through the central Labrador Sea. *Journal of Physical Oceanography,* 36, 606-628.

STRASS, V. H., FAHRBACH, E., SCHAUER, U. & SELLMANN, L. 1993. Formation of Denmark Strait Overflow Water by Mixing in the East Greenland Current. *Journal of Geophysical Research,* 98, 6907-6919.

STUIVER, M. & BRAZIUNAS, T. F. 1993a. MODELING ATMOSPHERIC C-14 INFLUENCES AND C-14 AGES OF MARINE SAMPLES TO 10,000 BC. *Radiocarbon,* 35, 137-189.

STUIVER, M. & BRAZIUNAS, T. F. 1993b. Sun, ocean, climate and atmospheric $^{14}CO_2$: an evaluation of causal and spectral relationships. *The Holocene,* 3, 289-305.

STUIVER, M., BRAZIUNAS, T. F., GROOTES, P. M. & ZIELINSKI, G. A. 1997. Is There Evidence for Solar Forcing of Climate in the GISP2 Oxygen Isotope Record? *Quaternary Research,* 48, 259-266.

STUIVER, M. A. P., H A. 1977. Discussion: Reporting of 14C Data. *Radiocarbon,* 19, 355-363.

SUTTON, R. T. & HODSON, D. L. R. 2005. Atlantic Ocean forcing of North American and European summer climate. *Science,* 309, 115-118.

SWIFT, J. H. 1984. The circulation of the Denmark Strait and Iceland-Scotland overflow waters in the North Atlantic. *Deep Sea Research Part A. Oceanographic Research Papers,* 31, 1339-1355.

SWIFT, J. H. & AAGAARD, K. 1981. Seasonal transitions and water mass formation in the Iceland and Greenland seas. *Deep Sea Research Part A. Oceanographic Research Papers,* 28, 1107-1129.

SWIFT, J. H., AAGAARD, K. & MALMBERG, S. A. 1980. CONTRIBUTION OF THE DENMARK STRAIT OVERFLOW TO THE DEEP NORTH-ATLANTIC. *Deep-Sea Research Part A -Oceanographic Research Papers,* 27, 29-42.

SWINGEDOUW, D., TERRAY, L., CASSOU, C., VOLDOIRE, A., SALAS-MELIA, D. & SERVONNAT, J. 2011. Natural forcing of climate during the last millennium: fingerprint of solar variability. *Climate Dynamics,* 36, 1349-1364.

TALLEY, L. D. 2003. Shallow, intermediate, and deep overturning components of the global heat budget. *Journal of Physical Oceanography,* 33, 530-560.

TALLEY, L. D. & MCCARTNEY, M. S. 1982. Distribution and circulation of Labrador Sea Water. *Journal of Physical Oceanography,* 12, 1189-1205.

TANHUA, T., OLSSON, K. A. & JEANSSON, E. 2005. Formation of Denmark Strait overflow water and its hydro-chemical composition. *Journal of Marine Systems,* 57, 264-288.

THORNALLEY, D. J. R., ELDERFIELD, H. & MCCAVE, I. N. 2009. Holocene oscillations in temperature and salinity of the surface subpolar North Atlantic. *Nature,* 457, 711-714.

TORRENCE, C. & G. P. COMPO 1998. A Practical Guide to Wavelet Analysis. *Bulletin American Metereological Society,* 79, 61-78.

TROUET, V., ESPER, J., GRAHAM, N. E., BAKER, A., SCOURSE, J. D. & FRANK, D. C. 2009. Persistent positive north atlantic oscillation mode dominated the medieval climate anomaly. *Science,* 324, 78-80.

TROUET, V., SCOURSE, J. D. & RAIBLE, C. C. 2012. North Atlantic storminess and Atlantic Meridional Overturning Circulation during the last Millennium: Reconciling contradictory proxy records of NAO variability. *Global and Planetary Change,* 84-85, 48-55.

UREY, H. C. 1947. The thermodynamic properties of isotopic substances. *Journal of the Chemical Society (Resumed),* 562-581.

VAGE, K., PICKART, R. S., SPALL, M. A., VALDIMARSSON, H., JONSSON, S., TORRES, D. J., OSTERHUS, S. & ELDEVIK, T. 2011. Significant role of the North Icelandic Jet in the formation of Denmark Strait overflow water. *Nature Geosci,* 4, 723-727.

VÅGE, K., PICKART, R. S., THIERRY, V., REVERDIN, G., LEE, C. M., PETRIE, B., AGNEW, T. A., WONG, A. & RIBERGAARD, M. H. 2009. Surprising return of deep convection to the subpolar North Atlantic Ocean in winter 2007-2008. *Nature Geoscience,* 2, 67-72.

VAN AKEN, H. M. 1995. HYDROGRAPHIC VARIABILITY IN THE BOTTOM LAYER OF THE ICELAND BASIN. *Journal of Physical Oceanography,* 25, 1716-1722.

VAN AKEN, H. M. & BECKER, G. 1996. Hydrography and through-flow in the north-eastern North Atlantic Ocean: the NANSEN project. *Progress In Oceanography,* 38, 297-346.

VAN AKEN, H. M., FEMKE DE JONG, M. & YASHAYAEV, I. 2011. Decadal and multi-decadal variability of Labrador Sea Water in the north-western North Atlantic Ocean derived from tracer distributions: Heat budget, ventilation, and advection. *Deep-Sea Research Part I: Oceanographic Research Papers,* 58, 505-523.

VELLINGA, M. & WU, P. 2004. Low-Latitude Freshwater Influence on Centennial Variability of the Atlantic Thermohaline Circulation. *Journal of Climate,* 17, 4498-4511.

VIEIRA, L. E. A., SOLANKI, S. K., KRIVOVA, N. A. & USOSKIN, I. 2011. Evolution of the solar irradiance during the Holocene. *Astronomy and Astrophysics,* 531.

VISBECK, M., CHASSIGNET, E. P., CURRY, R. G., DELWORTH, T. L., DICKSON, R. R. & KRAHMANN, G. 2003. The ocean's response to North Atlantic Oscillation variability. *The North Atlantic Oscillation: Climatic Significance and Environmental Impact.* Washington, DC: AGU.

WALSH, J, E., CHAPMAN & W, L. 1990. *Arctic contribution to upper-ocean variability in the North Atlantic,* Boston, MA, ETATS-UNIS, American Meteorological Society.

WANAMAKER, A. D., BUTLER, P. G., SCOURSE, J. D., HEINEMEIER, J., EIRÍKSSON, J., KNUDSEN, K. L. & RICHARDSON, C. A. 2012. Surface changes in the North Atlantic meridional overturning circulation during the last millennium. *Nat Commun,* 3, 899.

WANG, Y., CHENG, H., EDWARDS, R. L., HE, Y., KONG, X., AN, Z., WU, J., KELLY, M. J., DYKOSKI, C. A. & LI, X. 2005. The Holocene Asian Monsoon: Links to Solar Changes and North Atlantic Climate. *Science,* 308, 854-857.

WANNER, H., BEER, J., BÜTIKOFER, J., CROWLEY, T. J., CUBASCH, U., FLÜCKIGER, J., GOOSSE, H., GROSJEAN, M., JOOS, F., KAPLAN, J. O., KÜTTEL, M., MÜLLER, S. A., PRENTICE, I. C., SOLOMINA, O., STOCKER, T. F., TARASOV, P., WAGNER, M. & WIDMANN, M. 2008. Mid- to Late Holocene climate change: an overview. *Quaternary Science Reviews,* 27, 1791-1828.

WANNER, H., SOLOMINA, O., GROSJEAN, M., RITZ, S. P. & JETEL, M. 2011. Structure and origin of Holocene cold events. *Quaternary Science Reviews,* 30, 3109-3123.

WEAVER, C. E. (ed.) 1989. *Clays, Muds and Shales*: Elsevier.

WEEDON, G. 2003. Time-Series Analysis and Cyclostratigraphy. Examining stratigraphic
records of environmental cycles., Cambridge, Cambridge University Press.

WEI, G., Z., L., DENG W.F., LI X.H., LIU, Y. & CHEN Y, L. 2009. Mn/Ca ratio in planktonic foraminifer from ODP Site 1144, the northern South China Sea: A possible paleoclimate indicator. *Geochemical Journal,* Vol. 43, 235-246.

WERNER, K., SPIELHAGEN, R. F., BAUCH, D., HASS, H. C., KANDIANO, E. & ZAMELCZYK, K. 2011. Atlantic Water advection to the eastern Fram Strait - Multiproxy evidence for late Holocene variability. *Palaeogeography Palaeoclimatology Palaeoecology,* 308, 264-276.

WHITEHEAD, J. A. 1998. Topographic control of oceanic flows in deep passages and straits. *Reviews of Geophysics,* 36, 423-440.

WILKENSKJELD, S. & QUADFASEL, D. 2005. Response of the Greenland-Scotland overflow to changing deep water supply from the Arctic Mediterranean. *Geophysical Research Letters,* 32, L21607.

WILSON, P., MCGOURTY, J. & BATEMAN, M. D. 2004. Mid- to late-Holocene coastal dune event stratigraphy for the north coast of Northern Ireland. *Holocene,* 14, 406-416.
WOLD, C. N. 1994. Cenozoic Sediment Accumulation on Drifts in the Northern North Atlantic. *Paleoceanography,* 9, 917-941.

WOOLLINGS, T., CHARLTON-PEREZ, A., INESON, S., MARSHALL, A. G. & MASATO, G. 2010a. Associations between stratospheric variability and tropospheric blocking. *J. Geophys. Res.,* 115, D06108.

WOOLLINGS, T., LOCKWOOD, M., MASATO, G., BELL, C. & GRAY, L. 2010b. Enhanced signature of solar variability in Eurasian winter climate. *Geophysical Research Letters,* 37.

YASHAYAEV, I. 2007a. Changing freshwater content: Insights from the subpolar North Atlantic and new oceanographic challenges. *Progress In Oceanography,* 73, 203-209.

YASHAYAEV, I. 2007b. Hydrographic changes in the Labrador Sea, 1960-2005. *Progress In Oceanography,* 73, 242-276.

YASHAYAEV, I., VAN AKEN, H. M., HOLLIDAY, N. P. & BERSCH, M. 2007. Transformation of the Labrador Sea Water in the subpolar North Atlantic. *Geophysical Research Letters,* 34.

ZEEBE, R. E., BIJMA, J. & WOLF-GLADROW, D. A. 1999. A diffusion-reaction model of carbon isotope fractionation in foraminifera. *Marine Chemistry,* 64, 199-227.

ZHANG, R., DELWORTH, T. L., ROSATI, A., ANDERSON, W. G., DIXON, K. W., LEE,
H.-C. & ZENG, F. 2011. Sensitivity of the North Atlantic Ocean Circulation to an abrupt change in the Nordic Sea overflow in a high resolution global coupled climate model. *Journal of Geophysical Research,* 116, C12024.

ZHONG, Y., MILLER, G. H., OTTO-BLIESNER, B. L., HOLLAND, M. M., BAILEY, D. A., SCHNEIDER, D. P. & GEIRSDOTTIR, A. 2011. Centennial-scale climate change from decadally-paced explosive volcanism: A coupled sea ice-ocean mechanism. *Climate Dynamics,* 37, 2373-2387.

ZORITA, E., VON STORCH, H., GONZALEZ-ROUCO, F. J., CUBASCH, U., LUTERBACHER, J., LEGUTKE, S., FISCHER-BRUNS, I. & SCHLESE, U. 2004. Climate evolution in the last five centuries simulated by an atmosphere-ocean model: global temperatures, the North Atlantic Oscillation and the Late Maunder Minimum.

Radiocarbon Ages

RAPiD-35-25B

Publication Code	Depth (cm)	14C Enrichment (%modern)	14C ages (years BP)	+/- 1σ error	Years AD					
					Cal. Age +1σ	Cal. Age -1σ	Cal. Age +2σ	Cal. Age -2σ	Average 1σ	Average 2σ
OS-82608	0.25	96.4	285	30						
SUERC-35759	6.25	91.42	720	37	1541	1637	1503	1666	1589	1585
OS-86418	16.75	89.4	895	25	1425	1462	1403	1486	1444	1445
SUERC-35760	22.75	86.71	895	25	1230	1291	1185	1313	1261	1249
OS-86417	28.75	85.3	1270	25	1085	1175	1056	1216	1130	1136
SUERC-35761	36.25	83.62	1437	37	926	1017	876	1048	972	962
OS-82607	43.75	81.85	1610	35	720	815	692	876	768	784

RAPiD-35-14P

Publication Code	Depth (cm)	14C Enrichment (%modern)	14C ages (years BP)	+/- 1σ error	Years BP (Before 1950)					
					Cal. Age +1σ	Cal. Age -1σ	Cal. Age +2σ	Cal. Age -2σ	Average 1σ	Average 2σ
SUERC-13088	2.5	91.5	714	35	402	309	440	282	356	361
SUERC-35762	30.5	81.13	1680	37	1281	1205	1309	1155	1243	1232
OS-82609	39.5	78.71	1920	30	1509	1417	1547	1375	1463	1461
SUERC-35763	53.5	74.94	2317	35	1978	2019	2037	2068	1999	2053
SUERC-35764	65.5	73.25	2500	37	2219	2111	2292	2055	2165	2174
OS-82610	79.5	70.33	2830	30	2674	2540	2700	2469	2607	2585
SUERC-35765	99.5	66.99	3218	37	3096	2961	3167	2903	3029	3035
OS-82611	120.5	64.89	3470	20	3384	3297	3428	3285	3341	3357
OS-82612	160.5	61.94	3850	30	3865	3755	3904	3695	3810	3800
OS-82613	200.5	58.6	4290	40	4488	4363	4526	4277	4426	4402

RAPiD-17-5P

Publication Code	Depth (cm)	14C Enrichment (%modern)	14C ages (years BP)	+/- 1σ error	Years AD					
					Cal. Age +1σ	Cal. Age -1σ	Cal. Age +2σ	Cal. Age -2σ	Average 1σ	Average 2σ
SUERC-13088	0.5	92.91	591	35	1668	1729	1647	1827	1699	1737
SUERC-35762	34.5	89.69	874	35	1431	1480	1405	1514	1456	1460
OS-82609	67.25	83.84	1416	37	949	1035	895	1061	992	978
SUERC-35763	96.5	80.54	1738	37	627	694	579	733	661	656
SUERC-35764	200.5	70.11	2852	37	-749	-614	-771	-530	-666	-651
OS-82610	296	63.65	3629	35	-1625	-1518	-1683	-1477	-1576	-1580
SUERC-35765	750	-	8823	35	-7567	-7510	-7598	-7473	-7537	-7536

Data Tables

Table D1- Sortable Silt, *N. pachyderma, T. quinqueloba* and assemblage counts from RAPiD-35-COM (grey band indicates splicing point).

	Age			*Neogloquadrina pachyderma (s)*						*T.quinqueloba*		Counts
Mid-depth	**Age yrs AD**	**Age yrs BP**	**SS (µm)**	**δ^{18}O‰ PDB**	**δ^{13}C‰ PDB**	**Mg/Ca (mmol/mol)**	**Temp**	**δ^{18}Osw**	**Salinity**	**δ^{18}O‰**	**δ^{13}C‰**	**%Nps**
0.25	1961	-11	22.81	2.53	0.57	0.907	5.960	0.516	35.07	1.836	- 1.034	
0.75	1942	8	22.57	2.62	0.62	0.899	5.866	0.577	35.14	1.763	- 0.952	70.4
1.25	1923	27	22.58	2.71	0.68	0.873	5.574	0.601	35.16	1.836	- 0.830	74.0
1.75	1904	46	22.70	2.72	0.66	0.855	5.362	0.565	35.12	1.768	- 0.947	90.9
2.25	1885	65	23.73	2.61	0.68	0.917	6.060	0.619	35.18	1.988	- 0.724	82.7
2.75	1866	84	22.92	2.58	0.66	0.983	6.758	0.751	35.32	1.767	- 0.942	84.9
3.25	1848	102	24.83	2.51	0.69	0.856	5.376	0.357	34.90	1.485	- 1.057	76.7
3.75	1830	120	23.55	2.57	0.69	0.887	5.729	0.495	35.05	1.847	- 0.891	82.2
4.25	1812	138	23.52	2.57	0.68	0.883	5.686	0.488	35.04	1.556	- 0.936	79.0
4.75	1795	155	23.79	2.60	0.62	0.875	5.601	0.493	35.05	1.751	- 1.035	84.3
5.25	1778	172	23.91	2.57	0.69	0.879	5.643	0.481	35.03	1.683	- 0.799	73.7
5.75	1760	190	23.74	2.57	0.69	0.857	5.387	0.413	34.96	1.855	- 0.937	78.3
6.25	1744	206	23.54	2.52	0.68	0.851	5.317	0.354	34.90	1.711	- 1.012	94.4
6.75	1727	223	25.69	2.48	0.69	0.839	5.177	0.273	34.81	1.730	- 1.127	80.4
7.25	1710	240	24.56	2.52	0.67	0.838	5.163	0.316	34.86			95.6
7.75	1694	256	25.16	2.50	0.71	0.881	5.665	0.415	34.96	1.569	- 1.014	79.7
8.25	1678	272	24.88	2.47	0.71	0.833	5.105	0.248	34.79	1.742	- 1.077	84.4
8.75	1662	288	24.41	2.61	0.72	0.850	5.304	0.438	34.99	1.447	- 1.126	87.9
9.25	1646	304	24.24	2.60	0.75	0.824	5.000	0.357	34.90	1.976	- 0.898	93.1
9.75	1631	319	23.60	2.60	0.75	0.849	5.296	0.428	34.98	1.686	- 0.938	78.5
10.25	1615	335	23.00	2.53	0.57	0.850	5.307	0.356	34.90	1.762	- 1.021	84.8
10.75	1600	350	24.61	2.52	0.65	0.886	5.726	0.452	35.00	1.616	- 1.011	90.3
11.25	1585	365	23.56	2.61	0.76	0.805	4.762	0.310	34.85			93.7
11.75	1570	380	20.92	2.58	0.71	0.944	6.356	0.658	35.22	1.674	- 1.010	83.3

12.25	1556	394	18.65	2.55	0.74	0.817	4.916	0.285	34.82	1.699	-	1.116	77.5
12.75	1541	409	22.08	2.46	0.66	0.852	5.330	0.292	34.83	1.628	-	0.860	93.3
13.25	1527	423	21.47	2.52	0.65	0.772	4.338	0.120	34.65	1.669	-	0.811	95.6
13.75	1513	437	18.90	2.35	0.91	0.878	5.628	0.253	34.79	1.589	-	1.043	95.6
14.25	1499	451	23.42	2.61	0.69	0.867	5.507	0.485	35.04	1.879	-	0.935	91.2
14.75	1485	465	20.65	2.54	0.65	0.928	6.180	0.571	35.13	1.635	-	1.077	92.7
15.25	1471	479	24.10	2.50	0.70	0.827	5.035	0.263	34.80	1.604	-	1.004	90.0
15.75	1457	493	21.10	2.53	0.73	0.808	4.793	0.240	34.78	1.785	-	0.951	84.7
16.25	1444	506	23.33	2.56	0.69	0.826	5.024	0.321	34.86	1.782	-	1.109	88.2
16.75	1430	520	20.90	2.56	0.66	0.857	5.388	0.407	34.95	1.649	-	1.031	78.3
17.25	1417	533	22.70	2.58	0.75	0.844	5.234	0.390	34.94	1.744	-	1.104	81.9
17.75	1404	546	23.56	2.66	0.77	0.794	4.619	0.327	34.87	1.638	-	1.075	85.5
18.25	1391	559	23.50	2.60	0.69	0.857	5.391	0.450	35.00	1.566	-	1.207	78.6
18.75	1378	572	22.00	2.46	0.58	0.830	5.067	0.228	34.76	1.571	-	1.097	61.6
19.25	1365	585	22.97	2.59	0.64	0.804	4.745	0.281	34.82	1.481	-	1.067	56.3
19.75	1352	598	22.32	2.51	0.64	0.857	5.390	0.359	34.90	1.474	-	1.064	57.7
20.25	1339	611	21.82	2.60	0.59	0.853	5.339	0.433	34.98	1.583	-	1.077	65.6
20.75	1327	623	24.21	2.52	0.64	0.839	5.176	0.317	34.86	1.595	-	1.131	68.7
21.25	1314	636	22.99	2.43	0.64	0.857	5.387	0.281	34.82	1.617	-	1.152	85.9
21.75	1302	648	23.16	2.55	0.62	0.879	5.638	0.454	35.00	1.633	-	1.081	85.8
22.25	1290	660	22.85	2.57	0.59	0.816	4.903	0.301	34.84	1.594	-	1.111	82.8
22.75	1277	673	23.72	2.51	0.61	0.801	4.712	0.195	34.73	1.660	-	0.897	87.9
23.25	1265	685	22.02	2.46	0.64	0.819	4.931	0.196	34.73	1.746	-	1.099	92.4
23.75	1253	697	23.16	2.62	0.65	0.858	5.399	0.471	35.02	1.586	-	1.138	81.3
24.25	1241	709	20.46	2.60	0.63	0.837	5.156	0.396	34.94	1.653	-	1.125	84.4
24.75	1229	721	21.48	2.56	0.65	0.909	5.980	0.544	35.10	1.618	-	1.000	94.6
25.25	1217	733	24.33	2.66	0.76	0.779	4.429	0.278	34.82	1.563	-	1.156	84.4
25.75	1205	745	23.12	2.58	0.67	0.855	5.369	0.425	34.97	1.603	-	1.054	76.8
26.25	1193	757	23.53	2.57	0.68	0.840	5.187	0.366	34.91	1.685	-	1.073	79.2
26.75	1182	768	24.10	2.53	0.66	0.823	4.980	0.276	34.81	1.603	-	1.185	72.5
27.25	1170	780	24.51	2.52	0.61	0.857	5.392	0.372	34.92	1.526	-	1.136	84.0
27.75	1158	792	26.02	2.51	0.61	0.826	5.015	0.264	34.80	1.573	-	1.168	81.7
28.25	1146	804	21.09	2.58	0.67	0.852	5.331	0.409	34.96	1.602	-	1.059	51.2
28.75	1135	815	24.53	2.56	0.71	0.832	5.088	0.341	34.88	1.595	-	1.075	54.9
29.25	1123	827	24.11	2.58	0.63	0.845	5.248	0.390	34.94	1.662	-	1.036	92.6

29.75	1111	839	22.90	2.60	0.65	0.852	5.328	0.430	34.98	1.637	- 1.074	92.0
30.25	1099	851	23.61	2.63	0.62	0.835	5.129	0.418	34.97	1.817	- 0.897	
30.75	1088	862	23.55	2.54	0.63	0.876	5.611	0.437	34.99	2.003	- 0.955	
31.25	1076	874	21.27	2.58	0.66	0.818	4.919	0.319	34.86	1.748	- 1.154	
31.75	1065	885	23.60	2.40	0.60	0.815	4.880	0.125	34.65	1.719	- 1.060	54.8
32.25	1053	897	24.64	2.71	0.66	0.768	4.298	0.292	34.83	1.648	- 1.004	
32.75	1041	909	24.55	2.59	0.64	0.769	4.304	0.174	34.71	1.896	- 0.868	
33.25	1029	921	24.21	2.62	0.59	0.826	5.015	0.375	34.92	1.736	- 1.040	
33.75	1018	932	19.96	2.48	0.62	0.809	4.806	0.193	34.73	1.700	- 1.160	60.7
34.25	1006	944	21.45	2.59	0.68	0.794	4.624	0.260	34.80	1.584	- 1.069	
34.75	994	956	21.18	2.50	0.63	0.763	4.226	0.070	34.60	1.496	- 1.108	
35.25	982	968	24.42	2.53	0.68	0.864	5.465	0.395	34.94	1.547	- 1.054	
35.75	971	979	20.79	2.50	0.67	0.856	5.373	0.340	34.88	1.620	- 1.137	71.5
36.25	959	991	23.16	2.62	0.66	0.930	6.206	0.658	35.22	1.452	- 1.088	
36.75	947	1003	23.03	2.56	0.61	0.827	5.036	0.319	34.86	1.591	- 1.159	
37.25	935	1015	21.88	2.34	0.61	0.829	5.051	0.109	34.64	1.806	- 0.979	
37.75	923	1027	23.01	2.48	0.64	0.794	4.619	0.146	34.68	1.593	- 1.162	78.3
38.25	911	1039	23.25	2.60	0.69	0.825	5.011	0.358	34.90	1.601	- 1.185	
38.75	899	1051	23.51	2.47	0.61	0.851	5.316	0.301	34.84	1.561	- 1.160	
39.25	886	1064	20.69	2.54	0.63	0.829	5.058	0.306	34.85	1.727	- 0.963	
39.75	874	1076	22.41	2.55	0.68	0.839	5.181	0.346	34.89	1.588	- 1.089	61.3
40.25	862	1088	24.79	2.33	0.59	0.837	5.151	0.124	34.65	1.570	- 1.046	
40.75	849	1101	23.49	2.52	0.65	0.848	5.287	0.344	34.89	1.605	- 1.085	
41.25	837	1113	23.12	2.59	0.58	0.836	5.135	0.379	34.92	1.592	- 1.137	
41.75	824	1126	21.39	2.62	0.58	0.839	5.175	0.420	34.97	1.641	- 1.114	87.1
42.25	811	1139	22.12	2.59	0.67	0.883	5.691	0.509	35.06	1.729	- 1.052	
42.75	799	1151	22.85	2.44	0.60	0.857	5.392	0.292	34.83	1.613	- 1.094	
43.25	786	1164	20.35	2.52	0.65	0.851	5.315	0.355	34.90	1.631	- 1.139	
43.75	773	1177	20.56	2.36	0.60	0.860	5.315	0.188	34.72	1.771	- 1.139	75.2
30.5	701	1249	21.72	2.737	0.666							81.1
31.5	671	1279	21.36	2.622	0.622					1.851	-0.878	78.6
32.5	642	1308	20.89	2.681	0.753					1.567	-1.080	70.8
33.5	613	1337	20.08	2.686	0.504					1.597	-0.978	80.8
34.5	584	1366	21.57	2.517	0.511							70.5

35.5	555	1395	21.64	2.573	0.685					1.559	-0.896	70.0
36.5	526	1424	21.19	2.568	0.582					1.630	-1.196	70.2
37.5	497	1453	25.05	2.652	0.507					1.798	-1.078	78.8
38.5	469	1481	20.54	2.496	0.582					1.639	-0.862	88.1
39.5	440	1510	22.16	2.620	0.458					1.911	-0.986	94.7
40.5	412	1538	22.65	2.579	0.559					1.473	-1.144	
41.5	384	1566	21.61	2.761	0.647					1.669	-1.102	51.3
42.5	356	1594	23.54	2.526	0.507					1.649	-0.996	19.5
43.5	328	1622	24.90	2.642	0.574					1.647	-1.240	63.5
44.5	301	1649	23.35	2.565	0.546					1.516	-1.140	54.9
45.5	273	1677	22.59	2.830	0.605					1.688	-1.155	58.8
46.5	246	1704	22.38	2.464	0.570					1.650	-1.061	63.3
47.5	218	1732	23.01	2.801	0.635					1.550	-1.125	69.4
48.5	191	1759	24.71	2.662	0.610					1.651	-0.979	73.5
49.5	164	1786	23.02	2.604	0.595					1.679	-1.154	85.0
50.5	137	1813	23.35	2.702	0.613					1.747	-1.092	47.1
51.5	110	1840	22.80	2.807	0.626					1.605	-1.144	50.3
52.5	84	1866	20.99	2.794	0.595					1.669	-1.010	88.7
53.5	57	1893	22.10	2.814	0.623					1.683	-1.041	58.6
54.5	31	1919	21.92	2.782	0.622					1.910	-1.046	83.4
55.5	4	1946	22.67	2.655	0.648					1.750	-0.932	77.8
56.5	-22	1972	21.13	2.721	0.673					1.624	-1.221	69.9
57.5	-48	1998	21.68	2.671	0.628					1.683	-1.166	78.6
58.5	-74	2024	21.47	2.713	0.514					1.566	-1.252	66.2
59.5	-99	2049	23.43	2.670	0.645					1.566	-1.044	70.8
60.5	-125	2075	21.31	2.824	0.696					1.578	-1.242	35.4
61.5	-150	2100	21.00	2.767	0.612					1.529	-1.006	38.3
62.5	-176	2126	25.43	2.697	0.642					1.780	-1.020	55.6
63.5	-201	2151	25.76	2.793	0.649					1.514	-1.224	44.2
64.5	-226	2176	24.65	2.755	0.578					1.657	-1.168	55.2
65.5	-251	2201	23.78	2.747	0.649					1.822	-1.197	26.6
66.5	-276	2226	22.92	2.791	0.616					1.693	-1.156	58.8
67.5	-300	2250	23.50	2.811	0.636					1.700	-1.113	70.2
68.5	-325	2275	20.78	2.681	0.663					1.746	-1.182	65.5
69.5	-349	2299	21.48	2.732	0.653					1.636	-1.197	81.2

70.5	-374	2324	21.43	2.768	0.621					1.701	-1.162	59.6
71.5	-398	2348	21.98	2.701	0.696					1.635	-0.830	71.6
72.5	-422	2372	20.42	2.581	0.637					1.873	-1.038	90.2
73.5	-446	2396	21.49	2.747	0.641					2.002	-0.826	93.2
74.5	-469	2419	21.51	2.571	0.561					1.641	-1.133	82.0
75.5	-493	2443	19.11	2.701	0.596					1.751	-1.027	81.0
76.5	-517	2467	21.01	2.724	0.686					1.646	-1.194	86.7
77.5	-540	2490	21.73	2.685	0.585					1.735	-1.033	60.7
78.5	-563	2513	20.07	2.740	0.631					1.722	-1.026	70.9
79.5	-586	2536	21.22	2.723	0.617					1.750	-0.853	69.9
80.5	-609	2559	22.60									
81.5	-632	2582	21.41	2.623	0.617					1.753	-1.278	75.0
82.5	-655	2605	19.99	2.747	0.593					1.825	-1.157	39.5
83.5	-677	2627	22.43	2.779	0.661					1.667	-1.028	71.5
84.5	-700	2650	21.90	2.789	0.650					1.662	-1.059	63.5
85.5	-722	2672	21.59	2.751	0.681					1.702	-0.915	62.6
86.5	-744	2694	20.92	2.823	0.684					1.597	-1.153	71.5
87.5	-766	2716	21.72	2.796	0.561					1.709	-0.992	67.9
88.5	-788	2738	22.66	2.861	0.776					1.569	-1.075	85.0
89.5	-810	2760	19.76	2.758	0.661					1.592	-1.246	79.8
90.5	-832	2782	20.80	2.670	0.609					1.794	-1.105	62.2
91.5	-853	2803	21.74	2.720	0.644					1.708	-1.182	58.4
92.5	-874	2824	21.68	2.652	0.634					1.676	-1.134	94.9
93.5	-896	2846	20.46	2.741	0.644					1.611	-1.248	93.6
94.5	-917	2867	21.20	2.778	0.684					1.574	-1.109	92.8
95.5	-938	2888	18.95	2.826	0.643					1.806	-1.189	67.7
96.5	-959	2909	21.60	2.741	0.623					1.673	-1.160	77.9
97.5	-979	2929	21.10	2.818	0.711					1.941	-0.942	89.8
98.5	-1000	2950	19.91	2.710	0.622					1.881	-0.973	83.6
99.5	-1020	2970	21.75	2.709	0.632					1.644	-1.161	84.6
100.5	-1041	2991	20.48									
101.5	-1061	3011	20.79									
102.5	-1081	3031	20.35									
103.5	-1101	3051	21.42									
104.5	-1121	3071	21.79									

105.5	-1140	3090	20.05										
106.5	-1160	3110	21.04										
107.5	-1179	3129	20.07										
108.5	-1198	3148	21.39										
109.5	-1218	3168	22.55										
110.5	-1237	3187	21.78										
111.5	-1255	3205	20.79										
112.5	-1274	3224	21.47										
113.5	-1293	3243	21.84										
114.5	-1311	3261	22.31										
115.5	-1330	3280	21.69										
116.5	-1348	3298	24.50										
117.5	-1366	3316	21.74										
118.5	-1384	3334	21.35										
119.5	-1402	3352	21.73										
120.5	-1419	3369	21.87										
121.5	-1437	3387	21.86										
122.5	-1454	3404	18.73										
123.5	-1472	3422	20.55										
124.5	-1489	3439	20.76										
125.5	-1506	3456	22.42										
126.5	-1523	3473	20.77										
127.5	-1539	3489	20.76										
128.5	-1556	3506	20.49										
129.5	-1573	3523	19.55										
130.5	-1589	3539	21.48										
131.5	-1605	3555	20.25										
132.5	-1621	3571	21.39										
133.5	-1637	3587	20.52										
134.5	-1653	3603	21.83										
135.5	-1669	3619	21.11										
136.5	-1684	3634	21.92										
137.5	-1700	3650	23.39										
138.5	-1715	3665	20.01										
139.5	-1730	3680	22.72										

140.5	-1745	3695	21.22										
141.5	-1760	3710	22.38										
142.5	-1775	3725	23.40										
143.5	-1790	3740	22.40										
144.5	-1804	3754	21.40										
145.5	-1818	3768	22.17										
146.5	-1833	3783	21.74										
147.5	-1847	3797	20.98										
148.5	-1861	3811	21.28										
149.5	-1875	3825	22.42										
150.5	-1888	3838	21.99										
151.5	-1902	3852	20.60										
152.5	-1915	3865	21.46										
153.5	-1929	3879	21.18										
154.5	-1942	3892	19.23										
155.5	-1955	3905	20.83										
156.5	-1968	3918	21.44										
157.5	-1981	3931	22.02										
158.5	-1993	3943	22.92										
159.5	-2006	3956	21.41										
160.5	-2018	3968	20.60										
161.5	-2031	3981	21.86										
162.5	-2043	3993	21.68										
163.5	-2055	4005	19.78										
164.5	-2067	4017	22.00										
165.5	-2078	4028	20.72										
166.5	-2090	4040	23.24										
167.5	-2101	4051	22.26										
168.5	-2113	4063	22.79										
169.5	-2124	4074	23.40										

Table D2: *G.bulloides* data from RAPiD-35-COM (grey band indicates splicing point).

Globigerina bulloides									
Mid-depth Stable Isotopes	**Age for SI Gb (Years AD)**	**$\delta^{18}O$‰**	**$\delta^{13}C$‰**	**Mid-depth Mg/ca**	**Age for Mg/Ca Gb (Years AD)**	**Mg/Ca (mmol/mol)**	**Temp**	**$\delta^{18}Osw$‰**	**Salinity**
0.25	1961	2.470	-0.400	0.25	1961	1.469	7.505	0.136	34.665
0.75	1942	2.514	-0.325	0.75	1942	1.558	8.226	0.347	34.890
1.25	1923	2.581	-0.157	1.25	1923	1.445	7.302	0.199	34.733
1.75	1904	2.666	-0.144	1.75	1904	1.294	5.935	-0.037	34.482
2.25	1885	2.554	-0.112	2.25	1885	1.306	6.055	-0.120	34.394
2.75	1866	2.714	-0.120	2.75	1866	1.271	5.716	-0.040	34.478
3.25	1848	2.485	-0.286	3.25	1848	1.403	6.936	0.018	34.540
3.75	1830	2.468	-0.127	3.75	1830	1.294	5.939	-0.234	34.272
4.25	1812	2.754	-0.086	4.25	1812	1.452	7.358	0.386	34.932
4.75	1795	2.624	-0.039	4.75	1795	1.262	5.631	-0.150	34.361
5.25	1778	2.586	-0.053	5.25	1778	1.465	7.471	0.244	34.781
5.75	1760	2.612	-0.145	5.75	1760	1.368	6.622	0.071	34.597
6.25	1744	2.522	0.090	6.25	1744	1.275	5.755	-0.223	34.284
6.75	1727	2.570	0.210	6.75	1727	1.427	7.148	0.153	34.684
7.25	1710	2.392	-0.022	7.25	1710	1.426	7.136	-0.028	34.491
7.75	1694	2.347	0.079	7.75	1694	1.508	7.827	0.087	34.614
8.25	1678	2.557	0.040	8.25	1678	1.513	7.863	0.306	34.847
8.75	1662	2.590	0.116	8.75	1662	1.275	5.754	-0.155	34.356
9.25	1646	2.582	-0.056	9.25	1646	1.330	6.273	-0.041	34.478
9.75	1631	2.583	0.044	9.75	1631	1.375	6.688	0.057	34.582
10.25	1615	2.610	-0.117	10.25	1615	1.463	7.450	0.263	34.801
10.75	1600	2.444	0.113	10.75	1600	1.510	7.845	0.189	34.723
11.25	1585	2.723	-0.030	11.25	1585	1.188	4.877	-0.231	34.275
12	1563	2.566	-0.105	12	1563	1.352	6.477	-0.008	34.512

13	1534	2.510	0.087						
13.75	1513	2.551	0.310						
14.5	1506	2.590	0.110	14.5	1506	1.302	6.013	-0.094	34.421
15.5	1464	2.636	-0.034	15.5	1464	1.423	7.106	0.208	34.743
16.25	1444	2.535	-0.185	16.25	1444	1.660	9.011	0.549	35.105
16.75	1430	2.538	-0.189	16.75	1430	1.737	9.572	0.681	35.245
17.25	1417	2.472	-0.247	17.25	1417	1.506	7.810	0.209	34.743
17.75	1404	2.544	-0.274	17.75	1404	1.433	7.200	0.139	34.669
18.25	1391	2.595	0.031	18.25	1391	1.464	7.461	0.251	34.788
18.75	1378	2.480	-0.075	18.75	1378	1.697	9.284	0.556	35.113
19.25	1365	2.485	-0.292	19.25	1365	1.726	9.493	0.609	35.170
19.75	1352	2.487	-0.202	19.75	1352	1.695	9.269	0.561	35.118
20.25	1339	2.355	-0.201	20.25	1339	1.662	9.029	0.373	34.918
20.75	1327	2.495	-0.176	20.75	1327	1.440	7.259	0.104	34.632
21.25	1314	2.482	-0.153	21.25	1314	1.388	6.805	-0.016	34.505
21.75	1302	2.447	0.010	21.75	1302	1.474	7.544	0.121	34.651
22.25	1290	2.533	-0.071	22.25	1290	1.266	5.664	-0.234	34.272
22.75	1277	2.454	-0.156	22.75	1277	1.463	7.453	0.107	34.635
23.25	1265	2.577	-0.128	23.25	1265	1.437	7.233	0.179	34.712
23.75	1253	2.363	-0.019	23.75	1253	1.634	8.813	0.332	34.874
24.5	1235	2.598	-0.078	24.5	1235	1.407	6.969	0.139	34.669
25.25	1217	2.438	-0.027	25.25	1217	1.644	8.892	0.425	34.973
25.75	1205	2.329	0.143	25.75	1205	1.510	7.840	0.073	34.599
26.25	1193	2.415	-0.217	26.25	1193	1.350	6.461	-0.164	34.347
27	1176	2.330	-0.241	27	1176	1.489	7.673	0.035	34.558
27.75	1158	2.361	-0.222	27.75	1158	1.541	8.090	0.163	34.695
28.25	1146	2.473	-0.154	28.25	1146	1.392	6.837	-0.017	34.503
28.75	1135	2.432	-0.271	28.75	1135	1.405	6.954	-0.031	34.488
29.25	1117	2.446	-0.185	29.5	1117	1.546	8.137	0.259	34.797
30.25	1099	2.159	-0.051	30.25	1099	1.932	10.887	0.600	35.159

30.75	1082	2.194	-0.009	30.75	1082	1.407	6.967	-0.266	34.239
32	1059	2.220	-0.092	32	1059	1.361	6.557	-0.336	34.164
33.25	1029	2.288	-0.223	33.25	1029	1.570	8.322	0.143	34.673
33.75	1018	2.332	-0.361	33.75	1018				
34.25	1006	2.355	-0.385		1006				
34.75	994	2.293	-0.395	34.75	994	1.548	8.147	0.108	34.636
35.25	982	2.386	-0.176	35.25	982	1.652	8.950	0.386	34.932
35.75	971	2.376	-0.334	35.75	971	1.510	7.841	0.120	34.649
36.25	959	2.460	-0.134	36.25	959	1.436	7.225	0.061	34.586
36.75	947	2.294	-0.243	36.75	947	1.461	7.434	-0.057	34.460
37.25	935	2.354	-0.142	37.25	935	1.396	6.871	-0.128	34.385
37.75	923	2.106	-0.334	37.75	923	1.408	6.982	-0.350	34.149
38.25	911	2.482	-0.049	38.25	911	1.648	8.919	0.475	35.026
38.75	899	2.447	-0.200	38.75	899	1.409	6.991	-0.008	34.513
39.25	886	2.374	-0.210	39.25	886	1.549	8.160	0.192	34.725
39.75	874	2.276	-0.359	39.75	874	1.560	8.248	0.114	34.643
40.25	862	2.348	-0.401	40.25	862	1.667	9.061	0.373	34.918
40.75	849	2.293	-0.356	40.75	849	1.663	9.033	0.312	34.853
41.25	837	2.300	-0.351					-1.852	
41.75	824	2.280	-0.359	41.75	824	1.821	10.155	0.556	35.112
42.25	811	2.263	-0.141	42.25	811	1.755	9.696	0.433	34.982
42.75	799	2.494	-0.242	42.75	799	1.449	7.334	0.120	34.649
43.25	786	2.199	-0.381		786			-1.952	
43.75	773	2.202	-0.250	43.75	773	1.782	9.884	0.416	34.963
30.5		2.207	-0.413	30.5	701	1.812	10.090	0.468	35.019
31.5		2.381	-0.092	31.5	671				
32.5		2.337	-0.591	32.5	642	1.763	9.757	0.522	35.077
33.5		2.260	-0.291	33.5	613	1.900	10.677	0.653	35.216
35.5		2.433	-0.243	35.5	555	1.716	9.423	0.541	35.097

36.5		2.480	-0.063	36.5	526	1.683	9.181	0.533	35.089
37.5		2.257	-0.135	37.5	497	1.604	8.592	0.175	34.707
38.5		2.256	-0.286	38.5	469	1.249	5.500	-0.550	33.937
39.5		2.193	-0.399	39.5	440				
40.5		2.402	-0.314	40.5	412				
41.5		2.183	-0.175	41.5	384	1.489			34.521
42.5		2.189	-0.315	42.5	356	1.626	8.755	0.144	34.675
43.5		2.290	-0.321	43.5	328	1.618	8.693	0.231	34.767
44.5		2.290	-0.380	44.5	301	1.646	8.904	0.280	34.819
45.5		2.159	-0.355	45.5	273				
46.5		2.112	-0.278	46.5	246				
47.5		2.072	-0.330	47.5	218	1.670	9.086	0.104	34.631
48.5		2.253	-0.093	48.5	191				
49.5		2.283	-0.344	49.5	164	1.649	8.930	0.278	34.818
50.5		2.333	-0.325	50.5	137	1.698	9.289	0.411	34.958
51.5		2.324	-0.460	51.5	110				
52.5		2.227	-0.472	52.5	84				
53.5		2.284	-0.253	53.5	57	1.496	7.728	0.002	34.523
54.5		2.171	-0.350	54.5	31	1.312	6.109	-0.490	34.000
55.5		2.296	-0.316	55.5	4	1.659	9.007	0.309	34.850
56.5		2.395	-0.380	56.5	-22	1.683	9.181	0.448	34.997
57.5		1.934	-0.445	57.5	-48	1.724	9.480	0.056	34.580
58.5		2.437	-0.515	58.5	-74	1.498	7.748	0.160	34.691
59.5		2.305	-0.316	59.5	-99	1.518	7.909	0.065	34.591
60.5		2.082	-0.389	60.5	-125	1.545	8.129	-0.108	34.407
61.5		2.254	-0.482	61.5	-150	1.764	9.765	0.440	34.989
62.5		2.323	-0.479	62.5	-176				
63.5		2.244	-0.388	63.5	-201	1.708	9.366	0.340	34.882
64.5		2.063	-0.494	64.5	-226	1.687	9.211	0.123	34.652

65.5		2.294	-0.208	65.5	-251	1.599	8.553	0.203	34.737
66.5		2.294	-0.274	66.5	-276	1.526	7.975	0.069	34.595
67.5		2.141	-0.387	67.5	-300	1.785	9.907	0.359	34.904
68.5		1.963	-0.381	68.5	-325	1.511	7.852	-0.290	34.213
69.5		2.243	-0.478	69.5	-349	1.364	6.583	-0.307	34.194
70.5		2.165	-0.136	70.5	-374	1.638	8.847	0.141	34.671
71.5				71.5	-398	1.501	7.769	-2.273	32.103
72.5		1.852	-0.272	72.5	-422				
73.5		1.893	-0.340	73.5	-446				
74.5		2.158	-0.284	74.5	-469	1.479	7.583	-0.158	34.353
75.5		2.073	-0.344	75.5	-493	1.741	9.602	0.222	34.758
76.5		2.151	-0.508	76.5	-517	1.499	7.750	-0.126	34.387
77.5		1.872	-0.453	77.5	-540	1.969	11.121	0.365	34.910
78.5		2.090	-0.254	78.5	-563	1.726	9.494	0.215	34.750
79.5		2.005	-0.146	79.5	-586	1.626	8.760	-0.039	34.480
80.5		2.332	-0.566	80.5	-609	1.580	8.403	0.206	34.740
81.5				81.5	-632				
82.5		2.349	-0.263	82.5	-655	1.861	10.421	0.684	35.249
83.5		2.069	-0.242	83.5	-677	1.733	9.542	0.205	34.739
84.5		2.102	-0.560	84.5	-700	1.854	10.374	0.427	34.976
85.5		2.159	-0.493	85.5	-722	1.834	10.243	0.455	35.005
86.5		2.305	-0.288	86.5	-744	1.675	9.126	0.345	34.889
87.5		2.130	-0.467	87.5	-766	1.767	9.780	0.320	34.861
88.5		2.265	-0.291	88.5	-788	1.611	8.639	0.193	34.727
89.5		2.309	-0.432	89.5	-810	1.760	9.736	0.489	35.042
90.5		2.288	-0.490	90.5	-832				
91.5		2.263	-0.441	91.5	-853	1.890	10.612	0.641	35.203
92.5		2.053	-0.270	92.5	-874				
93.5		1.793	-0.663	93.5	-896	1.836	10.258	0.092	34.619
94.5		2.407	-0.516	94.5	-917	1.766	9.775	0.596	35.155

95.5		2.393	-0.351	95.5	-938	1.456	7.393	0.033	34.556
96.5		2.179	-0.373	96.5	-959	1.541	8.095	-0.018	34.502
97.5		2.126	-0.336	97.5	-979	1.702	9.317	0.210	34.745
98.5		1.913	-0.368	98.5	-1000				
99.5		2.229	-0.433	99.5	-1020	1.711	9.386	0.329	34.871

Table D3: Sortable Silt and *G. inflata* data from RAPiD-17-5P.

Mid-depth	Age		CF%	SS (μm)	*G. inflata*					
	Age yrs AD	Age yrs BP			$\delta^{13}C$‰	$\delta^{18}O$‰	Mg/Ca (mmol/mol)	Temperature	$\delta^{18}Osw$‰	Salinity
0.25	1766.4	183.6								
0.75	1761.1	188.9								
1.25	1755.8	194.2	9.6	31.4	1.211	1.863				
1.75	1750.5	199.5	10.0	31.2	0.983	1.789	1.24	6.619	-0.073	34.38
2.25	1745.2	204.8	9.2	30.4	1.166	1.967	1.17	5.489	-0.161	34.22
2.75	1739.9	210.1	9.7	31.4	0.863	1.989	1.24	6.056	-0.005	34.50
3.25	1734.6	215.4	7.1	29.4	1.026	2.009				
3.75	1729.3	220.7	7.4	29.0	1.109	2.098	1.19	5.634	0.004	34.52
4.25	1724.0	226.0	8.2	31.0	0.874	1.982	2.19	11.774	1.302	36.88
4.75	1718.7	231.3	9.2	30.8	1.149	1.930	1.64	8.859	0.589	35.58
5.25	1713.3	236.7	9.3	30.5	1.009	1.866	1.45	7.620	0.238	34.94
5.75	1708.0	242.0	8.7	31.9	0.996	2.025	1.51	8.023	0.491	35.40
6.25	1702.7	247.3	9.6	32.1	0.998	1.953	1.25	6.189	-0.010	34.49
6.75	1697.3	252.7	9.5	32.0	1.098	2.127	1.24	6.091	0.141	34.76
7.25	1692.0	258.0	13.7	31.0	0.952	1.777	1.23	6.003	-0.230	34.09
7.75	1686.6	263.4	9.7	30.4	0.943	1.910	1.40	7.280	0.203	34.88
8.25	1681.3	268.7	8.0	31.2	0.977	2.086				
8.75	1675.9	274.1	10.3	32.1	0.993	1.889	1.24	6.067	-0.102	34.32
9.25	1670.5	279.5	11.0	31.2	1.049	2.090	1.19	5.634	-0.004	34.50
9.75	1665.1	284.9	10.8	32.4	1.137	2.198	1.57	8.461	0.766	35.90
10.25	1659.8	290.2	11.1	31.0	1.172	2.054	1.37	7.087	0.302	35.06
10.75	1654.4	295.6	10.0	30.9	1.153	1.969	1.30	6.552	0.091	34.68

11.25	1649.0	301.0	11.1	30.2	1.231	2.012	1.25	6.139	0.038	34.58
11.75	1643.6	306.4	11.9	30.6	1.185	1.839	1.44	7.555	0.197	34.87
12.25	1638.2	311.8	11.9	31.8			1.66	8.987		
12.75	1632.8	317.2	12.6	31.5	1.164	1.977				
13.25	1627.4	322.6	12.6	32.0	1.070	1.906	1.67	9.031	0.605	35.61
13.75	1622.0	328.0	12.6	31.7	1.097	1.927	1.29	6.452	0.027	34.56
14.25	1616.6	333.4	12.5	31.7	1.053	1.852	1.30	6.588	-0.017	34.48
14.75	1611.2	338.8	12.8	32.1	0.999	1.888	1.36	6.973	0.109	34.71
15.25	1605.7	344.3	10.1	31.6	0.968	1.835	1.32	6.740	0.002	34.51
15.75	1600.3	349.7	10.8	30.3	1.124	2.080	1.56	8.396	0.632	35.66
16.25	1594.9	355.1	9.8	31.2	0.865	1.967	1.38	7.126	0.224	34.92
16.75	1589.4	360.6	12.7	31.7	1.022	1.939	1.45	7.643	0.317	35.09
17.25	1584.0	366.0	12.4	32.9	1.082	1.989	1.53	8.161	0.487	35.39
17.75	1578.5	371.5	12.7	31.7	1.181	1.942	1.69	9.164	0.672	35.73
18.25	1573.1	376.9	12.3	30.2	1.189	2.029	1.32	6.727	0.193	34.86
18.75	1567.6	382.4	13.0	31.7	1.043	1.880	1.33	6.770	0.054	34.61
19.25	1562.2	387.8	13.5	32.7	1.211	2.107	1.45	7.660	0.489	35.40
19.75	1556.7	393.3	13.3	31.1			1.43	7.483		
20.25	1551.2	398.8	12.8	31.6	1.056	1.881	1.28	6.421	-0.027	34.46
20.75	1545.8	404.2	12.7	31.6	0.943	1.858	1.60	8.635	0.466	35.36
21.25	1540.3	409.7	11.4	32.9	1.153	2.046				
21.75	1534.8	415.2	11.7	32.8	1.248	1.928	1.28	6.421	0.020	34.55
22.25	1529.3	420.7	11.9	32.5	1.044	1.945	1.50	7.981	0.402	35.24
22.75	1523.8	426.2	11.6	32.1	0.961	2.001	1.09	4.778	-0.297	33.97
23.25	1518.3	431.7	11.9	33.0	1.024	1.832	1.41	7.397	0.152	34.79
23.75	1512.8	437.2	12.5	32.2	0.770	2.007				
24.25	1507.3	442.7	11.4	32.6	0.841	1.805				
24.75	1501.8	448.2	11.2	31.8	1.057	2.033	1.34	6.853	0.226	34.92
25.25	1496.3	453.7	11.4	31.8	1.026	1.948	1.26	6.268	0.004	34.52
25.75	1490.8	459.2	11.1	33.4	1.104	1.975	1.14	5.199	-0.222	34.10

26.25	1485.2	464.8	11.6	32.8	0.990	2.120	1.23	6.009	0.115	34.72
26.75	1479.7	470.3	11.2	32.5	1.088	2.012	1.28	6.437	0.108	34.71
27.25	1474.2	475.8	11.8	32.9	0.970	1.944				
27.75	1468.6	481.4	17.6	31.6	1.038	1.950	1.22	5.910	-0.079	34.37
28.25	1463.1	486.9	10.8	31.4	1.014	1.944	1.60	8.642	0.553	35.52
28.75	1457.5	492.5	10.3	31.1	0.954	1.996	1.60	8.624	0.601	35.60
29.25	1452.0	498.0	11.1	32.0	0.867	1.885	1.53	8.172	0.386	35.21
29.75	1446.4	503.6	11.9	30.5	1.204	1.992	1.80	9.835	0.874	36.10
30.25	1440.9	509.1	11.8	32.1	0.786	1.916				
30.75	1435.3	514.7	11.5	31.7	0.970	1.939	1.30	6.570	0.066	34.63
31.25	1429.7	520.3	12.2	32.0	0.877	1.795	1.68	9.114	0.512	35.44
31.75	1424.2	525.8	13.2	32.3	0.770	1.807	1.41	7.344	0.115	34.72
32.25	1418.6	531.4	12.6	31.8	1.133	2.038	1.32	6.727	0.202	34.88
32.75	1413.0	537.0	12.3	31.4	0.984	1.924				
33.25	1407.4	542.6	12.3	30.4	0.991	1.713	1.82	9.941	0.619	35.64
33.75	1401.8	548.2	11.9	32.7	1.080	1.983	1.61	8.715	0.609	35.62
34.25	1396.2	553.8	13.6	30.9	0.900	1.891	1.50	7.986	0.349	35.14
34.75	1390.6	559.4	11.9	33.0	0.896	1.990	1.59	8.540	0.575	35.55
35.25	1385.0	565.0	12.8	32.5	1.188	2.141	1.47	7.800	0.556	35.52
35.75	1379.4	570.6	11.0	32.6	0.925	1.893	1.57	8.464	0.461	35.35
36.25	1373.8	576.2	15.7	31.6	0.942	2.005	1.66	9.013	0.699	35.78
36.75	1368.2	581.8	12.9	32.0	0.932	1.792	1.55	8.302	0.323	35.10
37.25	1362.5	587.5	14.4	32.7	1.003	2.071	1.32	6.730	0.235	34.94
37.75	1356.9	593.1	14.6	32.2	0.998	1.882	1.19	5.690	-0.198	34.15
38.25	1351.3	598.7	16.3	33.3	1.069	1.942	1.35	6.948	0.158	34.80
38.75	1345.6	604.4	16.1	31.8	1.213	2.090	1.21	5.827	0.042	34.58
39.25	1340.0	610.0	17.3	33.0	1.071	1.979	1.65	8.918	0.652	35.69
39.75	1334.4	615.6	16.7	33.0	1.162	1.937	1.30	6.577	0.066	34.63
40.25	1328.7	621.3	14.0	31.7	0.926	1.878	1.24	6.078	-0.111	34.31
40.75	1323.1	626.9	13.7	31.7	1.274	2.162	1.55	8.325	0.698	35.78

41.25	1317.4	632.6	15.5	32.0	1.056	1.867	1.28	6.384	-0.050	34.42
41.75	1311.7	638.3	15.8	31.1	1.052	1.906	1.32	6.675	0.058	34.61
42.25	1306.1	643.9	13.5	30.0	0.947	1.898	1.35	6.902	0.103	34.70
42.75	1300.4	649.6	13.3	31.4	1.144	1.889	1.52	8.126	0.379	35.20
43.25	1294.7	655.3	16.2	31.1	1.153	2.046	1.25	6.130	0.069	34.63
43.75	1289.1	660.9	15.1	31.1	0.774	1.863	1.26	6.214	-0.093	34.34
44.25	1283.4	666.6	15.9	31.7	0.955	1.933	1.46	7.710	0.326	35.10
44.75	1277.7	672.3	16.9	30.6	1.021	1.967	1.32	6.685	0.122	34.73
45.25	1272.0	678.0	15.4	29.7	0.943	1.808	1.60	8.645	0.418	35.27
45.75	1266.3	683.7	15.7	30.2	0.792	1.795	1.37	7.081	0.042	34.59
46.25	1260.6	689.4	15.3	30.5	0.975	1.928	1.41	7.391	0.248	34.96
46.75	1254.9	695.1	15.4	30.4	0.839	1.738	1.65	8.945	0.417	35.27
47.25	1249.2	700.8	14.8	31.6	1.202	1.952	1.58	8.487	0.525	35.46
47.75	1243.5	706.5	16.6	32.5	0.898	1.808	1.41	7.394	0.128	34.74
48.25	1237.7	712.3	14.2	32.5	0.907	1.720	1.59	8.539	0.306	35.06
48.75	1232.0	718.0	16.3	32.8	0.891	2.036	1.54	8.256	0.556	35.52
49.25	1226.3	723.7	15.4	33.7	0.992	1.870	1.41	7.353	0.181	34.84
49.75	1220.6	729.4	13.8	31.6	0.935	1.955	1.48	7.874	0.387	35.21
50.25	1214.8	735.2	12.5	31.7	1.032	1.818				
50.75	1209.1	740.9	13.7	31.2	1.033	1.914	1.40	7.313	0.215	34.90
51.25	1203.4	746.6	10.8	31.7	1.093	2.086	1.68	9.094	0.799	35.96
51.75	1197.6	752.4	14.7	32.1	1.026	1.883	1.43	7.539	0.237	34.94
52.25	1191.9	758.1	13.9	33.5	0.980	2.007	1.54	8.246	0.525	35.46
52.75	1186.1	763.9	15.7	34.3			1.39	7.212		
53.25	1180.3	769.7	16.2	34.0	1.016	1.940	1.21	5.851	-0.102	34.32
53.75	1174.6	775.4	16.7	33.4	1.041	1.992	1.29	6.453	0.092	34.68
54.25	1168.8	781.2	15.6	31.8	1.086	1.983	1.86	10.151	0.938	36.21
54.75	1163.0	787.0	16.2	31.5	1.053	1.905	1.26	6.254	-0.043	34.43
55.25	1157.3	792.7	16.3	32.4	1.031	1.749	1.34	6.876	-0.053	34.41
55.75	1151.5	798.5	16.1	33.4	1.003	1.781	1.20	5.768	-0.281	34.00

56.25	1145.7	804.3	12.4	31.3	0.971	2.020	1.97	10.725	1.105	36.52
56.75	1139.9	810.1	12.9	31.6	0.868	1.729	1.57	8.410	0.285	35.03
57.25	1134.1	815.9	14.4	32.6	0.793	1.904	1.43	7.526	0.255	34.97
57.75	1128.3	821.7	14.4	31.9	0.833	1.800				
58.25	1122.5	827.5	13.4	32.7	0.934	1.787	1.52	8.085	0.268	35.00
58.75	1116.7	833.3	13.6	32.6	0.971	1.832	1.33	6.789	0.010	34.53
59.25	1110.9	839.1	15.0	32.7	1.090	1.929	1.44	7.607	0.299	35.05
59.75	1105.1	844.9	15.4	31.8	0.808	1.868	1.66	8.998	0.559	35.53
60.25	1099.3	850.7	14.7	33.9	1.062	1.776	1.59	8.553	0.365	35.17
60.75	1093.5	856.5	16.2	32.1	0.956	2.056	1.60	8.612	0.658	35.71
61.25	1087.6	862.4	16.6	33.8	0.960	2.020	1.31	6.654	0.167	34.81
61.75	1081.8	868.2	16.6	32.8	0.979	1.893	1.41	7.366	0.207	34.88
62.25	1076.0	874.0	15.6	33.1	0.927	1.882	1.62	8.765	0.520	35.45
62.75	1070.2	879.8	15.4	33.3	0.872	1.905	1.33	6.815	0.089	34.67
63.25	1064.3	885.7	15.2	31.0	0.846	1.810	1.29	6.467	-0.087	34.35
63.75	1058.5	891.5	14.8	33.1	0.792	1.894	1.34	6.859	0.089	34.67
64.25	1052.6	897.4	12.7	31.2	0.870	1.827	1.29	6.464	-0.071	34.38
64.75	1046.8	903.2	13.2	31.2	0.940	1.799	1.45	7.646	0.177	34.83
65.25	1040.9	909.1	14.4	32.7	0.967	1.761	1.53	8.196	0.267	34.99
65.75	1035.1	914.9	14.2	31.9	0.887	1.823	1.51	8.042	0.294	35.04
66.25	1029.2	920.8	13.9	32.8	0.867	1.935	1.28	6.421	0.027	34.56
66.75	1023.3	926.7	13.0	31.6	0.894	1.861	1.63	8.807	0.508	35.43
67.25	1017.5	932.5	14.8	31.5	0.885	1.903	1.49	7.935	0.349	35.14
67.75	1011.6	938.4	13.8	32.7			1.48	7.868		
68.25	1005.7	944.3	13.5	32.1	1.063	1.919	1.48	7.840	0.343	35.13
68.75	999.8	950.2	13.7	31.1	0.974	1.804	1.88	10.248	0.780	35.93
69.25	993.9	956.1	14.0	30.9	0.918	1.734	1.67	9.076	0.443	35.31
69.75	988.0	962.0	14.0	32.3	0.847	1.753	1.54	8.264	0.274	35.01
70.25	982.1	967.9	16.5	31.8	0.914	1.780	1.38	7.145	0.041	34.58
70.75	976.2	973.8	16.6	33.7	1.039	1.950	1.40	7.269	0.241	34.95

71.25	970.3	979.7	18.3	33.0	0.962	1.918	1.52	8.089	0.400	35.24
71.75	964.4	985.6	19.0	33.8	0.978	1.766	1.42	7.403	0.088	34.67
72.25	958.5	991.5	19.7	34.3	0.836	1.803	1.52	8.092	0.285	35.03
72.75	952.6	997.4	20.2	34.4	1.186	2.079	1.58	8.520	0.660	35.71
73.25	946.7	1003.3	18.6	34.5	0.954	1.743	1.58	8.505	0.321	35.09
73.75	940.8	1009.2	17.6	34.2	0.992	1.717	1.51	8.084	0.197	34.87
74.25	934.8	1015.2	17.8	34.4	0.803	1.754	1.67	9.085	0.465	35.35
74.75	928.9	1021.1	16.6	33.6	0.957	1.872	1.58	8.521	0.453	35.33
75.25	923.0	1027.0	14.7	34.4	0.874	1.786	1.66	9.016	0.481	35.38
75.75	917.0	1033.0	15.6	34.2	0.933	1.713	1.58	8.482	0.285	35.03
76.25	911.1	1038.9	18.2	34.0	0.850	1.669	1.75	9.554	0.487	35.40
76.75	905.2	1044.8	16.3	32.7	0.805	1.740	1.72	9.370	0.516	35.45
77.25	899.2	1050.8	14.7	32.4	0.722	1.840	1.76	9.586	0.666	35.72
77.75	893.3	1056.7	16.8	34.2	0.849	1.612	1.74	9.476	0.413	35.26
78.25	887.3	1062.7	17.9	35.0	0.859	1.735	1.66	8.995	0.426	35.28
78.75	881.3	1068.7	15.9	35.0	0.825	1.766	1.50	8.011	0.230	34.93
79.25	875.4	1074.6	13.7	33.1	0.968	1.819	1.51	8.075	0.297	35.05
79.75	869.4	1080.6	13.3	32.7			1.44	7.598		
80.25	863.4	1086.6	14.9	33.9						
80.75	857.5	1092.5	15.4	34.9						
81.25	851.5	1098.5								
81.75	845.5	1104.5								
82.25	839.5	1110.5	13.2	34.1						
82.75	833.5	1116.5	14.6	34.9						
83.25	827.5	1122.5	15.2	33.2						
83.75	821.5	1128.5	12.2	32.9						
84.25	815.5	1134.5	15.3	32.7						
84.75	809.5	1140.5	14.2	33.5						
85.25	803.5	1146.5	15.2	34.1						
85.75	797.5	1152.5	15.4	33.8						

86.25	791.5	1158.5	15.2	33.5							
86.75	785.5	1164.5	13.8	30.9							
87.25	779.5	1170.5	14.3	32.3							
87.75	773.4	1176.6	13.2	32.1							
88.25	767.4	1182.6	12.7	31.7							
88.75	761.4	1188.6	17.5	32.7							
89.25	755.3	1194.7	12.3	33.2							
89.75	749.3	1200.7	13.8	31.8							
90.25	743.2	1206.8	14.7	32.2							
90.75	737.2	1212.8		33.3							
91.25	731.1	1218.9	14.6	32.5							
91.75	725.1	1224.9	14.1	32.7							
92.25	719.0	1231.0	15.4	30.6							
92.75	713.0	1237.0	16.4	32.6							
93.25	706.9	1243.1	17.7	32.9							
93.75	700.8	1249.2		34.1							
94.25	694.8	1255.2	20.0	34.2							
94.75	688.7	1261.3		33.3							
95.25	682.6	1267.4	18.3	32.3							
95.75	676.5	1278.0	17.3	32.6							
96.25	670.4	1279.6									
96.75	664.4	1290.2									
97.25	658.3	1291.7	17.2	32.7							
97.75	652.2	1297.8	16.0	32.7							
98.25	646.1	1303.9	0.2	34.3							
98.75	640.0	1310.0	17.9	34.2							
99.25	633.9	1316.1	20.4	34.1							
99.75	627.7	1322.3	19.1	33.3							
100.25	621.6	1328.4	15.1	34.3							
100.75	615.5	1334.5	15.2	32.8							

101.25	609.4	1340.6	15.9	32.4							
101.75	603.3	1346.7	17.5	33.3							
102.25	597.1	1352.9	17.2	35.3							
102.75	591.0	1359.0	16.6	34.0							
103.25	584.9	1365.1	19.8	32.1							
103.75	578.7	1371.3	19.1	34.0							
104.25	572.6	1377.4	18.7	35.1							
104.75	566.4	1383.6	20.8	34.3							
105.25	560.3	1389.7	20.4	33.5							
105.75	554.1	1395.9	20.4	35.2							
106.25	548.0	1402.0	20.8	33.3							
106.75	541.8	1408.2	22.1	35.8							
107.25	535.7	1414.3	20.7	33.8							
107.75	529.5	1420.5	20.0	29.8							
108.25	523.3	1426.7	19.5	33.2							
108.75	517.2	1432.8	20.7	34.8							
109.25	511.0	1439.0	20.7	32.3							
109.75	504.8	1445.2	19.3	36.2							
110.25	498.6	1451.4	20.9	34.8							
110.75	492.4	1457.6	20.0	33.6							
111.25	486.3	1463.7	18.0	34.3							
111.75	480.1	1469.9	20.0	34.8							
112.25	473.9	1476.1	18.3	34.0							
112.75	467.7	1482.3	17.4	33.2							
113.25	461.5	1488.5	19.0	34.4							
113.75	455.3	1494.7	19.2	33.2							
114.25	449.1	1500.9	17.2	32.4							
114.75	442.8	1507.2	17.1	33.4							
115.25	436.6	1513.4	18.9	32.4							
115.75	430.4	1519.6	16.7	32.0							

116.25	424.2	1525.8	16.3	33.7							
116.75	418.0	1532.0	17.0	32.0							
117.25	411.7	1538.3	21.2	30.7							
117.75	405.5	1544.5	17.4	30.9							
118.25	399.3	1550.7	16.8	33.8							
118.75	393.0	1557.0	16.4	32.2							
119.25	386.8	1563.2	16.7	31.1							
119.75	380.6	1569.4	17.9	32.6							
120.25	374.3	1575.7	14.9	28.9							
120.75	368.1	1581.9	14.3	31.7							
121.25	361.8	1588.2	13.4	33.1							
121.75	355.6	1594.4	13.7	32.6							
122.25	349.3	1600.7	13.4	31.8							
122.75	343.0	1607.0	13.7	32.5							
123.25	336.8	1613.2	15.2	32.7							
123.75	330.5	1619.5	14.5	32.6							
124.25	324.2	1625.8	14.1	28.7							
124.75	318.0	1632.0	15.7	31.7							
125.25	311.7	1638.3	15.2	30.7							
125.75	305.4	1644.6	17.1	31.3							
126.25	299.1	1650.9	16.6	30.0							
126.75	292.8	1657.2	16.8	31.7							
127.25	286.6	1663.4	15.9	33.4							
127.75	280.3	1669.7	15.9	31.3							
128.25	274.0	1676.0	18.7	35.0							
128.75	267.7	1682.3	16.7	34.3							
129.25	261.4	1688.6	16.6	31.1							
129.75	255.1	1694.9	14.7	31.7							
130.25	248.8	1701.2	14.3	27.5							
130.75	242.4	1707.6	14.6	33.4							

131.25	236.1	1713.9	14.8	30.1							
131.75	229.8	1720.2	14.3	33.1							
132.25	223.5	1726.5	14.8	30.1							
132.75	217.2	1732.8	14.1	30.9							
133.25	210.8	1739.2		30.0							
133.75	204.5	1745.5		32.6							
134.25	198.2	1751.8	15.3	31.0							
134.75	191.9	1758.1	15.8	29.2							
135.25	185.5	1764.5	16.4	31.7							
135.75	179.2	1770.8	15.5	31.3							
136.25	172.8	1777.2	15.1	32.4							
136.75	166.5	1783.5	16.3	32.9							
137.25	160.1	1789.9	15.9	30.1							
137.75	153.8	1796.2	15.3	30.9							
138.25	147.4	1802.6	16.2	33.5							
138.75	141.1	1808.9	15.3	33.5							
139.25	134.7	1815.3	16.2	33.7							
139.75	128.4	1821.6	15.3	32.7							
140.25	122.0	1828.0	17.0	33.1							
140.75	115.6	1834.4		33.6							
141.25	109.2	1840.8	18.3	34.6							
141.75	102.9	1847.1	18.4	33.5							
142.25	96.5	1853.5	18.1	35.2							
142.75	90.1	1859.9	18.0	30.5							
143.25	83.7	1866.3	17.8	32.2							
143.75	77.4	1872.6	21.2	30.5							
144.25	71.0	1879.0	18.6	32.8							
144.75	64.6	1885.4	17.9	34.1							
145.25	58.2	1891.8	18.6	31.1							
145.75	51.8	1898.2	18.8	30.4							

146.25	45.4	1904.6	17.8	32.7						
146.75	39.0	1911.0	16.8	33.9						
147.25	32.6	1917.4	16.9	33.6						
147.75	26.2	1923.8	15.4	32.3						
148.25	19.8	1930.2	16.6	32.3						
148.75	13.3	1936.7	19.2	33.6						
149.25	6.9	1943.1	20.5	34.4						